UNIVERSITÉ DE SHERBROOKE

Faculté de génie

Département de génie chimique et de génie biotechnologique

AMÉLIORATION DE LA RÉSISTANCE À LA CORROSION DE RÉFRACTAIRES EXPOSÉS À DES ALLIAGES D'ALUMINIUM LIQUIDE PAR DES REVÊTEMENTS DE NITRURE D'ALUMINIUM SYNTHÉTISÉS PAR SUSPENSION PLASMA

REFRACTORIES CORROSION RESISTANCE IMPROVEMENT AGAINST MOLTEN ALUMINUM ALLOYS BY ALUMINUM NITRIDE SUSPENSION PLASMA SYNTHESIZED COATINGS

Thèse de doctorat

Spécialité : Génie chimique

Faranak BARANDEHFARD

Sherbrooke (Québec) Canada Août 2022

MEMBRES DU JURY

Professeur François GITZHOFER

Directeur

Monsieur Alain SIMARD

Évaluateur industriel

Professeur Ali DOLATABADI

Évaluateur externe

Professeur Jocelyn VEILLEUX

Évaluateur

Professeur Patrick VERMETTE

Évaluateur et Rapporteur

To my parents, Maryam, and Mohammad…

&

To my love, Bijan…

Acknowledgment

I would like to express my deep and sincere gratitude to my supervisor Professor François Gitzhofer for all his invaluable scientific guidance, support, and encouragement. My special thanks go to Mr. Alain Simard for his patience, understanding, and belief in me.

I extend thanks to my supervisory committee members Professor Jocelyn Veilleux, Professor Patrick Vermette, and Professor Ali Dolatabadi for accepting to evaluate my thesis.

I cannot express enough thanks to Dr. Kossi Béré for his treasured technical support, and empathy. I would like to express my sincere appreciation to Dr. Alireza Hekmat, and Dr. James Aluha for their technical support, encouragement, and positive energy. I have learned a lot from their knowledge, patience, and professional behavior.

I confer special recognition to all the personnel at the Research and development center of Pyrotek Inc.: Dr. Behzad Majidi, Julien Hardy, Maxime Drolet for synthesis of ceramic samples, and corrosion test; plateforme de recherche et d'analyse des matériaux (PRAM): Mr. Stéphane Gutierrez, Mr. Charles Bertrand, Mrs. Sonia Blais, Bibliothèque des sciences, de génie et cartothèque: Mrs. Lyne Laroche, and Laboratory of chemical department: Mr. Paul-Ludovic Karsenti.

I am extending my heartfelt thanks to my love, Bijan without him and his unconditional love and enthusiastic support, I could never pass this stage of my life and completed this work.

I am extremely grateful to my parents Maryam and Mohammad, my sister Parisa and my brothers Alireza and Amir, for their never-ending love and support.

I would like to thank my friend Mojtaba, for being next to me through all the difficulties. My deepest thanks to Anneliese Speidel and Haleh Mazandaranian, with their training and always positive energy helped me to release my tension and control my stress during the Ph.D.

I would like to thank my friends, lab mates, colleagues, and research team Hamed Rashidi, Marie-Claude Fournier, Komlan Koumbogle, Romain Fernique, Sara Ghotb, Huidong Hou, and Jérôme Menneveux, for a cherished time spent together in the lab.

RÉSUMÉ

L'objectif de cette thèse est d'identifier et de synthétiser un matériau réfractaire résistant à la corrosion lorsqu'il est en contact direct avec l'alliage Al-Mg fondu qui est très agressif chimiquement. La revue de littérature suggère des solutions pour résoudre le problème de la corrosion : (i) l'ajout d'agents non mouillants (NWA) au réfractaire, et (ii) le dépôt d'un revêtement protecteur sur la surface réfractaire. La première partie de ce projet vise à trouver les NWA qui protégeraient le réfractaire de mullite fondue blanche (WFM) de la corrosion, et les résultats expérimentaux ont montré qu'un mélange de CaF_2 et de $BaSO_4$ est le NWA le plus efficace pour protéger ces réfractaires de la corrosion. Pour la solution (ii) c'est-à-dire le revêtement, la littérature existante suggère que : a) son point de fusion doit dépasser la température de service du four, b) son coefficient de dilatation thermique doit être proche de celui du substrat, et c) il doit être chimiquement résistant à l'alliages d'Al fondu.

La propriété de résistance à la corrosion du revêtement candidat sélectionné en contact avec l'alliage d'Al fondu a été évaluée à l'aide du logiciel thermochimique FactSage. Les résultats ont montré que le nitrure d'aluminium (AlN) répond aux critères requis. Sa synthèse et déposition in situ à l'aide de la technologie de projection par plasma de suspension par induction radiofréquence (RF) sur divers substrats (Ti, Mo et acier au carbone) a été réalisée et étudiée dans la deuxième partie de la thèse. Les performances de résistance à la corrosion des phases hexagonales et cubiques d'AlN en contact avec l'Al fondu ont été étudiées à l'aide du module de simulation de dynamique moléculaire ab initio (BOMD) du logiciel BIOVIA Materials Studio. Une telle analyse était nécessaire pour la quantification de la résistance à la corrosion des phases hexagonales par rapport aux phases cubiques d'AlN, ce qui n'est pas possible avec le logiciel FactSage. Les résultats montrent que les deux phases ont une énergie interfaciale dans le régime de physisorption confirmant que ni les phases AlN cubique ni hexagonale ne sont réactives au contact de l'Al fondu. Différentes études paramétriques ont été réalisées pour comprendre les paramètres les plus importants qui affectent la synthèse des revêtements d'AlN cubique. Les principaux résultats sont :

1) Le meilleur ratio de distribution granulométrique en masse est de 75 % de la gamme granulométrique (– 5 +1 μm) mélangé à 25 % de (– 35 + 17 μm). L'analyse quantitative de

Rietveld (RQA) utilisant des données de diffraction des rayons X (XRD) a indiqué que les meilleurs revêtements étaient constitués de 82 % d'AlN (80 % cubique + 2 % de structure cristalline hexagonale).

2) La mélamine est avantageuse par rapport à l'urée en produisant plus d'espèces azotées actives dans le plasma.

3) Le liquide de suspension d'hexadécane surpasse l'éthylène glycol, l'huile minérale légère et l'éthanol dans la formation d'AIN.

4) L'utilisation d'additifs promotionnels tels que le bore, le BN, le Mo, le Y_2O_3, l'AlN ou l'Al_4C_3 peut stimuler la formation d'AlN. La quantité optimale d'AlN promotionnel est de 0,22 % en poids de la masse totale de la suspension, produisant jusqu'à 72 % d'AlN dans le revêtement.

5) Parmi les substrats en Ti, Mo et acier au carbone, la formation d'AlN est significativement plus élevée avec ce dernier que pour les deux autres.

6) Entre 6 et 10 cm, la distance de déposition de 8 cm fournit un temps de séjour suffisant pour la réaction d'Al et des espèces actives d'azote, maximisant ainsi la formation d'AlN.

Enfin, le revêtement AlN synthétisé par plasma a été testé pour sa résistance à la corrosion par contact direct avec un alliage fondu Al-5wt%Mg à 1123 K et s'est avéré stable après le test.

Mots clés : Aluminosilicate réfractaire, essai d'immersion Alcan, revêtement non mouillant, corrosion par alliage d’aluminium fondu, synthèse et projection par plasma de suspensions (SPS), nitrure d'aluminium (AlN), mélamine.

ABSTRACT

The objective of this thesis is to identify and synthesize a corrosion-resistant refractory composition when in direct contact with the chemically aggressive molten Al-5wt%Mg alloy. The reviewed literature suggests solutions for resolving the corrosion issue: (i) the addition of non-wetting agents (NWAs) to the refractory, and (ii) deposition of a protective coating on the refractory surface. The first part of this project aims at finding the NWAs that would protect the white fused mullite (WFM) refractory from corrosion, and the experimental results showed that a mixture of CaF_2 and $BaSO_4$ is the most impactful NWA protecting the WFM refractories from corrosion. For solution (ii) i.e., the coating, the existing literature suggests that: a) its melting point should exceed the furnace service point, b) its thermal expansion coefficient should be close to that of the substrate, c) it should be chemically resistant to molten Al alloy. The corrosion-resistant property of the selected coating candidate in contact with molten Al alloy was assessed using FactSage thermochemical software. The results showed that aluminum nitride (AlN) meets the required criteria and its in-situ synthesis and deposition using radio-frequency (RF) induction suspension plasma spray (SPS) technology on various substrates (Ti, Mo, and carbon steel) was performed and studied in the second part of the thesis. The corrosion-resistant performance of hexagonal and cubic phases of AlN in contact with molten Al was studied using the ab initio molecular dynamic (BOMD) simulation module of BIOVIA Materials Studio software. Such analysis was needed for the quantification of corrosion resistance of hexagonal versus cubic phases of AlN which is not possible to get using FactSage software. The results show that both phases have interfacial energy within the physisorption regime confirming that neither cubic nor hexagonal AlN phases are reactive in contact with molten Al. Different parametric studies have been done to understand the most important parameters which affect the cubic AlN coatings synthesis. The main results are:

1) The best particle size distribution ratio by mass is 75% of the (– 5 +1 μm) size range mixed with 25% of (– 35 + 17 μm). Rietveld quantitative analysis (RQA) using X-ray diffraction (XRD) data indicated that the coatings consisted of up to 82% AlN (80% cubic + 2% hexagonal crystal structure).

2) Melamine is advantageous over urea by producing more active nitrogen species in the plasma.

3) Hexadecane suspension carrier outperforms ethylene glycol, light mineral oil, and ethanol in the formation of AlN.

4) The use of promotional additives such as boron, BN, Mo, Y_2O_3, AlN, or Al_4C_3 can stimulate the formation of AlN. The optimum amount of promotional AlN was 0.22-wt% of the total suspension mass, producing up to 72% AlN in the coating.

5) Among Ti, Mo, and carbon steel substrates, the formation of AlN was significantly higher with the latter than with the two others.

6) Between the range of 6 to 10 cm, the standoff distance of 8 cm provides a residence time long enough for the reaction of Al and nitrogen active species, maximizing the formation of AlN.

Finally, the plasma synthesized AlN coating was tested for corrosion resistance by direct contact with molten Al-5wt%Mg alloy at 1123 K and found to be stable after the test.

Key words: Aluminosilicate refractory, Alcan immersion test, non-wetting coating, corrosion by molten aluminum alloy, synthesis and deposition by suspension plasma spray (SPS), aluminum nitride (AlN), melamine.

Intentionally left blank.

TABLE OF CONTENTS

LIST OF FIGURES

LIST OF TABLES

LIST OF ACRONYMS

Abbreviations	Definition
AlN	Aluminum Nitride
Al	Aluminum
APS	Atmospheric/Air Plasma Spray
DC	Direct Current
DFT	Density Functional Theory
EB-PVD	Electron Beam Physical Vapor Deposition
EDX	Energy Dispersive X-ray Spectroscopy
ESPRESSO	opEn-Source Package for Research in Electronic Structure, Simulation, and Optimization
FS73 AL	Aluminosilicate substrate including 73% SiO_2
FS76 AL	Aluminosilicate substrate including 76% SiO_2
LPPS	Low Pressure Plasma Spray
MD	Molecular Dynamic
MMT	Million Metric Ton
MR	Molar Ratio
NWA	Non-Wetting Agents
P	Pressure
RF	Radio Frequency
SEM	Scanning Electron Microscope
SPS	Suspension Plasma Spray
SLPM	Standard Liter Per Minute

TGA	Thermogravimetric Analysis
T	Temperature
VLPPS	Very Low-Pressure Plasma Spray
VPS	Vacuum Plasma Spraying
XRD	X-ray Diffraction

CHAPTER 1 INTRODUCTION

1.1 Background

On the global scale, the aluminum (Al) industry plays a very important role in the manufacturing sector owing to the superb characteristics of Al and its alloys such as elasticity, malleability, lightness, corrosion resistance, and recyclability. However, Al production is a maintenance and energy intensive electro-pyrometallurgical process, which also requires a significant quantity of refractories that hold molten alloys and electrolytic baths (Dutta, Apujani and Gupta, 2016). For instance, for every ton of Al, the energy consumption varies between 12.8-16 MWh, depending on the technology, and the age of the smelters (Tost *et al.*, 2018). Furthermore, most of the maintenance in the Al industry is caused by corrosion-born refractory failures that the Al industry has been addressing (Vicario *et al.*, 2015).

Refractories used in the Al industry should be resistant to mechanical damage from scrap charging, during skimming, cleaning, and fluxing, as well as tolerant to thermal and mechanical shock during heating and cooling of the furnaces. Moreover, the refractories must be resistant to corrosion, especially at the bellyband (the triple point between molten Al alloy, refractory, and atmosphere), where the molten alloy attacks and penetrates the refractories. Common refractory materials used in Al melting and holding furnaces contain aluminosilicates, and when the molten Al reacts with the free silica of aluminosilicate refractory materials, corundum forms, which causes spalling in the refractory walls and reduces their thickness (Kaupuzs *et al.*, 2003). The stability of refractory materials in contact with molten Al alloys impacts severely the quality of the final Al alloy products and the lifespan of the linings (Yan and Fan, 2001). Consequently, the refractory materials that are used in molten Al alloy furnaces should meet all the following requirements:

- Sustain working temperatures in the range of 700 - 750 ºC
- Be corrosion resistant
- Have a low solubility in molten Al alloys
- Be resistant to thermal shock
- Have excellent volume stability

- Be resistant to abrasion, and both oxidation and reduction (Yurkov, 2015).

The surface of every ceramic refractory material used in molten Al alloy furnaces should be free of porosity, because molten alloys diffuse through porous materials and, consequently, corrosion occurs more quickly. Moreover, to avoid corrosion, ceramic components should not be prone to dissolve in molten Al alloys (Yurkov and Pikhutin, 2009).

1.2 Problem statement

In the process of producing Al-Mg alloys, the refractory linings are in direct contact with hot molten Al-Mg alloy and due to the aggressive behavior of Al and Mg elements, the refractories are exposed to severe corrosion. In addition, the refractories are subjected to various destructive mechanisms such as thermal shock, mechanical impact, and erosion. Chemical corrosion along with erosion are two main failure mechanisms for molten Al alloys in contact with refractories. Chemical corrosion consists of three stages: wetting of refractory, the penetration of molten Al alloys, and reaction with refractory components (X. M. Zhang and Chen, 2015), (Hou *et al.*, 2013), (Salomon *et al.*, 2017).

Two major regions of the refractory that are prone to corrosion by molten Al alloys are:

(i) The bellyband or the triple point between the refractory, the molten Al alloy, and air interfaces (Afshar, Allaire and Dajoux, 2004); and
(ii) Below the liquid metal line where the surface of the refractory is in constant contact with molten alloy (Kessman *et al.*, 2009).

Refractory corrosion is linked to two fundamental consequences:

(i) Alloy mixtures get contaminated with solid impurities and removal of such impurities (i.e., purification processes) is an expensive procedure, while the contamination changes the final alloy's characteristics.
(ii) The lifespan of the furnace is affected by corrosion, which consequently increases the maintenance cost (Afshar and Allaire, 2004).

High temperatures exacerbate the corrosion process leading to degradation of refractories, which chip off and cause impurities in the Al alloy products (X. Zhang and Chen, 2015).

1.2.1 Potential solutions

To tackle the corrosion of refractories in contact with molten Al alloy, two approaches are proposed:

(a) Addition of non-wetting additives such as $BaSO_4$, CaF_2, MgF_2, and AlF_3 to the mixture of refractories to improve their corrosion resistance against molten Al alloy (Adabifiroozjaei, Koshy and Sorrell, 2013). These additives minimize corrosion by lowering the wettability of refractories in contact with the molten metal.

(b) Application of coatings such as nitrides, borides, or carbides on the low-quality bulk refractories to protect them from chemical and physical reactions.

A comprehensive discussion on the pros and cons and applications of these approaches are given in chapters 2, 4, and 5.

1.3 Objectives of the project

1.3.1 General objective

To improve the lifespan of aluminosilicate refractories in contact with the molten Al-5wt%Mg alloy.

1.3.2 Specific objectives

Given the general objective of the project, the specific objectives of the project are:

1) Identify the causes of the corroded refractory: since the corrosion changes the phases and composition of the refractory in the melting process of Al alloy, the corroded refractory must be analyzed for the identification of new phases and compositions. This process was completed using X-ray diffraction (XRD) analysis and Energy Dispersive X-Ray (EDX) analysis.
2) Study the effect of non-wetting additives on the corrosion resistance of white fused mullite (WFM) refractories in contact with molten Al-5wt% Mg alloy by doing Alcan immersion test.
3) Identify the potential coating candidates: this step involves identification of the potential candidates based on required physicochemical properties using Cambridge engineering

selector (CES) software; the selection of the final coating material followed the results of computer modeling using FactSage for the reaction between molten Al and potential candidates. Among the most promising ceramic coatings, AlN was selected for its superior properties over materials such as Si_3N_4, TiB_2, and ZrB_2.

4) Synthesis of the selected coating: in this step, the AlN coating was synthesized using suspension plasma spray technology.
5) Investigating the effect of suspension plasma parameters on in-situ synthesis and deposition of AlN: in this step, the impact of particle size of Al powder, the nature of nitriding agents, liquid suspension carriers, promotional additives, substrate materials, and deposition standoff distance on the formation of AlN was investigated.
6) Analysis of corrosion performance of AlN coating: The corrosion resistance of synthesized AlN was assessed in contact with molten Al alloy at 850 ^{o}C for two hours.

1.4 Hypothesis

Spraying AlN coating on metallic substrates (carbon steel, Ti, Mo) can protect them from corrosion when in contact with Al-Mg alloys at high temperatures. These results will be applicable to the aluminosilicate- refractories using a suitable bond coat.

1.5 Novelties

In summary, the novelties of this research are as follows:

1- Application of RF induction suspension plasma spray (SPS) method for the first time for in-situ synthesis and deposition of AlN coatings.
2- Using melamine as a nitriding agent in suspension plasma spray technology to produce cubic AlN coating.

1.6 Organization of the thesis

Chapter 1: Introduction

This chapter provides a brief introduction on the importance of mechanical and chemical characteristics of refractories used in the Al industry and outlines the potential solutions and

opportunities to improve the existing practices. Then, the general and specific objectives of this research, the hypotheses, as well as the novelties are discussed.

Chapter 2: State of the art

This chapter is divided into two sections:

(a) **Refractories and non-wetting additives:** this section presents the reviewed literature on the refractories used in the Al industry, their corrosion mechanism, and reactions. Furthermore, to better understand the effect of non-wetting additives, the experimental results on the effect of non-wetting on corrosion resistance of white-fused mullite (WFM) refractories are presented at the end of this section.

(b) **Aluminum nitride (AlN): properties, applications, synthesis, and coating methods:** this section is comprised of brief background and general information about AlN, its properties and application, advantages of reactive suspension plasma spray over conventional plasma spray technology, followed by modeling and validation of results.

Chapter 3: Methodology

This chapter presents the step-by-step process of the experimental framework of the project of in-situ synthesis and deposition of AlN coating using suspension plasma spray technology.

Chapter 4: Plasma synthesis of cubic AlN

This chapter summarizes the results of the study on the effect of standoff distance, liquid suspension composition, substrate materials, and nitriding agent on the in-situ formation and deposition of AlN by SPS technology.

Chapter 5: Effect of Al size distribution and promoters on plasma synthesis of AlN

This chapter concerns the influence of Al particle size distribution and various promoters on the in-situ formation and deposition of AlN by the SPS method. Moreover, results from *Ab* initio modeling of Al and cubic/hexagonal AlN interaction at 1200K and calculated interfacial energy between Al and AlN are presented.

Chapter 6: Conclusion

This chapter discusses the key findings of this research, main conclusions followed by recommendations for future work.

CHAPTER 2 STATE OF THE ART

This chapter is divided into two sections, where part (a) defines and focuses on the existing problem in Al industry about refractories, their corrosion and degradation, and part (b) focuses on prescribing a potential solution to overcome the identified problem.

(a) Validation of literature data about refractories and non-wetting additives: this section presents the reviewed literature on the refractories used in the Al industry, their corrosion mechanism, and reactions. Furthermore, to better understand the effect of non-wetting additives, this review was supplemented by limited experimental results exploring the effect of non-wetting additives on the corrosion resistance of white-fused mullite (WFM) refractories, which are presented at the end of this section. These preliminary experiments were conducted to validate the information found in the literature.

(b) Aluminum nitride (AlN): properties, applications, synthesis, and coating methods: this section presents an introduction to the PhD project, comprising a brief background and general information about AlN, its properties and application as a coating, the advantages of reactive suspension plasma spray over conventional plasma spray technology, followed by modeling and validation of the results by corrosion tests.

2.1 REFRACTORIES AND NON-WETTING ADDITIVES

This chapter is based on a published journal article entitled "Improving corrosion resistance of aluminosilicate refractories towards molten Al-Mg alloy using non-wetting additives: A short review" with minor edition.

2.1.1 Avant-propos

Auteurs et affiliation :

Faranak Barandehfard: Étudiante au doctorat, Département de génie chimique et de génie biotechnologique, Université de Sherbrooke, Québec, Canada.

James Aluha: Chercheur postdoctoral Département de génie chimique et de génie biotechnologique, Université de Sherbrooke, Québec, Canada.

Alireza Hekmat-Ardakan: Chargé de projet, Centre de recherche et développement, Pyrotek Inc., Sherbrooke, Québec, Canada.

François Gitzhofer: Professeur titulaire, Département de génie chimique et de génie biotechnologique, Université de Sherbrooke, Québec, Canada.

Date d'acceptation: 9 septembre 2020

État de l'acceptation: version finale publiée

Revue: Materials (MDPI)

Référence :(Barandehfard *et al.*, 2020a)

Lien d'accès : https://doi.org/10.3390/ma13184078

Titre français : Amélioration de la résistance à la corrosion des réfractaires d'aluminosilicate vis-à-vis de l'alliage Al-Mg fondu à l'aide d'additifs non mouillants : une brève revue

Author Contributions: Conceptualization, F.B., A.R.H., and F.G.; methodology, F.B., A.R.H.; software, F.B. and A.R.H; validation, F.G., and J.A.; formal analysis, F.B., A.R.H. and J.A.; investigation, F.B.; resources, A.R.H.; writing—original draft preparation, F.B.; writing—review and editing, J.A. and F.G.; visualization, J.A.; supervision, F.G.; project administration, F.G.; funding acquisition, F.G. All authors have read and agreed to the published version of the manuscript.

Contribution à la thèse:

As discussed in Chapter 1, there are two solutions to tackle the corrosion problem in refractories used in the Al industry, namely: (a) the application of non-wetting agents, and (b) the deposition of a protective coating on the substrate material. In this chapter, the corrosion mechanism between aluminosilicate refractories and molten Al alloy is studied and a review is provided, which includes the corrosion mechanism, wetting phenomena, and different reactions of aluminosilicate refractories with molten Al alloy, and this is supplemented by some experimental data. The study investigated the effect of the addition of several non-wetting agents ($BaSO_4$, CaF_2, Secar®71, and wollastonite) to white fused mullite composition on its corrosion-resistant in contact with molten Al-5wt%Mg alloy. This work lays the foundation for the thesis, and it explores the challenges in the Al industry. Using a mixture of $BaSO_4$ and CaF_2 inhibits partially the formation of spinel and, therefore, prevents cracks and improves the corrosion resistance of the WFM refractories.

Résumé

La corrosion des réfractaires en contact avec des alliages aluminium-magnésium à haute température conduit à la contamination des produits d'alliage Al-Mg par des impuretés solides provenant de réfractaires dégradés. Lorsque les phases spinelle et corindon se forment dans les réfractaires, des fissures sont générées et propagées par diffusion d'Al-Mg fondu, conduisant à une corrosion sévère. Dans cet article de synthèse, le phénomène de corrosion est discuté et les travaux publiés sont résumés, complétés par nos récents résultats expérimentaux. À l'aide du test d'immersion d'Alcan d'une durée de 96 heures, des matériaux à base de mullite fondue blanche (WFM) ont été évalués pour leur résistance à la corrosion et leur comportement interfacial. WFM a été modifiée en utilisant différents additifs non mouillants avec une concentration de 2% (NWA) tels que le $BaSO_4$, le CaF_2, le ciment Secar®71 et la wollastonite pour améliorer leurs performances au contact de l'alliage Al-Mg fondu à 850ºC. Les propriétés mécaniques des échantillons telles que la résistance à la flexion et à la compression ont été évaluées, en plus de la diffraction des rayons X et de l'analyse microscopique (microscopie optique et électronique à balayage couplée à une cartographie élémentaire aux rayons X). Il a été observé que les fissures étaient formées dans les échantillons qui comportaient uniquement du ciment $BaSO_4$, CaF_2, Secar®71 ou de la wollastonite comme NWA. Cependant, aucune fissure n'est apparue dans l'échantillon promu à la fois avec 1 % en poids de CaF_2 et 1 % en poids de $BaSO_4$, en raison de propriétés anti-mouillantes améliorées en plus d'inhiber la formation de spinelle. Il s'agit d'une découverte importante dans la prévention des fissures et l'amélioration de la résistance à la corrosion des réfractaires.

Mots-clés : Réfractaire aluminosilicate ; alliage aluminium-magnésium fondu; test d'immersion Alcan; mullite; non mouillant; corrosion

Improving corrosion resistance of aluminosilicate refractories towards molten Al-Mg alloy using non-wetting additives: A short review

2.1.2 Abstract

Corrosion of refractories in contact with high temperature aluminum-magnesium alloys leads to contamination of the Al-Mg alloy products by solid impurities from degraded refractories. Where both the spinel and corundum phases form in the refractories, cracks are generated and propagated by diffusion of molten Al-Mg, leading to severe corrosion. In this review paper, the corrosion phenomenon is discussed, and published work is summarized, supplemented by our recent experimental results. Using the Alcan immersion test for 96 hours, materials based on white-fused mullite (WFM) were evaluated for their corrosion resistance and interfacial behavior. WFM was modified using different 2-wt% of non-wetting additives (NWAs) such as $BaSO_4$, CaF_2, Secar®71 cement, and wollastonite to improve their performance when in contact with molten Al-Mg alloy at 850°C. The mechanical properties of the samples such as flexural and compressive strength were evaluated, in addition to X-ray diffraction and microscopic analysis (optical and scanning electron microscopy coupled with X-ray elemental mapping). It was observed that cracks formed in samples promoted with only $BaSO_4$, CaF_2, Secar®71 cement, or wollastonite. However, cracks did not appear in the sample promoted with both 1-wt% CaF_2 and 1-wt% $BaSO_4$, because of improved anti-wetting properties in addition to partially inhibiting spinel formation. This is a significant finding in the prevention of cracks and improvement of the refractory corrosion resistance.

Keywords: Aluminosilicate refractory; molten aluminum-magnesium; Alcan immersion test; mullite; non-wetting; corrosion

2.1.3 Introduction

Aluminum and its alloys have unique properties such as a very high strength-to-weight ratio, exhibiting high elasticity, superior malleability, easy machining ability, excellent corrosion resistance, good thermal and electrical conductivity, and it can be recycled or used repeatedly without any change in its properties. These outstanding properties of Al and its alloys promote the extensive use of the materials in various industries. Such applications involve infrastructure

development and transportation machines or equipment. Consequently, the demand for Al production continues to increase annually, with the global market growing by about 5% year-over-year (The-Aluminum-Association, 2011). Since the Al industry has an annual turnover of about 60 million metric tons (MMT/year) in the world and represents about US$ 90 billion, this demonstrates its importance in the world economy. Consequently, the consumption of refractories for molten Al alloy furnaces is also increasing dramatically (Dutta, Apujani and Gupta, 2016). Some of the biggest concerns in the Al industry touch on the environmental footprint and energy consumption, as the International Aluminum Institute has reported (Alamdari, 2017). For example, producing one ton of Al requires 400 kg of carbon, which is a significant amount. In addition, depending on the technology used and the age of the smelters, the energy consumption varies between 12.8 – 16 MWh for every ton of Al produced. Some issues of concern being addressed by the Al industry are greenhouse gas emission (Tost *et al.*, 2018), (Guan *et al.*, 2019), (Weirauch, 2005), high energy demand (Obaidat *et al.*, 2018), (Yang *et al.*, 2017), loss of aluminum through oxidation (Bonner, 2015), recycling of Al scraps (Capuzzi and Timelli, 2018), corrosion of cathode lining (Guan *et al.*, 2019), and corrosion of the refractory used in Al melting furnaces (Vicario *et al.*, 2015). For example, Rio Tinto and Alcoa Corporation initiated a revolutionary Al manufacturing process through the Elysis project that produces oxygen and eliminates all direct greenhouse gas (GHG) emissions from the traditional smelting process. In order to reduce GHG emissions, carbon anodes can be replaced by inert anodes as is the case in the Canadian Elysis project (Solheim, 2018), (Solheim, 2019). In China, lithium is used in the aluminum electrolysis process to decrease the operational temperature of the smelters in order to diminish energy consumption (Haraldsson and Johansson, 2018). Given the high erosion rate of graphitized cathodes, modified copper-insert collector bars and graphitic cathodes are used (Liu, Zhou and Zhao, 2019), (Rivoaland, 2016). Some non-wetting additives (NWA) are added to refractories that regularly come in contact with molten Al alloys to diminish their susceptibility to corrosion (Adabifiroozjaei, Koshy and Sorrell, 2013).

The low density displayed by Al and its alloys with excellent mechanical, thermal and electrical properties (Davis, 2001), provides a combination of unique properties that makes Al and its alloys some of the most versatile and economically valuable metallic materials. The aluminum-magnesium (Al-Mg) series of alloys integrate lightweight and high strength with corrosion

resistance properties. These properties lend the alloys extensive application in marine or seawater operations, ship structures, and chemical plants where the alloys are exposed to robust corrosive environments (Cobden and Banbury, 1994). Since Mg is a chemically active element and is eminently suitable in various types of reactions, its presence in molten Al enhances the reactivity of the Al-Mg alloy (Jakovics *et al.*, 2002). Some authors (Bonadia *et al.*, 2006), have shown that when Mg as a highly reducing alloying element is added to molten Al, it exposes the furnace refractories to the aggressive and corrosive conditions of the molten alloys. The presence of Mg has two effects: (i) it reacts with aluminosilicate refractories to form magnesium aluminate spinel ($MgAl_2O_4$), which causes an expansion that consequently creates cracks and spalling in the refractories; and (ii) Mg diminishes the viscosity of the molten alloy and hence it increases the penetration of the molten alloy into the porous structure of the refractory (Siljan *et al.*, 2002). Therefore, frequent replacement of the refractories is required due to the constant physical and chemical damages experienced, and consequently the Al industry is a notable consumer of the refractories.

There are many physical and chemical parameters that strongly affect the corrosion resistance of refractories and they include grain size, the composition of the refractory and molten metal, the refractory density and its porosity (Yan and Fan, 2001). In order to tolerate high temperatures, refractories should be thermally resistant when in contact with hot molten metals, slags, and fluxes (Lee and Zhang, 1999). Refractory materials, which normally include a high fused silica (SiO_2) fraction, are used in molten Al furnaces because of its low thermal expansion coefficient and the presence of SiO_2 at high temperatures leads to low expansion variations. Although the corrosion resistance of SiO_2 is lower than that of Al_2O_3 when in contact with molten Al alloy, it is widely used in the refractory areas because of its low thermal expansion coefficient (Kaupuzs *et al.*, 2003). Higher Al_2O_3 to SiO_2 ratio in refractory composition increases the corrosion resistance against Al attacks. Furthermore, some non-wetting additives such as $BaSO_4$, CaF_2, MgF_2, AlF_3 are used to improve the corrosion resistance of the refractories in contact with molten Al alloys (Sakamoto, 2013).

Therefore, the purpose of this review paper is to summarize and discuss progress reports available in literature, supplemented by some recent experimental results by our research group using different non-wetting additives to improve the performance of a mullite-based refractory.

The modified materials were evaluated for their effect on the corrosion resistance of white fused mullite (WFM) materials in direct contact with a molten Al-Mg alloy. WFM was selected for this project because it has a high melting point (over 1800 ºC), exhibiting excellent thermal stability, it has low reversible thermal expansion, in addition to displaying high resistance to chemical corrosion when exposed to high temperatures and excellent thermal shock resistance. Although there is significant diffusion of gases and volatile species from the molten alloy infiltrating the refractory lining through existing porosities, this paper only focuses on the penetration effects of the molten Al and Al-Mg.

Refractory materials are used in all steps of production of Al and its alloys, from the alumina calciners to the cast house furnaces and other metal handling equipment (Siljan *et al.*, 2002). The Al industry is one of the biggest consumers of refractories in Canada, with Quebec province in particular being one of the preeminent producers of Al in the world. Therefore, Pyrotek Inc. (Canada), which is also based in Quebec and is a major producer of refractories for the Al industry sponsored this study. Notwithstanding Al-Li alloys with corresponding corrosive chemical reactions, the attention of this paper focuses on the corrosion of furnace refractories used in producing Al and Al-Mg alloys.

2.1.4 Application of refractories in the aluminum industry

2.1.4.1 Refractory selection criteria

Since refractory materials have high melting points, fusing them is difficult except at extremely high temperatures. These materials are thermally stable and do not decompose easily when heated and thus, they retain their chemical and physical properties at high temperatures (Nwaogu and Tiedje, 2011). Their melting point is the most critical physical property because it determines the temperature limit at which the material can be used without melting or decomposing (Hlavac, 1982). Other important criteria used for selecting suitable refractory materials include density and porosity, mechanical resistance, thermal conductivity, thermal shock resistance and chemical resistance (Vicario *et al.*, 2015).

Some authors have observed that refractories in contact with molten Al alloys easily get corroded and degraded because of the extremely reducible behavior of the molten Al alloys (Adabifiroozjaei, Koshy and Sorrell, 2013). Therefore, selection of the refractory material is a

critical matter, which depends on the interaction between molten Al alloys and the refractory materials as well as the nature of their reactions at high temperatures. There are some ceramic refractory materials that have excellent chemical and thermal stability when in contact with molten Al, and they include nitride-based materials such as aluminum nitride (AlN) (Long and Foster, 1959), silicon nitride (Si_3N_4) (Mouradoff *et al.*, 1994), and boron nitride (BN) (Reusch, Gmbh and Rudolph, 2015). Other examples involving yttria-based materials are $Y_2Ti_2O_7$ (Nagasaka *et al.*, 2015), (Nguyen *et al.*, 2015) and nano scale coatings of Y_2O_3 which shows high density, uniform structure and high hardness (Kitamura *et al.*, 2011). Among all refractories used in the Al industry, although $Al_2O_3.SiO_2$ refractories are prone to corrosion by molten Al alloys specially Al-Mg, they are popular in the Al industry due to cost advantages, their ease of availability, and remarkable versatility. Knowledge of reaction thermodynamics is a prerequisite in the selection of suitable refractory materials for molten Al-Mg alloys because it provides real insight into the reactivity potentials of the materials. Figure 2-1 is an image derived from FactSage^{TM} thermodynamic software (Montreal, Canada) (C. W. Bale *et al.*, 2016), which is a theoretical calculation between 100g of mullite ($3Al_2O_3.2SiO_2$) when it comes into direct contact with 100 g of molten 5-wt%Mg/Al between 850 ^oC and ambient temperature. The model confirmed the potential formation of Al_2O_3 and $MgAl_2O_4$ that exists below 850^oC accompanied by the reduction of SiO_2 to release Si. It is shown that about 13% of SiO_2 diffuses from mullite to the molten Al alloy changing the liquid concentration from Al-(5-wt%) Mg to 81.8% Al + 13% Si + 0.1% Mg. It is also shown that 4.9%Mg out of the initial 5% reacts with mullite to form the spinel. By cooling, the liquid solution solidifies to A4 (13% Si + $2x10^{-5}$% Al) and A1 (81.8% Al + $1.3x10^{-3}$% Mg + 1% Si) indicating a total destruction or corrosion of mullite. Therefore, choice refractory materials that should be used with molten Al alloy furnaces must have the following characteristics:

- They should have a low solubility in molten Al alloys;
- They should have excellent volume stability;
- They must be resistant to abrasion, oxidation, and reduction (Yan and Fan, 2001); and
- They must lower the chemical potential difference between the refractory and the molten alloy (X. Zhang and Chen, 2015).

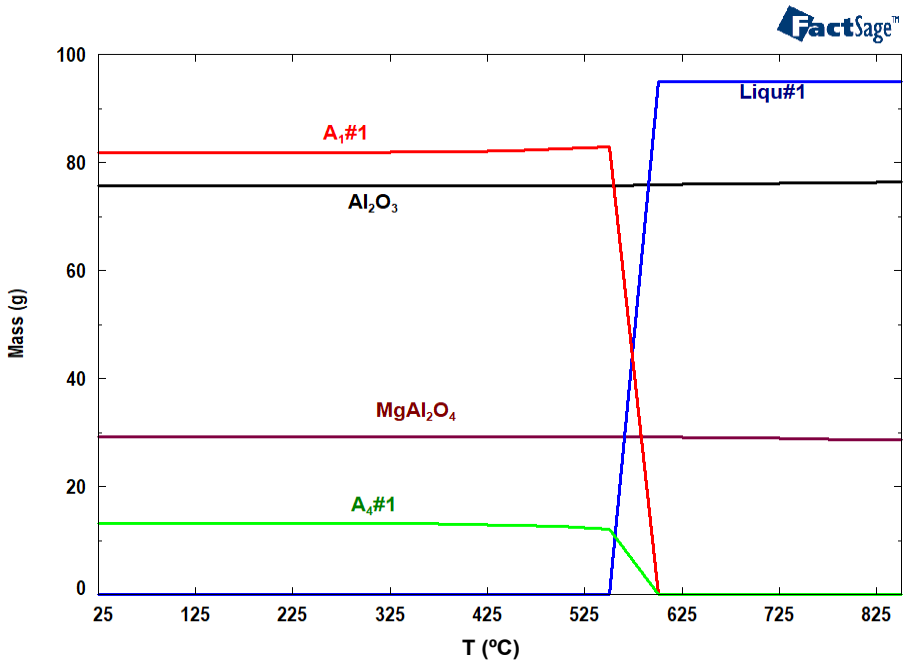

Figure 2-1. Equilibrium calculation of $3Al_2O_3.2SiO_2$ and molten Al-Mg alloy. Liq#1: liquid solution containing: 81.79%Al + 13%Si + 0.11%Mg, A1#1: solid solution containing: 81.8%Al + $1.3x10^{-3}$ %Mg + 1% Si, A4#1: Solid solution containing 13%Si + $2x10^{-5}$ %Al.

2.1.4.2 Properties of aluminosilicate refractories

Typical refractories used in the Al industry are based on aluminosilicate refractories. However, their main limitation is the infiltration and reaction of the molten Al alloy into them, which leads to their corrosion. As a result, the non-wetting properties of these refractory materials should be boosted against molten Al alloy to avoid infiltration. Applications of aluminosilicate refractories include insulations behind hot-face materials, furnace linings, and laboratory crucibles. These refractories are extensively used in melting and holding Al alloy furnaces due to their availability and cost advantages (Yan and Fan, 2001). Not only should refractories be resistant to high temperatures and thermal shocks (Ribeiro *et al.*, 2016), but should also be resistant to corrosion when in contact with molten alloys and slag (Sadik, Amrani and Albizane, 2014).

Some investigations into the corrosion kinetics of aluminosilicate materials under static and dynamic conditions have been conducted using molten 5-wt%Mg/Al and the influence of SiO_2 amount (Afshar and Allaire, 2000). The researchers reported that the corrosion depth has a direct relationship with the SiO_2 content in the aluminosilicate refractory during immersion tests in Al-5wt%Mg at 850°C. Therefore, the higher the SiO_2 amount, the greater the corrosion depth. Increasing the amount of SiO_2 decreases the incubation time, which is defined as the time that

a trace of corrosion (less than 1 mm) can be observed on a refractory by the unaided eye (Afshar and Allaire, 2000). However, some authors observed that content higher than 20-wt% SiO_2 did not show any remarkable difference in the incubation period (Lee and Zhang, 1999). The authors advanced the idea that perhaps the diffusion process that controls the refractory corrosion under dynamic conditions is more severe than under static conditions. Mullite (the only stable binary crystalline phase in the aluminosilicate phase diagram) belongs to the category of aluminosilicate refractories with compositions of different Al_2O_3 to SiO_2 ratios ranging from $3Al_2O_3.2SiO_2$ to $3Al_2O_3.SiO_2$ (Lee and Zhang, 1999). When the SiO_2 in the aluminosilicate refractories comes into contact with molten Al, they form corundum, and therefore, the higher the Al_2O_3, the greater the corrosion resistance to the molten Al alloy (Nandy and Jogai, 2013).

2.1.5 Corrosion of refractories in Al industry

2.1.5.1 The origin of corrosion

Different parts of the refractory linings experience different contact times with molten Al alloys and consequently, they are exposed to different destructive mechanisms such as thermal shock, mechanical impact, corrosion, and erosion. Among them, corrosion and erosion are the worst damages experienced because the two have a severe effect on the purity of the resulting alloys and also on the lifetime of the refractory linings (Afshar and Allaire, 2004). Therefore, one of the chief limitations in the production of Al alloys is the destructive behavior of Al and Mg in contact with refractories. There are two main failure mechanisms when molten Al alloys come into contact with refractories:

Chemical corrosion, which is related to the penetration of molten alloys and reactions that lead to the dissolution of the refractory materials to form a new interphase layer (Yan and Fan, 2001), where the two main channels for the initial penetration of molten metal into the refractories are open pores and microcracks (Lee and Zhang, 1999);

Erosion, which refers to a swift flow of molten alloy in the furnace, and if it includes some hard particles, the problem becomes worse, and mechanical wear occurs on the surface of the refractories (Yan and Fan, 2001).

These problems are tackled by making dense refractories that lack any form of porosity and dissolvable components in molten Al alloy in order to improve the refractory life span (Yan and

Fan, 2001). Wear originating from corrosion as a result of refractory contact and reaction with molten metal alloy is accelerated by high temperature (Hou *et al.*, 2013), in addition to material losses and the synergetic effects between increased surface roughness, wear, and corrosion processes (Ayyagari *et al.*, 2018). In this process, dissolution, penetration, and reaction mechanisms occur between the liquid and solid phases (Scheid, Schreiner and D'Oliveira, 2012). These phenomena result in considerable changes in the microstructure, morphology, and composition of the refractory, and consequently altering the chemical and physical properties of the materials (Zhang, Hosemann and Maloy, 2010).

When two different metals contact each other at high temperatures, the formation of a new phase between them strongly depends on three factors: (i) their chemical potentials, (ii) the nucleation and chemical reaction conditions at the start of the inter-diffusion process, and (iii) the mobility of the elements (Zhang, Hosemann and Maloy, 2010). Therefore, a method to retard the corrosion is required. For example, in Fe-based crucibles, the addition of Al in the refractory components could diminish the discrepancy in their chemical potential, thereby, decreasing the driving force towards corrosion (Cheng and Wang, 2009). Moreover, grain boundaries are normally regarded as the main diffusion paths in the corrosion of refractories, and the grain size is an essential parameter for the improvement of the corrosion-wear resistance of refractories (X. Zhang and Chen, 2015). Based on the amount of Mg in the Al-Mg alloy, MgO, $MgAl_2O_4$, or both can be the product of the reaction between the Al alloys and the refractory, besides the presence of enough oxygen aiding the oxidation of the Al.

It is important to note that refractories in the Al industry should be resistant to detrimental effects of the process, both physical and chemical. Physical impacts include mechanical abuse arising from scrap charging, thermal and mechanical shocks during skimming, cleaning, and fluxing. The chemical effects comprise, molten alloy attacks, penetrations, and corrosion, especially in the bellyband area (the triple point between molten alloy, refractory, and atmosphere) as exemplified in Figure 2-2.

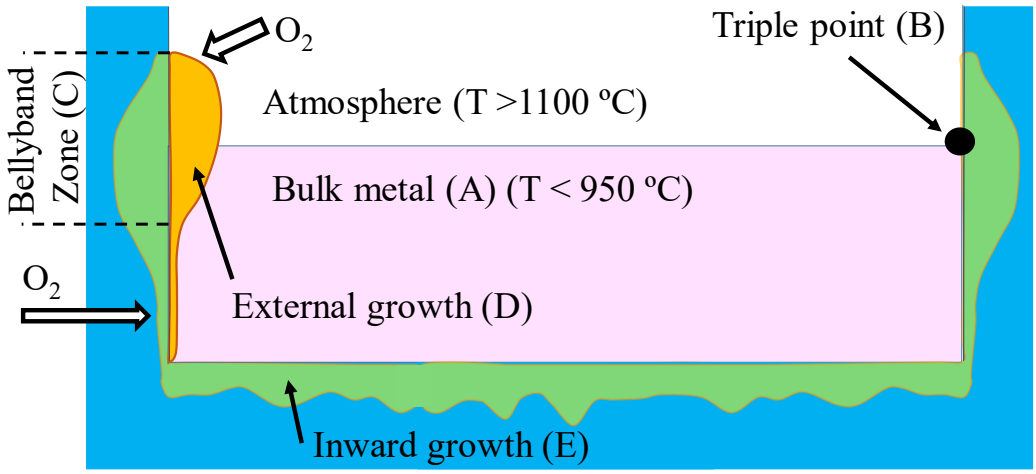

Figure 2-2. A schematic of internal and external corundum growth in Al-treatment furnaces modified after (Allaire, 2000a).

Zone A represents molten Al, and the triple point B is where the liquid Al meets the refractory and air. The belly band zone C represents the region where the fluctuating meniscus of the molten metal meets the refractory. When molten Al reacts with atmospheric oxygen in the belly band area, it builds external corundum at the interface between the atmosphere, aluminum bath, and the refractory, which is shown by zone D. With the penetration of molten Al into the refractory and its reaction with refractory oxides such as SiO_2, it produces internal corundum represented by zone E.

Two major undesirable products are arising from the reaction between Al and the free silica of aluminosilicate refractory materials, that is, the spinel, and corundum, which causes spalling of the refractory walls and reduces their thickness (Kaupuzs *et al.*, 2003). This in turn affects the durability of refractory materials and impacts negatively the lifetime of the refractory linings as well as the quality of the final Al product as a consequence of contamination from the impurities that migrate into the Al alloys (Yan and Fan, 2001). Normally, corrosion is initiated by the molten Al alloy wetting the refractory surface, followed by infiltration of the molten metal and subsequently the formation of a new phase at the interface of the refractory and the molten metals (Lee and Zhang, 1999).

2.1.5.2 Corrosion mechanisms

Since refractory linings are subjected to various degradation phenomena such as thermal shock, mechanical impact, abrasion, corrosion, and erosion, corrosion is the worst case and impacts

severely on both metal quality and refractory lifetime (Ntakaburimvo and Allaire, 2004). In summary, it has been illustrated that aluminosilicate refractories in contact with molten Al alloy face mainly three problems: (a) penetration of molten alloy to the refractory (b) side-wall build-up, and (c) silicon pickup by the metal (Brondyke, 1953). The diffusion of Al and Si is a crucial factor in governing penetration rates. During melting and holding of Al alloy in aluminosilicate refractories, molten Al penetrates the refractory by a reaction between Al and SiO_2. Then corundum and free Si are formed as demonstrated in Figure 2-1 by FactSage™. Consequently, the volume expansion due to the penetrated materials causes and exacerbates cracking. Furthermore, the ultimate life of refractories could be predicted by calculating the amount and rate of liquid penetration using models that incorporate both thermodynamic and kinetic studies (Siljan *et al.*, 2002). There are four main zones of corrosion in furnaces, as shown in Figure 2-2:

(i) Zone A below the metal line that is continuously in direct contact with the molten Al alloy (Kessman *et al.*, 2009);
(ii) The zone C and D below and above the metal line, which is alternately exposed to the Al alloy and the furnace atmosphere (Brondyke, 1953);
(iii) The zone above the metal line, which is exposed to the furnace atmosphere and gases (Brondyke, 1953);
(iv) The triple point B between the refractory, the molten alloy, and the air interfaces (Afshar, Allaire and Dajoux, 2004).

It has been reported that corundum is formed at the surface of molten Al alloys due to the presence of oxygen from the atmosphere, and that molten metal can flow through channels of the corundum (Quesnel, Afshar and Allaire, 1996). When the corundum grows upwards, the molten alloy can reach the refractory wall above the metal line. A combination of high temperature and capillary action of the corundum growth provides an ideal opportunity for more penetration of metal alloys inside the refractory. Similarly, the molten alloy can diffuse through the open porosity of the refractory, with oxidation occurring in the pores (Quesnel, Allaire and Afshar, 1998).

2.1.5.3 The effect of the porosity in the refractory

It has been observed that the purity of any Al alloy under synthesis has a direct relationship with the characteristics of the refractory materials, such as their chemical and mineralogical

composition, types of binders utilized (Kazemi, 2019), and their permeability (Nandy and Jogai, 2013). If, for example, the permeability of the refractory to air increases, it will promote corrosion since it allows gases such as oxygen and water vapors to diffuse through the refractory pores (Allaire, 2000b). When molten Al alloy finally penetrates the refractory, it reacts with aluminosilicate to form corundum, and through a redox reaction (Equation 2-5), free Si is released (Yan and Fan, 2001). The formation of corundum starts just below the bellyband and extends upwards, penetrating and sticking strongly to the porous refractories, and this makes it difficult to remove, and cleaning the furnace becomes a challenging and expensive process (Engel, 2015).

2.1.5.4 The effect of corundum formation

The two critical destructive mechanisms, which reduce the lifespan of refractories, are chemical attack (corundum growth or corrosion from flux addition) and mechanical damage (from ingot loading, cleaning practices, or thermal shock). Although the creation of the corundum layer in the refractory prevents further infiltration of the molten Al, the formation of corundum leads to an expansion in the refractory volume and, consequently, distortion and finally creating cracks (Wynn, Coppack and Steele, 2014). There are two forms of corundum, internal and external:

(i) Internal corundum exists where the molten alloy penetrates the refractory and reacts with the refractory oxides such as SiO_2, corroding the refractory while at the same time, corundum precipitates below the liquid metal line on the refractory surfaces, as illustrated in Figure 2-2. The reactions can be described through Equation 2-1 and Equation 2-2 (Shukla, 2009).

(ii) External corundum at the bellyband (the triple point where the liquid metal, atmospheric oxygen, and solid refractory contact each other), thereby inducing maximum corrosion to form corundum. Alloy penetration into the refractories is initiated by capillary action, and in the presence of atmospheric oxygen produces corundum, which adheres severely to the refractory's surfaces (Nandy and Jogai, 2013). With the presence of Mg in molten Al, the corrosion process accelerates and reduces the refractory oxides more aggressively than with Al alone.

2.1.5.5 The effect of molten alloy infiltration

Thermodynamically, the reaction between SiO_2 and Al is possible at all temperatures above the melting point of Al. At the surface, due to the direct contact between molten Al alloy and the refractory, the corrosion process begins with wetting of the refractory followed by a reaction that creates an interface with a different chemical composition. In this process, the molten Al diffuses to the refractory through existing cracks and open pores. The amount and rate of diffusion is related to the pore size, the temperature, composition, and texture of the refractory materials as well as the type of alloy under synthesis (Yurkov and Pikhutin, 2009).

2.1.5.6 Effect of enhanced wetting on refractories

One of the most critical interfacial phenomena occurring at the refractory surface is the wetting process because it facilitates the penetration of the molten alloys through the open pores and then initiates various chemical reactions with the refractory (Brondyke, 1953). Results from various studies show that the principal genesis of corrosion is related to the wetting, penetration, and reaction of Al alloys with the refractory. It has been observed that the penetration of the molten Al alloys is highest at the zone of the refractory that is exposed to both air and molten Al alloy (the bellyband). For instance, at the onset of corrosion in aluminosilicate refractories, the SiO_2 is reduced by molten Al to Si, which is accompanied by a negative volume change (Yurkov and Pikhutin, 2009), by as much as 26 % volume reduction (Hemrick, Headrick and Peters, 2008). Therefore, this volume contraction may generate cracks that allow further metal penetration into the refractory (Gao, Afshar and Allaire, 2004), and the amount of Al alloy diffusing into the unreacted refractory controls the rate of corrosion (Brondyke, 1953). Furthermore, an increase in air permeability of the refractory will raise the probability of corrosion by molten alloys and allow gases such as oxygen and water vapor to diffuse through the refractory pores (Allaire, 2000b).

2.1.6 Corrosion of typical refractories in Al industry

2.1.6.1 Aluminosilicate refractories and corrosion

In aluminosilicate refractories, the molten Al alloy on the surface reacts with the atmospheric oxygen in air to form a porous corundum film, which has channels that direct molten alloy to the surface of the refractory and this process is intensified at the bellyband (Yurkov and

Pikhutin, 2009). When the metal penetrates the refractory to reduce SiO_2, this part of molten Al is gradually saturated by free Si. However, the SiO_2 does not release Si into the metal bath spontaneously, because there is a Si concentration gradient created, and the diffusion rate of Si to the metal bath controls the corrosion kinetics (Gao, Afshar and Allaire, 2004). The reaction between aluminosilicate refractories and molten Al is almost immediate, and it is possible to prove it by measuring the amount of Si in the molten alloy, with the results showing that the amount of Si increases significantly during the first 2–3 days (Yurkov, 2017).

When in contact with molten Al, the corrosion of aluminosilicate refractories initiates the decomposition of $3Al_2O_3 \cdot 2SiO_2$ to Al_2O_3 and SiO_2. Then the SiO_2 is reduced by Al metal to form the primary corundum (α-Al_2O_3) and releases the free Si to molten Al (Hemrick, Headrick and Peters, 2008), and if the molten Al-Mg alloy is in contact with the refractory, then MgO, $MgAl_2O_4$ (spinel), and $MgSiO_3$ are formed. Formation of spinel causes a 17% volume expansion, which is accompanied by spalling of refractories, and by creating cracks, higher penetration of molten alloy is achieved (Siljan *et al.*, 2002). During the process, the formation of additional metastable phases like η- and θ-Al_2O_3 or suboxides like AlO and SiO are observed (Salomon *et al.*, 2017). The primary Al_2O_3, which is obtained from the decomposition of $3Al_2O_3.2SiO_2$, builds a scaffold for the precipitation of secondary corundum and spinel. The Al_2O_3 that is formed from the reduction of SiO_2, at first is in a metastable phase (η, θ-Al_2O_3), but later transforms to the thermodynamically more stable corundum phase (α-Al_2O_3) (Salomon *et al.*, 2017). Since there is a competition towards the formation of MgO, $MgAl_2O_4$ and Al_2O_3 because SiO_2 has a higher affinity for Mg in comparison to Al, the reaction products are in direct relation to the Mg concentration in the Al-Mg alloy. Replacement of SiO_2 by MgO, $MgAl_2O_4$ or Al_2O_3 increases volume contractions by about 18%, 27%, or 38%, respectively (Shi *et al.*, 2016a). Various reactions that occur in the above-mentioned process are summarized in Table 2-1, with values recorded to one decimal point.

Table 2-1. Calculated Gibbs free energy and enthalpy of reactions of Al industry refractories at 750 ^{O}C using FactSage thermochemical software.

Equation No.	Reaction	ΔG^{o}(kJ)	ΔH^{o}(kJ)	Ref.
Equation 2-1	$4Al(l) + 3O_2(g) \rightarrow 2Al_2O_3(s)$	-2708	-3387	(Afshar and Allaire, 2004)
Equation 2-2	$3SiO_2(s) + 4Al(l) \rightarrow 2Al_2O_3(s)^* + 3Si(s)$	-528	-673	(Allahverdi, Afshar and C.Allaire, 1998)
Equation 2-3	$3Mg(l) + 4Al_2O_3(s) \rightarrow 3MgAl_2O_4(s)^{**} + 2Al(l)$	-208	-202	(Allahverdi, Afshar and Allaire, 1996)
Equation 2-4	$3Mg(l) + 1.5SiO_2(s) \rightarrow 3MgO(s) + 1.5Si(s)$	-383	-469	(Nandy and Jogai, 2013)
Equation 2-5	$3(3Al_2O_3.2SiO_2)(s) + 8Al(l) \rightarrow 13Al_2O_3(s) + 6Si(s)$	-1033	-1416	(Adabifiroozjaei, Koshy and Sorrell, 2015)
Equation 2-6	$Mg(g) + ½O_2(g) \rightarrow MgO(s)$	-491	-609	(Allaire, 2001)
Equation 2-7	$2SiO_2(s) + 2Al(l) + Mg(l) \rightarrow MgAl_2O_4(s) + 2Si(s)$	-422	- 516	(Yurkov and Pikhutin, 2009)
Equation 2-8	$MgO(s) + Al_2O_3(s) \rightarrow MgAl_2O_4(s)$	-30	-230	(Lidsay, Bakker and Dewing, 1964)
Equation 2-9	$2Mg(l) + SiO_2(s) \rightarrow 2MgO(s) + Si(s)$	-255	313	(Yurkov and Pikhutin, 2009)
Equation 2-10	$3Mg(l) + Al_2O_3(s) \rightarrow 3MgO(s) + 2Al(l)$	-119	-133	(Lidsay, Bakker and Dewing, 1964)
Equation 2-11	$3MgO(s) + 2Al(l) \rightarrow 3Mg(l) + Al_2O_3(s)$	+119	133	(Lidsay, Bakker and Dewing, 1964)
Equation 2-12	$Mg(l) + ½O_2(g) + Al_2O_3(s) \rightarrow MgO.Al_2O_3(s)$	-520	-632	(Yurkov and Pikhutin, 2009)
Equation 2-13	$3Mg(l) + MgA1_2O_4(s) \rightarrow 4MgO(s) + 2A1(l)$	-88	-109	(Lidsay, Bakker and Dewing, 1964)
Equation 2-14	$2Mg(l) + Si(s) \rightarrow Mg_2Si(s)$	-100	-63	(Shi *et al.*, 2016a)
Equation 2-15	$BaAl_2Si_2O_8(s)^{❁} + 2⅔Al(l) \rightarrow 2Si(s) + BaAl_2O_4(s) + 1⅓Al_2O_3(s)$	248.0	-	(Ibarra C *et al.*, 2015)
Equation 2-16	$8Al(l) + 3Al_6Si_2O_{13}(s) \rightarrow 13Al_2O_3(s) + 6Si(s)$	-1040	-1415	(Koshy, 2009)
Equation 2-17	$CaO(s) + Al_2O_3(s) + 2SiO_2(s) \rightarrow CaAl_2Si_2O_8(s)^{❁❁}$	-126	-104	(Adabifiroozjaei, Koshy and Sorrell, 2015)
Equation 2-18	$CaF_2(s) + Al_2O_3(s) + 2SiO_2(s) \rightarrow CaAl_2Si_2O_8(s) + SiF_4(g)$	-1440	-1082	(Adabifiroozjaei, Koshy and Sorrell, 2015)

*Corundum; ** Spinel; ❁Celsian; ❁❁Anorthite

Based on the information in the Table 2-1, Equation 2-1 indicates the oxidation reaction of Al metal to form alumina, while Al can reduce SiO_2 to produce corundum according to Equation 2-2. Mg can reduce alumina to form the $MgAl_2O_4$ spinel based on Equation 2-3, or it can reduce SiO_2 to form MgO and free Si as given in Equation 2-4. Free Si may also be produced by the reaction between the molten Al and aluminosilicate refractory, according to Equation 2-5, while Equation 2-6 shows the oxidation reaction of Mg in air to form MgO. Equation 2-7 shows that both metallic Al and Mg can combine with SiO_2 to form the $MgAl_2O_4$ spinel, and based on the Gibbs free energy provided in Equation 2-8, it is comparatively less likely for the spinel to form by the reaction between MgO and Al_2O_3. Further, from Gibbs free energy values, it is easier to reduce the SiO_2 in a refractory (Equation 2-9), than the Al_2O_3 (Equation 2-10), and both produce MgO and free Si or Al respectively. Equation 2-11 shows that it is not possible for molten Al to reduce MgO, but the presence of atmospheric oxygen can enhance the spinel formation based on Equation 2-12, while the probability of excess Mg reacting to decompose the spinel into MgO and free Al in the absence of air is very remote, according to Equation 2-13. From Equation 2-14, there exists some possibility that the presence of Mg in the molten alloy can react with the free Si released from Equation 2-2 to produce $MgSi_2$, although the probability is low. On the other hand, Equation 2-15 shows that celsian ($BaAl_2Si_2O_8$), which is a good anti-corrosion material in the refractories can be decomposed so as to produce corundum and free Si, and the same is also possible for mullite ($Al_6Si_2O_{13}$), according to Equation 2-16. From the small ΔG^o values, Equation 2-17 and Equation 2-18 indicate the formation of anorthite as a stable phase since it can hardly decompose to produce corundum.

From the above equations, the FactSage^{TM} modelling provided in Figure 2-1 correctly predicts the reaction between mullite ($3Al_2O_3.2SiO_2$) and molten 5-wt%Mg/Al. Equation 2-2 shows that the SiO_2 in mullite produces corundum. With negative ΔG^o (as -528 kJ), it means that the reaction will definitely occur. Based on the model, Al_2O_3 (corundum) easily forms at all temperatures (black line). Similarly, from Equation 2-5, corundum forms when mullite reacts with molten Al (ΔG^o = -1033 kJ). In the presence of Mg, spinel forms at all temperatures (maroon line). In Equation 2-3, when Mg reacts with Al_2O_3 arising from Equation 2-2, the ΔG^o is -208 kJ; while in Equation 2-7, the concurrent presence of Al and Mg reacts with the SiO_2 in mullite to form the spinel (ΔG^o is -422 kJ). The negative Gibbs free energy values mean the

reactions will easily take place. This implies that the model sufficiently predicts the destruction of pristine mullite in contact with molten Al-Mg alloy.

There are two practical ways of avoiding the corrosion of refractory materials that are in direct contact with molten Al alloys:

(i) Chemical means, by the addition of non-wetting additives (NWA) as components of the refractory materials (Sudha *et al.*, 2018); and
(ii) Physical means, through surface modification and densification by, for example, creating a protective coating on the surface of the refractory, which comes in direct contact with the molten alloy (Nandy and Jogai, 2013).

Since wetting plays a crucial role in initiating the corrosion process, followed by infiltration of the molten metal into the refractory, and then a reaction between molten alloy and the refractory, in this work, an approach is developed where NWAs are added to refractories in direct contact with the molten Al alloys. The central substrate under review in this work is based on mullite, and the anti-wetting additives are incorporated in order to improve the corrosion resistance of the refractories by forming new phases.

Refractories produced with mullite attract much attention, especially for high temperature applications not only in the Al industry, but also among others, the steel industry, because of their high thermal stability and excellent resistance to thermal shock, creep, and corrosion. Mullite can be added to the initial refractory paste or generated in situ during firing, which intrinsically creates different microstructure from that formed by mullite when added initially (Ribeiro *et al.*, 2016). It has been observed that the presence of mullite minimizes the corrosion of alumina refractories (Sudha *et al.*, 2018).

2.1.7 Wettability and surface tension

2.1.7.1 Origin of wettability theory: Young's regime

Thomas Young introduced the relationship between the contact angle and surface energy of different interfaces using Equation 2-19 (Asadollahi, 2017), and this definition has been used to quantify the wetting behavior of surfaces. Therefore, the wettability of a surface by a liquid is measured based on the contact angle between the solid and the liquid droplet, as shown in Figure 2-3. According to Young's equation in our situation, it was expected that enhanced wetting of

refractories would occur when the contact angle between molten Al alloy and the refractory substrate was lower than 90°. If the angle was greater than 90°, then the refractory becomes non-wetting when in contact with a droplet of molten alloy.

$$\cos\theta_Y = \frac{(\gamma_{sg} - \gamma_{sl})}{\gamma_{lg}} \qquad \text{Equation 2-19}$$

where:

θ_Y= Young's contact angle at equilibrium, and

γ = Surface energy for liquid-gas (LG), solid-gas (SG), and solid-liquid (SL) interfaces

Since the wettability of a surface is governed by the chemical properties and the microstructure of the surface, which is mainly determined by its free surface energy or surface tension (γ_{SG}), the greater the free surface energy, the easier it is for the liquid to spread upon the surface and vice versa (Jafari, Asadollahi and Farzaneh, 2013). Equation 2-19 is therefore valid for perfectly flat and uniform surfaces, which limits its application for real surfaces. Besides, other external forces such as change of properties with increasing temperature can enhance wetting (Bormashenko, 2015).

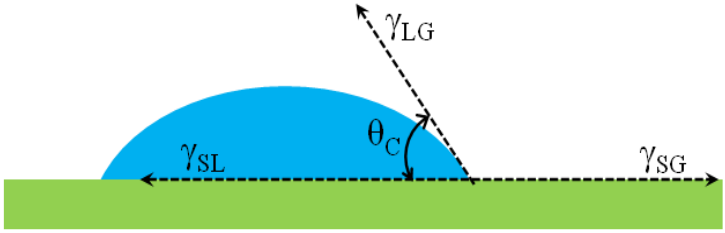

Figure 2-3. Contact angle as defined by Young modified after (Asadollahi, 2017).

2.1.7.2 Wetting heterogeneous surfaces: The Wenzel regime

Since Young's equation is applicable for ideal surfaces that are free from inhomogeneities, the study of wetting behavior puts into consideration the surface roughness of refractories. Wenzel and Cassie-Baxter models account for surface defects in the wetting of rough and heterogeneous materials (Jafari, Asadollahi and Farzaneh, 2013). In the Wenzel state, which Robert Wenzel first introduced in 1936 (Wenzel, 1936), the relationship between the contact angle and surface roughness is highlighted. It is assumed that the liquid completely penetrates into the surface roughness grooves, for which reason this surface is considered as a wetted regime (Barbieri,

2007). It is further asserted that surface roughness increases the contact angle when it is higher than 90^{o}, which implies that hydrophobicity is enhanced by an increase in surface roughness (Guo, Liu and Su, 2008).

2.1.7.3 Penetration of a liquid on a rough surface: Cassie-Baxter regime

About eight years after the postulation of the Wenzel theory, Cassie and Baxter (Cassie and Baxter, 1944), both investigated the contact angle of a liquid drop in contact with a rough surface before the liquid penetrated into the surface grooves and they predicted the relationship between roughness and contact angle. The Cassie-Baxter wetting regime is a quasi-stable state, which, over time, transforms to the Wenzel state (Ishino and Okumura, 2008). In reality, a combination of these two regimes is usually observed for example, as a water drop partially diffuses into the grooves of a solid surface (Ishino, Okumura and Quéré, 2004), (Bormashenko and Grynyov, 2012).

2.1.7.4 Surface wetting by a moving droplet: Hysteresis contact angle

On most occasions, contact angles will be measured and derived for a static water drop, which is not in motion. However, for a moving water drop, it can display dynamic contact angles with some differences in the advancing (front side) and the receding (rear side), which defines the hysteresis contact angle (HCA), as shown in Figure 2-4 (Asadollahi, 2017). HCA is one of the critical factors in the roll-off behavior of a liquid. Lower contact-angle hysteresis causes a lower adhesion force between the droplet and the surface and results in easier sliding of the droplet on the surface (Jafari, Asadollahi and Farzaneh, 2013). The magnitude of HCA is affected by different factors such as surface roughness, surface chemical heterogeneity, droplet size effect, surface deformation, and adsorption/desorption phenomena (Barbieri, 2007). Among them, the HCA is more affected by surface roughness, where it changes a homogeneous surface to heterogeneous one (Zhou and De Hosson, 1995). It has been observed that the roughness parameter enhances the hysteresis and static contact angle of hydrophobic surfaces. However, in some cases an increase in the static contact angle lowers the HCA. This decrease in HCA can qualitatively be explained by the switch from Wenzel to Cassie-Baxter regime, with air trapped at the macroscopic liquid-solid interface (Johnson, 1964).

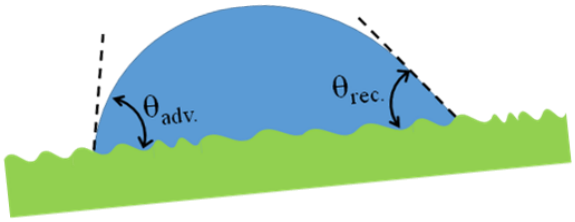

Figure 2-4. Dynamic contact angles at the interfaces of a moving droplet modified after (Asadollahi, 2017).

2.1.7.5 Wettability and the triple line

Another factor whose influence has a vital role in the wetting phenomenon is the triple line, which is defined as the line where the solid, liquid and air phases meet (Bormashenko, 2015). It has been illustrated that there is a strong relationship between the HCA value on very rough surfaces and triple line characteristics such as shape and continuity (Chen *et al.*, 1999). As a case study, three hypothetical roughness topologies were considered and the best case for minimizing the HCA was obtained from the use of thin pillars creating a discontinuous triple line (Ibarra Castro *et al.*, 2010). It was observed that surface roughness generated by slender pillars with the smallest thickness in proportion to the height and periodic spacing displayed the best hydrophobic properties. Decreasing the ratio between the thickness of the pillar and its height results in a higher-energy barrier system, which means that the roughness height has a significant impact on the magnitude of the energy barrier as it is at maximum, for the microstructure with very tall and slender pillars. So, nanopillars with suitable spacing render great superhydrophobic surfaces. In can therefore be concluded that the wettability of a surface depends on its physicochemical properties in addition to its micro or nano roughness. These two factors determine the extent of adhesive forces between a liquid droplet and the surface (Kubiak and Mathia, 2014).

2.1.7.6 Surface wettability and interface formation

In the metal industry, wetting by molten alloy must be controlled to protect refractories against corrosion, which is impacted by factors such as impurities, the alloying elements in the melt and the surface roughness of the refractories (Nogi *et al.*, 2004). Since in many material processing techniques such as casting, the molten metals and refractories are in direct contact, the properties of the final product are profoundly affected by the high-temperature properties of molten metal,

and the interfacial wetting/reaction phenomena. Therefore, the interaction between molten metal and substrate is one of the critical factors considered when choosing suitable materials and processing parameters (Sobczak *et al.*, 2010). For the Al-SiO_2 system, there is a significant reduction in the droplet volume during the reactive wetting, and this is due to the formation of a new interfacial compound between Al and SiO_2 to produce Al_2O_3-Al(Si) composite (Equation 2-2). Modeling has shown that the final contact angle is governed by the interfacial reaction, and that the wetting process by contact angle only is not sufficient (Nogi *et al.*, 2004).

Some researchers who investigated the reactivity of molten Al with various ceramic oxides such as Al_2O_3, SiO_2 and mullite, have demonstrated that a strong relationship between wettability and reactivity in the system cannot be established (Sobczak, 2005). However, other researchers have reported that the wetting of a ceramic substrate is usually accompanied by an interfacial reaction between the metal and the ceramic. Hence, a new composition was formed during the reaction at the interface, with a strong effect on the magnitude of the interfacial free energy and subsequently changes in the contact angle (Fujii, Nakae and Okada, 1993). It has been observed that in the reactive wetting of molten Al on different α-Al_2O_3 surfaces, the process is reaction-limited and the spreading rate is dominated by the change in the solid–liquid interfacial free energy per unit time (Shen *et al.*, 2003a).

2.1.7.7 Improvement of aluminosilicate corrosion resistance by non-wetting additives

Today, researchers are focusing on a new generation of refractories in order to decrease the infiltration and attack from molten Al alloys. To achieve this goal, the use of some NWAs has been attempted, which includes aluminum phosphate ($AlPO_4$) (Luz, Gomes and Pandolfelli, 2015), vanadium pentoxide (V_2O_5) (Adabifiroozjaei, Koshy and Charles Christopher Sorrell, 2012), barium sulphate ($BaSO_4$) (Aguilar-Santillan, 2008), strontium sulphate ($SrSO_4$) (Ibarra Castro *et al.*, 2010), calcium fluoride (CaF_2), aluminum fluoride (AlF_3) (Afshar and Allaire, 2001), aluminum titanite (Al_2TiO_5) (Soofi, Binz and Anderson, 2018), wollastonite ($CaSiO_3$) and boron nitride (BN) (Afshar and Allaire, 2001). The NWAs lessen the wettability capacity of refractories in contact with molten Al alloy, and after reaction with SiO_2, they produce a more stable phase than free Si, which improves the corrosion resistance of the materials. Some additives containing fluorides such as AlF_3 and CaF_2 also act as mineralizers, and during high-

temperature calcination of aluminosilicate refractories, they favor the formation of mullite (Afshar and Allaire, 2001).

Furthermore, when molten Mg is in contact with AlF_3 or CaF_2, it forms MgF_2, which can also act as a non-wetting agent (Decker, 2011). The presence of wollastonite in refractories improves their corrosion resistance by reducing the permeability of the materials (Allaire and Guermazi, 1999). Incorporating BN improves corrosion resistance of the refractories by the formation of the thermally stable aluminoborate phase and it also lowers the solubility of boron in the molten Al, which drastically increases the corrosion resistance of andalusite refractories when in contact with molten Al alloys (Adabifiroozjaei, Koshy and Charles Chris Sorrell, 2012).

For $BaSO_4$ additives, it has been reported that $BaSi_2Al_2O_8$ forms and therefore, the amount of free Si in the matrix decreases to improve the corrosion resistance of the refractory (Koshy, 2009), making $BaAl_2Si_2O_8$ exhibit good corrosion resistance when in contact with molten Al alloy (Adabifiroozjaei *et al.*, 2015). The most effective application of $BaSO_4$ in protecting the refractory matrix against corrosion is when particles in the size range of less than 50 Tyler mesh are use (Allaire, 2000b). The reaction of barite ($BaSO_4$) with Al_2O_3 and SiO_2 in aluminosilicate refractories forms a stable and less reducible phase of celsian ($BaAl_2Si_2O_8$) and/or hexacelsian, during the firing process, which creates a barrier against increased penetration of molten Al alloy (Adabifiroozjaei, Koshy and Sorrell, 2015). It should be considered that $BaSO_4$ is the most effective NWA in the firing temperature between 815°C and 1050°C, but it has been shown that as the temperature rises to more than 1050°C, the $BaAl_2Si_2O_8$ phase becomes undetectable in the refractory and it loses its efficiency (Afshar and Allaire, 1996). This is attributed to either the phase transformation of celsian ($BaAl_2Si_2O_8$) or its decomposition based on Equation 2-15 (Koshy *et al.*, 2011), when in contact with molten Al alloy.

For AlF_3 and CaF_2, this temperature reduces to less than 950°C. Anorthite ($CaAl_2Si_2O_8$), which is similar to $BaAl_2Si_2O_8$, characterizes the CaO-ceramics and results in a dense structure and thus, the reaction in anorthite predominantly advances through solid diffusion. Most of the Ca is concentrated in the β-Al_2CaSi_2 phase formed, adhered at the interface (Ortiz-Covarrubias *et al.*, 2015).

2.1.8 Experimental methods and analysis

2.1.8.1 Experimental procedure

To tackle the corrosion issues, researchers have proposed two solutions. The first one consists in the addition of non-wetting additives against molten Al alloy to the mixture of the refractory materials. These additives minimize corrosion by reducing the wettability of refractories in contact with the molten metal. The second solution involves coating the refractories with thin films to protect them from chemical and physical reactions. The reason why the industry can use coatings instead of modifying the substrate composition is to improve the surface functional performance, and to expand lifetime of the refractory substrates by decreasing the wear due to abrasion, erosion and/or corrosion. An increase of the profitability is expected as the coatings allow the use of a low-cost base refractory materials (Pfender, 1999).

In this work, mullite samples whose composition includes the presence of $3Al_2O_3.2SiO_2$ were investigated for their corrosion resistance behavior. An attempt to lower the wettability of the white fused mullite (WFM) refractory was made by incorporation of NWAs, and their mechanical properties and corrosion resistance were evaluated and characterized. The objective of this research project was to find and develop new refractory materials that can be used in the Al industry for lengthening the life span of the refractories that come into direct contact with molten Al alloy. The hypothesis advanced in this study involves evaluating the impact of adding NWAs to increase the corrosion resistance of the refractories. It is thought that the refractory materials get damaged due to the diffusion of molten alloy through their pores and subsequently react with the materials. Anti-wetting additives improve the corrosion resistance by the formation of new phases that create a barrier, which reduces the diffusion rate of molten Al alloy through the existing pores of the refractory materials. Since it is suspected that the formation of the $MgAl_2O_4$ spinel is the leading cause of cracking in the refractories, the NWAs are seen to inhibit the spinel formation and therefore prevents the cracking process.

2.1.8.2 Materials and methods

2.1.8.2.1 Materials and reagents

The proposed refractory family used in this work is the white fused mullite (WFM) whose composition and particle size are shown in Table 2-2, which also includes the company name of suppliers and other ingredients used. Additives to improve the non-wetting capacity of the

refractories included CaF_2 from VWR-Anachemia, Canada (particle size: 44 µm), $BaSO_4$ from EXbar, USA (particle size: 44 µm), Wollastonite from Nyad, USA (particle size: 37 µm), and Secar®71 (calcium aluminate) cement from Kerneos Inc., USA (particle size D50, 73.4 µm).

Table 2-2. Ingredients used to produce the plain WFM[1].

Ingredient	Composition	Particle size (µm)	Solid Wt. %	Supplier
Aggregates	Mulcoa 70-80	2380	12.6	Imerys, USA
	Mulcoa 70-20	840	18	Imerys, USA
	40 white fused mullite	420	30.1	Imerys, USA
Fines	Tabular Alumina - 325 TA	44	4.5	Aluchem, USA
	0.08 White fused mullite	80	11.8	Imerys, USA
	Reactive Alumina A20SG	D50 = 3.3	7.6	Almatis, USA
	Reactive Alumina CTC50	D50 = 1.5	10.9	Almatis, USA
Liquid	Ludox 1144 (Colloidal silica) *	0.015	(Silica) 4.5	NALCO, USA

* Colloidal silica contains 40-wt% solid (15 nm particles) suspended in liquid.

2.1.8.2.2 Materials synthesis

The WFM supplied by Pyrotek Inc., (Sherbrooke, Canada) was modified by NWAs (2-wt% CaF_2, $BaSO_4$, Wollastonite, Secar®71 cement, and mixture of CaF_2 and $BaSO_4$). The microstructure components of the samples were mainly mullite and alumina. Secar®71 cement was added to one sample to facilitate formation of anorthite. In the production of WFM, both large and fine particles were necessary in order to produce a dense refractory. Other studies have established the critical role of adding minute quantities of $BaSO_4$ to high alumina refractories, where 1-wt% of $BaSO_4$ produces anorthite due to the reaction of the calcium cement phases with the refractory constituents (Koshy, 2009). Raising the $BaSO_4$ content to 5-wt% forms barium silicates instead of anorthite, and the addition of more than 10-wt% $BaSO_4$ creates

[1] The solid wt% column of the table is modified.

celsian phase. In this work, four steps were involved in making the refractory bricks during the modification and it required Ludox1144 as the liquid medium:

(i) Step 1: Mixing of precursors

(a) Half of the total amount of Ludox 1144 was poured in the mixing pot;

(b) Predetermined mass of the powder (WFM + 2-wt% NWA) was added;

(c) The rest of Ludox 1144 was added;

(d) The mixture was stirred for 5 minutes;

(e) The final mixture was then tested by determining the flow rate.[2]

(ii) Step 2: Mold casting

(a) The mixture was poured into a mold set on a vibrating table to level the concrete;

(b) A piece of plastic was placed on top of the mold.

(iii) Step 3: Setting and curing

(a) After 16 to 18 hours, the cast was removed from the mold;

(b) Samples were placed in a plastic container and covered with a damp cloth for 1 day;

(c) The samples were further kept in the open air for 1 day.

(iv) Step 4: Firing process

The samples were calcined at various temperatures with the firing cycle in Table 2-3:

Table 2-3. Firing conditions.

Temperature range (°C)	Heating rate (°C.min^{-1})	Holding time (h)
20 – 350	10	5
350 – 1400	15	12
1400 – 1400	0	5
1400 – 1000	10	5
1000 – 25	Cooling in furnace	-

2.1.8.2.3 Materials testing: Alcan immersion corrosion test

This test is routinely used to evaluate the suitability of refractories for applications in melting and holding furnace linings. It is also used to determine the resistance of metal penetration in

[2] Standard test (No. ASTM-C 1611/C 1611M – 05) method for slump flow of self-consolidating concrete.

the furnace linings. In this study, the Alcan immersion test was used to evaluate the corrosion resistance of the samples under investigation performed at 850 ^{o}C for 96 h to determine the extent of molten Al metal penetration (Shi *et al.*, 2016a). For this purpose, two refractory samples in size of 51 x 25 x 25 mm were placed in a clay-bonded graphite crucible including 2 kg of molten Al-(5-wt%)Mg alloy, in a vertical electrical furnace. Since Mg is volatile, 40 g Mg was added to the molten alloy (total mass is 2000g) every day to keep its concentration constant. After the high temperature testing, the samples were taken from the cup and sectioned in order to evaluate (a) the level of cracking in the refractory, (b) the extent of metal infiltration into the refractory, and (c) the degree of metal adherence.

2.1.8.3 Materials characterization

2.1.8.3.1 Optical microscopy

Fresh samples and those tested by the Alcan immersion test were analyzed for corrosion by an optical microscope (Keyence VHX-5000, Canada).

2.1.8.3.2 X-ray diffraction (XRD) analysis

X-ray diffraction (XRD) analysis is a valuable method in distinguishing different phases and crystallite sizes in powder and coated samples. The samples were analyzed before and after the corrosion test on a “Philips Panalytical X’pert PRO MRD” X-ray diffractometer, using Cu Kα1 radiation with a wavelength, $\lambda = 1.54$ Å, in the 2θ-angle range from 10 – 90^{o} at a scanning speed of 0.04^{o} 2θ-angle per min and a step size of 0.02^{o} and step time of 0.5 s.

2.1.8.3.3 Scanning Electron Microscopy (SEM)

To investigate morphology, particle size and composition of materials microscopic imaging by SEM coupled with energy dispersive X-ray spectroscopy (EDX) are used. In this work, SEM imaging and analysis was done on a “Hitachi S-4700” Field-Emission Scanning Electron Microscope, equipped with an EDX X-Max Oxford spectrometer.

2.1.8.3.4 Wettability test

Wettability of the samples was studied using the Krüss Advance goniometer model DSA25E. In order to measure the surface energy of the samples at 25°C, Van Oss theory was applied (Good, Chaudhury and Oss, 1991), because it works best for inorganic surfaces (Rulison, no date). In the approach, diiodomethane (CH_2I_2) was used as the non-polar liquid, while water

(H_2O) and formamide (CH_3NO) were used as the polar liquids (Amama *et al.*, 2013). In the Van-Oss-Goods theory represented by Equation 2-20, the surface energy calculation is dependent on the contact angle between the liquid and the solid materials, which are related by Equation 2-21 (Yildirim, 2001).

$$(1+\cos\theta)\gamma_L = 2\left(\sqrt{\gamma_S^{LW}\gamma_L^{LW}} + \sqrt{\gamma_S^{+}\gamma_L^{-}} + \sqrt{\gamma_S^{-}\gamma_L^{+}}\right) \quad \text{Equation 2-20}$$

$$\gamma_S = \gamma_S^{LW} + \gamma_S^{AB} = \gamma_S^{LW} + 2\sqrt{\gamma_S^{+}\gamma_S^{-}} \quad \text{Equation 2-21}$$

where θ is the contact angle;

γ_L and γ_S are the surface tensions of the liquid and the solid, respectively;

$\gamma_L^{LW}$and $\gamma_S^{LW}$are the apolar or Lifshitz–van der Waals (LW) interactions;

γ_S^{AB}, $\gamma_L^{+}\gamma_S^{-}$ and $\gamma_S^{+}\gamma_L^{-}$ are polar or Lewis acid–base (AB) interactions for liquid (L) and solid (S). [3]

In this experiment, polycarbonate was used as reference material in the analysis, and the surface energy was found to be 45.5 $mJ.m^{-2}$, which is in agreement with literature data (Hild, 2009). Since surface energies of solids are usually measured at room temperature, for most adhesion energy works, it is assumed to be similar at elevated temperatures (Rulison, 2005).

2.1.9 Results and discussion

2.1.9.1 Materials testing

Figure 2-5 shows the optical microscopy image of the samples after the corrosion test. Two distinct corrosion zones were observed. The first zone arises from the direct reaction occurring at the interface between the sample and the molten metal, while the second zone is by infiltration of the molten Al-Mg alloy into the cracks formed in the samples.

[3] Calculation process is explained step by step in Appendix B.

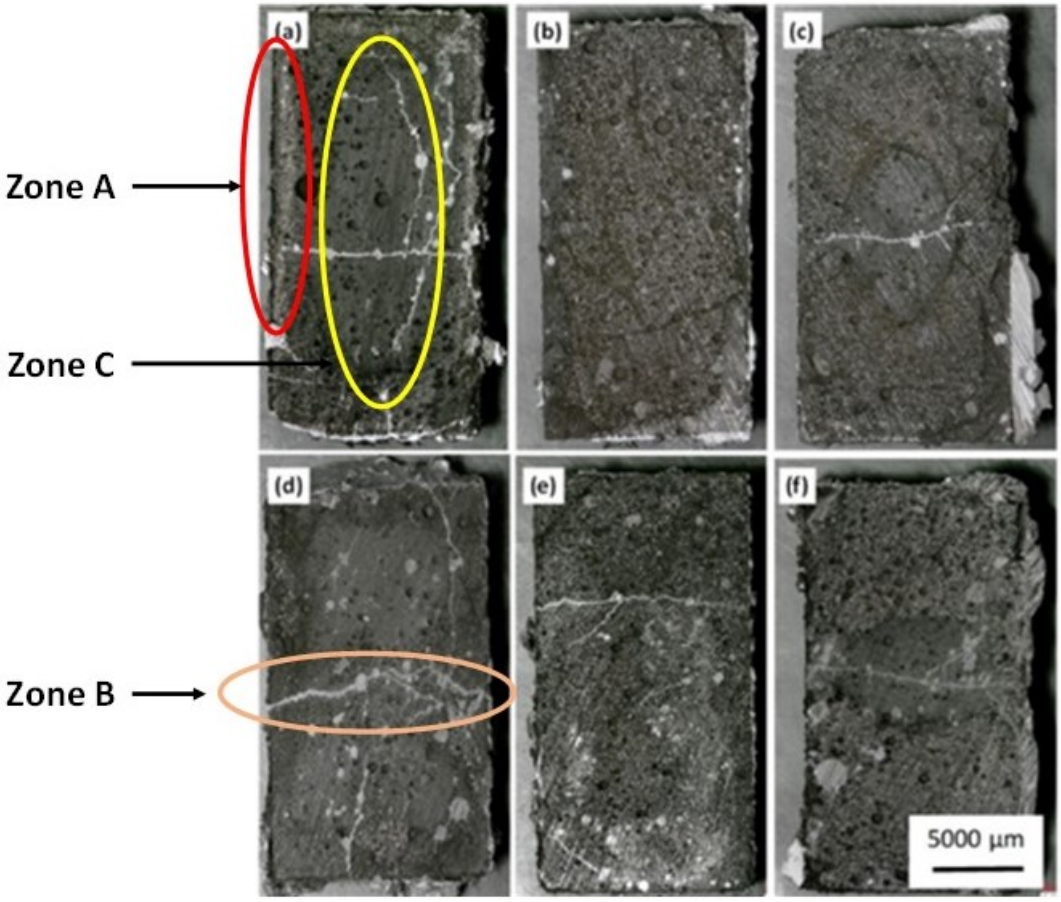

Figure 2-5. Optical microscopy images of samples after Alcan immersion test for (a) plain WFM showing cracks and diffusion of Al; (b) addition of CaF_2 and $BaSO_4$ to WFM which prevents cracking; while the rest indicate cracking after addition of (c) Secar®71; (d) $BaSO_4$; (e) CaF_2 and (f) Wollastonite. Zone (A): direct contact between refractory and molten alloy, Zone (B): diffusion of molten alloy through the cracks, Zone (C): corrosion occurs due to infiltration of Al through the sample and react with refractory composition.

The image of the plain WFM shown in Figure 2-5 (a) reveals that the entire sample was totally corroded, with a reaction occurring at the interface and the molten Al-Mg penetrating the sample through the cracks. By adding NWAs, the corrosion resistance increased, and this can be observed from Figure 2-5 (b) by the addition of both CaF_2 and $BaSO_4$ to the plain WFM, which has limited corroded area. The addition of Secar®71, $BaSO_4$, CaF_2 and Wollastonite to the pristine WFM did not improve the corrosion resistance of the WFM as shown by the cracks in Figure 2-5 (c,d,e,f), respectively. Samples promoted using a mixture of both CaF_2 and $BaSO_4$ presented better corrosion resistance when compared to the samples with individual NWAs. No corrosion was observed for the entire sample except for a small interfacial zone around the

sample surface. Although there were some cracks in the sample, the Al alloy, could not diffuse into the sample cracks.

2.1.9.2 Mechanical tests

Table 2-4 indicates the mechanical characteristics of the modified samples after the addition of the NWAs. The test parameters in the three-point flexural and compressive strength analysis were selected according to ASTM C133-97. The samples size for flexural test were 51 x 51 x 228 mm and for the compressive strength test were 51 x 51 x 51 mm. These tests were repeated three times for each sample. Furthermore, the loading rate for flexural strength test was 1.3 $mm.min^{-1}$ and for compressive strength 13608 $kg.min^{-1}$. It was observed that the inclusions weakened the flexural strength of the pristine WFM sample, and the same applies to the Young's modulus where the additives introduced in the sample seem to create interruptions in the continuity of the phases. Changes in the phase composition of the WFM + 1-wt.%$BaSO_4$ + 1-wt.%CaF_2 sample is perceived to inhibit corrosion by interrupting the propagation of cracks in the refractory. It was observed that samples containing CaF_2 were more brittle and showed lower flexural strength.

Table 2-4. Mechanical properties of modified refractory samples.

Sample ID	Mechanical strength (MPa)		Young's modulus (GPa)
	Flexural	Compressive	
Pristine WFM	16.3 ± 1.3	148 ± 15	4.9 ± 0.3
WFM + 2-wt.% Secar®71	14.3 ± 1.3	125 ± 15	4.2 ± 0.3
WFM + 2-wt.%$BaSO_4$	13.9 ± 1.3	153 ± 15	4.6 ± 0.3
WFM + 2-wt.%CaF_2	13.1 ± 1.3	100 ± 15	4.2 ± 0.3
WFM + 2-wt.%Wollastonite	13 ± 1.3	165 ± 15	4.4 ± 0.3
WFM + 1-wt.%$BaSO_4$ + 1-wt.%CaF_2	12.9 ± 1.3	121 ± 15	4.4 ± 0.3

2.1.9.3 Characterization

2.1.9.3.1 XRD results

The pristine WFM contained mullite, alumina, and SiO_2 phases and after the corrosion test, it was found to contain an additional spinel ($MgAl_2O_4$) phase as shown in Figure 2-6. In Figure 2-6(a), the XRD peak present at 22° (2θ angle) in the pristine WFM, before the Alcan test,

disappears after modification with NWAs in Figure 2-6(b). This peak is related to the presence of crystalline SiO_2 in the refractory. The crystalline SiO_2 reacts with the additives to form more corrosion-resistant phases such as anorthite (Adabifiroozjaei, Koshy and Sorrell, 2015) or barium aluminosilicate (Yurkov and Pikhutin, 2009). The ICDD cards used include: [98-000-2103] for mullite ($3Al_2O_3.2SiO_2$), [98-001-3213] for SiO_2, [98-000-0174] for corundum (Al_2O_3), and [98-000-4595] for spinel ($MgAl_2O_4$).

It is suspected that the formation of the spinel and corundum is the origin of the cracks in the samples as some researchers explained (Shi *et al.*, 2016b). The XRD analysis in Figure 2-6(a) shows that pristine WFM contained the spinel phase (identified with the peak labelled X), only after the Alcan immersion test. However, with the addition of both CaF_2 and $BaSO_4$ as seen in Figure 2-6(b), the formation of the spinel phase was significantly suppressed, which improved the corrosion resistance of the sample. In both Figure 2-6 and Figure 2-7, the XRD analysis indicates that all the samples contained the spinel phase, which led to the formation of the cracks seen in Figure 2-5.

The addition of Secar®71 cement to WFM proved inconsequential. Comparatively, by observing the intensity of the peaks, this sample was the worst performer because it contained the highest amount of the spinel phase. The other non-wetting additives such as wollastonite, CaF_2, and $BaSO_4$ produced less of the spinel phase. Equation 2-1 and Equation 2-2 show the circumstances under which Al_2O_3 may be produced, which in turn generates the spinel as shown in Equation 2-3.

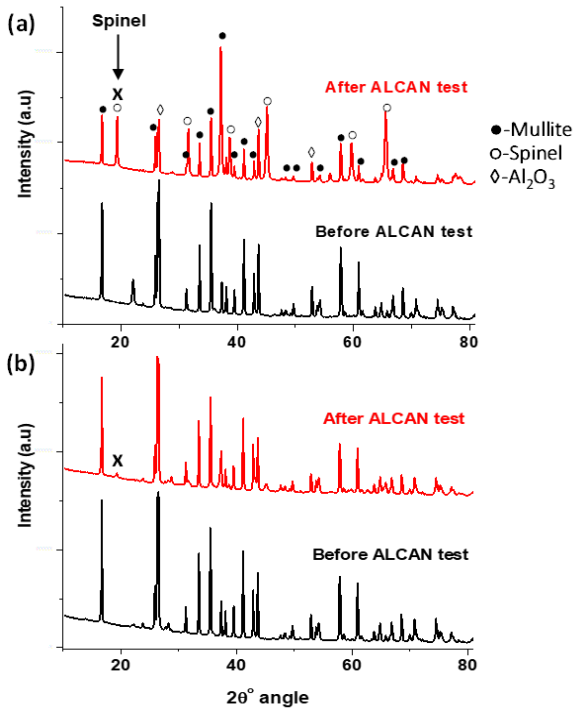

Figure 2-6. XRD patterns of (a) pristine WFM before and after Alcan test showing formation of spinel (peak X); and (b) addition of CaF_2 and $BaSO_4$ to WFM prevents spinel formation.

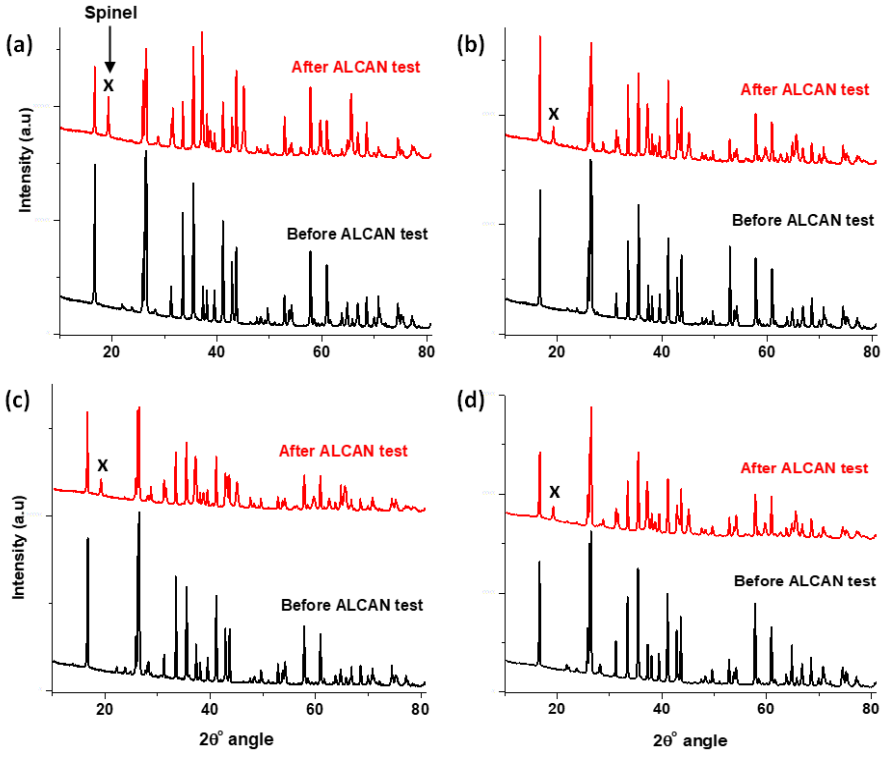

Figure 2-7. XRD patterns of plain WFM with the addition of (a) Secar®71; (b) $BaSO_4$; (c) CaF_2; and (d) Wollastonite before and after the Alcan test, showing spinel formation (peak X).

According to Equation 2-4 and Equation 2-6, the presence of oxygen in the refractory as well as in air at the triple point reacts with Mg to produce MgO that facilitates the formation of spinel, based on Equation 2-7 and Equation 2-8. Since it is suspected that the production of the $MgAl_2O_4$ spinel accelerates the cracking and degradation of the refractories, any process that halts the formation of the spinel will be beneficial to the protection of the refractories. It was observed that the intensity of Al_2O_3 in the XRD patterns dropped after the Alcan immersion test, possibly because it was consumed in the production of $MgAl_2O_4$. The addition of NWAs was meant to inhibit the spinel formation, which was only successful with the combination of $BaSO_4$ and CaF_2. Table 2-5 provides a summary of the phases identified in the refractories after the Alcan immersion test.

Table 2-5. Summary of phases detected by XRD analysis[4] in the samples after Alcan immersion test shown in Figure 2-6 and Figure 2-7.

	Al_2O_3	SiO_2	$MgAl_2O_4$	$CaAl_2Si_2O_8$	Al_2BaO_4	MgF_2	AlF_3	$3Al_2O_3.2SiO_2$	Others
WFM (Fig 7a&b)	√	X	√	X	X	–	X	–	–
WFM+$BaSO_4$	√	√	√	X	√	–	X	√	MgO
WFM+CaF_2	√	√	√	–	X	√	–	√	Mg_2Si
WFM+$BaSO_4$+CaF_2	√	√	–	√	–	√	–	√	CaS
WFM+Wollastonite	√	√	√	–	X	–	X	√	$MgSiO_3$
WFM+ Secar®71	√	–	√	–	X	–	X	√	$Ca_3Al_2Si_2$

$CaAl_2Si_2O_8$ (Anorthite); Al_2O_3 (Corundum), $MgAl_2O_4$ (Spinel), $3Al_2O_3.2SiO_2$ (Mullite), Al_2BaO_4 (Barium aluminate). (√): Phase detected; (X): Phase was not detected; (–): Possible formation.

It is clear that none of the NWAs (including $BaSO_4$ and CaF_2 separately) obstructed the production of the spinel. However, where the two were used in combination, many phases such as anorthite ($CaAl_2Si_2O_8$), MgF_2 and CaS, which contain significant amounts of both Al and Mg elements were formed. These findings confirm certain studies, which indicated that samples containing 3% CaF_2 and 2% $BaSO_4$ displayed the best wetting resistance to the Al-alloy (Koshy, 2009). The concomitant presence of $BaSO_4$ and CaF_2 prevented the two elements from feeding

[4] After the Alcan corrosion test and removal of superficial Al alloy, the samples were ground., pressed and analyzed using XRD.

into the formation of $MgAl_2O_4$ spinel, and in so doing improved the corrosion resistance of the refractories. From the XRD data, the intensity ratio of the spinel peak (x) to mullite peaks in Figure 2-6 and Figure 2-7 was extracted and compared, and they appeared in the respective ratio of 1:2:3:3:4:5 in the ascending order of:

$WFM+BaSO_4+CaF_2$ < WFM + Wollastonite < $WFM+BaSO_4$ = $WFM+CaF_2$ < WFM+ Secar®71 < pristine WFM

2.1.9.3.2 SEM results

From SEM imaging it was observed that all samples developed cracks after the Alcan test except the sample containing both $BaSO_4$ and CaF_2, which are thought to partially prevent spinel formation.

(i) Pristine WFM sample

Figure 2-8 shows typical SEM images with EDX map scans of WFM sample after the Alcan test. Since XRD analysis detected the spinel phases in the sample, it can be assumed that the formation of the $MgAl_2O_4$ spinel is a strong indication of corrosion because it has already been reported as the reaction between alumina of the mullite with the Mg of the alloy (Iizuka and Ouyang, 2014). On the other hand, corundum is the product of the reaction between the SiO_2 of mullite with Al. Although some unreacted mullite was also detected in the XRD analysis, the EDX elemental map in Figure 2-8 shows the formation of the spinel network, which is totally dispersed in the cross-sectional area of the sample. Therefore, pristine mullite without NWAs exhibits poor corrosion resistance when contacted with molten Al-Mg alloy.

(ii) WFM-CaF_2-$BaSO_4$ sample

SEM images and EDX elemental mapping of the WFM promoted with $BaSO_4$ and CaF_2 are presented in Figure 2-9. The XRD analysis indicated that this sample contained unique phases namely, anorthite ($CaAl_2Si_2O_8$), MgF_2, and CaS (Table 2-5).

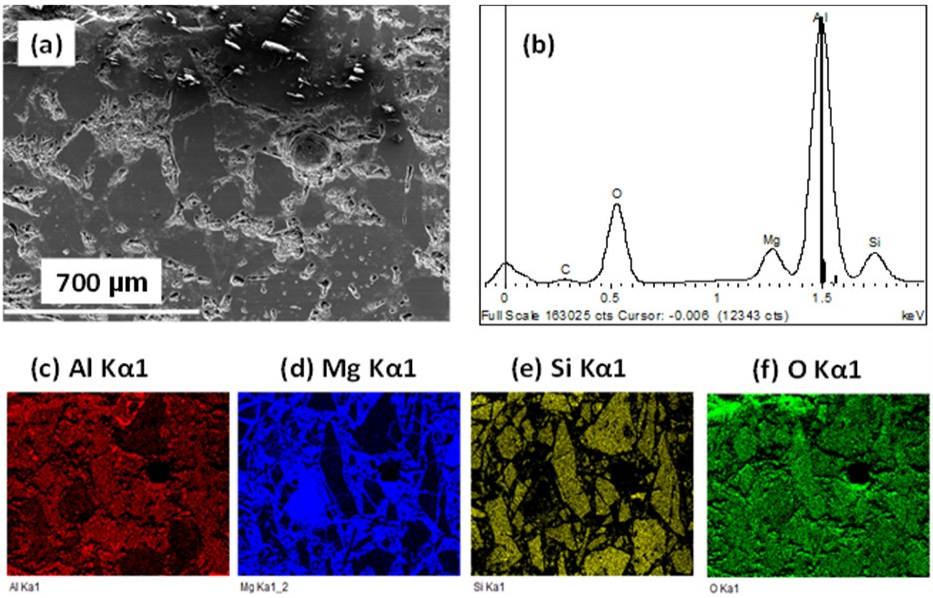

Figure 2-8. Top view SEM imaging after Alcan test indicating (a) the secondary electron image of pristine WFM; (b) EDX spectrum of the sample; (c-f) EDX elemental mapping of Al, Mg, Si, and O, respectively.

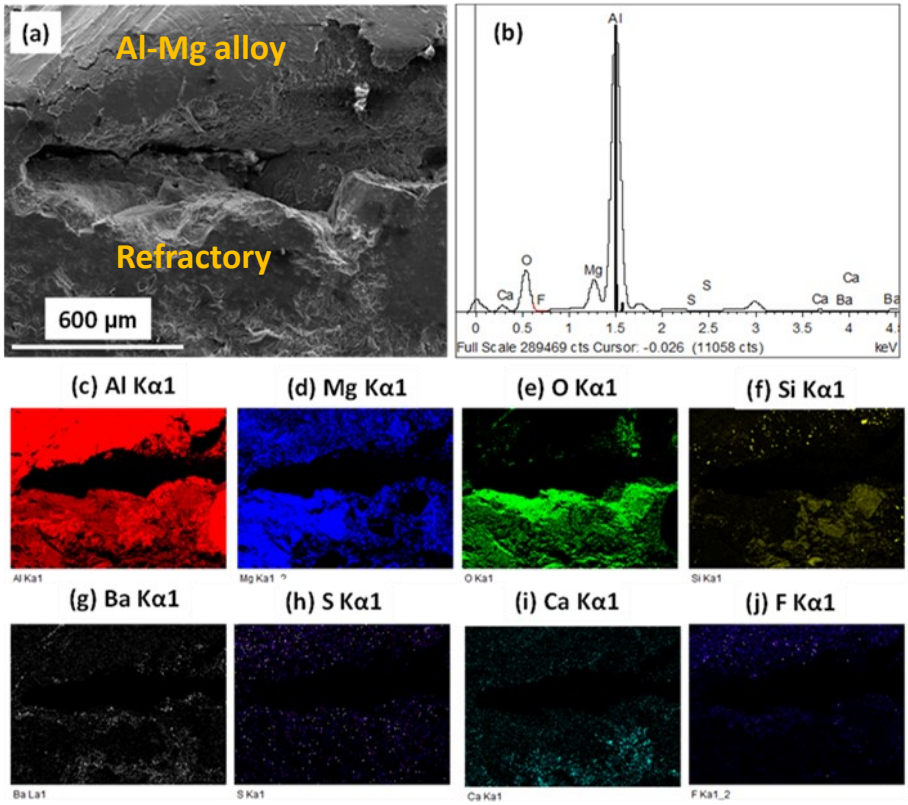

Figure 2-9. SEM cross sectional view of WFM-CaF_2-$BaSO_4$ after Alcan test indicating (a) the secondary electron image of the sample; (b) EDX spectrum of the sample; (c-j) EDX elemental mapping of Al, Mg, O, Si, Ba, S, Ca and F, respectively.

Since these phases inhibit the formation of corundum and consequently the production of the spinel, it is harder for molten Al to stick and react with the surface. It has been shown that the sticking efficiency or the adhesion of molten Al is much stronger on the α-Al_2O_3 (corundum) surfaces that are oxygen-terminated than on the Al-terminated or O-deficient surfaces (Shen *et al.*, 2003b). This is because of the instability in O-terminated surfaces arising from their polarity, while Al-terminated surfaces are nonpolar, and therefore more stable. It is asserted that the presence of H_2 and/or water vapor may change the Al-terminated surfaces to O-terminated ones.

We think that at the bellyband where atmospheric oxygen and water vapor are readily available in the furnace, the corundum surfaces are O-rich and therefore, the adhesion forces of molten Al are stronger. However, the addition of $BaSO_4$ and CaF_2 to the refractory lowers the formation of corundum and therefore the spinel. Where the formation of spinel is minimized as observed in the XRD patterns (Figure 2-6), the presence of cracks diminishes (Figure 2-5), and the diffusion of molten Al-Mg into the refractory, as well as the capacity to stick to the surface, is suppressed. Figure 2-9 (a) is a SEM image of the WFM-CaF_2-$BaSO_4$ sample after the Alcan immersion test, and it portrays a gap between the molten Al-Mg alloy and the refractory surface. This is a clear sign of the weakening of the interfacial bonds between molten Al-Mg and the refractory surface. Figure 2-9 (b) indicates EDX spectrum of the sample, while Figure 2-9 (c-j) is the EDX elemental mapping of Al, Mg, O, Si, Ba, S, Ca, and F, respectively.

(iii) WFM-$BaSO_4$, WFM-CaF_2, WFM-Secar®71 cement, and WFM-Wollastonite sample

Figure 2-10 displays SEM images and EDX map scans of WFM containing $BaSO_4$, CaF_2, and a blend of $BaSO_4$ and CaF_2 after the Alcan immersion test. The growth of cracks and diffusion of the molten Al-Mg alloy into the refractory is evident in the EDX elemental mapping shown in Figure 2-10(a) for the sample containing CaF_2 only and Figure 2-10(b) for the sample containing $BaSO_4$ only.

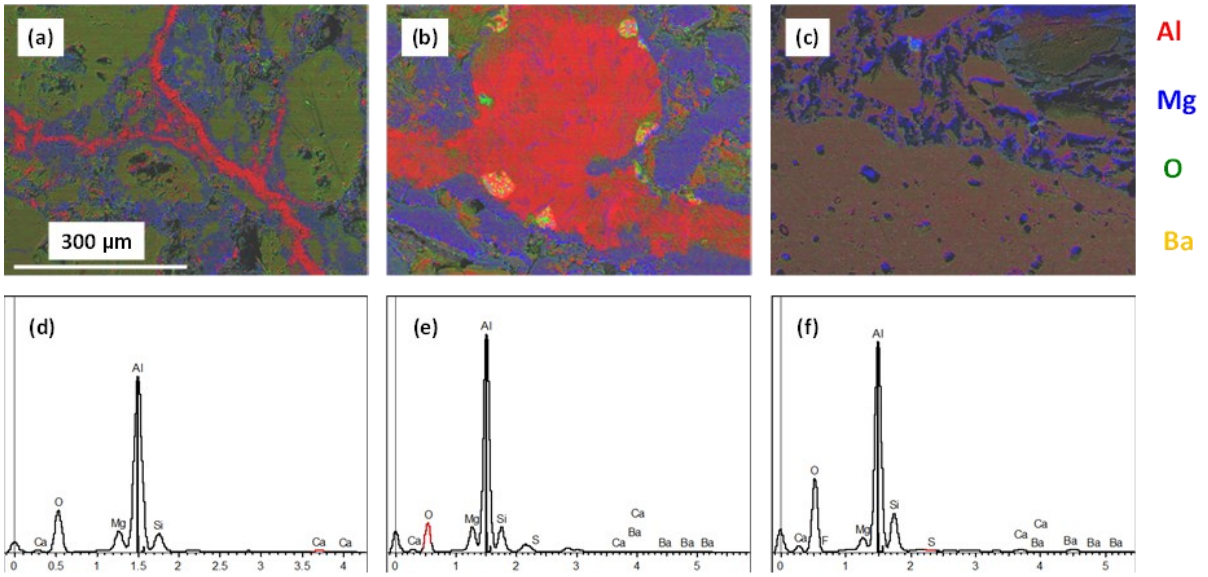

Figure 2-10. EDX elemental mapping by SEM imaging indicating the growth of cracks in (a) WFM+CaF_2 and (b) WFM+$BaSO_4$ while there are no cracks in (c) WFM+$BaSO_4$+CaF_2 with (d-f) showing the corresponding EDX spectrum of the samples.

These are typical images for all the other WFM samples modified using Secar®71 cement and wollastonite. On the other hand, no cracks were observed in Figure 2-10(c), which is the sample that was promoted by a combination of both $BaSO_4$ and CaF_2. The red coloration in Figure 2-10(a) and (b) is an indication of the Al-filled cracks, which are absent in Figure 2-10(c). Figure 2-10(d-f) show the corresponding EDX spectra of the samples.

Where both $BaSO_4$ and CaF_2 were used to improve the performance of WFM, less of the spinel was evident and more anorthite was detected. Generation of anorthite has been perceived to be beneficial in the process because it is a stable phase, which does not easily react with Al-Mg alloy to form a layer of corundum. It has been observed that both CaF_2 and anorthite are individually resistant materials when in contact with molten Al (Adabifiroozjaei, Koshy and Sorrell, 2015).

2.1.9.3.3 Wettability results

Table 2-6 summarizes the surface energy measurements of the samples. It is observed that pristine WFM had the highest surface energy with a value of 22.5 $mJ.m^{-2}$, while those of the modified samples were in the range of 20 (±1) $mJ.m^{-2}$. The wettability of a material is generally reduced when the overall surface energy of the solid surface is lowered (Song *et al.*, 2019).

From these results, it is not possible to infer a ranking for the wetting behavior at high temperatures, other than that the pristine sample is likely more prone to wetting. Corrosion of refractories begins with wetting, followed by a chemical reaction between the molten Al and the refractory. The surface energy of the sample influences the creation of the bond between the liquid and the solid surface. From the results shown in Table 2-6, it is clear that although the samples have very close total surface energy, the materials have different basic components surface energy, and the sample with mixed non-wetting additives has the lowest basic component surface energy among all the samples, confirming non-wetting properties of this sample. This method provides a rough estimate of the surface energies of the samples. However, the method has limitations which include (i) surface contamination that can interfere with interaction between the liquid and the surface, even after the cleaning process, and (ii) the variation of the contact angle value on the surface of the sample based on the location of the liquid at the top of the sample, which can be explained by the variation of the surface roughness.

Table 2-6. Measured surface energies of the refractories at room temperature using the Van Oss theory.

Sample	**Basic component of surface energy (mJ/m^2)**	Surface energy @ 25°C (mJ/m^2)
Pristine WFM	5.7 ± 0.1	22.5 ± 0.8
WFM-$BaSO_4$	5.9 ± 0.1	21.1± 0.8
WFM-Wollastonite	3.7 ± 0.1	19.2 ± 0.8
WFM-CaF_2	5.9 ± 0.1	21.0 ± 0.8
WFM-CaF_2+$BaSO_4$	2.9 ± 0.1	21.1 ± 0.8
WFM-Secar	5.9 ± 0.1	21.1± 0.8

2.1.10 Conclusion

With strong economic and environmental forces driving changes in the Al industry, the Alcoa and Rio Tinto Elysis consortium has developed an innovative process to produce clean Al. The next big concern therefore is corrosion of refractories in contact with molten Al or its alloys. Two main problems associated with the corrosion of refractories include contamination of the final Al product and shortened lifespan of the refractories due to degradation. Currently, many

researchers are seeking ways of improving the corrosion resistance of these refractories, and a possible solution involves the addition of non-wetting additives (NWAs) to their formulations.

In this review, some research has been conducted on corrosion, its mechanisms and potential solutions using a mullite-based ($3Al_2O_3.2SiO_2$) refractory. A case study, which involves white fused mullite (WFM) was presented using the standard Alcan immersion test (performed at 850ºC for 96 h). However, since a high percentage of SiO_2 is added to lower porosity, the refractories are prone to corrosion by molten Al and its alloys. As predicted by thermodynamics the refractory aggregates start to react with molten Al at 850 ºC. Even for samples with almost no open porosity (of less than 0.6%), silica or silica-containing minerals will react with molten Al metal. Reaction with silica-rich refractories leads to a volume contraction due to the formation of corundum. The voids formed in the materials as a result of this volume decrease act as "suction pipes" causing molten Al to penetrate the material, thus triggering corrosion above the metal line in the melting furnace. On the other hand, reactions causing volume expansions may equally generate cracks in the samples and as such advance further metal diffusion and reaction.

Using FactSage™ thermodynamic software, Gibbs's free energy of the corrosion reaction on aluminosilicate refractories was calculated. From the reactivity potential of pure mullite in direct contact with molten 5-wt%Mg/Al between 850ºC and ambient temperature, the formation of corundum and spinel was confirmed. In our tests, six samples were synthesized and tested for corrosion at Pyrotek Inc., (Sherbrooke, QC, Canada). The NWAs added to WFM to improve its corrosion resistance included 2-wt% of $BaSO_4$, CaF_2, Wollastonite, Secar®71, and another sample having a mixture of 1-wt% $BaSO_4$ and 1-wt% CaF_2.

The samples were characterized by XRD, optical microscopy, SEM imaging coupled with X-ray elemental mapping, and surface energy measurement at room temperature. It was observed that cracks formed in the refractories where the concurrent formation of spinel and corundum occurred after the Alcan immersion test. However, the sample containing a mixture of both $BaSO_4$ and CaF_2 did not generate cracks, potentially because of a combination of two reasons: (i) improved non-wetting properties assessed by room temperature surface energy measurements from 22.5 mJ/m² for the pristine WFM dropping to 21.1 mJ/m²; (ii) the absence of the spinel phase formation, which was not detected after the Alcan immersion test.

2.2 ALUMINUM NITRIDE (ALN): PROPERTIES, APPLICATIONS, SYNTHESIS, AND COATING METHODS

The second section of the state of the art is focused on AlN, its properties and application as well as its deposition methods as a potential candidate for protecting substrates in contact with molten Al alloy. Furthermore, modeling the interaction between AlN and molten Al using FactSage and Materials Studio software and validation of data using corrosion test and sessile drop measurement method are presented.

2.2.1 General properties of AlN

Among the family of nitrides, AlN has a combination of outstanding properties, which attract a lot of attention for various industrial applications (Shahien *et al.*, 2010a). These properties which depend on the nature of the material, that is, either cubic or hexagonal phase, include:

(a) High thermal conductivity in the range of 180 – 260 W/(m·K);
(b) High hardness (1400 – 5000 HV); and
(c) Electrical resistivity (10^{13}-10^{16} Ω.cm).

Furthermore, AlN is recognized as a refractory material because of its

(a) High corrosion and wear resistance in molten metals and many aggressive media (Farokhzadeh and Edrisy, 2017);
(b) Good thermal shock resistance (Baba, Shohata and Yonezawa, 1989);
(c) Low linear thermal expansion coefficient (4.03×10^{-6} K^{-1} at 300 – 500 K, 5.64×10^{-6} K^{-1} at 500 – 1300 K) (Smolen and Dominik, 2013); and
(d) High thermal stability up to 2400 K in an inert atmosphere, whereas oxidation in the air starts at 1200 K.

Moreover, the application of AlN as a semiconductor can be found in high temperature as well as in electronic equipment, and in photonic devices, which cover the deep ultraviolet spectrum (Thompson *et al.*, 2001) because of (a) having a wide band gap (about 6.2 eV) (W.McCauley, 1994); and high specific electrical resistance (Elagin *et al.*, 2013a).

2.2.2 The thermal stability of AlN phases

Aluminum nitride has two phases; a) hexagonal closed packed (hcp) phase with wurtzite structure; and b) cubic phase with zinc blende and rock salt structure. The hexagonal structure of wurtzite is a thermodynamically stable phase under ambient conditions; however, the rock salt structure is a metastable phase, which is more stable at high pressure (15-20 GPa) (Siegel, Parlinski and Wdowik, 2006). The cubic phase can be formed by epitaxy at fairly low temperatures on substrates with the cubic crystal structure (Kudyakova *et al.*, 2017). In comparing the two phases, it was observed that the cubic phase has higher thermal conductivity (250–600 W/m*K), greater electrical resistance (10^{16} Ω cm) owing to its higher symmetry (Shahien *et al.*, 2010a), and higher mechanical strength (Thompson *et al.*, 2001).

Since hcp-AlN is a stable phase at ambient conditions, while cubic-AlN is a metastable phase, the synthesis of cubic-AlN is more challenging than that of hcp-AlN. It is also not possible to synthesize cubic-AlN directly from the hcp phase, and to transform the hcp phase to the cubic phase since either static or shock compression of over 14 GPa is required (Mashimo *et al.*, 1999).

2.2.3 Industrial applications of AlN

Aluminum nitride is a versatile material and finds many industrial applications due to its unique properties:

(a) In electronic industry: The tendency of the electronic industry to decrease the weight and size of electronic devices with high-performance materials has opened a new path for using AlN widely, for example, in the compact and high-performance tablets market. A thin layer of AlN is deposited on processors, integrated circuit (IC), and chip to increase their thermal conductivity to enable them to cool down quickly and avoid passage of electric current by acting as an electric insulator (Farokhzadeh and Edrisy, 2017);

(b) Applications in the production of brackets for light-emitting diode (LED) technology and thermal interface of electronic lasers due to its high thermal conductivity (Kim *et al.*, 2015);

(c) Production of solid-state cells, which are photosensitive to ultraviolet radiation due to its wide bandgap;

(d) AlN is used as printed-circuit-boards (PCB) owing to its optoelectronic properties (Farokhzadeh and Edrisy, 2017);
(e) In metallurgy and ceramic refractories, AlN is used as a lining material for electrolytic baths, tanks, crucibles, and vessels for preparing molten Al, Sn, Ga, glass, (Yamada, Nakamura, *et al.*, 2006), etc. as well as handling corrosive chemicals (Shahien *et al.*, 2010a); and
(f) In the nuclear industry: because of AlN's outstanding corrosion resistance to molten salt media its coating may be used in a nuclear reactor (Elagin *et al.*, 2013b).

Owing to its hardness and intrinsic inertness in contact with molten Al alloy, AlN is a good candidate for coatings in contact with molten metals in both argon and CO atmospheres. It shows incredible corrosion resistance to molten Al at a temperature as high as 2000 ºC, but in an oxidizing atmosphere such as wet or dry air, the resistance lessens, whereby beyond 1200 ºC a noticeable reaction occurs with AlN (Long and Foster, 1959). AlN compares very well with Si_3N_4, which is a corrosion-resistant refractory when in contact with molten Al because of the formation of a dense protective layer of AlN at the surface of the refractory (Mouradoff *et al.*, 1994), (Büchel *et al.*, 1980).

2.2.4 Coatings and surface engineering

Surface engineering is a well-known highly economic method of modifying surface characteristics by various coatings and other surface modification methods without disturbing the substrate, and it has been employed in different areas such as aerospace engineering, creation of thermal barriers, cutting tools, and agricultural equipment among others (Roberts, 1987). A coating is mainly applied to improve the surface performance of the substrate and protect it from wear, corrosion, and erosion (Amin and Panchal, 2016), and provide a wide variety of functions to the in-service substrate. The advancement of coatings in recent years has opened a world of new opportunities for the selection of materials based on their performance and properties. This revolution in materials engineering facilitates the utilization of expensive and high-performance materials as a thin or thick layer on cheap and low-quality substrates to take advantage of their properties based on industry needs.

In industry, materials are selected based on the application and the desired surface properties. For example, furnace refractories holding molten Al are always in contact with hot and corrosive

molten metal and the reaction between the refractory and molten metal starts from the surface. Coating methods provide this opportunity to protect the refractory surfaces to avoid direct contact between the molten metal and the refractory surface by depositing a layer of high-performance material that can survive longer and protect the substrate in this corrosive environment (Tejero-Martin *et al.*, 2019). There are several reasons which encourage the industry to use coatings instead of modifying the substrate composition:

i. To improve surface functional performance;
ii. To expand the lifetime of the substrates by decreasing wear due to abrasion, erosion, and/or corrosion;
iii. To increase the profitability of a low-cost base material by coating it with a very effective but more expensive coating; and
iv. To facilitate repairing of the coating (Pfender, 1999).

Adhesion of coating layers to the substrate and the chemical inertness of this layer in contact with molten alloys or molten salts are two crucial factors, which have a significant effect on the performance of the coating. As coatings are usually used to protect the substrate from wear and corrosion, the hardness and corrosion resistance of the coating materials to the corrosive environment is very important.

There are different methods to vapor-deposit nanostructured coatings, such as chemical or physical vapor deposition, plasma-enhanced chemical vapor deposition (PE- CVD), etc. Given the low deposition rate in vapor deposition methods, the corresponding coatings are very thin, hardly few micrometers. However, for high-temperature applications, thermal spray is a good candidate, which has been extensively used to protect substrates against wear, high-temperature corrosion, and erosion (Bolelli *et al.*, 2006). The thermal spray coating is one of the most successful methods to provide a hard, thick, and dense coating layer on substrates, which leads to increased substrates lifetime (Amin and Panchal, 2016).

2.2.5 Production of coatings by thermal spray techniques

Thermal spray is a common word for a group of coating processes, which can deposit thin or thick layers of metallic or nonmetallic coatings on a substrate. An energy or heat source is used to transfer the heat to the feedstock, and then the particles are accelerated to impinge onto the

substrate using a gas stream (Shahien *et al.*, 2013a). Thermal spraying is effectively utilized because it provides wide flexibility of the selection of the material (Tejero-Martin *et al.*, 2019), depending on the required properties (Pratap, Bhatt and Chaudhary, 2015). Coating by thermal spray has a wide range of applications including thermal barrier, wear resistance, and corrosion-resistant coating in various key industrial sectors, including aerospace, automotive, power generation, petrochemical, and offshore (Amin and Panchal, 2016). This method is cost-effective with a high production rate, forming an adequate adhesion between the coating and the substrate (Pratap, Bhatt and Chaudhary, 2015). The thermal spray process differs based on the precursor's materials and the heat source. Table 2-7 summarized the process, feedstocks, and heat or energy source (Shahien *et al.*, 2012).

Table 2-7. A summary of thermal spray methods based on feedstock and heat sources

Process	Feedstock form	Heat source	References
Wire arc spraying	wire	Electric arc	(Abkenar, 2007), (Kumar, Handa and Kumar, 2019)
Flame spraying	Powder, wire, rod	Oxyacetylene flame	(Fauchais, Heberlein and Boulos, 2014)
Detonation flame spraying	Powder	O_2-acetylene-N_2 gas detonation	(Ke *et al.*, 2005)
Atmospheric plasma spraying (APS)	Powder	Plasma arc	(Shahien *et al.*, 2010b)
Vacuum plasma spraying (VPS)	Powder	Plasma arc	(Young *et al.*, 2000)
High velocity oxy-fuel (HVOF)	Powder	Oxygen, fuel	(Oksa *et al.*, 2011)

Thermal spray is firstly categorized according to the source of energy or heat, whether originating from combustion or electrical discharge to create a plasma to melt the material and form the coating. Secondly, the division is based on the precursor type such as powder, wires, suspension, solution, or rods. A further group is divided using the environment upstream or downstream of an accelerating nozzle, (i) high pressures upstream the nozzle with atmospheric pressure downstream, or (ii) reduced pressure and controlled atmosphere in the chamber downstream the nozzle. Classification of thermal spray technologies based on the heat source is summarized in Figure 2-11 (Fauchais, Heberlein and Boulos, 2014).

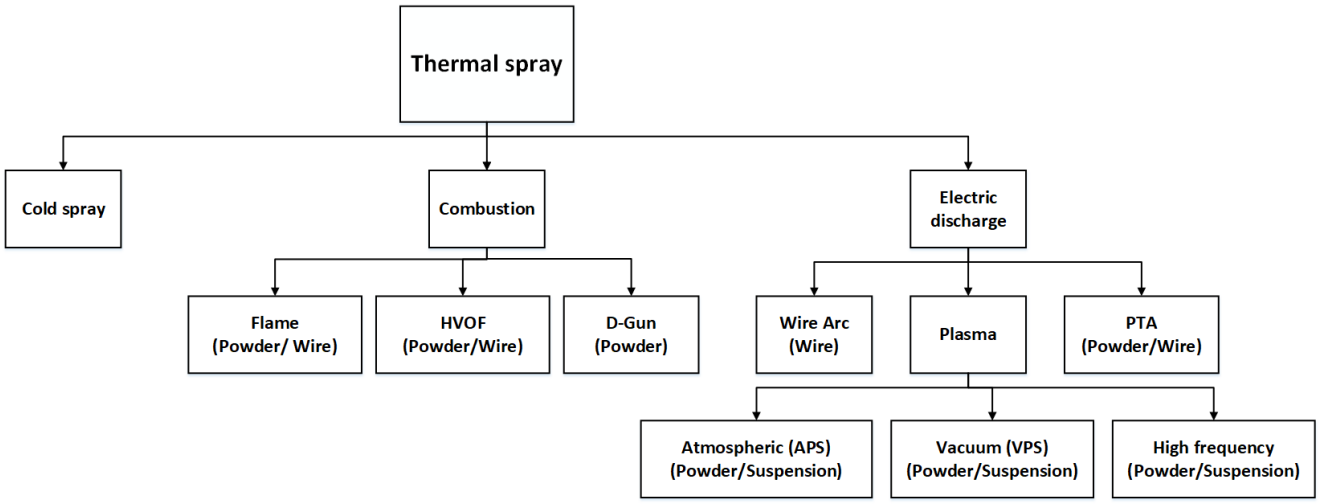

Figure 2-11. Classification of thermal spray technology (Fauchais, Heberlein and Boulos, 2014).

Thermal spray is a well-established technology due to the combination of a wide range of deposition methods and accessible materials for coating. Numerous major advantages of this technology are as follow:

(a) Selection of a wide range of materials with the practical injection of feedstock that can melt without decomposition (Amin and Panchal, 2016);
(b) It facilitates recoating of worn and damaged coatings without changing the dimensions and properties of the part; and
(c) Coating of substrates without the necessity of heating and changing their properties.

The major disadvantage of the thermal spray method is that it can only coat the part of the substrate which is directly in front of the gun or torch. In addition, there is a size and shape limitation where, the deposition rate of thermally sprayed droplets is low for smaller substrates having a small curvature or deep cavities (Amin and Panchal, 2016).

2.2.5.1 Cold spray

Cold spray or kinetic spray is one of the thermal spray methods which is divided into two categories based on the pressure: (a) high-pressure cold spray (HPCS, >1MPa) and (b) low-pressure cold spray (LPCS, <1MPa) (Karthikeyan, 2018). In this process, instead of using a high temperature source to produce heat and transfer it to the feedstock to melt them, a supersonic jet of compressed gas is used to accelerate powder particles to ultrahigh velocity (up to 1,500

m/s). The unmolten accelerated powder particles at speed 500-1500 m/s propelled to the substrate and plastically accumulate on the substrate to build up the coating (Yin *et al.*, 2018).

2.2.5.2 Flame spraying

This process is the oldest thermal spray process, which was developed by Dr. Schoop in 1912. The feedstocks are in form of powder, wire, rod, or cord and use heat from the combustion of fuel gases (commonly propane or acetylene) combined with oxygen to melt the feedstocks. The created gas flow in combination with compressed air produces a jet to accelerate the materials toward the substrates to build up the coating. The flame temperature is usually 3000 – 3350 K with the particles' velocity being in the range of 80 – 100 m/s, and the final coating typically has porosity between 10 – 20% and thickness of 100 – 2500 μm (Tejero-Martin *et al.*, 2019). In the flame wire process, the amount of material that can be injected is limited by the size of the wires (Fauchais, Heberlein and Boulos, 2014).

2.2.5.3 Detonation gun (D-Gun) spraying

In this process, a mixture of oxygen and fuel gas (commonly acetylene) is fed into the water-cooled gun barrel with a particular amount of feedstock powder. With a spark plug, the combustion process starts to create a high-pressure shock wave, which accelerates the powder along the gun barrel into the substrate to produce a coating. The flame temperature will reach 4000 K with particle velocities up to 1000 m/s (Ke *et al.*, 2005). In-between detonations the gun barrel is flushed with nitrogen gas. The procedure of detonation deposition is repeated leading to the formation of a dense and thick coating. Detonation coatings are more common for producing coatings made from hard materials especially carbides on the surfaces exposed to aggressive wear (Fauchais, Heberlein and Boulos, 2014), (Tejero-Martin *et al.*, 2019).

2.2.5.4 High-velocity oxy-fuel (HVOF) spraying

The idea of HVOF spraying method was derived from jet engine having some common features with the detonation gun process. A mixture of fuel gases and oxygen inside a combustion chamber is burnt to create a highly pressurized mixture that produces high velocity exhaust jet (Sidhu, Prakash and Agrawal, 2005). A small diameter nozzle is utilized to lead gases toward the substrate surface. The feedstock powder is injected axially into the created jet with the aid of carrier gas. The flame temperature is typically 3000 – 3500 K and particle velocity around

1000 m/s (Oksa *et al.*, 2011). Mostly the thickness of the coating produced by this method is about 100 – 300 µm with porosity lower than 1% (Tejero-Martin *et al.*, 2019).

2.2.5.5 Wire-arc spraying

This process varies from other thermal spray processes because there are no external heat sources similar to the combustion gas/flame spray techniques. The electric arc as the heat source is used to melt metallic wires by charging one wire as positive and another one as negative and forcing them to produce an electric arc. Like the flame process, compressed air is utilized to atomize the molten metal and spray it onto the substrate with the aid of compressed air. In comparison to the other thermal spray processes, high deposition rate, absence of unmolten or semi-molten particles, and low heat transfer to the substrate are observed. Accordingly, the wire arc process is less expensive, but it creates a porous coating, which limits its usage (Tejero-Martin *et al.*, 2019).

2.2.5.6 Plasma spray

In decades, plasma spraying has become a well-known and versatile coating method with wide applications in corrosion, high temperature, and abrasion-resistant coatings due to having few restrictions on the sprayed materials, size, and shape of the substrate, and it facilitates concomitant synthesis and deposition of the coating composition (Pfender, 1999). Thermal plasma generated through direct current (DC) arc or Radio-frequency (RF) discharge is utilized as a source of heat to partially ionize the gases and after the collision of the ionized gas with the injected precursor, the coating material in molten or in a semi-molten state is propelled to the substrate. Gas mixtures of nitrogen and hydrogen due to their high enthalpy are used in situations where high deposition rates and high power levels are required (Fauchais, Heberlein and Boulos, 2014). The plasma gas is heated and exits from the nozzle as a high temperature, and high-velocity jet, Figure 2-12 (Fauchais, Heberlein and Boulos, 2014).

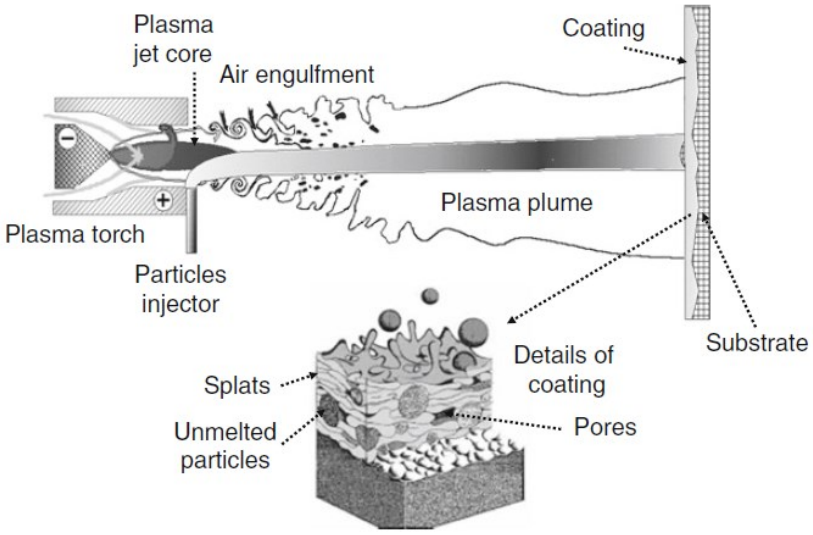

Figure 2-12. Schematic of the plasma spray process of powder in DC plasma jet (Fauchais, Heberlein and Boulos, 2014).

Based on torch design, DC or RF plasma, and operating parameters, temperatures at the nozzle exit can reach a maximum of 12,000–15,000 K, and the gas velocities range is between 500 and 2,500 m/s. The precursors of the coatings can be injected perpendicularly or axially in a DC or RF process. In this method, the motion of the torch relative to the substrate and/or of the substrate relative to the torch provides the opportunity to reach homogeneous coatings on substrates with different shapes (Fauchais, Heberlein and Boulos, 2014).

Furthermore, plasma spraying is categorized based on the chamber environment:

1. Atmospheric plasma spraying (APS)

2. Low-pressure plasma spraying (LPPS) with pressure in the range of 5 to 20 kPa, very low-pressure plasma spray (VLPPS) operating in the range of 100-200 Pa, and vacuum plasma spraying (VPS) in any pressure lower than VLPPS.

To spray high-temperature ceramics and oxides, APS is a more common method. The heat source for the deposition process is produced through DC or RF discharge and the flame temperature is about 8000 K and may reach 14000 K in the jet core (Fauchais, Vardelle and Dussoubs, 2001). A combination of elevated temperatures and high velocity leads to superb deposition densities, bond strengths, and low porosity coatings. The final coating in this method is dense having lower than 1% porosity (Zatorski and Davis, 2005).

2.2.5.6.1 Radiofrequency (RF) plasma spraying

Radiofrequency induction plasma spraying, also known as vacuum induction plasma spray (VIPS) utilizes an inductively coupled RF plasma torch to produce plasma. Three types of precursors are commonly used in VIPS i.e., powder, suspension, or solution that is axially introduced into the center of the discharge cavity. VIPS has the capacity to easily melt relatively large feedstock particles due to its typical large-volume and long residence time, hence forming a pure and dense coating deposition (Boulos, 1992). The RF induction plasma spraying system is schematically shown in Figure 2-13.

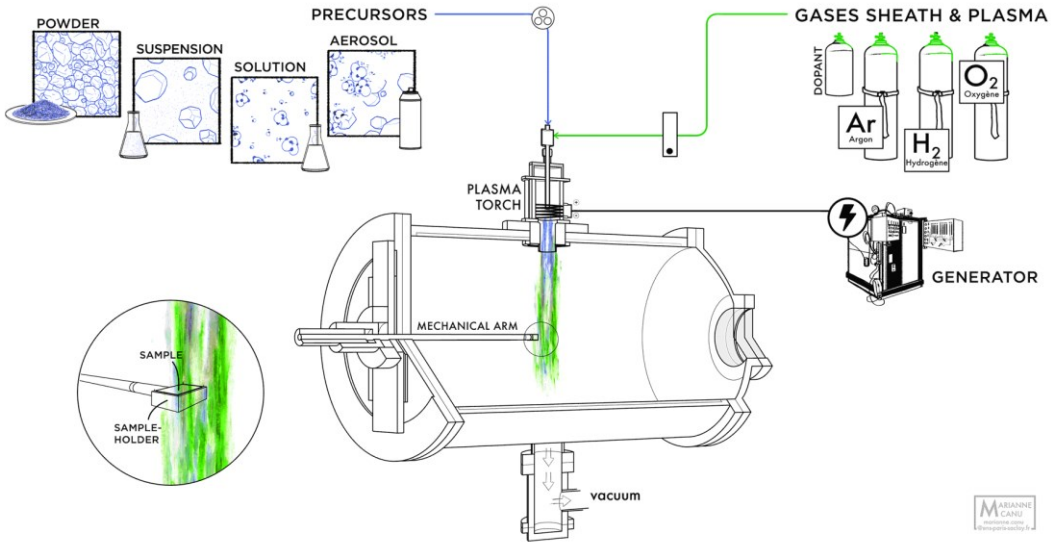

Figure 2-13. Schematic of the RF induction plasma spraying (Courtesy of Marianne Canu).

2.2.5.6.2 Reactive plasma spray

The reactive plasma spraying is a special coating process in which the plasma spraying technique, is used, in a controlled reactive environment. This technique is often used for the fabrication of non-oxide ceramic coatings such as nitrides, carbides, and borides that are difficult or impossible to directly inject and deposit with conventional thermal spraying because of their decomposition at high temperature without a stable melting phase (Fauchais, Vardelle and Denoirjean, 1997).

In this technique, heated elemental metals or non-metallic powders react with the surrounding active species such as atoms, ions, and radicals in plasma. The reactants can be in form of

powder, liquid, gas, or any combination thereof (Shahien *et al.*, 2012). This process can be done using DC plasma (Tsunekawa *et al.*, 1996), or RF plasma (Tsunekawa, Hiromura and Okumiya, 2000) where the latter is much more superior, thanks to its flexibility in providing the high temperature and low particle velocity that facilitate the reaction between species in the plasma. Furthermore, given the absence of electrodes in RF technology, there will be no electrode-born impurities in the coating (Shahien, Yamada and Fukumoto, 2016).

2.2.5.6.3 Suspension plasma spray (SPS)

In conventional thermal plasma spray technology, the coating is built up by impinging and solidification of the molten or semi-molten particles onto the substrate. In this process, the injected materials are in the form of powder carried into the hot plasma core with a carrier gas. However, injection of powder with sub-micron or nano-sized particles is challenging as the small particles tend to agglomerate and consequently clog the injection tubes and probe. The agglomeration could be a result of electrostatic forces and/or humidity. The irregular injection flow, caused by the agglomeration of feedstock prevents the formation of homogeneous coatings. Another difficulty is the injection of fine or light particles into the viscous jet. It is harder to introduce light particles into the hot core of the plasma and therefore they do not receive enough heat for the successful coating deposition process. To overcome this problem, a liquid carrier is used instead of high gas flow rate (Lima and Marple, 2007), (Gitzhofer, Bouyer and MI Boulos, 1997). Once the suspension is injected into the plasma, it is broken down and the liquid is vaporized by the hot plasma flow. The suspended feedstock particles are heated, accelerated, and impinge onto the substrate as shown schematically in Figure 2-14. In comparison to the conventional plasma spray process with powder feedstock, the SPS is more complicated because the mechanism of formation of the final coating is controlled by the fragmentation and vaporization process (Fauchais, Rat, *et al.*, 2008). Besides, SPS technology facilitates the formation of a nanostructured thick layer in the range of a few micrometers up to a few hundred micrometers (Fauchais, Rat, *et al.*, 2008).

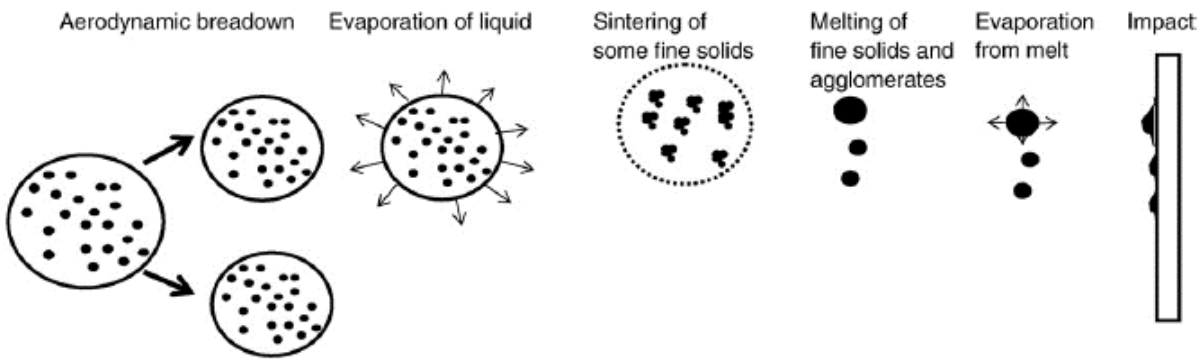

Figure 2-14. Schematic representation of in-flight suspension droplet in high temperature plasma (Pawlowski, 2009).

To prepare the suspension feedstock, the precursor is dispersed in water or other organic liquid such as ethanol. The viscosity of suspension feedstock determines the facility of pumping and transporting the precursor into the plasma. When the suspension is submitted to the hot core of the plasma, it is fragmented by a gas (generally Ar) expanding within the body of the nozzle, and the liquid is vaporized (Fauchais *et al.*, 2015). The fragmentation is a function of Weber number (*We*) (Equation 2-22) and Ohnesorge (*Oh*) number (Equation 2-23) with the former being more important than the latter. The Weber number is defined as the ratio of the force applied by the flow on liquid (gas velocity) to the surface tension force of the liquid with a viscosity between a few tenths to tens of mPa (Fauchais, Etchart-Salas, *et al.*, 2008). The Ohnesorge (*Oh*) number is defined as the ratio of internal viscosity dissipation to the surface tension energy (Fauchais and Vardelle, 2012).

$$We = \frac{\rho_g . u_r^2 . d_l}{\sigma_l} \qquad \text{Equation 2-22}$$

$$Z = \frac{\mu_1}{\sqrt{\rho_l} . d_l . \sigma_l} \qquad \text{Equation 2-23}$$

Where ρ_g is the atomizing gas mass density (kg/m^3), u_r the relative velocity between the gas and the liquid (m/s), d_l the diameter of the droplet (m) and σ_l the surface tension of the liquid phase (N/m), and μ_1 the liquid viscosity (Fauchais and Vardelle, 2012).

For example, water cannot fragment as small as ethanol, so droplets are large, because water has higher surface tension, and it needs higher energy to fragment and get vaporized. However,

using ethanol as a suspension liquid increases the chance of carbon contamination in the final coating. In addition, ethanol evaporates fast in plasma, and it forms carbon which clogs the outlet of probe and leads to formation of big droplets that are not good for the reaction. In this process, since the suspension plays the feedstock role, the liquid should be introduced into the hot core (central zone) of plasma through an atomizer by using a pneumatic system or a peristaltic pump (Pawlowski, 2009).

2.2.6 Aluminum nitride coating methods

Nitride ceramic films/coatings are commonly produced on different substrates for different kinds of applications. AlN thin films have been fabricated by various vapor deposition methods. Although these methods facilitate the fabrication of high-quality and pure coatings due to their relatively low deposition rate, their application is limited to AlN thin films. Thermal plasma spray owing to its high deposition rate eases the formation of thick coating about 100 µm and in this process, the feedstock doesn't need to go to the vapor phase. Therefore, the molten or semi-molten particles can deposit and fabricate coating (Yamada *et al.*, 2007). However, it is difficult to deposit AlN coatings by conventional plasma spray methods due to the decomposition of AlN. In Table 2-8 different coating methods and their experimental condition for fabrication of AlN coatings are listed.

Table 2-8. Summary of AlN coating methods, modified after (Barandehfard, Aluha and Gitzhofer, 2021).

Category	Method	Precursors	Pressure (Torr)	Coating Substrate	Reference
Thermal spray	RF plasma spray	Al + N_2	~ 50	stainless steel, quartz plate	(Yamada *et al.*, 2007)
	DC plasma spray	Al + NH_4Cl	760	mild steel (SS400)	(Shahien *et al.*, 2011a)
	DC plasma spray	Al + N_2 + H_2	760	soft steel (SS400)	(Shahien *et al.*, 2010a)
	Reactive DC plasma spray	Al_2O_3 + N_2	760	mild steel (SS400)	(Shahien *et al.*, 2013b)
PVD	DC magnetron sputtering	Al + Ar + N_2	~1.8×10^{-3}	stainless steel (SS) 304L	(Choudhary *et al.*, 2015)
	DC magnetron sputtering	Al + N_2	~7.5×10^{-6}	silicon nitride	(Metel *et al.*, 2020)
	DC Reactive magnetron sputtering	Al + Ar + N_2	~2×10^{-7}	crystal Si, amorphous SiN	(Belkerk *et al.*, 2012)
	RF magnetron sputtering	AlN + Ar	~ 7.5×10^{-10}	glass, mica, and silicon	(Musa *et al.*, 2020)
	RF reactive sputtering	Al +Ar + N_2	<5×10^{-6}	(100) Si wafer	(Cheng *et al.*, 2003)
	Pulsed laser deposition	AlN + N_2	~ 7.5×10^{-8}	(100) Si wafer	(Kolaklieva *et al.*, 2019)
	Ion beam sputtering (IBS)	Al, Ar, N_2	~ 2×10^{-6}	(100) Si wafer	(Han *et al.*, 2004)
CVD	Atomic layer deposition	$Al(C_4H_9)_3$ + N_2H_5Cl + $C_{12}H_{27}Al$		silicon	(Dallaev *et al.*, 2020)

2.2.7 The role of gas species during nitridation through plasma spraying

Several important RF plasma spray parameters affect the formation of nitride coatings in plasma, and they include plasma gases, RF power, spraying distance, spraying time, and chamber pressure among others. The choice of gases has the highest impact on nitridation reactions. The most important gases in this process are N_2 and H_2 where N_2 produces the necessary N species, which largely contribute to the formation of the nitrides. In fact, the plasma chamber should be full of N species to facilitate the reaction between metals and nitrogen to generate nitride. In addition, the presence of H_2 in the plasma chamber is necessary because it produces NH radicals, which improve the nitriding process while at the same time removing the oxide layer from the metal surface. Moreover, H_2 enhances the thermal conductivity of plasma, improves heat transfer to the in-flight particles in plasma thereby increasing the RF power which contributes to the nitriding reaction (Yamada *et al.*, 2004b).

There are numerous examples of nitrogen-containing precursors which have been used, such as urea (CH_4N_2O) for the formation of TiN powder by reactive ball milling method (Sun *et al.*, 2009), melamine ($C_3H_6N_6$) for the formation of AlN nanopowders by mechanochemical reaction method (Rounaghi *et al.*, 2016), hydrazinium chloride (N_2H_5Cl) for deposition of AlN nanofilms by atomic layer deposition method (Dallaev *et al.*, 2020), hydrazine (N_2H_4) for deposition of atomic layer of AlN by atomic layer deposition method (Abdulagatov *et al.*, 2018), and ammonium chloride (NH_4Cl) for the synthesis of AlN powders by Low-Temperature Synthesis (Kato and Sugawara, 2019).

2.2.8 Main challenges in the synthesis of AlN coating

It is impossible to produce AlN coatings by injection of AlN powder through conventional thermal spraying methods because AlN decomposes at high temperatures (2000-2300 °C) without a stable melting point (Shahien, Yamada and Fukumoto, 2016). Therefore, reactive plasma spraying technology is a method for in situ formation and deposition of AlN through the reaction of pure Al or Al-containing substances with surrounding active nitriding species in the plasma. Nitriding of Al metal is normally prevented by the naturally occurring oxide layer that inhibits the diffusion of nitrogen into the metal matrix (Freiberg, 2018), due to poor solubility and the low diffusion rate of nitrogen in Al (Farokhzadeh and Edrisy, 2017). Thus, injection of

H_2 gas through the plasma is essential to remove the oxide layer on the surface of Al particles (Yamada *et al.*, 2004a). The low N-diffusion coefficient into Al leads to the slow growth rate of AlN by normal plasma nitriding (Visuttipitukul, Aizawa and Kuwahara, 2003). It has been claimed that formation of AlN is challenging due to its decomposition (2000-2300 ^{o}C) of AlN in plasma (Yamada *et al.*, 2005). A schematic illustration of the nitridation process is shown in Figure 2-15. When Al particles are injected into the nitriding atmosphere of plasma, Al particles melt and then react with surrounding nitrogen species. However, the nitridation reaction begins on the surface of Al during flight to form AlN. When Al melts, it expands and breaks down facilitating the reaction between Al and N. Below Al melting point temperature, nitridation is negligible due to the oxide layer on the surface of Al which hinders the reaction of nitrogen with Al.

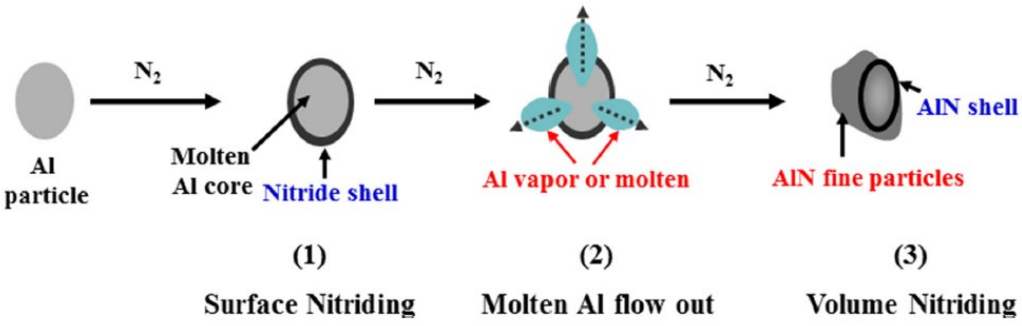

Figure 2-15. Schematic of the nitridation process of Al particle in plasma (Shahien *et al.*, 2011d).

If the nitridation reaction is complete in-flight, the nitride particles cannot stick on the substrate, and they splash. However, when particles with nitride surface hit the substrate they explode, and the molten Al flows. Therefore, under nitriding plasma irradiation, the post-deposition reaction of liquid Al completes the nitridation of the coating. The most challenging step in nitridation reaction is to increase the efficiency of deposition by adjusting experimental conditions to both inflight and post-deposition nitriding reactions. Moreover, plasma temperature and quantity of nitrogen active species strongly affect the amount of AlN content in the coating. Plasma temperature should provide enough heat for the reaction; however, it should not be too high as it causes decomposition of in flight and deposited AlN which leads to the formation of porosity in the coating. Also, if the nitridation reaction is complete in-flight, particles cannot deposit on the substrate to produce a coating.

2.2.9 Modeling and validation of results

In this work, the prediction of corrosion tendencies of refractories and coating was modeled using Materials Studio and Factsage software and the results were validated by sessile drop and Alcan immersion test experiments. The step-by-step of this process is as follows:

1. Density functional theory (DFT) was used to study the interaction between molten Al and hexagonal and cubic AlN coating at 1200 K, to determine the interfacial surface energy of Al-AlN as well as the possibility of interatomic diffusion at the interface.
2. FactSage thermochemical software was utilized to predict the possibility of a reaction between molten Al alloy and refractory materials, and the potential reaction products that can create suitable corrosion-resistant coatings.
3. The sessile drop method measures the contact angle between several liquids and solid surfaces at room temperature to determine the surface energy of the solid material, which influences the wettability of the material.
4. Alcan immersion test was used to investigate the corrosion resistance of the modified WFM refractories and plasma synthesized AlN coating in contact with molten Al alloy.

2.2.9.1 Modeling of interfacial energy between AlN and molten Al based on Density functional theory (DFT)

Density functional theory (DFT) is a type of electronic structure calculation, which is used to determine the total energy of a system, applying wave functions to compute some parts of the energy, and the electron density to calculate the other parts of the energy. Electronic structure calculations serve an important role in the understanding of chemical structure and reactivity (Baseden and Tye, 2014). For example, simulation by DFT has been used to model structural, energetic, electronic, reactivity, and stability properties of aluminum nitride nanotubes (AlNNTs). The results indicated that AlNNTs with larger diameters exhibited higher binding energies, and thus increasing diameter enhances the stability of AlNNTs (Muz, Kurban and Kurban, 2021). Some authors have used DFT to calculate the interfacial properties of interacting materials, with many results revealing their atomic configuration and electronic distribution. The work of adhesion for interfaces has been modeled in metal-ceramic interfaces such as Al/nitrides (VN, CrN, TiN) (Siegel, Hector and Adams, 2003), and AlN with selected four metals (Al, Cu, Ti, and Zr) showing that the adhesion energy is mainly affected by lattice

mismatch and does not have a linear relationship with either enthalpy of formation or the surface energy (Tao *et al.*, 2015). A comparison of adhesion energies and relaxed structures of Al/TiC and Al/TiN interfaces shows weaker bonding and less relaxation in the Al/TiN, with lower surface energy, and the larger overlapping bonding states at the Al/TiC interface reveals why it displays larger adhesion energy in comparison (Liu *et al.*, 2003). In comparing adhesion energies for Al/ceramic interfaces with ceramics involving carbides (WC, VC), nitrides (VN, CrN, TiN), and oxides (α-Al_2O_3), it was observed that adhesion was lowest among interfaces constructed from non-polar surfaces, regardless of the ceramic component, while adhesion was largest for those interfaces created with polar surfaces (Siegel, Hector and Adams, 2003). Other authors have modeled the work of separation in AlN/Ti interfaces, in addition to studying their microstructure, electronic structure, the most stable interface structure, and the interfacial bonds. It was observed that the covalent interaction for the N-Ti bond is stronger than the Al-Ti bond, while the N-terminated and the Al-terminated interfaces exhibit a mix of covalent and ionic bonding (Jin *et al.*, 2018).

On the other hand, *ab* initio simulations of AlN using the Vienna Ab Initio Simulation Package (VASP) have been utilized to investigate the structural and the electronic properties (elastic, piezoelectric, and dielectric tensors) of hexagonal AlN structures (Alsaad *et al.*, 2020). Although DFT results can be useful, the findings have limitations. For example, it has been observed that the formation energetics involving direct diffusion of nitrogen atoms into either fcc-Al octahedral or tetrahedral interstitial sites to create rocksalt or zincblende AlN crystal lattice, cannot be explained wholly as a thermodynamical process (Yadav, Wang and Liu, 2016).

2.2.9.2 Thermodynamic equilibria modeling

In order to predict the reaction potential between different compounds under specific reaction conditions, researchers have recently used thermodynamics software, which is based on the renowned CALculation of PHAse Diagram (CALPHAD) methodology for thermodynamic calculations (Jung and Van Ende, 2020). Several commercial thermodynamic software packages have been developed since the 1970s: FactSage (www.factsage.com) (C. W. Bale *et al.*, 2016), ThermoCalc (www.thermocalc.com) (Andersson *et al.*, 2002), MTDATA (National Physical Laboratory, UK) (Davies, Dinsdale and Gisby, 2002), Pandat (www.computherm.com) (S.-L.Chen *et al.*, 2002), and MatCalc (www.matcalc-engineering.com) (Kozeschnik *et al.*, 2004).

Two main requirements that should be met to precisely perform thermodynamics calculations are: (i) the user's access to the accurate thermodynamics database covering the needs of the specified system and (ii) the precision of the algorithm that minimizes the total Gibbs energy of a system with a set of limitations (Jung and Van Ende, 2020). The FactSage thermochemical software is a powerful package that consists of a series of modules with access to thermodynamics databases for thermochemical calculations to provide information on the reactions, phase diagrams, created phases, and compositions at different temperatures and pressure in equilibrium (C. W. Bale *et al.*, 2016), (Luz *et al.*, 2011a). The FactSage package is divided into four categories namely (i) Info, (ii) Databases, (iii) Calculate, and (iv) Manipulate, where each of them includes various modules. The "Calculate" category consists of numerous modules such as Reaction, Equilib, and Phase Diagram, which facilitate performing extensive thermochemical calculations based on Gibbs free energy minimization and it creates tables, graphs, and figures with the main application being in corrosion, glass technology, and ceramics. The most popular module in FactSage is "Equilib", which is performed based on Gibbs energy minimization. It computes the concentration of resulting chemical species when several elements or chemical compounds completely or partially react in particular conditions to reach a state of chemical equilibrium. Moreover, this module eases performing the cooling calculations and exhibiting the phase transitions and compositions during equilibrium cooling. The "Reaction" module computes alterations in widespread thermodynamic properties of different species like pure elements, compounds, or ions (both plasma and aqueous ions), their mixture as well as their chemical reactions (www.factsage.com), (C W Bale *et al.*, 2016). The main limitation of this software is that it cannot consider all the factors in a chemical process especially parameters related to the kinetic aspects (Luz *et al.*, 2011b).

This thermochemical software can predict the corrosion of crucibles, refractories in contact with a chemically aggressive molten metal such as Al and Mg, and detect the reaction products (Harvey *et al.*, 2020). In addition, the thermodynamic simulation of refractories in contact with molten metal alloys using FactSage software can predict the composition of refractory-slag systems. However, there are several limitations in considering the factors that can affect the corrosion, especially for the lack of all the factors that relate to the reaction kinetics (Munoz, Camelli and Martinez, 2017). Results of thermodynamic calculation in the literature involving Al–$Al_6Si_2O_{13}$, Al–$SrAl_2Si_2O_8$, and Al–$BaAl_2Si_2O_8$ systems at 1173 K using FactSage have

indicated that mullite and strontium celsian are not chemically resistant to molten Al. Mullite reacted with Al to produce alumina and Si, while $SrAl_2Si_2O_8$ produced Al_2O_3, Si, and $SrSiO_3$. However, $BaAl_2Si_2O_8$ showed the best corrosion resistance in contact with molten Al (Bocardo and Torres, 2010). A ternary phase diagram system CaO, Al_2O_3, and SiO_2 with constant MgO at 1673 K created by FactSage software indicates that a liquid slag can be produced for practically any slag basicity ratio (slag basicity is defined as the (CaO% + MgO%)/SiO_2% ratio of the liquid: if this ratio exceeds 1, the slag is basic; if it is less than 1, it is acidic) (Elliott, 1988), (Balomens and Panias, 2013).

In another research, a FactSage calculation has been done to predict the effect of N_2 and NH_3 gases in plasma, reacting with Al to produce AlN. Gibbs's free energy of the reactions was calculated and the results revealed that the use of NH_3 was more effective than N_2 as a nitriding agent (Kim, Choi and Park, 2013). In another study, simulating the synthesis of AlN powder, the theoretical calculation showed that the plasma temperature should be maintained in the range of 2500 to 2700 K (Kim, Choi, Kim, *et al.*, 2014). In the synthesis of AlN particles, nucleation and crystal growth occur by reacting Al gas and N_2 between 2500 and 2700 K, and the reaction does not seem to occur below 2350 K (Kim, Choi, Han, *et al.*, 2014).

In this project, in order to better understand the corrosion reaction between refractories and Al-Mg alloy, and compound formation as a function of temperature, an investigation on thermodynamic properties of this phenomenon was carried out using the Factsage software (version 7.3) developed by the CRCT group at Ecole Polytechnique de Montreal using the FSlite, FToxide, and FactPS database. The FactSage's FSlite light-alloy database was derived from the European COST Action 507 (COST 507, Thermochemical database for light metal alloys) designed for thermodynamic and phase equilibrium calculations of Al alloys in the commercial series 1000, 2000, 3000, 4000, 5000, 6000 and 7000 as well as Mg alloys. This database is reliable for temperature ranges between ambient temperature and 2200 ^oC, while the results are valid at a higher temperature for alloys comprising high melting point metals. The FToxid databases for ceramics, refractories, slags, etc. contain data for pure oxides, oxide solutions mostly Al_2O_3, MgO, SiO_2, CaO, and their combination. The FactSage's FactPS database comprises pure substances data for 4777 compounds.

2.2.9.3 Wetting phenomena and surface energy measurement using sessile drop method

When a molten material encounters a solid surface, it can produce a wetting or a non-wetting system. The wetting system can be further categorized as reactive or non-reactive, while the reactive system may involve the dissolution or the formation of a new compound (Eustathopoulos, 2015). Modeling of the wettability of a solid by a liquid at a high temperature has shown that the final contact angle is governed by some form of interfacial reaction (Nogi *et al.*, 2004). Yet, evaluation of the wetting process by contact angle only is not sufficient. Various factors such as droplet base diameter, height, and the time scale are suggested to be applied to reach a reliable evaluation of wetting. The wetting model must satisfy the conditions of $d\theta_t/dt<0$ (reduction in contact angle) and $dD_t/dt>0$ (increase in base diameter) as shown in Figure 2-16. The reactivity of molten Al with some ceramic oxides such as Al_2O_3, SiO_2, and mullite has been investigated and reported in the literature. The experimental results show that molten Al reacts with ceramic oxides and gives Al_2O_3. It was also noticed that no strong relationship exists between wettability and reactivity in the system (Sobczak, 2005).

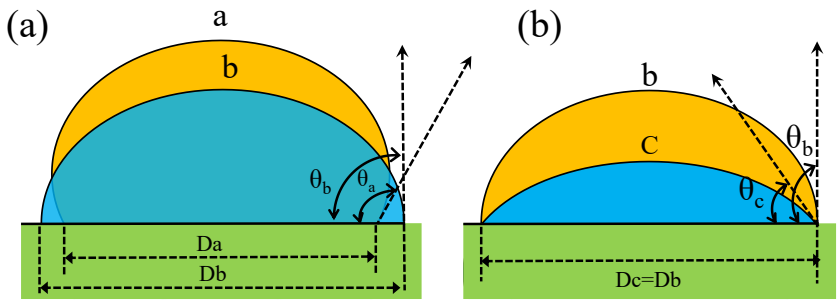

Figure 2-16. Schematic illustration of the two cases of contact angle decreasing: (a) with an increase in the droplet base diameter, and (b) without an increase in the droplet base diameter, modified after (Nogi *et al.*, 2004).

When molten metal and ceramic substrates are in contact, the wetting of ceramic substrate is usually accompanied by an interfacial reaction between the metal and the ceramic (Fujii, Nakae and Okada, 1993). Hence, a new composition is formed during the reaction at the interface, which has a strong effect on the magnitude of their interfacial free energy and subsequently changes in contact angle. For example, in some reactive systems (AlN + Y_2O_3 as substrate, and molten Al), due to the formation of a new component in the interfacial surface, the degree of wetting changes over time (Fujji, Nakae and Okada, 1993). It was reported that considering a

logarithmic time scale, the wetting process of a reactive system passes through four distinct phases: (I) dynamic non-equilibrium phase, (II) quasi-equilibrium phase, (III) non-equilibrium chemical phase, and (IV) equilibrium phase.

Phase I is known as the original wetting phase, which is the physical wetting for the reactive and non-reactive systems. The wetting is so fast that it terminates in much less than 1 s for the molten Al at 1373 K. Phase II is known as the interfacial-reaction wetting due to the interfacial reactions. The rate of this phase is much lower than phase I (less than l/l000 in this system). So, using a logarithmic time scale, separation of these two wetting types is possible. It should be noted that phase III includes four distinct stages (1, 2, 3, 4) through which the contact angle is reduced. The change in the drop shape during phase III is illustrated schematically in Figure 2-17. It is clear from the figure that, in the first stage, the contact angle decreases while the interfacial area increases. In the second stage, the interfacial area is constant, but the contact angle decreases. In the third stage, the contact angle decreases with diminishing interfacial area, and finally, in the fourth stage, the contact angle remains constant with decreasing interfacial area. These four stages arise due to interfacial reactions, with the liquid being consumed and therefore, the equilibrium contact angle cannot be observed (Fujii and Nakae, 1996).

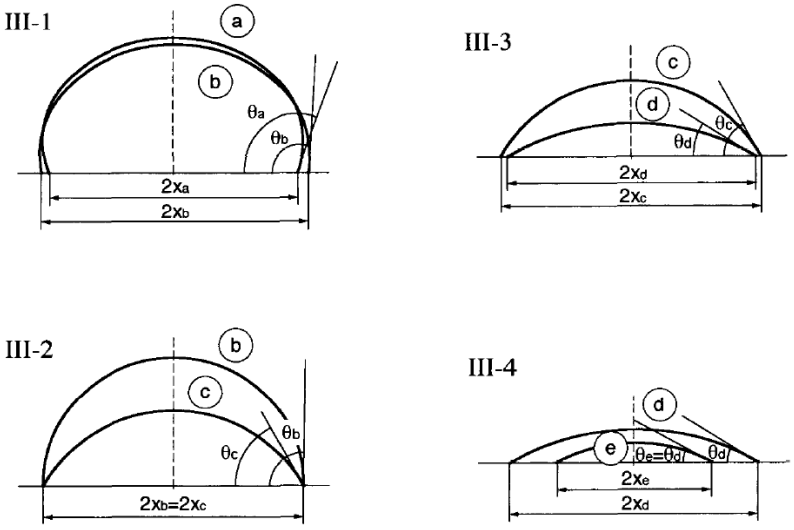

Figure 2-17. schematic model of phase transition in phase III (Fujii and Nakae, 1996).

However, in non-reactive systems such as AlN-molten Al, only phases I and IV occur. Nevertheless, with the addition of Y_2O_3, the interfacial reaction and all of the four phases occur.

The main part of the wetting takes place in phase I and the original wettability can be measured only during phase II, after the wetting in the previous phase (Fujji, Nakae and Okada, 1993). The contact angle of phase II follows the Cassie-Baxter law as it is in a metastable state, while interfacial conditions determine the contact angle of the phase. Therefore, the process should be designed in such a way as to apply Cassie's law throughout phases II to IV. From Figure 2-18 it is interpreted that AlN has the highest contact angle, which is constant with time, while additives seem to lower the contact angle and hence increase wettability. A similar observation has been made with the addition of carbon in AlN as shown in Figure 2-19 (Fujji, Nakae and Okada, 1993).

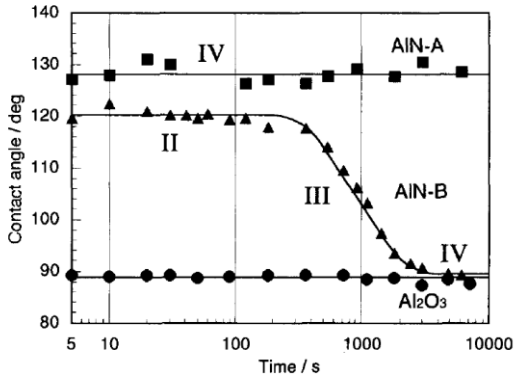

Figure 2-18. Contact angle curve for AlN-A (Pure AlN), AlN-B (AlN+Y_2O_3), Al_2O_3 at 1373 K (Fujji, Nakae and Okada, 1993)

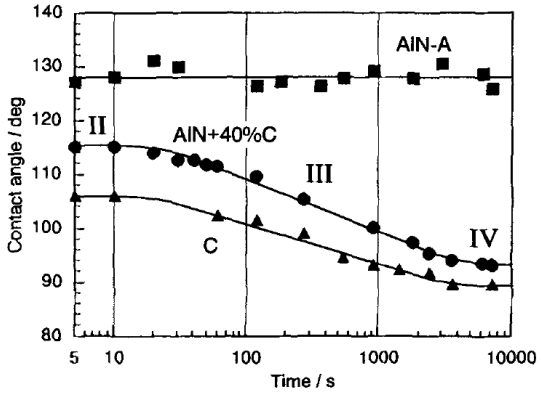

Figure 2-19. Contact angle curve for AlN-A (Pure AlN), AlN-40%C, C at 1373 K (Fujji, Nakae and Okada, 1993).

In laboratories, the wettability of a solid sample can be studied using the sessile-drop test with the contact angle being measured on a Krüss Advance goniometer. It is worth mentioning that the surface energy value of solids strongly depends on which liquids are selected for the

measurement and which theory is utilized in the calculation and analysis of data (Rulison, 1999). According to solid composition, one of the following common theories can be applied to calculate the surface energy of a solid surface from a set of liquid/solid contact angles:

(a) Zisman theory (Zisman, 1964) is the most applicable to polymeric surfaces such as poly(ethylene) and poly(propylene).
(b) Owens/Wendt theory (Owens, 1969) works best for polymerics surfaces containing heteroatoms, like polyimides, polyesters, polyacrylates, and polycarbonates.
(c) Fowkes theory (Fowkes, 1964) is more applicable for poly(methyl methacrylate) surfaces.
(d) van Oss theory (Good, Chaudhury and Oss, 1991) works best for inorganic surfaces, organometallic surfaces, pigments, pharmaceutical powders, ceramics and paper.

In this project, as WFM refractories and AlN coatings are inorganic ceramics the van Oss theory was applied to calculate their surface energies. For this purpose, diiodomethane (CH_2I_2) was used as a non-polar liquid, while water (H_2O) and formamide (CH_3NO) were used as polar liquids (Amama *et al.*, 2013). Since surface energies of solids are usually measured at room temperature, for most adhesion energy works, it can be assumed to be similar at elevated temperatures (Rulison, 2005). This assumption is valid for several solids such as chrome-plated steel and not for Al foils for instance. It is important to highlight that the contact angle measurement for the system of Al-ceramic is not simple for two main reasons:

a) The oxidation of Al: the presence of the oxide layer on the surface of the Al will prevent the interface to move, so a non-reliable contact angle will be obtained.
b) Al is a highly reactive metal and due to interfacial reaction between Al and the ceramic, the contact angle will change over time (Fujii and Nakae, 1996).

2.2.9.4 Corrosion test of modified WFM and plasma synthesized AlN coatings

During the melting of Al alloys in industry, the main problem is related to the wetting, penetration, and reaction of Al alloys with the refractory and this leads to corrosion (Brondyke, 1953). One of the most important interfacial phenomena happening at the surface of the refractory is wetting because it provides an opportunity for the penetration of molten alloys through the pores and then initiates chemical reactions with refractory compositions. Penetration occurs at increasing rates at the zone of the refractory that is exposed to the atmosphere and

molten alloy alternatively. Therefore, the corrosion reaction begins with the molten alloy wetting and permeating the refractory. At the onset, the silica of the refractory is reduced by molten Al, which is accompanied by a negative volume change; therefore, this phenomenon may allow further metal penetration into the refractory. Finally, the rate of reaction is controlled by the amount of Al alloy that diffuses through the open pores of refractory material (Gao, Afshar and Allaire, 2004), (Brondyke, 1953).

One of the most important factors in wetting of the aluminosilicate refractories by molten Al alloys is the reaction of Al with the atmospheric oxygen to form a porous corundum film on the surface of the molten alloy. This film includes channels that direct molten alloy to the surface of the refractory and this process is intensified in the substrate, at the triple point of solid-liquid-gas phases (Yurkov and Pikhutin, 2009). The wettability of the refractory affects its propensity for corrosion and hence, the wetting of refractories by molten Al alloys must be controlled to protect them against corrosion. Many factors affect the wettability of the molten alloy-ceramic system such as alloying elements, impurities, surface roughness, and the porosity of the refractory materials (Nogi *et al.*, 2004). Therefore, the interaction between molten metal and substrate is one of the key factors for choosing suitable material and processing parameters (Sobczak *et al.*, 2010).

The Alcan test is routinely used to evaluate the suitability of refractories for applications involving melting materials and holding furnace linings. The Alcan test is normally used to evaluate the corrosion resistance of the refractory materials suspended in molten metal or metal alloys for 96 h at 850 $^{\circ}$C to determine the extent of liquid metal penetration (Adabifiroozjaei, Koshy and Sorrell, 2013). For this purpose, two refractory samples in size of 51 x 25 x 25 mm are placed in a clay-bonded graphite crucible including 2 kg of molten Al- 5wt % Mg alloy, in a vertical electrical furnace (Allaire, no date). Since Mg is volatile, to keep the concentration of magnesium constant, 40 gr Mg should be added to the molten alloy every day. Upon testing, the refractory materials are evaluated according to the degree of infiltration, metal adherence, and level of cracking in the refractory. To measure the corrosion resistance of the plasma synthesized AlN coatings and pure substrates (Figure 2-20), the samples were put in direct contact with a molten Al-5 wt% Mg alloy for 2 h at 850 °C. During the corrosion test, the plasma synthesized AlN coatings were placed in specially designed plate with conical funnels in which the samples were

inserted before pouring liquid Al alloy as shown in Figure 2-20 (A) and (B); then molten Al-5wt%Mg alloy was poured on the surface of samples as shown in Figure 2-20 (C) and left in the furnace at 850 ºC for 2 h.

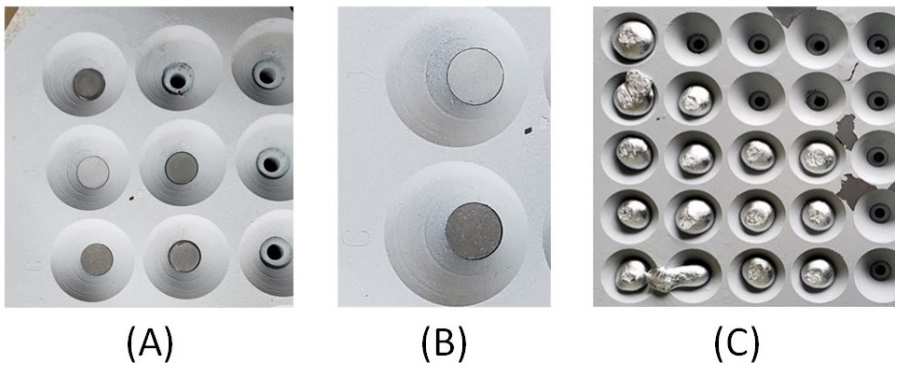

Figure 2-20. Corrosion test of AlN coatings: (A) and (B) samples were placed in the holes; (C) after pouring molten Al-5wt%Mg alloy on the surface of samples, the sample holder was placed in furnace at 850 ºC for 2 h.

CHAPTER 3 RESEARCH DESIGN

In this chapter, the step-by-step methodology developed in the thesis is presented. The process is schematically illustrated in Figure 3-1. From Figure 3-1, it can be seen that the developed methodology consists of three main parts: literature review and identification of coating material (shown as the blue box), synthesis of cubic AlN and investigation of the effect of nitriding agents, liquid suspension, standoff distance, substrate material, Al particle size distribution and promotors on the formation of AlN (shown as the orange box). In the following, the steps associated with phases are discussed.

As also discussed in chapter 1, the ultimate objective of this thesis is to meet the industrial need for corrosion-resistant materials in contact with molten Al alloy. Therefore, the first step of the methodology is to investigate the feasibility of two different approaches for the protection of refractories against molten Al-Mg: (a) effect of addition of several non-wetting agents to the composition of white fused mullite (WFM), and (b) deposition of aluminum nitride (AlN) coating on metal substrates. The presented literature review in chapter 2 revealed that AlN possesses corrosion-resistant property making it an appealing candidate for coating refractories of the Al melting and holding furnaces. Therefore, the developed methodology was based on the second solution which is the in-situ synthesis and deposition of AlN coating using SPS technology.

The second part, which is the core of the thesis is the synthesis of AlN and investigation of the aforementioned parameters on the formation of AlN. From Figure 3-1, it can be seen that the synthesis process is in fact an iterative one meaning that multiple factors related to plasma set up as well as the feedstock properties influence the final composition of the coating material. Not all of the variables, however, are sensitive, highlighting the necessity of grouping them based on their effect on the formation of AlN coating.

Initially, about 200 experiments considering 16 variables i.e., plasma torch (PL50, PL35), nozzle (supersonic, subsonic), carrier gas (argon, nitrogen), central gas (nitrogen, argon), injection flow rate (2 to 5 ml/s), chamber pressure (60-500 Torr), plasma power (15-55 kW), suspension concentration (2-20 wt%), nitriding agent (nitrogen gas, ammonia, urea, melamine), standoff distance (4-12 cm), liquid suspension carrier (light mineral oil, ethanol, hexadecane,

ethylene glycol), substrate (stainless steel, carbon steel, molybdenum, titanium), ratio Al/nitriding agent, number of deposition loops (30-500 loops), plasma mask, radial injection of nitrogen, Al size distribution (-35µm +1µm), and promoters (AlN, Al_4C_3, B, BN, Mo, Y_2O_3) were conducted to distinguish the impactful variables.

The system was initially set up following previous studies on the synthesis of AlN coating using conventional plasma spray technology, but since our synthesis methodology is based on SPS technology, the values suggested in the literature were not applicable in our case. For example, the power range of 4-5 kW is suggested by (Yamada, Nakamura, *et al.*, 2006) for powder injection of Al and nitrogen gas which was found to be not applicable in our plasma system. Another dissimilarity between the two plasma technologies (conventional *vs.* SPS) is related to their differences in the nitriding agent. Whereas nitrogen gas with 60 Torr pressure resulted in the formation of AlN using the conventional plasma technology method, this nitriding agent was found not to be a suitable nitriding agent in SPS technology. This is because of the dissociation of N_2 and quick recombination of N atoms. Therefore to produce more active nitrogen species in SPS technology, it was essential to apply high pressure (above 400-550 torr). Conversely, one requires low pressure to deposit a coating. Although at high chamber pressure all active species have a long residence time which facilitates their reaction, their velocity is not high enough to impinge and stick to the substrate and form a coating layer. For this reason, the rest of the experiments were carried out with other nitriding agents i.e., urea, melamine.

With regards to the standoff distance, the optimum value in the conventional plasma method was found to be 2-6 cm (Yamada *et al.*, 2005). However, the coating formed using this value in the SPS method was very thin (smaller than 1 µm), containing Al as the major phase. The formation of AlN, in the SPS method, as it will be discussed in the next chapter, was detected with standoff distance values smaller than 10 cm.

Once the plasma setup is complete, the next step is preparing the feedstock and injection. It should be noted that the synthesis of AlN for the purpose of the coating was necessary as the experiments with the injection of AlN powder directly into the plasma resulted in decomposition of the AlN and deposition of an Al coating. This was also found in other studies (Shahien, Yamada and Fukumoto, 2016), confirming the necessity of in-situ synthesis and deposition of AlN. The detailed process of feedstock preparation including the optimum ratios is given in

chapter 4. To prepare the feedstock composition, Al powder was mixed with either urea or melamine in various ratios given in chapter 4, and then suspended in a liquid carrier (hexadecane, mineral oil, ethanol, or ethylene glycol), before being injected into the plasma using a peristaltic pump and Ar as a carrier gas. Once the deposition loops (varied between 30 to 500) are complete, the sample was immersed in ethanol and the container was placed in the ultrasonic bath for 15 minutes as an integrity test to assess the cohesion/adhesion of the coating to the substrate. The analysis of the sample for detection of phases in the deposited coating followed in the next step where the samples were analyzed using X-ray diffraction. A threshold based on the percentage of AlN (70%) was prescribed to identify the plasma set up with the successful formation of AlN coating. In case the AlN did not form, the experiments were repeated with new values... Note that the 70% threshold satisfied the corrosion resistance of the coating as the corrosion test of samples with less than 70%AlN resulted in the formation of cracks on the surface, spalling of the coating, severe adhesion, and reaction between the molten alloy and coating.

The iterative experiments conducted with different factors and levels showed that among the aforementioned 16 synthesis variables, the formation of AlN was more sensitive to 6 variables i.e., nitriding agents, liquid suspension, standoff distance, substrate material, Al particle size distribution, and promotors. The experiments were thereby continued with further adjusting these variables for a maximized formation of AlN. In chapters 4 and 5, a comprehensive investigation of the effect of each of these variables and their combination on the formation of AlN is presented.

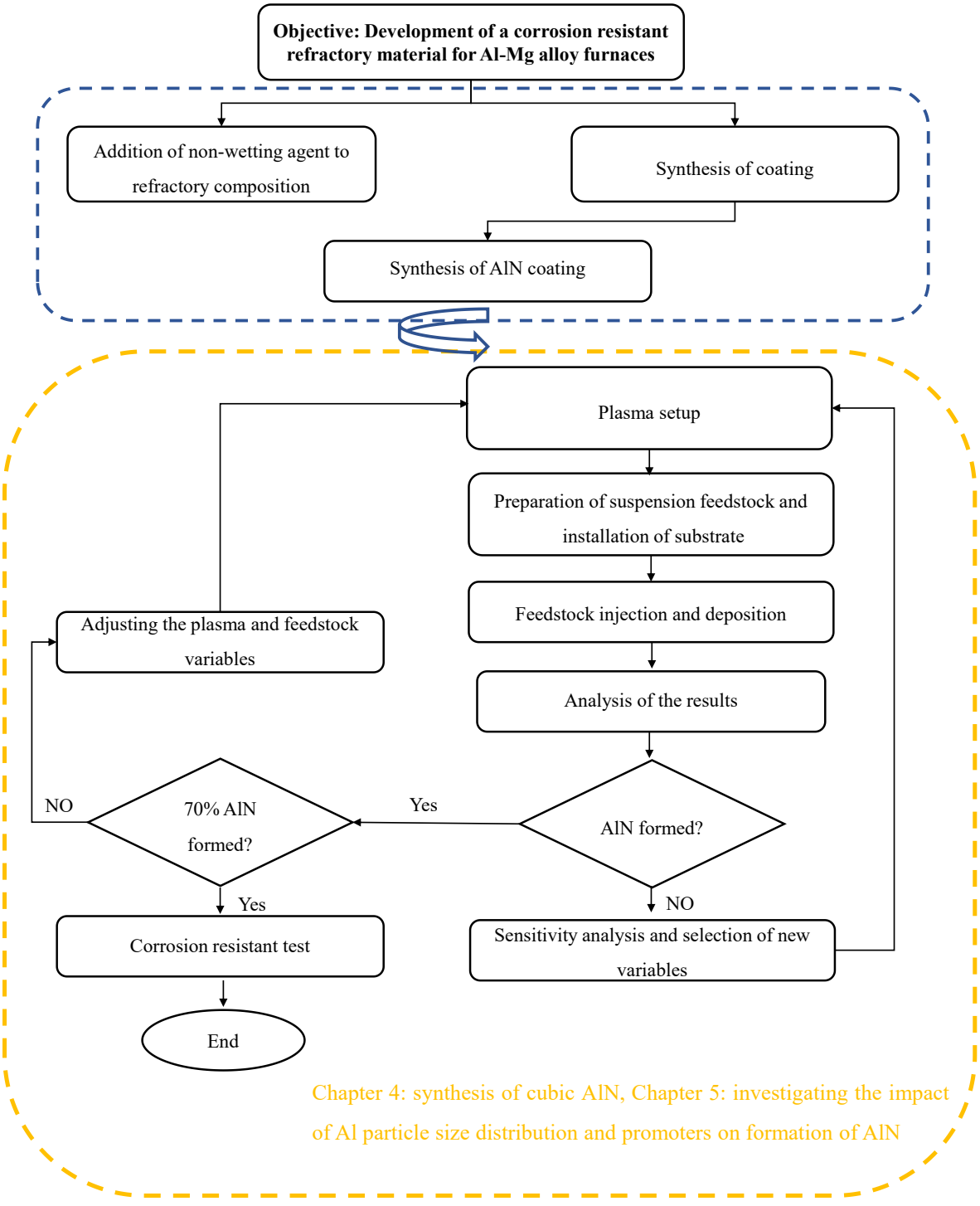

Figure 3-1. The flowchart of the developed methodology for this project.

CHAPTER 4 PLASMA SYNTHESIS OF CUBIC ALN

This chapter is based on a published journal article entitled "Synthesis of cubic aluminum nitride (AlN) coatings through suspension plasma spray (SPS) technology" with minor edition.

4.1 Avant-propos

Auteurs et affiliation :

Faranak Barandehfard: Étudiant au doctorat, Département de génie chimique et de génie biotechnologique, Université de Sherbrooke, Québec, Canada.

James Aluha: Chercheur postdoctoral, Département de génie chimique et de génie biotechnologique, Université de Sherbrooke, Québec, Canada.

François Gitzhofer: Professeur titulaire, Département de génie chimique et de génie biotechnologique, Université de Sherbrooke, Québec, Canada.

Date d'acceptation : 15 April 2021

État de l'acceptation : version finale publiée

Revue: Coatings

Référence : (Barandehfard, Aluha and Gitzhofer, 2021)

Lien d'accès : https://doi.org/10.3390/coatings11050500

Titre français : Synthèse de revêtements de nitrure d'aluminium cubique (AlN) grâce à la technologie de projection par plasma de suspensions (SPS)

Author Contributions: Conceptualization, F.B., and F.G.; methodology, F.B., and F.G.; software applications, F.B. and J.A.; validation, F.G., and J.A.; formal analysis, F.B., and J.A.; investigation, F.B.; writing—original draft preparation, F.B.; writing—review and editing, J.A. and F.G.; visualization, J.A.; supervision, F.G.; project administration, F.G.; funding acquisition, F.G. All authors have read and agreed to the published version of the manuscript.

Contribution au document:

In this paper, the effect of nitriding agents, liquid suspension, standoff distance, substrate material on the formation of AlN using SPS technology is investigated. As these variables were identified to be sensitive following the iterative experimental procedure explained in Chapter 3, this chapter can help to better understand the underlying mechanism of in-situ synthesis and deposition of AlN using SPS technology. In addition, the corrosion resistance of the plasma synthesized coatings was tested in contact with a molten Al-Mg alloy. Details of the synthesis process, characterization of the coatings, and the test results thereof are presented in this chapter.

Résumé

La projection thermique de nitrure d'aluminium (AlN) est un problème difficile car il se décompose à haute température. Dans cette recherche, l'utilisation de la technologie de projection par plasma de suspension est proposée pour le dépôt de revêtements d'AlN à structure cubique sur des substrats métalliques. Les effets de l'agent de nitruration, du liquide de la suspension, des matériaux du substrat et de la distance de projection pendant le dépôt par SPS ont été étudiés. Les revêtements synthétisés par plasma ont été analysés par diffraction des rayons X (XRD), microscopie optique (OM) et microscopie électronique à balayage (MEB). Les résultats montrent une teneur en AlN plus élevée dans les revêtements déposés sur un substrat en acier au carbone (~82 %) par rapport au substrat en titane (~ 30 %) ou en molybdène (~ 15 %). La mélamine mélangée à de la poudre d'aluminium pur a produit des revêtements plus riches en AlN jusqu'à 82 % par rapport à l'urée mélangée à l'Al (~25 % d'AlN). L'hexadécane était un liquide de suspension plus performant que les liquides contenant de l'oxygène tels que l'éthanol ou l'éthylène glycol. Lorsque les matériaux ont été exposés à un alliage aluminium-magnésium fondu à 850 °C pendant 2 h, la résistance à la corrosion du substrat en acier au carbone revêtu d'AlN a montré des performances améliorées par rapport au substrat non revêtu.

Mots-clés : nitrure d'aluminium cubique ; projection par plasma de suspension revêtements; mélamine; urée.

Synthesis of Cubic Aluminum Nitride (AlN) Coatings through Suspension Plasma Spray (SPS) Technology

4.2 Abstract

Thermal spraying of aluminum nitride (AlN) is a challenging issue because it decomposes at a high temperature. In this work, the use of suspension plasma spray (SPS) technology is proposed for the in-situ synthesis and deposition of cubic-structured AlN coatings on metallic substrates. The effects of the nitriding agent, the suspension liquid carrier, the substrate materials and the standoff distance during deposition by SPS were investigated. The plasma-synthesized coatings were analyzed by X-ray diffraction (XRD), optical microscopy (OM) and scanning electron microscopy (SEM). The results show higher AlN content in the coatings deposited on a carbon steel substrate (~82%) when compared to titanium substrate (~30%) or molybdenum (~15%). Melamine mixed with pure aluminum powder produced AlN-richer coatings of up to 82% when compared to urea mixed with the Al (~25% AlN). Hexadecane was a relatively better liquid carrier than the oxygen-rich liquid carriers such as ethanol or ethylene glycol. When the materials were exposed to a molten aluminum–magnesium alloy at 850 °C for 2 h, the corrosion resistance of the AlN-coated carbon steel substrate showed improved performance in comparison to the uncoated substrate.

Keywords: cubic aluminum nitride; suspension plasma spray (SPS); coatings; melamine; urea

4.3 Introduction

4.3.1 Background

Aluminum nitride (AlN) is a promising material that can find diverse applications in the aluminum industry (Long and Foster, 1959), for example, in crucibles for handling corrosive chemicals and reaction vessels (Yan and Fan, 2001). In addition, AlN has become the key component of semiconductor equipment, which is appropriate in piezoelectric and electronic applications (Iqbal and Mohd-Yasin, 2018). Some of these amazing properties of AlN are summarized in Table 4-1, as high thermal conductivity (Oh and Park, 1998), low thermal expansion coefficient (Sung *et al.*, 2017), and a large band gap, which is a major factor that determines a solid's electrical conductivity (Yaddanapudi, 2018), and this makes AlN an

electrical insulator. Other characteristics include AlN's chemical and physical stability at fairly high temperature regions, high hardness (Kim, 2005), and high resistance to molten metals, wear and corrosion (Sung *et al.*, 2017).

AlN exists in several crystal structures with different properties: hexagonal (wurtzite) crystal structure and two types of cubic structures (rock salt and zinc-blende). The cubic AlN is a metastable phase at ambient conditions, which renders its synthesis a difficult process (Shahien *et al.*, 2010a). In comparison to the hexagonal crystal structure, the rock salt cubic AlN by having a higher symmetry in its crystal structure shows greater thermal conductivity (250–600 $W \cdot m^{-1} \cdot K^{-1}$), electrical resistivity (10^{16} Ω·cm) and hardness (4079–5098 Hv) (Kudyakova *et al.*, 2017).

Table 4-1. Selected AlN properties[5].

Properties	Values
Thermal expansion coefficient	$\alpha = 4.3 \times 10^{-6}\ K^{-1}$
Thermal conductivity	$k = 319\ W \cdot m^{-1}\ K^{-1}$
Crystalline structure	Hexagonal or cubic
Hardness	1400 Hv
Electrical resistivity	10^{13} Ω.cm
Band gap	6.2 eV

4.3.2 Synthesis Methods of AlN

Some of the conventional synthesis methods of AlN powder involve the carbothermal reduction–nitridation of alumina (Jackson *et al.*, 1997), direct nitridation of Al powder (Da Cruz and Munz, 1999), non-transferred arc plasma method (Kim, Choi and Park, 2013), chemical routes (Ahn *et al.*, 2017), microwave-assisted urea route (Ahn *et al.*, 2016), pulsed laser ablation (Grigoriu *et al.*, 2000) and transferred type arc plasma (Iwata *et al.*, 2004). Table 4-2 and Table 4-3 summarize the different methods of producing AlN coatings and powder, respectively.

[5] Hexagonal AlN.

Table 4-2. Summary of different methods used in producing cubic and hexagonal AlN coatings[6].

Method	Precursors	Coating Substrate	Reference
RF plasma spray	Al powder + N_2	stainless steel, quartz plate	(Yamada *et al.*, 2007)
DC plasma spray	Al powder + NH_4Cl	mild steel (SS400)	(Shahien *et al.*, 2011a)
Atmospheric plasma spraying (APS)	Al powder + N_2 + H_2	soft steel (SS400)	(Shahien *et al.*, 2010a)
Magnetron sputtering	Al-disc + Ar + N_2	stainless steel (SS) 304L	(Choudhary *et al.*, 2015)
LT reactive magnetron sputtering	Al powder + Ar + N_2	crystal Si, amorphous SiN	(Belkerk *et al.*, 2014)
Reactive DC magnetron sputtering	Al powder + Ar + N_2	crystal Si, amorphous SiN	(Belkerk *et al.*, 2012)
Reactive plasma spray	Al_2O_3 + N_2	mild steel (SS400)	(Shahien *et al.*, 2013b)
RF magnetron sputtering	AlN + Ar	glass, mica, and silicon	(Musa *et al.*, 2020)
Atomic layer deposition	$Al(C_4H_9)_3$ + N_2H_5Cl + $C_{12}H_{27}Al$	silicon	(Dallaev *et al.*, 2020)
Wet-thermal treatment (WTT)	NH_3 + N_2 + $AlCl_3$	carbon fiber	(Kim *et al.*, 2017)
Pulsed laser deposition	AlN + N_2	Si (100)	(Kolaklieva *et al.*, 2019)
Magnetron sputtering system	Al + N_2	silicon nitride	(Metel *et al.*, 2020)

RF = Radio frequency; DC = Direct current; LT = Low temperature.

Thermal plasma technology is a well-adapted technology for synthesizing crystalline nano materials because of the fast reaction rates achieved due to the high plasma temperatures (Sung *et al.*, 2017), its flexibility in the choice of various feedstock materials (Kim, Choi, Kim, *et al.*, 2014), its high conversion rates and energy efficiency (Jackson *et al.*, 1997) and its rapid quenching (Ageorges *et al.*, 1993). Furthermore, plasma spray technology provides the opportunity for inflight reaction of the precursors and in-situ formation of the coatings in a wide range of thicknesses. Dense coatings can be produced by a combination of high reaction rates

[6] Modified version of this table is presented in chapter 2.

and relatively high velocity of melted particles. Among all the thermal spray methods, plasma spraying is extensively used to produce coatings due to its high enthalpy, with the molten or semi-molten particles being propelled to adhere and solidify on the substrate (Venkatramani, 2002). However, sometimes it is not necessary to melt the particles fully, because it is possible for particles in a semi-molten state to be deposited as a coating. Moreover, a thermal plasma process can allow for a wide range of coating thicknesses, stretching from nm to mm (Shahien, Yamada and Fukumoto, 2018). In order for the deposited coating to stick to the substrate, the injected particles must melt or be in a semi-molten state when they pass through the hot core of the plasma. The high melting point of AlN (2200 °C), as well as its decomposition at high temperatures,[7] does not facilitate the deposition of AlN particles injected through the plasma (Shahien, Yamada and Fukumoto, 2018).

Table 4-3. Summary of different methods used for producing AlN powder.

Method	Precursors	Reference
Carbothermal reduction	$Al_2O_3 + N_2 + C/CH_4$	(Gálvez *et al.*, 2009)
CVD	$AlCl_3 + NH_3 + N_2$	(Wu *et al.*, 2000)
Reaction at 500–1000 °C for 5 h[8]	$Al_2S_3 + NH_3$	(Jung and Ahn, 2000)
Sol-gel	$C_9H_{21}O_3Al$ + dextrose + HNO_3	(Chaundhuri, 2016)
Mechanochemical	Al_2O_3 powder + N_2	(Li, Xi and Zhou, 2009)
Mechanochemical	Al powder + Melamine	(Rounaghi *et al.*, 2012)
Transferred Arc-plasma	Al powder + N_2 + NH_3	(Iwata *et al.*, 2004)
Microwave plasma	Al powder + NH_4Cl + N_2 + H_2	(Li *et al.*, 2012)
Solvent thermal synthesis	$AlCl_3 + NaN_3$	(Li *et al.*, 2003)
Low-temperature synthesis	$Al + NH_4Cl$	(Kato and Sugawara, 2019)
Reactive plasma spray	Al + AlN powders + N_2	(Shahien *et al.*, 2011b)

CVD = Chemical vapor deposition; LT = Low temperature.

Besides ammonia (Qiu and Gao, 2003), nitrogen gas is usually used as a nitriding agent (Li, Xi and Zhou, 2009), but recently urea (Sun *et al.*, 2009), and melamine to produce Si-C-N

[7] Decomposition temperature of AlN is range of 2000 to 2300 °C.

[8] In tubing furnace solid Al_2S_3 reacts with ammonia gas to produce AlN powder.

(Shatnawi, Al-Mansi and Arafa, 2008), or AlN ceramics (Rounaghi *et al.*, 2017) have been proposed for nitriding reactions. Melamine ($C_3H_6N_6$), an organic compound containing about 67 wt% nitrogen is a trimer of cyanamide, with a 1,3,5-triazine skeleton, that releases nitrogen at high temperatures (Bretterbauer and Schwarzinger, 2012), and has been used to produce AlN powder by mechanochemical reaction with Al (Rounaghi *et al.*, 2019). Direct injection of nitriding powders such as urea or melamine with Al into plasma, unlike N_2 gas (Shahien, Yamada and Fukumoto, 2018), is challenging, particularly when there are different precursor components with various particle sizes and densities.

To alleviate the injection problems, suspension liquids have been utilized as carrier media for transporting micro and nano particles into the high temperature zones of plasma, with the added benefits of providing chemical reactions within the suspension liquid. Indeed, powder precursors are dispersed in the liquid media and when injected into plasma, the liquid phase evaporates, while the solid particles melt and vaporize to form clusters. Suspension plasma spray (SPS) was invented to create a homogenous precursor to facilitate direct injection of small particles into plasma by dispersing them in a liquid carrier (Gitzhofer, Bouyer and Maher Boulos, 1997).

In order to produce a durable coating that can withstand thermal shocks, the linear thermal expansion coefficient of both the coating and the substrate should ideally resemble as much as possible. Substrate materials should have a) high melting points to be stable upon exposure to high speed and high temperature plasma jet, and b) low thermal expansion coefficient difference between coating and substrate (Yamada, Akamura, *et al.*, 2006). An interlayer coating can be used to adapt the thermal expansion coefficient difference between coating and substrates (Cai *et al.*, 2002).

4.3.3 Non-Wetting Properties

In many material processing techniques, for example, in casting processes, molten metals are ordinarily in direct contact with ceramic refractories. Therefore, the properties of the final alloy product are highly affected by the high-temperature properties of the molten metal as well as the interfacial wetting or reaction phenomena. Many factors influence the wettability of the molten alloy–ceramic system such as the alloying elements, defects, impurities and surface roughness of the refractory (Nogi *et al.*, 2004). Besides the processing parameters, the

interaction between the molten metal and the substrate is one of the key factors considered in choosing a suitable material that will be in direct contact with the molten alloys (Sobczak *et al.*, 2010). It has been reported that when a molten metal and a ceramic substrate are in contact, the wetting of the ceramic substrate is usually accompanied by an interfacial reaction between the metal and the ceramic (Fujii, Nakae and Okada, 1993). Hence, a new composition is formed at the interface during the reaction, and this has a strong effect on the magnitude of the interfacial free energy and subsequently alters the contact angle between the molten metal and the ceramic. The contact angle measurement for an Al-ceramic system is not simple for two main reasons: (a) the oxidation of Al where the oxide layer on Al surface modifies the properties and behavior of the alloy, and (b) Al being a highly reactive metal corrodes the ceramic and its wettability changes over time (Fujii and Nakae, 1996).

Ceramics such as AlN are considered as suitable electrolysis cell material because of their non-wettability and non-reactivity towards molten Al or its salts (Mutale, Weirauch and Cramb, 2008). Some of these ceramics (rare earth oxide) such as Ce_2O_3, Yb_2O_3 and etc. have been synthesized as coatings using solution precursor plasma spray (SPPS) technology, with the authors investigating the effect of different direct current (DC) plasma parameters such as standoff distance, torch power, number of torch-passes, types of solvents and plasma velocity on the superhydrophobicity properties of the final coating (Cai *et al.*, 2016). They concluded that a short standoff distance, a high arc current, a low number of torches passes, the addition of ethanol to the solvent, and a high plasma velocity result in a dense superhydrophobic coating. In addition, the coated layer demonstrated a hierarchical surface roughness structure.

4.3.4 Research Objectives

The objective of this study is to produce cubic AlN-rich coatings deposited on various substrates to improve their corrosion resistance when in contact with molten Al-5 wt% Mg. SPS technology has been chosen because it provides flexibility in the selection of precursors and substrates. Moreover, since the injection rate of the precursor has a significant effect on the reaction and formation of the coating, the powder mixture can be suspended in a liquid carrier at various mass concentrations and injected into plasma using a peristaltic pump. The effect of synthesis parameters such as precursor composition, suspension liquid, substrate materials, and standoff distance on final coating composition was investigated. Coatings were characterized

by microscopy and X-ray methods. The anti-wetting properties of AlN were ascertained by the sessile drop test and a corrosion test using liquid Al-5 wt% Mg.

4.4 Materials and Methods

All experiments involving the synthesis of AlN coatings in this study were carried out using a radio frequency (RF) induction suspension plasma spray (SPS) reactor. The SPS system consists of a plasma chamber and atomization probe (of 7–12 μm water droplet size), a plasma torch (supplied by TEKNA Inc., Sherbrooke, QC, Canada), and a plasma power supply (Lepel Co., Edgewood, NY, USA).

4.4.1 Materials and Reagents

a) Substrates: 12.7 mm × 2.0 mm disks,
   1) Titanium disk, Ti-6A-4V (McMaster-Carr, Chicago, IL, USA) of composition Ti (88.10–90.92%), Al (5.50–6.75%), C (0.08%), Fe (0.40% Max), V (3.5–4.5%), and 0–0.30% others;
   2) Molybdenum disk, Mo (99%, American element, USA);
   3) AISI 1144 Carbon steel disk (McMaster-Carr, Chicago, IL, USA) of mainly Fe with inclusions of composition C (0.40–0.48%), Mn (1.35–1.65%), P (0.04% Max) and S (0.24–0.33%).

b) Suspension liquid carriers: Hexadecane (99% $C_{16}H_{34}$, Sigma Aldrich, St. Louis, MO, USA), ethylene glycol (99.8% $C_2H_6O_2$, Sigma Aldrich, St. Louis, MO, USA), mineral oil (light oil, $C_{16}H_{10}N_2Na_2O_7S_2$, Sigma Aldrich, St. Louis, MO, USA) and anhydrous ethyl alcohol (C_2H_5OH, commercial alcohol).

c) Powders: Pure aluminum metal powder (99.9% Al, Atlantic equipment engineers) with particle size range (-35 + 1 μm), urea grains (CH_4N_2O, -37 μm, Sigma-V1428), Melamine (99% $C_3N_6H_6$, -37 μm Alfa Aesar, Fisher Scientific, Tewksbury, MA, USA).

4.4.2 Preparation of Substrates

In order to increase surface roughness, the substrates were initially sandblasted by alumina particles to improve the coatings' sticking efficiency to the substrate. However, contamination was a weakness with this approach since the presence of alumina was detected by XRD in the

samples. Therefore, SiC paper (180) was used to scratch the substrates to obtain the desired surface roughness (~0.5 μm Ra) and this proved to be more effective.

4.4.3 Suspension Feedstock for SPS Injection

Metal Al powder was mixed with nitriding agents (either melamine or urea powder) and dispersed in different suspension liquid carriers such as ethanol, ethylene glycol, hexadecane, or light mineral oil. First, the Al powder was dispersed in the liquid carrier using an ultrasonic bath to break the agglomerated particles for 10 min. Then, the melamine or urea powder was added to the suspension and the mixture stirred for another hour, detailed in Table 4-4. The suspension feedstock was finally injected into the plasma using an atomization probe.

4.4.4 Synthesis of Cubic AlN Coatings by SPS

In preparation, the plasma chamber was first evacuated while purging with an inert gas (Argon, Ar), to obtain the pressure set at 16 kPa. Table 4-4 provides a summary of the plasma conditions employed for the deposition of the AlN coatings. During the injection of the suspension, the sample holder with the substrate was kept at a constant standoff distance in the plasma plume. In order to produce a homogeneous thin film, the coating was deposited in several spray cycles of typically 200 loops where the sample was mounted on a sliding stage that moves back and forth at a speed of 50 mm per second. In addition, since steady spraying can cause the substrates to overheat, therefore, intermittent deposition by loops allows for some cooling. Moreover, the sample holder is water-cooled to protect the substrates from melting. One effective way of avoiding the agglomeration of un-vaporized Al droplets on the cold substrate is by preheating the substrate. Nevertheless, in this work, the deposition commenced without preheating the substrates because AlN formation is an exothermic reaction (Yamada *et al.*, 2007).

Table 4-4. Reaction conditions for the in-situ production of plasma-synthesized AlN coatings.

Process condition	Parameters	Value
Plasma system	Power system	40 kW (3 MHz)
	Plasma torch	Tekna PL-50
Plasma gas flow rate (SLPM)	Sheath gas	Ar: 52, H_2: 5.5, N_2: 40
	Central gas	Ar: 22
	Atomization gas	Ar: 10
Reactor pressure	Initial pressure	Below 2 kPa
	Working Pressure	16 kPa
Suspension flow rate	Flow	2.0 mL·min^{-1}
Standoff distance	Distance	8.0 cm
Substrate	Ti, Mo, Carbon steel	12.7 mm × 2.0 mm
Suspension composition: (a) **Suspension = Precursor + Liquid** (b) **Precursor = (Al + melamine) or (Al + urea)**	Suspension liquid: Ethanol, Ethylene glycol, Hexadecane, light mineral oil	100 mL
	Precursor concentration	5, 10, 20 g in 100 mL
	Al powder	1.0 g
	Melamine	9.0 g
	Urea	13 g
	Concentration (precursor: liquid)	e.g., 10 g: 100 mL
Number of loops	Deposition cycles	200

4.4.5 Materials Characterization

The coatings were characterized by various analytical techniques including X-ray diffraction (XRD) for phase and crystal structure analysis. Optical microscopy (OM) and scanning electron microscopy (SEM) coupled with energy dispersive X-ray spectroscopy (EDX) was used for

morphological and elemental analysis. Contact angle measurements between the coatings and water by the sessile-drop test were used to determine the wettability of the coatings.

4.4.5.1 X-ray Diffraction (XRD) Analysis

The samples were analyzed using a "Philips Panalytical X'pert PRO MPD" X-ray diffractometer (PANalytical, Almelo, The Netherlands) (Barandehfard *et al.*, 2020b). The diffractometer uses Cu Kα1 radiation with a wavelength, λ = 1.54 Å, in the 2θ-angle range from 20 to 100°, at a scanning speed of 0.04° 2θ-angle per min and a step size of 0.02° and step time, 0.5 s. Data collection and data analysis were performed using factory-installed JADE software (version 7.8.4 @2020-04-23 © MDI). The amount of AlN in the coating was determined by Rietveld quantitative analysis (RQA) in the region of 20–60° 2θ-angle. Although there was some degree of amorphicity displayed by the coatings, phase quantification by RQA using Equation 4-1 was attempted in order to determine the various amounts of each species in the coatings (H. M. Rietveld, 1969).

$$W_\rho = \frac{S_\rho (ZMV)_\rho}{\sum_{i=1}^{n} S_i (ZMV)_i} \qquad \text{Equation 4-1}$$

where W_ρ = relative weight fraction of phase ρ in a mixture of n phases, S_ρ = Rietveld scale factor, Z = number of formula units per cell, M = mass of the formula unit (in atomic mass units), and V= the unit cell volume (in $Å^3$).

4.4.5.2 Optical Microscopy (OM)

The Keyence VHX-5000 optical microscope (KEYENCE CORPORATION OF AMERICA, Itasca, IL, USA) was used to investigate the surface properties of coatings in relation to their corrosion resistance when in contact with molten Al-Mg alloy.

4.4.5.3 Scanning Electron Microscopy (SEM)

Microscopic imaging by SEM coupled with energy dispersive X-ray spectroscopy (EDX) was used to investigate the morphology, particle size, and composition of the materials. In this work, SEM imaging and analysis was done on a "Hitachi S-4700" Field-Emission Scanning Electron Microscope (Hitachi High-Technologies Corporation, Tokyo, Japan), equipped with an EDX X-Max Oxford spectrometer (Abingdon, UK).

4.4.5.4 Surface Roughness Test and the Coating Thickness Measurements

The surface roughness was measured by Mitutoyo Surftest SJ-210- Series 178-Portable surface roughness tester (Mitutoyo Corporation, Kawasaki-shi, Kanagawa, Japan). The measurement range is automatically set with a resolution between 0.0016 and 0.0256 μm. The stylus material is diamond with a tip radius of 2 μm and the force utilized is 0.75 mN. The surface roughness of the substrate was measured before and after the deposition of the coatings. In addition, coating thickness of samples was measured by Mitutoyo digital thickness gauge equipped with an absolute digimatic indicator as well as SEM imaging from coating's cross-sectional view.

4.5 Materials Testing

(a) Wetting test: The wettability of the samples was studied using a drop shape analyzer, the Krüss Advance goniometer model DSA25E (KRÜSS, Hamburg, Germany). The test was done using three probe liquids and for each liquid, the measurements were done three times for each sample per liquid. Various models can be applied to do the measurements, and in this work, the Krüss was setup to provide the average values of the 2 contact angles, and this gives the same angle on both the left and the right side of the droplet. In order to validate the analysis method, the static contact angle was calibrated at ambient conditions by depositing a droplet of water or ethylene glycol on the surface of Teflon (polytetrafluoroethylene, PTFE). From the manufacturer's database, the contact angle of water on PTFE is known to be 113.7°, which we validated to be 112.1° as indicated in Figure 4-1a, while that of ethylene glycol was found to be 98.1° as shown in Figure 4-1b against 94.9° of the database (Hild, 2009). A liquid on a solid surface with a contact angle below 90° is considered to be a wetting liquid, while a contact angle above 90° indicates non-wetting properties (Majeed, 2014). Superhydrophobic surfaces with the 'Lotus Effect' that exhibit an extremely high contact angle with water (>150°) have been broadly investigated and can be considered as a perfect example in anti-corrosion applications (Latthe *et al.*, 2014).

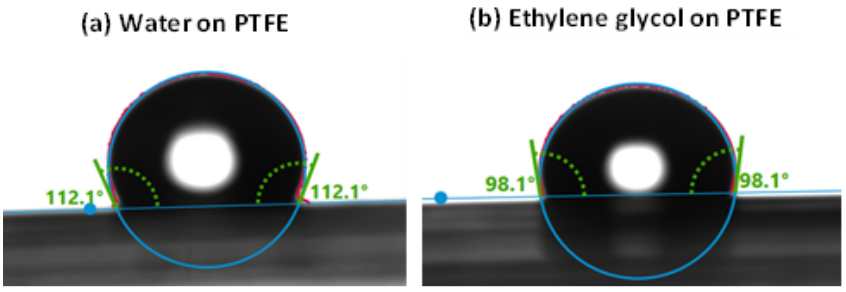

Figure 4-1. Dynamic contact angles at the interfaces of a moving droplet for (a) water on PTFE and (b) ethylene glycol on PTFE.

(b) Corrosion test: The fresh coatings synthesized by SPS technology were tested for corrosion resistance by contacting them directly with a molten Al-alloy containing 5% magnesium (Al-5 wt% Mg) for 2 h at 850 °C. OM was used to observe the surface properties of the coatings to investigate their corrosion resistance when in contact with molten Al-Mg alloy.

4.6 Results

4.6.1 FactSage™ Modelling for the In Situ Synthesis of AlN in Plasma

In plasma, at temperatures above 3000 °C, FactSage™ (Montreal, QC, Canada) can predict the composition of materials at thermodynamic equilibrium in a vapor phase[9]. At lower temperatures, or when multiphase materials are present, the kinetics of the reactions may be considered, but FactSage™ in our context is used to simulate or predict the outcome of targeted reactions during synthesis and the performance of materials in realistic industrial applications. FactSage™ modeling predicted that using a feedstock of hexadecane, metallic Al, and melamine in the presence of plasma gases (including hydrogen and nitrogen), AlN begins to form at temperatures below 2300 °C as portrayed in Figure 4-2, noting that not all the reactions and species occurring in the simulation results are published on the graph.

[9] It is necessary to mention that FactSage (EQUILIB Module) will only give the equilibrium conditions for the generation of gaseous ions under thermal equilibrium.

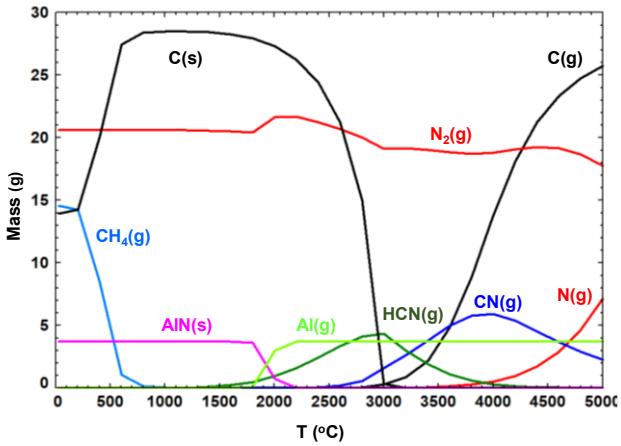

Figure 4-2. Thermodynamics plots showing the potential of producing AlN from melamine through plasma synthesis.[10]

Since H_2 and N_2 gases dissociate to atomic H and N above 5000 °C, the presence of a significant quantity of hydrogen and other gas species in the chamber helps to delay the recombination of nitrogen to N_2 at lower temperatures. Gaseous nitrogen is in fact, not a good nitriding agent because when it decomposes to atomic N, it prefers to recombine to N_2 instead of reacting with other plasma species. Therefore, NH_3 is deemed as a better nitriding agent because once it decomposes at high temperature, it forms N radicals that can react with Al to form AlN. When melamine is injected into the hot core of plasma, it decomposes to nitrogen, hydrogen, ammonia and HCN, besides forming some radicals such as $CH^{\cdot}$, $NH^{\cdot}$, $CN^{\cdot}$, and ions including C_2N^{2+}, C_3N^{2+} and C_3N^{3+} that facilitate the reaction with Al to produce AlN.

FactSage™ results in Figure 4-2 show that at temperatures below 2700 °C, solid carbon starts forming, and at about 700 °C half of the carbon in the chamber is drastically consumed by the formation of CH_4. Formation of AlN starts at ~2300 °C through the reaction between Al and HCN. Atomic nitrogen reacts with atomic hydrogen and carbon to form HCN at 4100 °C. As the temperature drops, production of HCN increases to the maximum at 3000 °C. It is confirmed by some authors that the formation of HCN gas plays an important role in producing AlN (Rounaghi *et al.*, 2016). It is clear that the role of N_2 in the formation of AlN is negligible, but the CN species seems to facilitate the nitridation of Al. Other researchers have demonstrated that at the stoichiometric reactant ratios, the reaction between Al and melamine is mainly

[10] The graph with all gas species is illustrated in Appendix E.

governed by the polymerization of melamine and the formation of a carbon nitride (CNx) phase (Rounaghi *et al.*, 2017).

The presence of oxygen in urea prohibits the nitriding reaction below 1500 °C as predicted from FactSage™ modelling in Figure 4-3 because it generates alumina (Al_2O_3). From the quantities produced between the AlN and Al_2O_3, it is clear that the two products are in direct competition. It means that in presence of oxygen, production of Al_2O_3 is favored. Therefore, besides using an oxygen-free nitriding agent, the chamber must be evacuated of oxygen to facilitate the reaction between Al and nitrogen. For this reason, suspension liquids with a lot of oxygen such as ethanol and ethylene glycol performed poorly. With urea, the production window of AlN is narrow (1200–2000 °C), while with melamine the AlN's stability window is wider stretching from 2300 °C to ambient temperature.

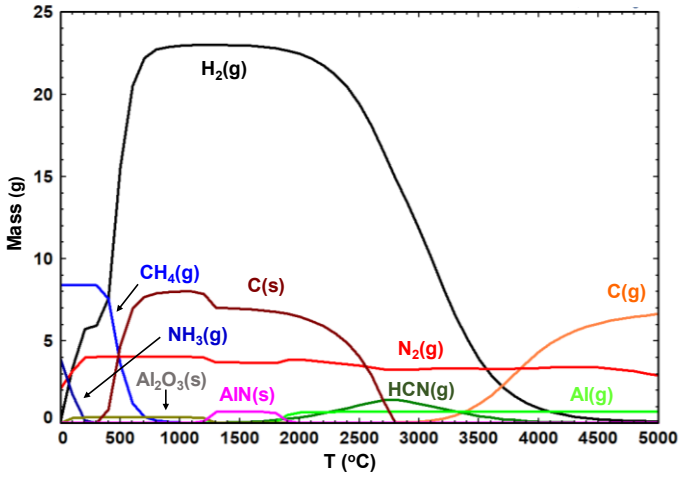

Figure 4-3. Modelling by FactSage™ showing the limited potential of producing AlN from urea through plasma.

4.6.2 Materials Characterization of AlN Coatings

4.6.2.1 SEM Analysis

The freshly synthesized coatings showed that the splats produced in the plasma were in the mean size range of about 2 µm. A sample secondary electron image (SEI) of AlN coating produced from melamine is presented in Figure 4-4(a) and (b) depicts the mixed color EDX elemental mapping of Al and N, while the individual EDX elemental mappings of Al and N are indicated in Figure 4(c,d), respectively. The highly dispersed and concomitant presence of Al and N indicates

the success of producing AlN using SPS technology. The EDX spectrum is displayed in Figure 4e. The atomic percentage of each element calculated by EDX were Al (40%), N (35%), and O (23%) for the coating deposited on carbon steel substrate, and the rest of the analyses are summarized in Table 4-5 for Ti and Mo substrates. Since these values are semi-quantitative, they should be used conservatively because of the high surface roughness of the coatings, which normally lowers the signal intensity in some areas under analysis.

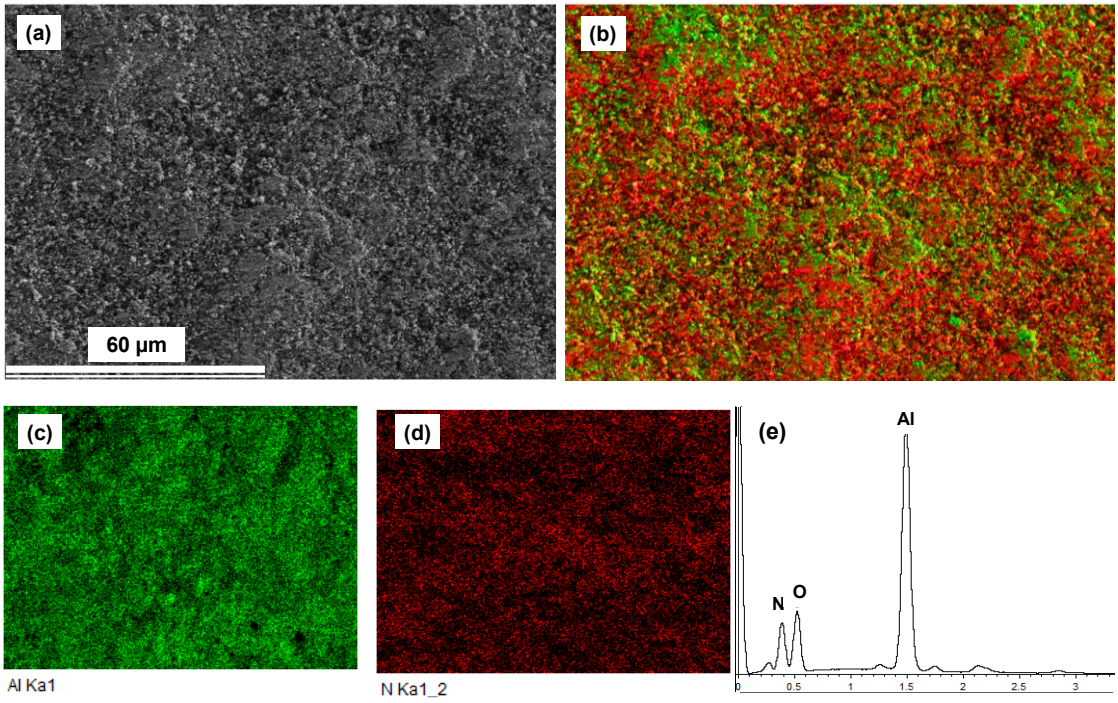

Figure 4-4. (a) A SEM image of AlN coating produced from melamine on the carbon steel substrate in X500 magnification; (b) the mixed EDX elemental mapping of Al and N; (c,d) individual elemental mapping of Al and N, and (e) EDX spectrum.

Table 4-5. A summary of the atomic percentage of each element in coatings sprayed on carbon steel, Ti, and Mo substrates as calculated by EDX.

Substrates	Elements (Atomic-%)		
	Al	N	O
Carbon steel	41	35	24
Titanium	55	30	15
Molybdenum	50	22	28

Figure 4-5 provides the surface view of the coating deposited on a carbon steel substrate. The morphology of the coating tends towards agglomerated splates. In addition, Figure 4-6 displays the cross-sectional view of the same coating showing good bonding between the coating and the substrate. The coating and the bonding remain intact when placed in an ultrasonic bath suspended in ethanol for 15 min. Moreover, after exposure to molten Al-Mg alloy, no peeling was observed.

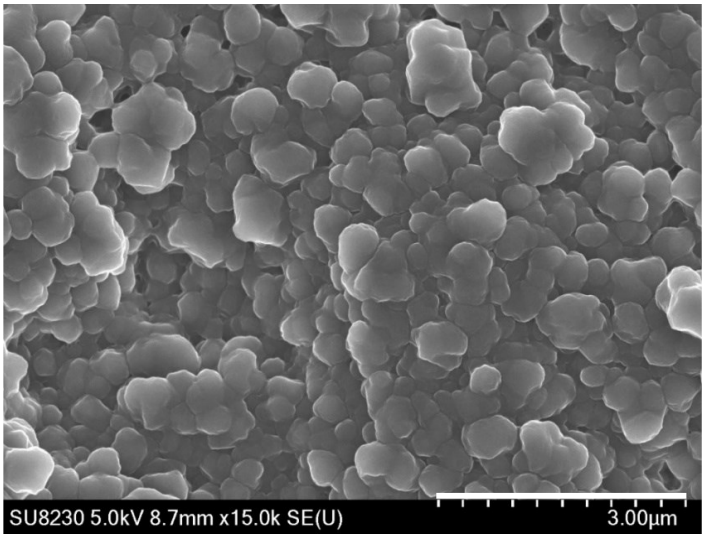

Figure 4-5. A top surface view by SEM imaging for plasma-synthesized AlN-rich coating on carbon steel in ×15,000 magnification.

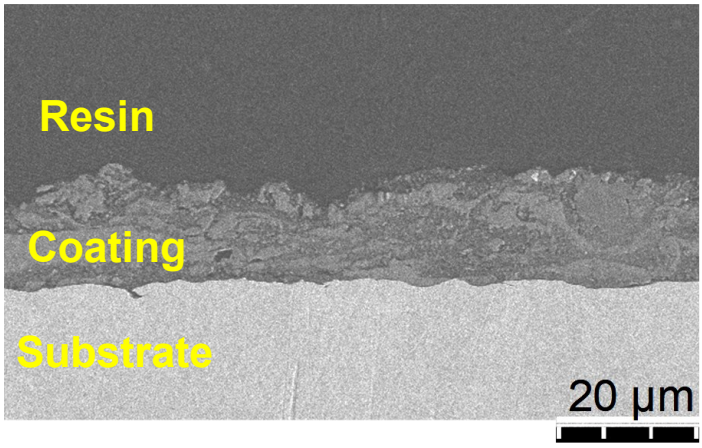

Figure 4-6. Cross-sectional view of the AlN-rich coating on carbon steel by SEM imaging in ×2500 magnification.[11]

[11] Cross-sectional view with higher magnification is presented in Appendix D.

4.6.2.2 XRD Analysis

Various parameters were used to optimize the production of AlN coating as the target product. Figure 4-7 shows the XRD patterns of the two major peaks that were used to semi-quantitively determine the amount of the cubic AlN in the coatings[12], where the main peak at 44.85° 2θ-angle represents the (200) plane, followed by the smaller (111) peak at approximately 38.59° 2θ-angle. A comparatively higher intensity of the (111) peak than the (200) peak implies the presence of metallic Al, while an intense (200) peak accompanied by a smaller (111) peak implies the presence of AlN.

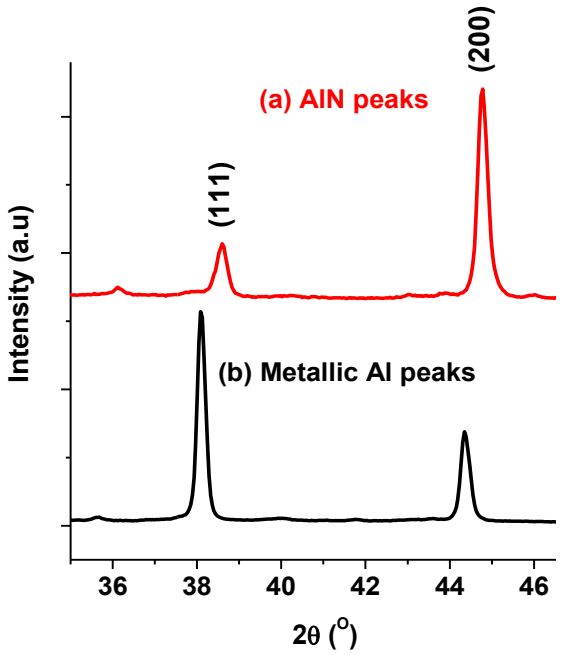

Figure 4-7. XRD patterns with the two major peaks used to identify AlN in the coatings, showing (a) AlN peaks; and (b) metallic Al peaks.

Quantification of the various phases in the AlN coatings by RQA using XRD data is exemplified in Figure 4-8, which indicates the percentage of the AlN formed in the coatings alongside other by-products. The ICDD cards used to identify the phases include: [00-039-1950] (Mayer and Schneider, 1988) for melamine, [04-010-6160] (Rizolli *et al.*, 2002) for Al, [04-007-4280] (Von

[12] Rietveld quantitative analysis derived from XRD data can lead to relatively accurate analysis of the quantity of the materials composition in sample as long as there are no amorphous phases or unknown impurities.

Stackelberg and Spiess, 1935) AlN hexagonal, [04-004-8344] (Vollstadt *et al.*, 1990) for AlN rock-salt cubic, [01-088-2331] (Haglund *et al.*, 1993) for Mo, [00-046-1212] (Huang *et al.*, 1990) for Al_2O_3, [00-055-0142] (Louer, 2004) for urea, [01-085-4874] (Brauer, 1938) for $TiAl_3$, [04-011-9045] (V.M. Bulanova *et al.*, 2005) for Ti and [04-014-0164] (Zoriasatin *et al.*, 2006) for Fe. This approach was used to analyze all the other samples, where the raw data extracted from the RQA curve fitting are summarized in Table 4-6. The best condition for these series of experiments: melamine as nitriding agent, carbon steel as a substrate, hexadecane as a suspension liquid, and standoff distance of 8 cm. For each experiment one of the mentioned parameters change and the rest kept constant. Details can be found in Table 4-4.

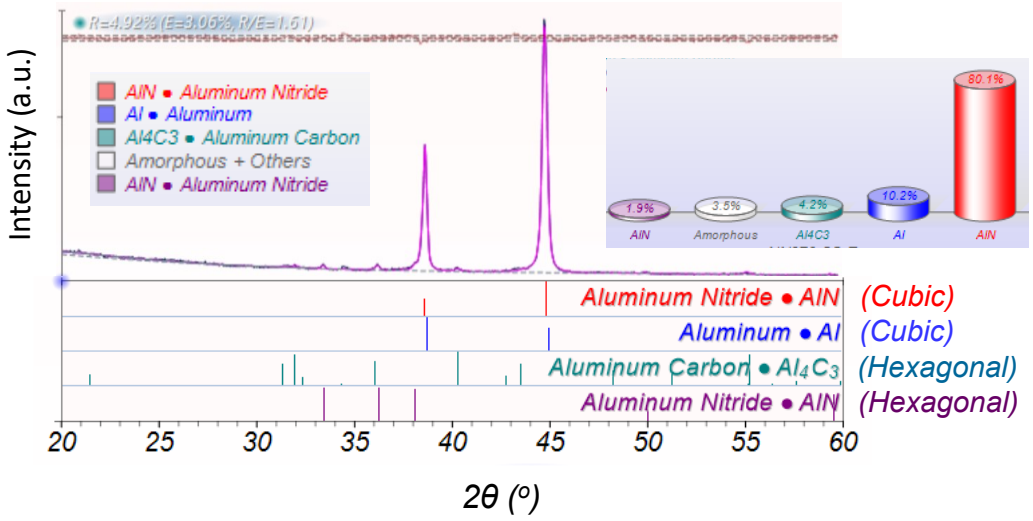

Figure 4-8. A typical result from the Rietveld quantitative analysis of a plasma synthesized sample.

Further, the quantity of AlN (%) was plotted versus the standoff distance, the substrate materials, the liquid suspension carriers, and the nitriding agents as provided in Figure 4-9. Figure 4-9a illustrates the impact the substrate materials have on the formation of AlN in the coatings, while Figure 4-9b shows that comparatively, melamine is a stronger nitridation agent than urea. The presence of oxygen in urea seems to have a negative impact on the nitridation reaction because Al has a higher affinity for oxygen than nitrogen. In addition, melamine by having a higher concentration of nitrogen per unit mass than urea as well as absence of oxygen in its structure increases the chance of the reaction between Al and nitrogen in the plasma.

Table 4-6. A measured amount of the various phases in the plasma-synthesized coatings by RQA using XRD data.

Synthesis Parameters		Phase Concentration in the Coatings (%)					
		Cubic-AlN	hcp-AlN	Al	Al_4C_3	Others	
Substrates	Carbon steel	80	2	10	4.5	3.5% amorphous	
	Ti	17	13	50	-	18% Ti_3Al	2% $TiAl_3$
	Mo	15	-	62	-	23% Mo	
Suspension liquids	Ethylene glycol	13	12	70	-	1% Al_2O_3	4% Fe_5C_2
	Ethanol	-	5	85		10% carbon	-
	Hexadecane	80	2	10	4.5	3.5% amorphous	
	Light mineral oil	22	16	60	-	2% FeN	
Standoff distance	6 cm	10	-	28	-	60% Melamine	2% amorphous
	7 cm	20	-	5	-	5% Carbon	70% Fe
	8 cm	80	2	10	4.5	3.5% amorphous	
	9 cm	27	15	46	8	2% Fe	2% Fe_3C
	10 cm	-	35	2	15	40% Carbon	8% Fe_3O_4
Nitriding agent	Urea	25	-	65	-	10% TiAl	-
	Melamine	80	2	10	4.5	3.5% amorphous	

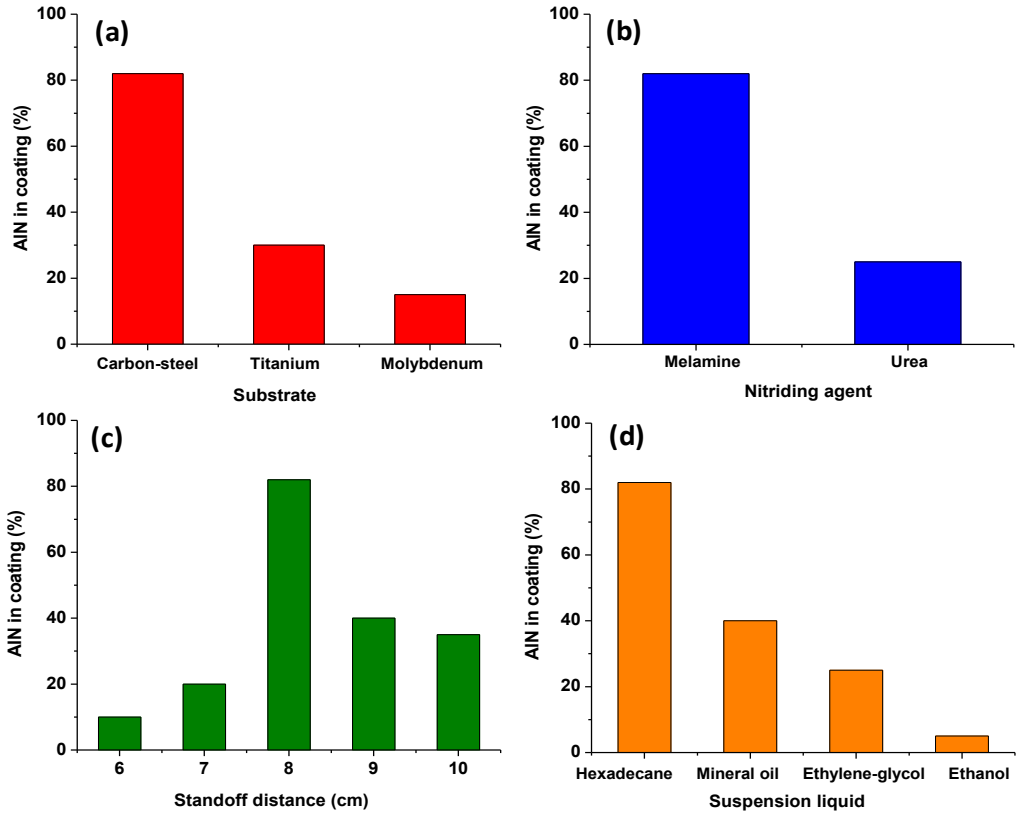

Figure 4-9. Calculated amount of AlN% in the coatings by RQA using XRD data where (**a**) shows the impact of different substrates; and by using carbon steel substrate, (b) the effect of nitriding agents; (c) different standoff distances and (d) the suspension liquid was studied.[13]

Figure 4-9c shows the effect of standoff distance on the formation of AlN, with the optimum distance being found to be 8 cm. On one hand, decreasing the standoff distance to 6 cm saw the formation of AlN decrease drastically, because of insufficient residence time for the species to react and produce AlN. On the other hand, increasing the standoff distance to 10 cm equally lowered the production of AlN, although there was enough time for the materials to react. However, by lengthening the residence time, two other negative phenomena emerged: (a) the in-situ produced AlN decomposed and could not make it into the coating based on preliminary experimental results of direct injection of AlN through plasma, and (b) the AlN particles formed and hardened in such a way that they could no longer produce splats onto the substrate. It is

[13] In experiments illustrated in Figure 4-9, conditions related to three variables were set to their maximized % AlN in coating and only the effect of the fourth variable on formation of AlN was considered.

necessary that coating materials should be in the molten or semi molten state in thermal plasma to stick on the substrate.

Figure 4-9d, shows that at a standoff distance of 8 cm, using melamine and a carbon steel substrate, the hexadecane liquid carrier produced the highest amount of AlN in the coatings as compared to the other liquid carriers.

4.7 Discussion

4.7.1 Effect of Nitriding Agent on AlN Formation

In this study, two nitriding agents were used, namely melamine ($C_3H_6N_6$) and urea (CH_4N_2O). From the XRD analysis using RQA, it was observed that melamine produced a higher percentage (82%) of AlN in the coatings in comparison to urea (25%). Melamine having more nitrogen in its structure (67% by mass N) than urea (47% by mass N), introduced more nitrogen into the system, and it does not have any oxygen in its structure, thereby increasing the chance of Al reacting with nitrogen. Since the mass transfer in plasma is characterized by the laminar flow, mixing is restricted and any reactant that would increase the chance of reaction is crucial. Figure 4-10 shows XRD pattern of coatings produced using different nitriding agents. It was observed that in materials where the (200) peak was more intense than the (111) peak, then the material was richer in cubic Rock-salt AlN. However, the presence of metallic Al was characterized by an intense (111) peak accompanied by a smaller (200) peak.

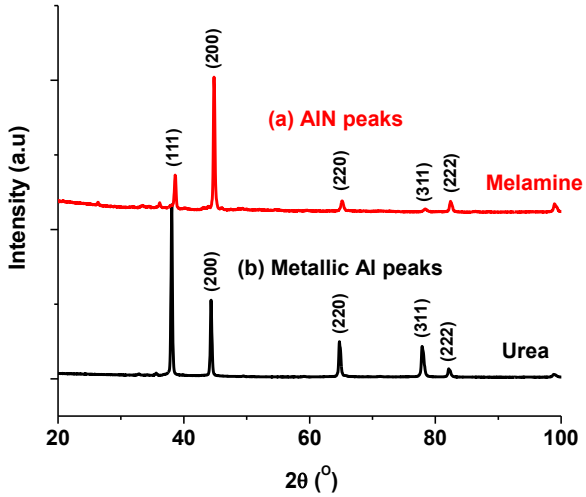

Figure 4-10. XRD patterns of in situ produced coatings in plasma by the reaction between Al powder and the two nitriding agents: (a) melamine and (b) urea.

When urea was used as a nitriding agent, there was a poor conversion of Al to AlN, but melamine produced more AlN under similar plasma conditions with the dominant phase of the cubic crystal structure. In effect, urea did not react well with Al, but melamine performed comparatively better. This confirmed what a number of authors have suggested in using melamine as a nitriding agent to generate nano-structured AlN powder (Elagin *et al.*, 2013b). It has been reported that melamine releases NH_3 to form melem ($C_6N_{10}H_6$) intermediate at temperatures of about 550 °C, and at higher temperatures to produce chemically reactive hydrogen-, carbon- or nitrogen-containing atomic species such as CN^{2+} and $NCNH^{+}$ (Zhao *et al.*, 2006). CN group is so reactive that it easily produces charged nitriding species in plasma due to the instability of the triple bond between C and N, especially with the presence of the π electron bonds.

Figure 4-11(a) shows SEM analysis of the AlN coating produced by urea. Figure 4-11(b) is the EDX spectrum of the coating, while Figure 4-11(c–f) represents the respective EDX elemental analysis for N, Al, Ti and oxygen. When compared, the coating deposited on Ti substrate using urea, shown in the EDX spectrum of Figure 4-11(b), contained more oxygen and less AlN than the sample derived from melamine, as seen in Figure 4-4. The atomic percent of elements calculated by EDX were Al (39.9%), N (5.5%), Ti (5.8%) and O (51.4%).

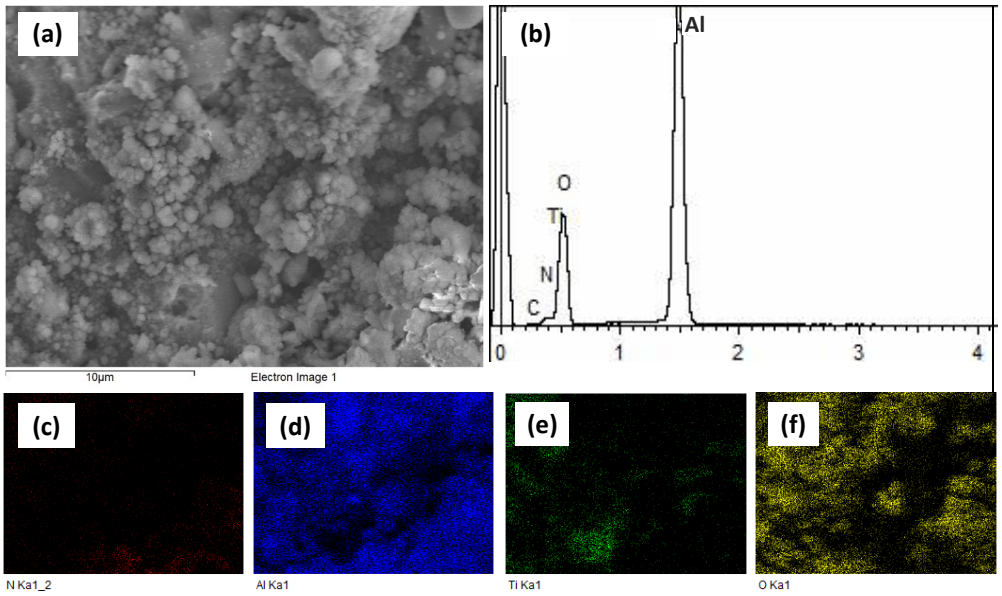

Figure 4-11. SEM imaging of AlN coating derived from Al and urea on Ti substrate in X5000 magnification, indicating its (a) secondary electron image; (b) EDX spectrum; and (c–f) EDX elemental mapping for N, Al, Ti, O, respectively.

4.7.2 Effect of Standoff Distance on AlN Formation

In testing our hypothesis, it was postulated that the standoff distance can affect the quality of the coating. It was observed that an optimum distance destined for the maximum formation of AlN in plasma exists, which is about 8 cm as shown in Figure 4-9c. The XRD data from which this information was derived are provided in Figure 4-12. The two scenarios that were observed to influence the quality of the coating in relation to standoff distance were:

i. Long standoff distance: where after the nitridation, AlN failed to stick to the substrate, which was too far because either the AlN decomposed before reaching the substrate, or the AlN condensed and reached the substrate after hardening.
ii. Short standoff distance: characterized by low residence time in the reactor because the materials did not have enough time to react and produce AlN.

These observations imply that at a standoff distance of 8 cm, the materials have enough residence time to react during nitridation, and with high velocity at suitable particle temperature, the coatings are deposited on the substrate more effectively. At the extreme standoff distances of, for example, 10 cm there were many by-products such as carbon and Al_4C_3 formed as shown by the many peaks in the XRD pattern, while at a standoff distance of 6 cm the Al and melamine remained unreacted. The melamine peaks are visible below the 2θ angle of 30°.

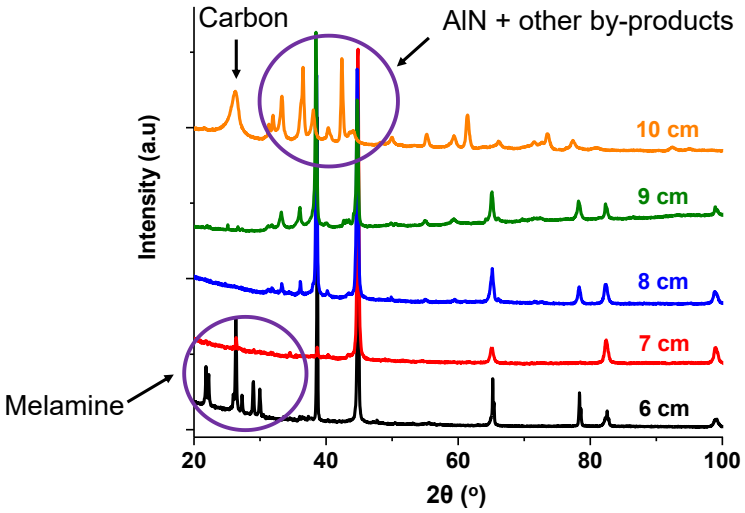

Figure 4-12. XRD patterns revealing the optimum distance for depositing AlN on carbon steel substrate using melamine and Al powder in hexadecane.

4.7.3 Effect of Suspension Liquids on AlN Formation

It was observed that with the application of RQA using the XRD data shown in Figure 4-13, utilizing hexadecane produced the highest percentage of AlN in the coatings (~82%) in comparison to using other suspension liquid carriers. Initial experiments of this project were conducted by injecting powder precursors directly into the plasma. However, the difficulty with powder injection involved irregular powder flow due to high particle friction, clogging, and particle agglomeration, which led to poor coating quality. Nevertheless, by suspending the powder in an oily liquid, the smooth flow of the feedstock was enhanced. With the SPS method, we overcame the problem of irregular powder injections. Several liquids were used to create the powder suspensions, and it was observed that suspension liquids richer in oxygen (i.e., ethanol, ethylene glycol, and light mineral oil) inhibited the formation of AlN, because the oxygen preferentially reacts with Al to form Al_2O_3 instead of AlN.

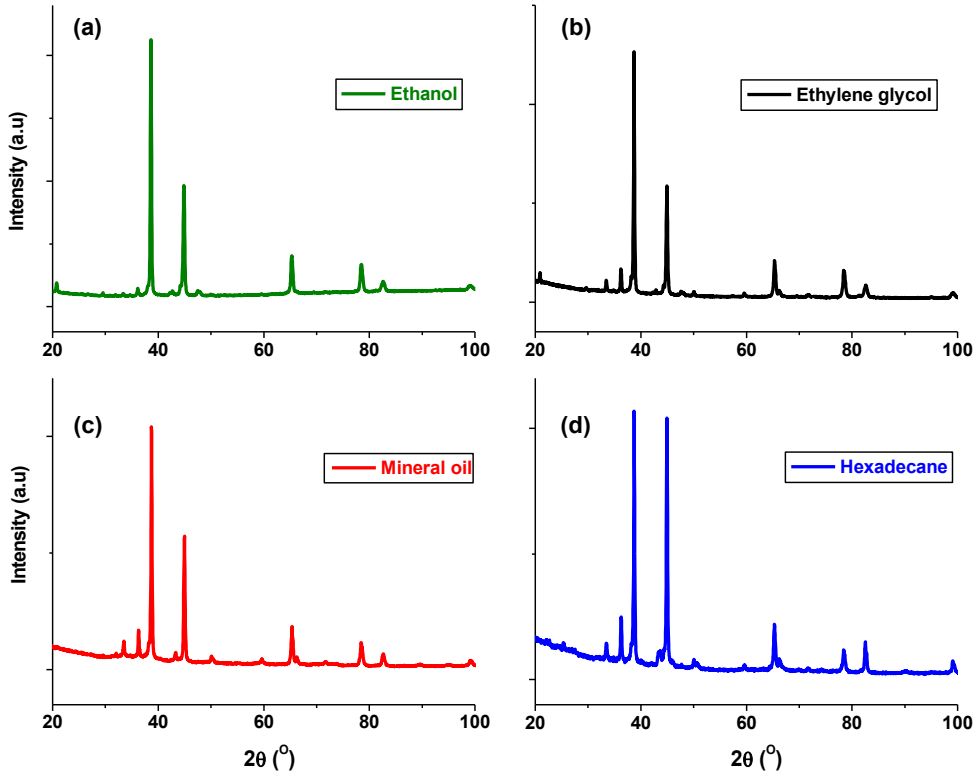

Figure 4-13. XRD patterns of coatings produced from Al powder and melamine in different suspension media: (a) ethanol, (b) ethylene glycol, (c) mineral oil and (d) hexadecane.

4.7.4 Effect of Substrate on AlN Formation

Several substrates were used to deposit the AlN coatings by SPS technology and carbon steel performed better than Mo or Ti. Their performance is related to the substrates' thermal conductivity, whose values are 143, 54 and 24 W/m K for Mo, carbon steel and Ti, respectively (Engineering ToolBox, 2005). We suppose that Mo with a high thermal conductivity leads to a much colder surface of the substrates that quenches the nitridation reaction. On the other hand, Ti having the lowest thermal conductivity exhibits the hottest surface temperature, which prevents the deposition of AlN. The carbon steel with a medium thermal conductivity is neither too hot nor too cold for nitridation reaction. Controlling the temperature of a plasma and the substrate is therefore an important parameter in the formation of AlN coating (Yamada *et al.*, 2007). The overlaid XRD pattern of the AlN coatings on Ti, Mo, and carbon steel substrates are provided in Figure 4-14. Several observations were made:

(a) The surface of the Mo substrate was exposed and detectable by XRD analysis because very little (15% cubic) of the coating was formed.
(b) Ti reacted with Al to produce several TiAl alloys. In addition, the AlN produced on the Ti took after the hexagonal (hcp) crystal structure of the substrates, showing with two main peaks in (110) and (002) planes belong to hexagonal AlN
(c) Carbon steel had the highest amount (80%) of cubic AlN coating, which is typical of the cubic (fcc) crystal structure of carbon steel substrate at high temperature.
(d) Prolonged deposition periods led to the substrates overheating, consequently resulting in less AlN deposition, and enhancing surface carbon formation by producing aluminum carbide.

Figure 4-15 shows the SEM images of the freshly synthesized coatings using Al powder and melamine on different substrates, where Figure 4-15a is for carbon steel, Figure 4-15b represents Ti and Figure 4-15c is for Mo. Although surface roughness was evident after coating deposition, the carbon steel sample comprised the highest AlN content (80% cubic phase + 2% hcp), while Mo had the least amount of AlN (15% cubic, with no hcp phase). Ti substrates consisted of 17% cubic and 13% hcp.

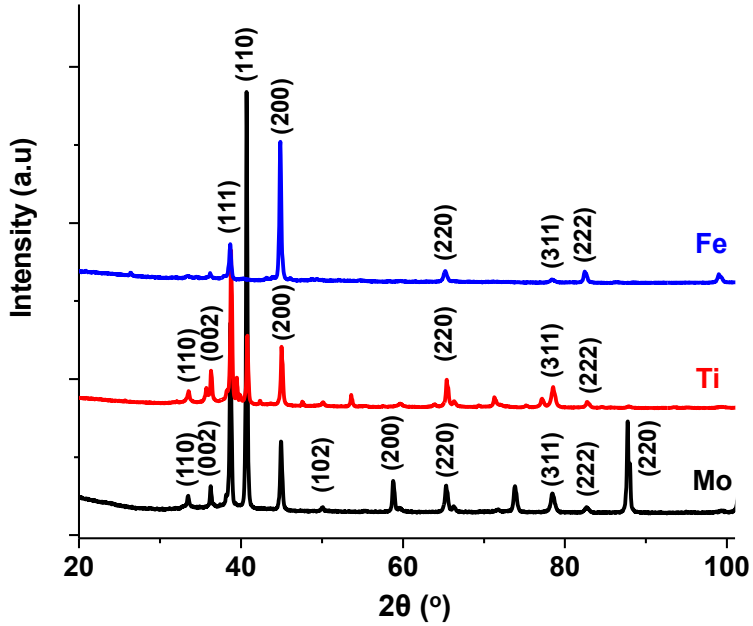

Figure 4-14. XRD patterns of coatings produced from Al and melamine on different substrates.

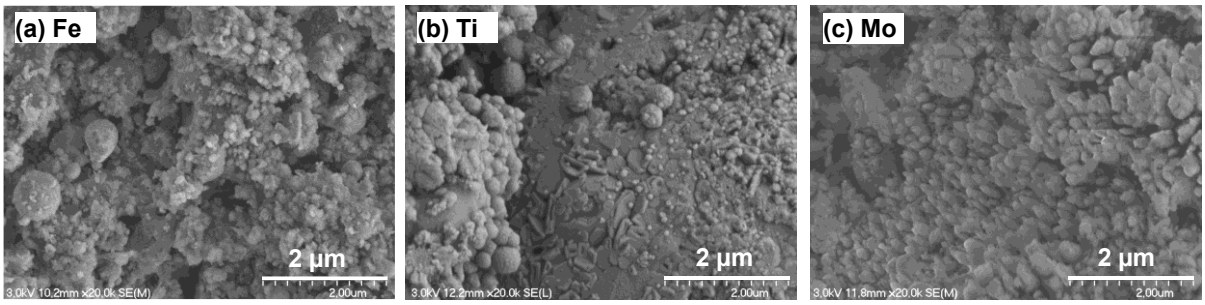

Figure 4-15. SEM images of coatings produced from Al powder and melamine on different substrates: (a) carbon steel, (b) Ti and (c) Mo, in ×20,000 magnification.

4.7.5 Materials Testing

4.7.5.1 Roughness and Thickness Measurements

Table 4-7 summarizes the results obtained from roughness and thickness tests. It was observed that surface roughness increased after the deposition of the coatings, with Mo recording the highest roughness.

Table 4-7. Surface roughness measurements of substrates and coatings.

Substrates	R_a values (µm)		Coating Thickness (µm)
	Before Coating	After Coating	
Carbon steel	0.54 ± 0.02	2.7 ± 0.4	~20–40
Titanium	0.38 ± 0.03	2.2 ± 0.3	~20–30
Molybdenum	0.51 ± 0.03	4.0 ± 0.6	~15–20

4.7.5.2 The Wetting Test

It was observed that samples containing a high percentage of AlN demonstrated an increased contact angle as illustrated in Figure 4-16a. Materials with a contact angle of less than 90° are normally considered to be more hydrophilic, while those with a contact angle higher than 90° are perceived to be more hydrophobic (Majeed, 2014). For example, the sample containing ~82% AlN displayed a contact angle of 136° which confirms the SPS synthesized coatings is hydrophobic, while the sample with a lower quantity of AlN (~25%) displayed a decreased contact angle to 73° and it is hydrophilic as seen in Figure 4-16b. The measured water contact angle on PVD-deposited AlN by (Yang and Cho, 2013) was 119° which shows hydrophobic properties of their coatings. Furthermore, it has been observed that the contact angle between molten Al and AlN surface is 136° at 850 °C, which confirms the non-wettability of AlN by Al (Mutale, Weirauch and Cramb, 2008). The summary of contact angle measurements on each sample presented in Table 4-8.

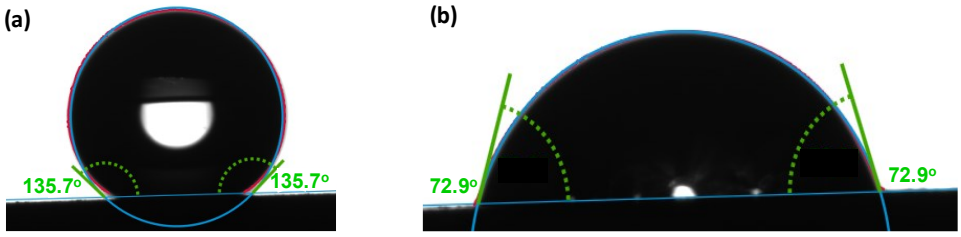

Figure 4-16. How the presence of AlN in a material improves its non-wetting properties, (a) a coating with 82% AlN shows a contact angle of 136°, and (b) a coating with 25% AlN shows a contact angle of about 73°.

Table 4-8. Contact angle measurements of sample containing 82% and 25% AlN with water.

Sample	**Contact angle °**	**σ**
Coating with 82% AlN	133.0, 135.7, 138.0	± 2.5
Coating with 25% AlN	74, 72.9, 78	±3

4.7.5.3 Corrosion Test

The samples with coated substrates were exposed to molten Al-Mg alloy at 850 °C for 2 hrs and their top view optical microscopy photos are shown in Figure 4-17.

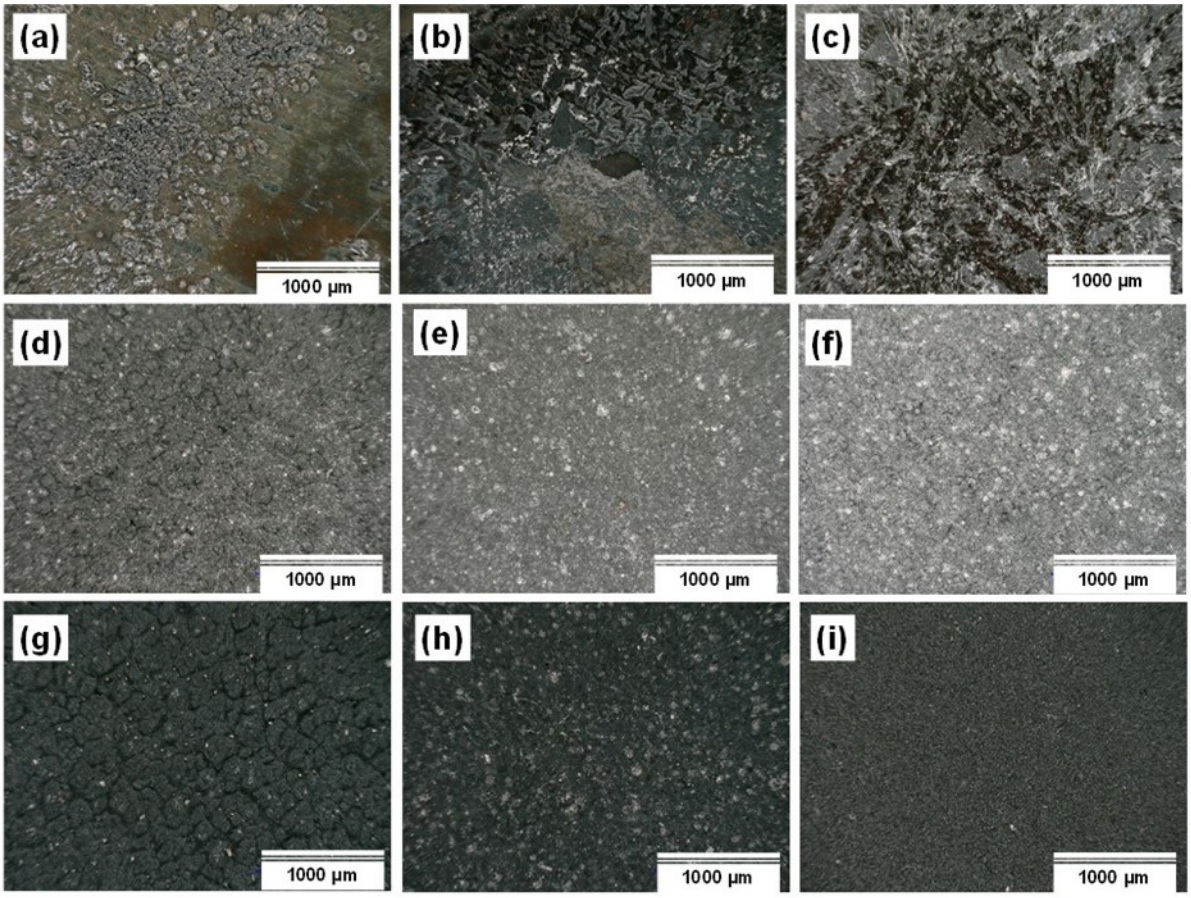

Figure 4-17. Optical microscopic images of the substrates after corrosion test for (a) Ti, (b) carbon steel, and (c) Mo; plasma synthesized coatings for (d) Ti, (e) carbon steel, and (f) Mo; and the coated samples after corrosion test for (g) Ti, (h) carbon steel and (i) Mo.

Figure 4 17(a-c) shows the corrosion test results of metal substrates (Ti, carbon steel, and Mo) in contact with molten Al alloy before deposition of coating. Figure 4-17(d-f) represents the freshly plasma-synthesized coatings for Ti, carbon steel and Mo, respectively. Figure 4-17(g-i) presents the coated samples after the corrosion test for Ti, carbon steel, and Mo, respectively.

All the coated samples indicated better corrosion resistance to the hot molten alloy, and it means that the coatings provided some form of protection to the substrates. However, in the Ti and Mo based samples, the presence of AlN coating was relatively lower with a significant amount of metallic Al. Some forms of islands or micro-cracks were witnessed in the Ti and Mo samples,

which could be related to poor thermal shock resistance. Since the coating materials are richer in metallic Al (linear thermal expansion coefficient, $\alpha_L \approx 22 \times 10^{-6}$ K^{-1}), the difference in the thermal expansion of the coatings and the substrates (Ti, $\alpha_L \approx 9 \times 10^{-6}$ K^{-1}; Mo, $\alpha_L \approx 5 \times 10^{-6}$ K^{-1}) (Engineering ToolBox, 2003), could generate some cracks in the coatings. Nevertheless, in the carbon steel sample ($\alpha_L \approx 12 \times 10^{-6}$ K^{-1}), there was less cracking on the surface of the coating, perhaps because of the enhanced presence of AlN (82%) with $\alpha_L \approx 5.3 \times 10^{-6}$ K^{-1}. However, in the Ti and Mo based samples, the presence of AlN coating was relatively lower with a significant amount of metallic Al. As thermal resistance (R_θ) can be calculated by dividing the thickness of the samples by its thermal conductivity (W/m K), and cross-sectional area (m^2), it was observed that the R_θ of Mo, carbon steel and Ti substrates were 0.114, 0.29 and 0.65 ($K \cdot W^{-1}$), respectively. This implies that the samples on the two extremes (either too high, that is Ti, or too low, which is Mo) performed poorly as a substrate.

4.8 Conclusions

AlN has attracted a lot of attention for different applications in the industry due to its unique properties. In the Al industry, AlN coatings may find useful when in direct contact with molten Al alloys due to their non-wetting and corrosion-resistant properties. Therefore, this work proposes in situ production of AlN-rich coatings by SPS technology, which has successfully produced up to approximately 80% cubic AlN coating on a carbon steel substrate with about 2% AlN in the hexagonal phase. Temperature control for AlN synthesis is an important parameter and it is demonstrated by changing standoff distance and substrate thermal conductivity. The thermal resistance of Mo, carbon steel, and Ti substrates are 0.114, 0.29, and 0.65 ($K \cdot W^{-1}$), respectively, and it was observed that the samples on the two extremes (either too high or too low) performed poorly. It suggests that the surface temperature of the substrates may play a role in the production of the AlN-rich coatings, and this is influenced by both the standoff distance during spraying and the substrates' thermal conductivity. The optimum plasma conditions included a standoff distance of 8 cm, the use of hexadecane liquid carrier, and reacting metallic Al powder with melamine as opposed to urea. Results show that favorable in situ AlN synthesis conditions by SPS includes a nitrogen-rich precursor (e.g., melamine), a system without oxygen in the suspension liquid carrier (e.g., hexadecane), and depositing AlN on a carbon steel substrate.

CHAPTER 5 EFFECT OF AL SIZE DISTRIBUTION AND PROMOTIONAL ADDITIVES ON PLASMA SYNTHESIS OF ALN

This chapter is based on a published journal article entitled "Synthesizing AlN coatings using suspension plasma spraying: effect of promotional additives and aluminum powder particle size" with minor edition.

5.1 Avant-propos

Auteurs et affiliation :

Faranak Barandehfard: Étudiante au doctorat, Université de Sherbrooke, Faculté de génie, Département de génie chimique et de génie biotechnologique.

James Aluha: Chercheur postdoctoral, Université de Sherbrooke, Faculté de génie, Département de génie chimique et de génie biotechnologique.

Thabang A. Ntho: Cerdo Trading (Pty) Ltd., Johannesburg, Afrique du Sud

François Gitzhofer: Professeur, Université de Sherbrooke, Faculté de génie, Département de génie chimique et de génie biotechnologique.

Date d'acceptation: 30 April 2022

État de l'acceptation: version finale publiée le 22 juin 2022

Revue: Journal of Thermal Spray Technology

Titre français : Synthèse de revêtements d'AlN par projection par plasma de suspensions: effet des additifs promoteurs et de la taille des particules de poudre d'aluminium

Author Contributions: Conceptualization, F.B., and F.G.; methodology, F.B., F.G., and T.A.N; software, F.B. and T.A.N; validation, F.G., T.A.N., and J.A.; formal analysis, F.B., and J.A.; investigation, F.B.; modeling resources, T.A.N.; writing—original draft preparation, F.B.; writing—review and editing, J.A., T.A.N., and F.G.; visualization, J.A.; supervision, F.G.; project administration, F.G.; funding acquisition, F.G. All authors have read and agreed to the published version of the manuscript.

Contribution au document:

As explained in chapter 3, the synthesis of AlN coating using SPS technology was sensitive to 6 variables in total, four of which were studied in chapter 4. In this chapter, the effect of two other plasma variables i.e., Al particle size distribution and promoter additives, on the formation of AlN is presented. As shown in Figure 3-1 box orange, the values attributed to the standoff distance, nitriding agent, liquid suspension, and substrate material studied in chapter 4 were set to their optimum values. A further investigation of two other variables such as Al particles size distribution and promotional additives is important for two reasons. First, fine Al particle size has an affinity to agglomerate which causes irregular injection flow rates and, consequently, the deposited coating would not be homogeneous. The second reason is related to the post-deposition nitridation reaction. To synthesize enriched AlN coating, both inflight and post-deposition nitridation is essential. Investigating the effect of Al size distribution and the addition of promoters in this chapter provides a better understanding of the importance of the post-deposition nitridation reaction on the formation of purer AlN.

Résumé

Les revêtements en nitrure d'aluminium (AlN) ont été sélectionnés comme matériaux résistants à la corrosion applicables à l'industrie de l'aluminium (Al). Le revêtement d'AlN entre alors en contact direct avec l'Al fondu au-dessus de 933 K plutôt que les réfractaires. Les revêtements d'AlN ont été synthétisés par la technologie de synthèse de matériaux par projection de suspensions par plasma (SPS) en utilisant de la poudre d'Al mélangée à de la mélamine en suspension dans de l'hexadécane. L'utilisation de particules fines d'Al (1-5 μm) n'a pas donné plus de 10% d'AlN dans les revêtements. Le mélange de la poudre Al avec des additifs promotionnels tels que B, BN, Mo, Y_2O_3, AlN ou Al_4C_3 résout l'agglomération de particules fines et stimule la formation d'AlN dans les revêtements, ce qui améliore leur résistance à la corrosion. La quantité optimale de promoteur AlN était de 0,22 % en poids de la masse totale de suspension, produisant jusqu'à 72 % d'AlN dans le revêtement tel que déterminé par l'analyse quantitative de Rietveld (RQA) utilisant la diffraction des rayons X (XRD). Une autre façon d'augmenter le pourcentage d'AlN dans le revêtement est par la nitruration post-dépôt tout en éliminant l'agglomération des particules fines d'Al. En effet, en utilisant une distribution granulométrique d'Al plus large, avec un rapport optimal de 3: 1 pour (1-5 μm) :(17-35 μm), il est possible d'atteindre jusqu'à 80% d'AlN tel que mesuré par l'analyse Rietveld en DRX. La dureté Vickers des revêtements est liée à leur teneur en AlN atteignant 1644 Hv pour 80% AlN. Les revêtements ont été testés pour leur résistance à la corrosion par exposition directe à l'alliage fondu Al-5 wt.%Mg à 1123 K (test de 2 heures) et ils se sont avérés stables. La simulation par les calculs ab initio Born-Oppenheimer (BOMD) a prédit ces résultats expérimentaux. En effet, à 1200 K, AlN et Al fondus présentent de faibles interactions van der Waals. L'énergie interfaciale $AlN_{(s)}$-$Al_{(l)}$ a été calculée à 18,2 kJ mol^{-1} pour la phase hexagonale d'AlN et à 56,4 kJ mol^{-1} pour l'AlN cubique, ce qui signifie qu'elle se situe dans le régime de physisorption, et donc aucune réaction ne se produit entre $Al_{(l)}$ et $AlN_{(s)}$ ce qui confirme l'intérêt d'AlN dans l'industrie de l'aluminium.

Mots-clés : nitrure d'aluminium cubique et hexagonal; projection par plasma de suspension revêtements; mélamine; résistance à la corrosion, additifs promotionnels, modélisation ab initio.

5.2 Synthesizing AlN Coatings Using Suspension Plasma Spraying: Effect of Promotional Additives and Aluminum Powder Particle Size

Abstract

Aluminum nitride (AlN) coatings have been considered for corrosion-resistant materials applicable to the aluminum (Al) industry where the AlN comes in direct contact with molten Al above 933 K. AlN coatings were synthesized by suspension plasma spray (SPS) technology using Al powder mixed with melamine suspended in hexadecane. The use of fine Al (1–5 μm) particles did not yield more than 10% AlN in the coatings. Mixing the Al powder with promotional additives such as B, BN, Mo, Y_2O_3, AlN, or Al_4C_3 solves the fine particle agglomeration and stimulates the formation of AlN in the coatings which enhances their corrosion resistance. The optimum amount of AlN promoter was 0.22wt% of the total suspension mass, producing up to 72% AlN in the coating as determined by Rietveld quantitative analysis (RQA) using X-ray diffraction (XRD). Another way to improve the AlN formation in the coating by post-deposition nitridation and also solve fine Al particle agglomeration is to use a wide particle size distribution of Al, with the optimum ratio being 3:1, that is, (1–5 μm):(17–35 μm). XRD analysis indicated that the coating exhibited up to 80% AlN. The coatings Vickers hardness is related to their AlN content reaching 1644 Hv (80% AlN). The coatings were tested for corrosion resistance by direct contact with molten Al-5wt%Mg alloy at 1123 K (2 hours) and found to be stable. Ab initio Born-Oppenheimer molecular dynamics (BOMD) simulation predicted these experimental results. Indeed at 1200 K, molten Al and AlN exhibit weak van der Waals interactions. The AlN(s)–Al(l) interfacial energy was calculated to be 18.2 kJ/mol for hexagonal AlN phase and 56.4 kJ/mol for cubic AlN, which means that it lies within the physisorption regime, and therefore, no reaction occurs between Al(l) and AlN(s) which confirms non-wetting application in the Al industry.

Keywords: Suspension plasma spray (SPS), Aluminum nitride, Coating, Corrosion resistance, Promotional additives, Precursor particle-size distribution, Ab initio modeling, Hexagonal AlN, Cubic AlN, Melamine nitriding agent.

5.3 Introduction

Aluminum nitride (AlN) has received great attention for its potential application in semiconductor equipment (5.3 eV bandgap for cubic) (Thompson *et al.*, 2001), crucibles for

handling corrosive chemicals, and reaction vessels (Yamada, Nakamura, *et al.*, 2006). AlN has high thermal conductivity (Oh and Park, 1998), low thermal expansion coefficient (Sung *et al.*, 2017), chemical and physical stability at fairly high temperature regions, high hardness (Kim, 2005), and high corrosion resistance to molten metals (Li *et al.*, 2021), and molten salts, including chlorides and cryolite (Pradhan *et al.*, 2015). AlN has potential applications for coatings in direct contact with molten Al and allows lower cost refractories or base metals to be coated and benefit from the performance of the AlN coating exposed to molten Al. This solution also extends the component's life by rebuilding the worn-out part to its original dimensions and lowers damage due to abrasion, erosion or corrosion (Fauchais and Vardelle, 2012). Some modelling work has indicated that in an Al-rich environment, the N-terminated AlN surface tends to bond with the Al atoms, thereby getting reconstructed, which results in an Al-terminated surface structure (Cao, Liu and Ning, 2018). This result is supported with experimental data (Taranets and Naidich, 1996). Although Al-AlN contact angle is about 135^{o} at 1173 K (Toy and Scott, 1997), when increasing the temperature beyond 1273 K, wettability of AlN increases drastically with a significant decrease in the contact angle to below 90^{o}.

Industrial synthesis of AlN through carbothermal reduction-nitridation of alumina (Jackson *et al.*, 1997), direct nitridation of Al powder (Da Cruz and Munz, 1999), (Mao *et al.*, 2017) are more common than other synthesis methods in the lab. The most popular techniques at lab scale include non-transferred arc plasma method (Kim, Choi and Park, 2013), chemical routes (Ahn *et al.*, 2017), microwave-assisted urea route (Ahn *et al.*, 2016), solvothermal process (Sardar and Rao, 2005), pulsed laser ablation (Grigoriu *et al.*, 2000), ball milling (Rounaghi *et al.*, 2017), CVD (Zheng *et al.*, 2008), (Chen *et al.*, 2019), transferred type arc plasma (Iwata *et al.*, 2004), magnetron sputtering (Choudhary, Mishra and Hubli, 2016), (Metel *et al.*, 2020), pulsed DC magnetron sputtering (Mazur *et al.*, 2015), RF magnetron sputtering (Musa *et al.*, 2020) and suspension plasma spray (Barandehfard, Aluha and Gitzhofer, 2021). The quality of AlN and its application is related to the morphology, size distribution, and purity of precursors. For example, the thermal conductivity of AlN is affected by impurity (Oh and Park, 1998). Cubic AlN is a metastable phase usually obtained at high temperature and high pressure (15–20 GPa), which can be however synthesized in the form of powders and thin-film coatings by various approaches (Kudyakova *et al.*, 2017), which include:

- Reduction of Al_2O_3 in nitrogen or nitrogen-containing materials;
- The reaction of molten or gaseous Al with nitrogen-containing materials;
- The reaction of highly volatile inorganic Al compounds with nitrogen or nitrogen-containing gases;
- The reaction of Al compounds with nitrogen-containing inorganic compounds; and
- The polymorphic transition of the AlN hexagonal phase into the cubic phase.

Thermal plasma techniques provide high enthalpy, which helps to accelerate reaction rates between the species (Sung *et al.*, 2017), and has been used to synthesize hexagonal AlN nanoparticles (Kim, Choi, Kim, *et al.*, 2014). Thick coatings of metallic and non-metallic materials can be generated owing to the high deposition rates of the plasma spray technology (Shahien *et al.*, 2013a). High temperature gradients in plasma produce rapid quenching (Venkatramani, 2002), which depresses the excessive formation of byproducts (Kim, Choi and Park, 2011). Moreover, suspension plasma spray (SPS) technology (Gitzhofer, Bouyer and Maher Boulos, 1997), provides flexibility in the selection of precursors to facilitate the synthesis of materials with different compositions. In this technology, which is different from conventional thermal plasma spraying, the atomized droplets are fragmented and the suspension liquid evaporated, while the solid particles sinter, melt, evaporate, ionize and finally impinge as clusters to the substrate (Pawlowski, 2009). By dispersing the feedstock solid particles in a liquid suspension, it eases injection of sub-micron or nanosized feedstock particles (Fauchais, Rat, *et al.*, 2008). The SPS technology is a great process for injection of precursors particles (even of nanometric size) dispersed in a liquid medium atomized in the plasma thus taking advantage of the momentum of the atomized liquid to penetrate the highly viscous plasma. (Fauchais and Montavon, 2010). The precursor particles are then propelled to the substrate to form a coating in vapor, clusters, molten or semi-molten form (Kassner *et al.*, 2008).

Some of the benefits that thermal plasma spraying technology offer to the industry involves (i) spraying a wide range of materials that include metals, ceramics, and complex composites, (ii) using suspension liquid carriers instead of conventional powders injected as feedstock, which can yield more refined and unique coating microstructures, thus providing more control on coating properties (porosity, density, or columnar microstructure), as well as in the production of functional and smart coatings, (iii) additional system capability exists for axial injection of

feedstock by SPS, which facilitates the thermal exchange between feedstock particles and the plasma plume, and (iv) the capacity to produce multilayer, mixed component and composite coating architectures (Joshi and Nylen, 2019). The axial injection method of radiofrequency (RF) induction plasma increases the possibility of injecting a wide range of feedstock materials almost at the center of the RF coil. Furthermore, RF induction plasma provides the potential for prolonged residence time and large plasma volumes, which helps the reaction of Al particles and nitrogen to form AlN (Amirhossein Pakseresht, 2018).

Nitriding of Al is normally prevented by the naturally occurring oxide layer that inhibits the diffusion of nitrogen into the metal matrix (Freiberg, 2018), due to poor solubility and low diffusion rate of nitrogen in Al (Farokhzadeh and Edrisy, 2017). Low N-diffusion coefficient into Al leads to the slow growth rate of AlN by normal plasma nitriding (Visuttipitukul, Aizawa and Kuwahara, 2003). The presence of H_2 gas in the plasma is important because it etches away the thin oxide layer on Al metal. Adding H_2 in the plasma results in a higher particle and substrate temperature, which contributes positively to nitridation. However, spectroscopic measurement of plasma temperature indicates that addition of H_2 does not increase the plasma temperature significantly but improves the plasma thermal conductivity (Yamada *et al.*, 2004b).

The use of NH_3 (Smolen and Dominik, 2013) and N_2 gas is more common as a nitrogen source for the synthesis of AlN, with NH_3 being the more effective nitrogen reactant source (Iwata *et al.*, 2004) than pure N_2 because (i) it is difficult to decompose the strong diatomic (N_2) bonds, and (ii) even if it is decomposed into N radicals, it recombines rapidly and easily back to N_2 (Kim, Choi and Park, 2011). Therefore, nitrogen-containing solid substances such as urea (CH_4N_2O) (Sun *et al.*, 2009), melamine ($C_3H_6N_6$) (Rounaghi *et al.*, 2016), hydrazinium chloride (N_2H_5Cl) (Dallaev *et al.*, 2020), or liquid substances such as hydrazine (N_2H_4) (Abdulagatov *et al.*, 2018) have been used to synthesize nitride ceramics. As the hydrazine is very unstable and the hydrazinium chloride can become corrosive to the reactor, and as the urea contains oxygen, the nitrogen feedstock source selected in this study is melamine ground as a powder added to the suspension.

It has been observed that the particle size of the powder feedstock is a key factor in producing homogenous coatings through SPS because the suspension atomization probe controls the particle trajectory and the dispersion of the droplets in the plasma jet. Furthermore, the

deposition efficiency is influenced by the particles size of the precursors as large particles normally demand longer residence times for complete reaction (Shahien *et al.*, 2011d).

The objective of this research is to synthesize cubic AlN coatings with SPS, using Al powder precursor and melamine as the nitriding agent. Melamine has been chosen to avoid toxic ammonia commonly used as a typical nitriding agent (Bretterbauer and Schwarzinger, 2012). Since it is difficult to directly deposit AlN onto a substrate (Shahien *et al.*, 2011c), it is proposed to synthesize and deposit AlN on carbon steel substrate in situ through SPS. Several studies have shown the production of AlN coating by plasma spray in-situ (Shahien *et al.*, 2011c), using melamine to produce nano powder AlN (Rounaghi *et al.*, 2012), utilizing promoting additives (Shahien, Yamada and Fukumoto, 2018), and the modeling of the synthesis reaction between metallic Al with melamine to produce hexagonal closed-packed aluminum nitride (hcp-AlN) (Rounaghi *et al.*, 2017).

In this study, parameters such as the effect of the particle size of Al powder and promotional additives i.e., AlN, BN, B, Mo, Y_2O_3, and Al_4C_3 in the SPS of AlN coating were explored. Concerning the choice of the promotional additives, it is expected that Al-based or nitride-based additives should promote the formation of AlN-rich coatings by helping avoid agglomerates in the suspension and by initiating the nitridation of Al. The coatings were tested for their corrosion resistance under realistic industrial conditions. Modeling using *Ab initio* molecular dynamic (BOMD) simulations using PWscf code in the Quantum Espresso package was carried out in this study at 1200 K to ascertain the atomic level interaction between molten Al with pristine AlN (100) non-polar surface which is one of the most stable planes of AlN at. In the computer simulation a purer AlN coating was used because of its potential application for providing corrosion resistant surfaces in contact with a molten Al alloy. The modeling aims to determine the likelihood of AlN corrosion susceptibility with molten Al using the magnitude of the interfacial energy. In addition, modeling by Factsage™ thermochemical software (C. W. Bale *et al.*, 2016) was used to predict both the thermal and chemical stability of AlN when in contact with a liquid Al-Mg alloy.

5.4 Research methodology

5.4.1 Equilibrium thermodynamic modeling of pure AlN in contact with molten Al-5wt%Mg alloy

An equilibrium thermodynamic simulation was done using FactSage to predict potential reactions between AlN and molten Al-Mg. For this purpose, the databases utilized were FTlite (FactSage Al-alloy and Mg-alloy databases), FToxid (FactSage oxide database for slags, glasses, ceramics, and refractories), and FactPS (for pure substances database). Calculations were carried out using the "Equilib" module of the FactSage thermochemical software developed by the CRCT group at École Polytechnique de Montréal, Canada. The software calculates the concentrations of chemical species of specified elements or compounds when they react fully or partially to attain a state of chemical equilibrium (C. W. Bale *et al.*, 2016). Modeling was done for the interaction between AlN and molten Al-Mg alloy in the temperature range of 273–1123 K at ambient pressure with a constant composition of 95wt.% Al, 5wt.% Mg and 100wt.% AlN. The output data indicates the change in mass against temperature to show possible reactions.

5.4.2 *Ab initio* Computational detail

Ab initio density functional theory (DFT) (Hohenberg and W.Kohn, 1964) calculations were performed using the plane wave and pseudo-potential method in the generalized gradient approximation, as implemented in the PWscf (Quantum Espresso) package (Giannozzi, 2009), (P.Giannozzi, 2017). Electron exchange and correlation energies are assessed with the generalized gradient approximation (GGA) (Perdew JP, Burke K, 1996). The grimme-d3 (DFT-D3) dispersion correction scheme (Grimme *et al.*, 2010), has been used in all calculations. All pseudo-potentials were extracted from the Standard Solid-State Pseudo-Potentials (SSSP) Library (Efficiency Version 1.1) maintained by Materials Cloud (Lejaeghere, 2016). Kinetic energy cut-off set to 25 Ry and charge density cut-off set to 225 Ry. Gamma point Monkhorst-Pack grid of k-points was used to sample the Brillouin Zone (BZ) (Hu *et al.*, 2019). The constraint-free geometry optimization was obtained using the Broyden-Fletcher-Goldfarb-Shanno (BFGS) quasi-Newton algorithm (Pfrommer *et al.*, 1997), with the self-consistent field (scf) convergence threshold set to 10^{-8} Ry during variable cell relaxation of ions. The metallic

nature of the system leads to a discontinuous variation of the orbital occupancies across the Brillouin zone. To deal with this problem, the Marzari-Vanderbilt 'cold' smearing (Marzari, Vanderbilt and Payne, 1997), was used with a smearing width of 0.01 Ry. Due to the size and inhomogeneous nature of the model, local-density-dependent Thomas-Fermi (local-TF) charge mixing was used to improve convergence (Raczkowski, Canning and Wang, 2001).

One of the fundamental principles underlying the description of quantum states of molecules is the Born-Oppenheimer approximation, which allows the motion of the nuclei and the movement of the electrons to be isolated. When explaining electrons movement in a molecule, the Born-Oppenheimer approach discounts the movement of the atomic nuclei. The physical basis for the Born-Oppenheimer approximation is that the mass of an atomic nucleus in a molecule is much greater than the mass of an electron (more than 1000 times), and because of this imbalance, the nucleus moves much more slowly than the electrons (Sutcliffe and Woolley, 2012).

In this work, the Born-Oppenheimer molecular dynamics (BOMD) simulation (Kühne *et al.*, 2007) of the initial relaxed heterostructures was carried out at 1200 K (slightly above experimental temperature) with fixed unit cell parameters and volume (canonical ensemble, NVT, i.e. a constant number of particles–volume–temperature). For the hcp-AlN model, the equation of motion was solved via the velocity Verlet algorithm with an integration time step of 2 fs and overall simulation time of 2 ps, while for the zinc-blende cubic-AlN the applied integration time step was 4 fs over a simulation period of 0.4 ps. In this work, modelling was done from zinc blende cubic AlN because the software found it to be the most stable structure. The difference in time scales was used to compensate for the sizes of the crystal models since large models take along to converge during *ab initio* DFT simulation. The system temperature was kept constant by re-scaling the velocity. Only the Γ point was used in the BZ integration. The variation of the total energy was considered during each MD time step.

5.4.3 Plasma synthesis of cubic AlN coating

The coatings were synthesized by in-situ reaction of Al and melamine powder using RF- SPS system according to the method already described (Barandehfard, Aluha and Gitzhofer, 2021). The plasma synthesis parameters, the materials, and chemicals used in this study are summarized in Table 5-1 as follow:

Table 5-1. Experimental conditions used for the in-situ plasma synthesized AlN coatings

Process condition	Parameters	Value
Plasma system	Power system	40 kW
	Plasma torch	Tekna PL-50 (3 MHz)
	Nozzle	supersonic
Plasma gas flow rate (SLPM)	Sheath gas	Ar: 52, H_2: 5.5, N_2: 40
	Central gas	Ar: 22
	Atomization gas	Ar: 10
Reactor pressure	Initial pressure	Below 2 kPa
	Working Pressure	16 kPa
Standoff distance (cm)	Distance	8.0
Substrate	1144 Carbon steel	12.7 × 2.0 mm
Precursor materials (Al + melamine)	Al powder	0.9 g
	Melamine	9.0 g
	Promotional additives	0.1 g
Suspension liquid	Hexadecane	100 ml
Suspension composition (Precursor + Suspension liquide)	Precursor concentration	5, 10, 20 g in 100 ml
Suspension flow rate ($ml.min^{-1}$)	Flow	2.0
Number of loops	Deposition cycles	200 at 50 $mm.sec^{-1}$

a) Substrate: 12.7 mm x 2.0 mm disks of 1144 Carbon steel scratched with sandpaper grit of gauge number 180 µm (McMaster-Carr, Canada);
b) Suspension liquid carrier: Hexadecane ($C_{16}H_{34}$ Sigma Aldrich, USA);

c) Powders (precursor materials): (Al, 1–5 μm, Atlantic equipment engineers), Al (17–35 μm, Alfa Aesar, Canada), melamine ($C_3N_6H_6$, Alfa Aesar, Fisher Scientific, Canada), aluminum nitride (AlN, Alfa Aesar, < 4 μm, APS, Canada), aluminum carbide (Al_4C_3, Alfa Aesar, < 10 μm), boron (B, 15 μm, Stanford advance materials, Canada), boron nitride (BN, 10 μm, Goodfellow, England), molybdenum (Mo, <10 μm, Aldrich chemical company, Inc.), and yttria (Y_2O_3, 5–10 μm, Goodfellow, England) are used as precursors and promotional additives to the synthesis of the coating in this project.

In Figure 5-1, a schematic of the suspension injection system is provided. The suspension liquid (hexadecane) containing the solid powders (Al plus melamine with or without some additives) was stirred vigorously for 30 minutes to obtain a homogenous suspension. Then the suspension was gradually moved to the double-wall water cooled glass container by peristaltic pumping while under sonication with 40 kW power to protect the glass and prevent particles agglomeration. From sonicator the suspension was returned to the main container and recirculated for 10 minutes and then delivered to the atomization probe in plasma at the rate of 2 $cm^3.min^{-1}$. It was observed that no agglomeration and sedimentation occurred and the injection was regular.

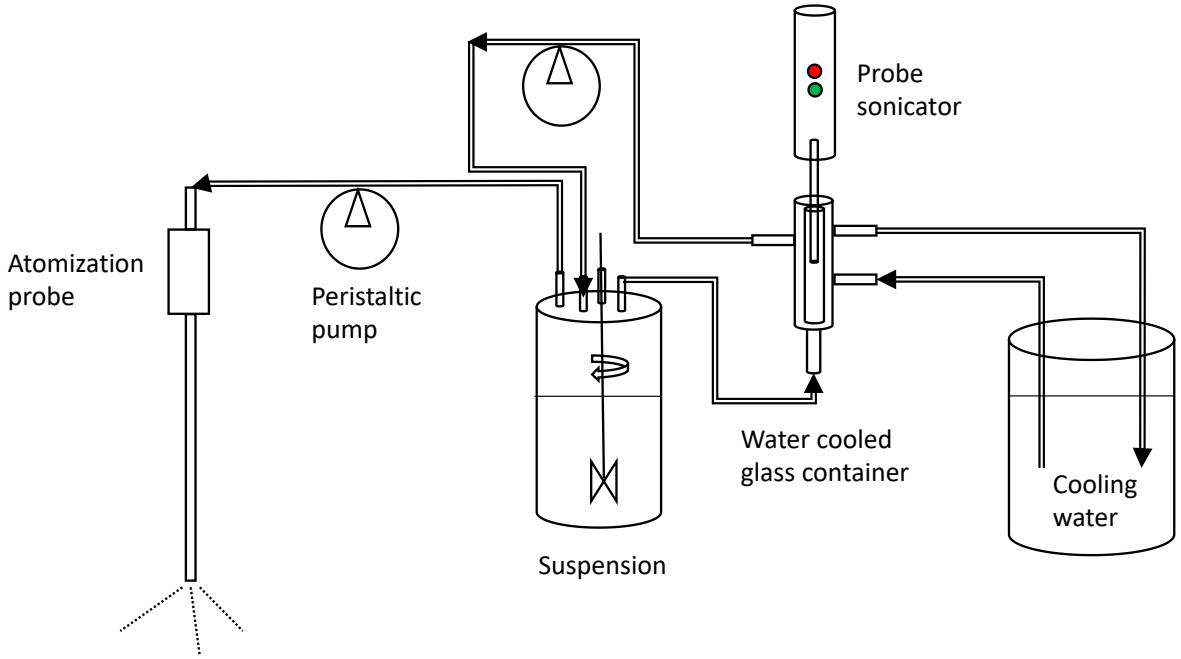

Figure 5-1. schematic showing the features of suspension injection system

5.4.4 Hardness test on plasma sprayed coatings

The hardness of the plasma sprayed coatings was determined using a Micro Durometer (Buehler Micromet II, Germany) with a pyramidal diamond point having a square base and an objective lens of 40X for a real magnification of 400X. The hardness of the original substrate without a coating was measured first, and then identical forces (25 – 400 g) were applied on the coated substrate. The measured values are used to calculate the Vickers hardness (Hv) according to Equation 5-1:

$$HV = \frac{2F \times sin(\frac{136^\circ}{2})}{g \times d^2} \qquad \text{Equation 5-1}$$

where F is the load (N), d is the average diagonal length of the footprint (mm), and g is the acceleration of gravity (9.80665 m/s^2).

5.4.5 Roughness test and topology of the coating

To measure the surface roughness and visually display the topology of the plasma sprayed coatings, the optical profilometer instrument (Bruker Contour GT-K, USA) was used. Measurements were performed using green light, at a magnification of 5X. This corresponds to a total scan area of 1268 x 951 μm and a lateral sampling value of 1.98 μm (each pixel represents a square with dimensions 1.98 μm x 1.98 μm). Three scans were performed in different locations of each sample. The data collected was processed using the Bruker Vision64 software that operates the profilometer. The analysis component of Vision64 is based on the "Mountains" software from Digital Surf.

5.4.6 Corrosion test

The plasma synthesized coatings were tested for corrosion resistance by contacting them directly with molten Al-alloy containing 5% magnesium (Al-5wt%Mg) at 1123 K, for 2 h. Details are available in (Barandehfard, Aluha and Gitzhofer, 2021).

5.4.7 Characterization

Evaluation of the crystal structure of the synthesized AlN powder coatings was performed on an X-ray diffractometer "Philips PAN analytical X'pert PRO MPD", using Cu Kα1 radiation

with a wavelength, λ = 1.54 Å. It is worth mentioning that XRD analyses were done on plasma-sprayed samples without any dissolution of unreacted Al by HCl. Morphology of the deposited coating was investigated using the Scanning Electron Microscope (SEM, Hitachi S-4700).

5.5 Results and discussion

5.5.1 FactSage modeling of AlN in contact with molten Al-Mg alloy

Figure. 5-2 shows the high temperature stability of 100 g pure AlN in contact with 100 g molten Al-5wt%Mg in the temperature window from 850 °C to room temperature. The hypothesis for the FactSage modeling was to test the thermochemical stability of AlN at the experimental temperature when in contact with molten Al-5%wt Mg alloy. It indicates that AlN remains thermally and chemically stable along with the presented temperature range without reacting with molten Al-5wt%Mg alloy.

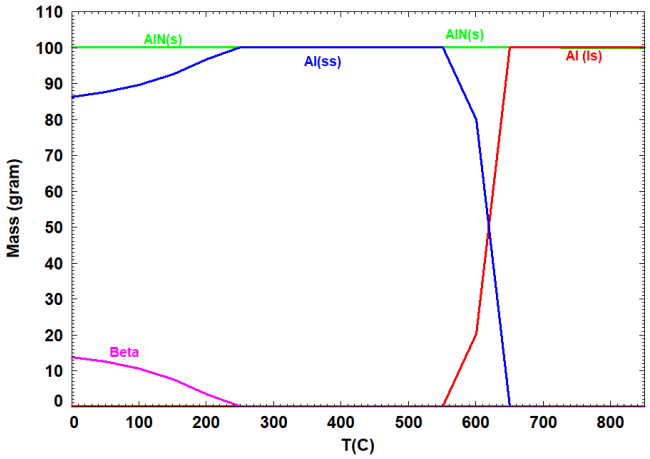

Figure. 5-2. Equilibrium calculation of AlN and molten Al-5wt%Mg alloy.

5.5.2 Ab initio modeling of AlN electronic structure for hcp and metastable cubic AlN

5.5.2.1 Optimization of model lattice parameters

All the hcp-AlN models of this work are built starting from an Al_2N_2 unit cell with a wurtzite primitive-centered hcp crystal structure (B4, space group P63mmc) as shown in Figure 5-3. An Al_4N_4 unit cell with a zinc blende face-centered cubic (fcc) structure (B3, space group F-43M),

has been modeled as presented in Figure 5-4. The lattice parameters of the DFT-optimized unit cell and the models exposed to molten Al are summarized in Table 5-2.

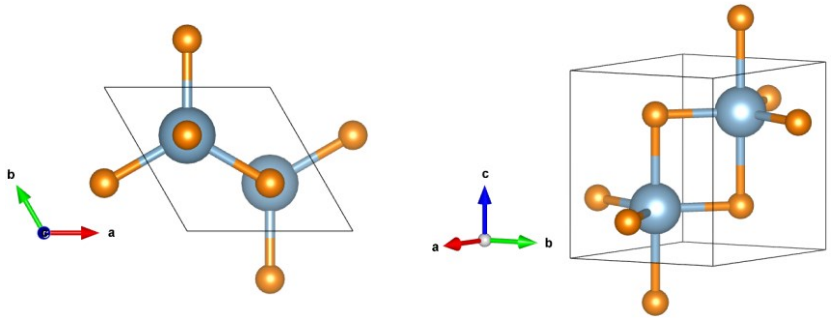

Figure 5-3. Model of hcp-Al_2N_2 B4 unit cell showing Al (blue), N (orange).

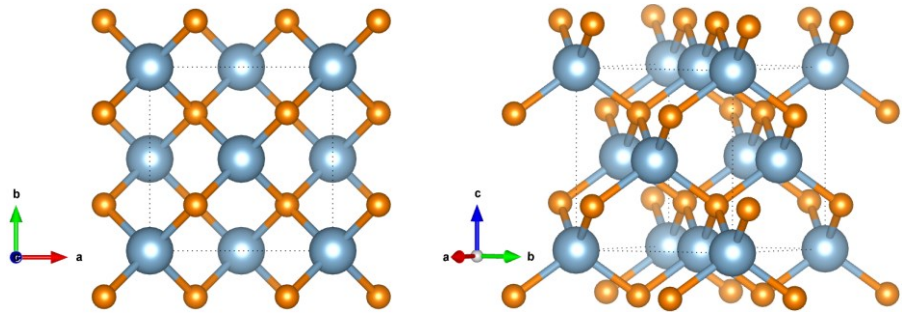

Figure 5-4. Model of the cubic crystal lattice of a cubic-Al_4N_4 B3 unit cell showing Al (blue), N (orange).

Table 5-2. Optimized unit cell and model lattice parameters of hcp-Al_2N_2 and cubic-Al_4N_4 parameters.

Lattice parameters	Optimized unit cells		Model in contact with molten Al	
	hcp (B4) Al_2N_2	cubic (B3) Al_4N_4	hcp (B4) $Al_{87}N_{20}$	cubic (B3) $Al_{212}N_{64}$
a	3.31 Å	4.4 Å	6.62 Å	12.3 Å
b	3.31 Å	4.4 Å	8.38 Å	12.3 Å
c	4.19 Å	4.4 Å	30.74 Å	33.7 Å
α	90°	90°	90°	90°
β	90°	90°	90°	90°
γ	120°	90°	90°	90°

5.5.2.2 Relaxing AlN–Al interface at 0 K

To build the interface between solid coating in contact with molten Al, designated as the {$AlN_{(s)}$–$Al_{(l)}$} model, the aforementioned hcp-AlN and cubic-AlN unit cells were cleaved along the (100) low index plane using the Building tool in Materials Studio ('Dassault Systèmes BIOVIA. Materials Studio.', 2019). The parameters top and thickness were set to 2.217 and 6.996 Å, respectively, and the resulting model, after U x V = 2 x 2 scale-up, had a stoichiometry of $Al_{20}N_{20}$ made up of five layers, as seen in Figure 5-5.

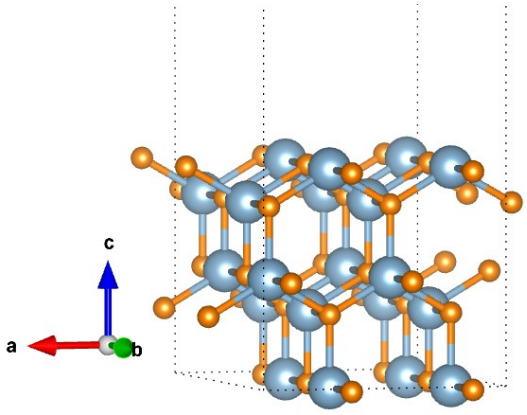

Figure 5-5. Model of triclinic $Al_{20}N_{20}$ with (100) surface. Al (blue), N (orange)

After the lattice parameters of the model defined in Figure 5-5 were relaxed, the vacuum component was filled with amorphous Al and the density used was determined by its melting point density, $\rho = 2.368$ g.cm^{-3} (Aluminum Association et al., 1984). The resulting model had a stoichiometry of $Al_{87}N_{20}$, and Figure 5-6 shows snapshots before and after the $AlN_{(s)}$–$Al_{(l)}$ model was relaxed at GGA/PBE level of theory and 0 K. Keeping the previously defined lattice parameters, the model was relaxed so as not to alter the density of Al. The figure shows that the amorphous Al crystallized after optimization at 0 K. A well-defined layer of AlN forms at the interface with the Al coming from the amorphous Al part of the model. The underlying (100) morphology of the N atoms is adopted by the new interface layer of the AlN.

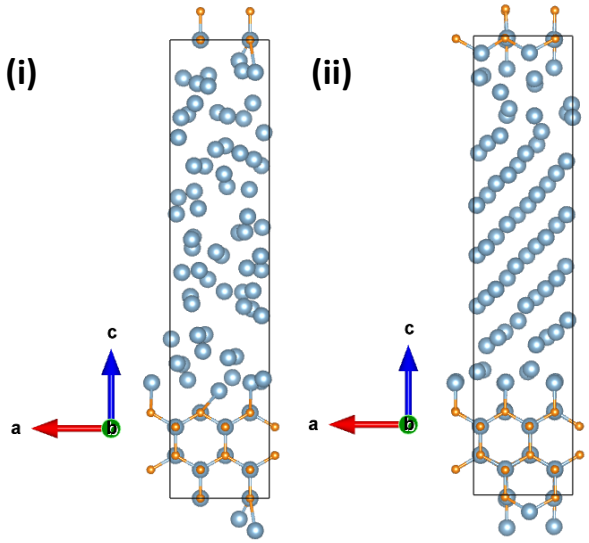

Figure 5-6. Model of $Al_{87}N_{20}$ optimized at 0 K showing Al (blue), N (orange); (i) input model for the Al melt; and (ii) relaxed model, with fixed lattice parameters.

In addition, the resulting substrate model for zinc blende, cubic-AlN had a stoichiometry of $Al_{64}N_{64}$. Then a vacuum component was filled with amorphous Al whereby the density used was determined by its melting point density, $\rho = 2.368$ g.cm^{-3} (Aluminum Association et al., 1984). The resulting model of amorphous Al interacting with AlN (100) had a stoichiometry of $Al_{212}N_{64}$, and Figure 5-7 shows a snapshot after the $AlN_{(s)}$–$Al_{(l)}$ model was relaxed at GGA/PBE level of theory at 0 K.

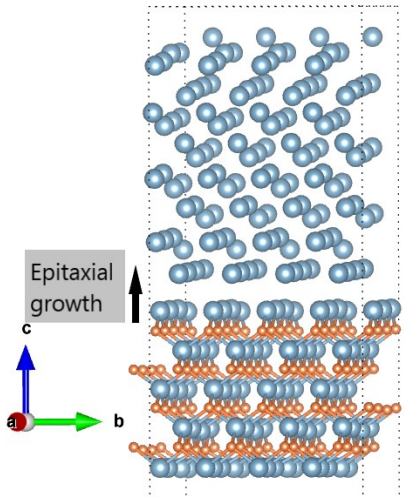

Figure 5-7. Model of $Al_{212}N_{64}$ showing the interaction of Al melt with cubic-AlN (100) surface at 0 K. Al (blue), N (orange)

Keeping the previously defined lattice parameters, the model was relaxed so as not to alter the density of Al. It was observed that amorphous Al crystallized after optimization at 0 K, with a well-defined layer of AlN forming at the interface with the Al melt. The underlying (100) morphology of the N atoms was epitaxially adopted by the new interface layer of Al as depicted in Figure 5-7.

5.5.2.3 Molecular dynamics simulation

Figure 5-8 shows the temperature evolution during the BOMD simulation of hcp-$AlN_{(s)}$–$Al_{(l)}$ and it indicates that the model thermolyzes rapidly with a mean temperature of 1181 K around the target temperature of 1200 K. Figure 5-9 summarizes an analogous BOMD simulation for the cubic-$AlN_{(s)}$–$Al_{(l)}$ and shows that the model thermolyzed to a mean temperature of 1205 K. The difference in the thermalization temperature is statistical depending on the model size and modeling time, but it is within an acceptable margin of error (~2%). The difference in the number of steps is determined by how quickly the model converges. On the other hand, Figure 5-10 and Figure 5-11 also indicate that there was no energy drift during the course of the BOMD simulation. Energy drifts are usually an indication of simulation errors in BOMD, but can be minimized by choosing good extrapolation schemes and other clever ways to propagate the wavefunction (Pulay and Fogarasi, 2004), and this demonstrates that the model was properly designed for the system under research.

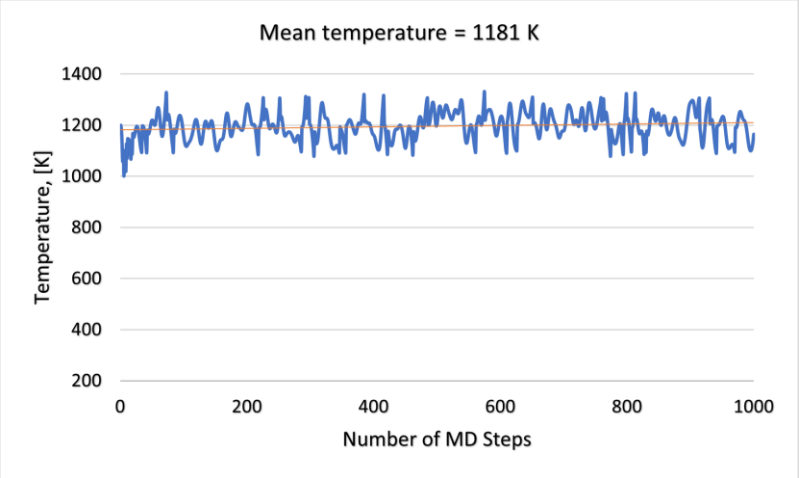

Figure 5-8. Temperature evolution during NVT BOMD simulation of hcp-$AlN_{(s)}$–$Al_{(l)}$ system at 1200 K

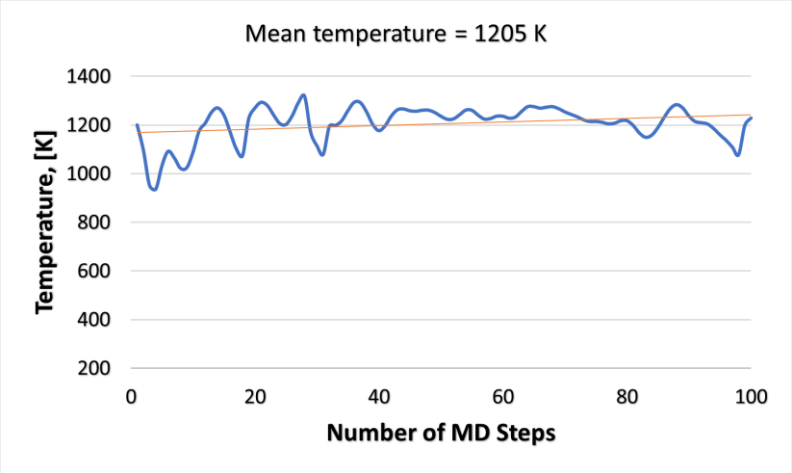

Figure 5-9. Temperature evolution during NVT BOMD simulation of cubic-$AlN_{(s)}$–$Al_{(l)}$ system at 1200 K

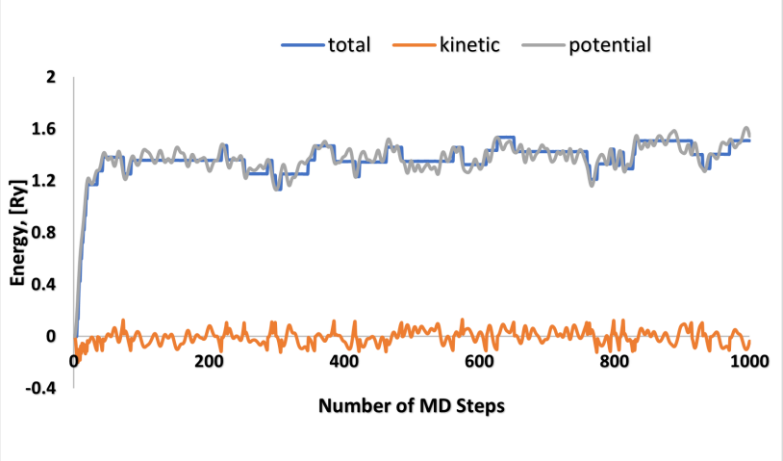

Figure 5-10. Energy evolution during NVT BOMD simulation of hcp-$AlN_{(s)}$–$Al_{(l)}$ system at 1200 K

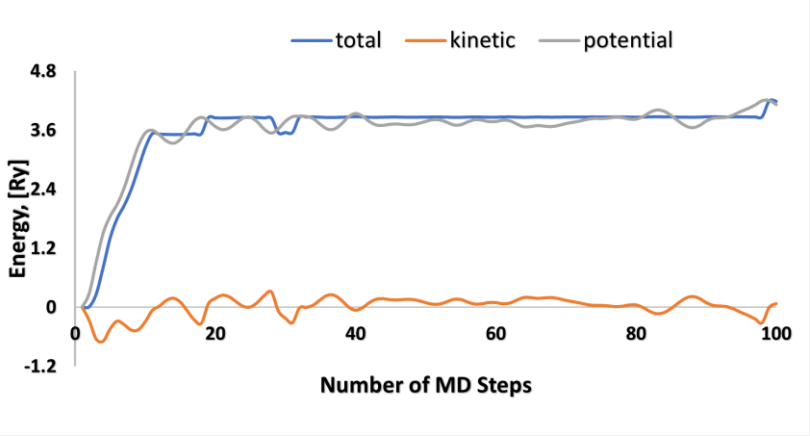

Figure 5-11. Energy evolution during NVT BOMD simulation of cubic-$AlN_{(s)}$–$Al_{(l)}$ system at 1200 K

Figure 5-12 and Figure 5-13 show the models captured as the last frames of the BOMD simulation for hcp-$AlN_{(s)}$–$Al_{(l)}$ and cubic-$AlN_{(s)}$–$Al_{(l)}$, respectively. Even at 1200 K, the AlN interface-layer formed between the surface N and Al from the amorphous liquid phase seems to be stable and it essentially adopts the underlying (100) morphology. The average Al-N bond length of the new interface layer was found to be 1.90 Å for hcp-AlN and 1.87 Å for cubic-AlN. No surface reconstruction appears under the simulation model-parameters used.

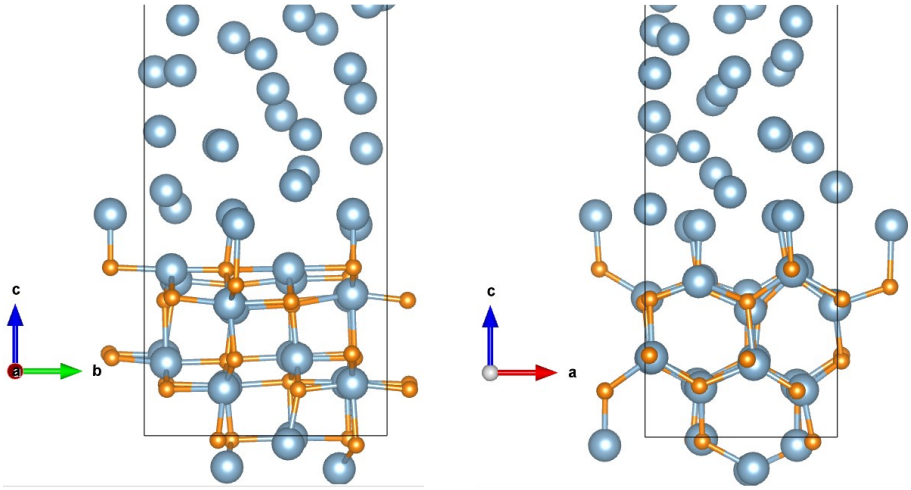

Figure 5-12. Last frame of NVT BOMD simulation showing hcp-AlN formation at the interface of hcp-AlN(s)–Al(l); Al (blue), N (orange) with (i) View from “a” direction; and (ii) View from “b” direction.

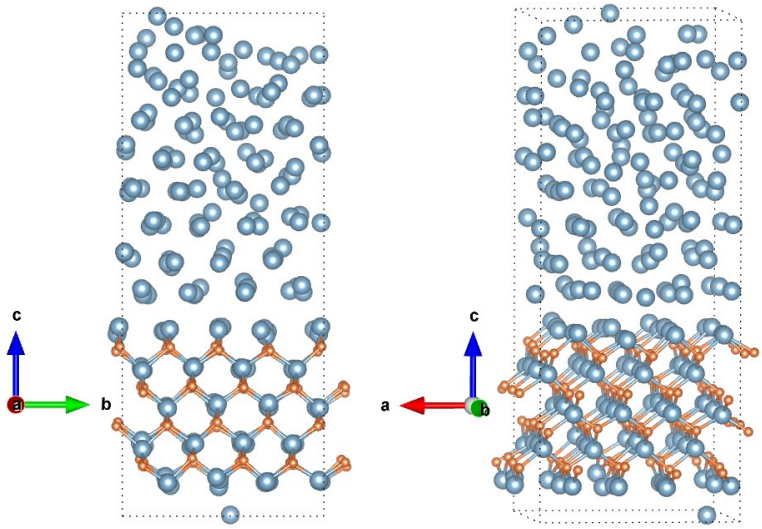

Figure 5-13. Last frame of NVT BOMD simulation showing cubic-AlN formation at the interface of cubic-AlN(s)–Al(l); Al (blue), N (orange) with (i) View from “a” direction; and (ii) View from “b” direction.

5.5.2.4 Interaction Energy

Calculation of interaction energy, (γ_{int}) between the amorphous molten Al and AlN (100) surface represented by $E_{Al_{(l)}}$ and $E_{AlN_{(100)}}$ respectively, was done using Equation 5-2:

$$\gamma_{int} = \frac{E_{Al_{(l)}} + E_{AlN_{(100)}} - E_{total}}{2 * A} \qquad \text{Equation 5-2}$$

The models were set up as shown in Figure 5-12 and Figure 5-13. The system was simulated at temperature *T* in NVT ensemble until it reached a steady state with final total energy, E_{total}, and surface is *A*, where the surface is multiplied by 2 for cases without a vacuum in the model. The BOMD-relaxed $Al_{87}N_{20}$ structure consisting of 107 atoms gave an interaction energy value of 2018 kJ.mol^{-1} (or 18.2 kJ.mol^{-1} per unit cell area), while the BOMD-relaxed $Al_{212}N_{64}$ structure showed interaction energy of 8512.6 kJ.mol^{-1} (56.4 kJ.mol^{-1} per unit cell area). The cubic-$AlN_{(s)}$–$Al_{(l)}$ contact can be characterized as moderately strong van der Waal interaction. The Al-N bonds are partly covalent, but they could also have certain ionic properties, and the weak interaction energy involved indicates that the bonding between the layers is no more than a physisorption kind of interaction, which typically exists in the range of 50 kJ.mol^{-1} or less. The higher interfacial energy associated with the cubic-AlN originates from its metastable state. Principal factors which have been determined to form the metastable cubic-AlN phase in plasma include nucleation rate and growth under highly non-equilibrium conditions, the particle 'size effect', and optimization of the system parameters to improve its yield (Kudyakova *et al.*, 2017).

5.5.3 Materials characterization

XRD analysis was utilized to optimize and investigate the potential effect of several parameters during the synthesis of the AlN coatings through SPS. Three factors examined were (i) the influence of Al powder particle size on the percentage of AlN in the coatings, (ii) the promotional effect of additives on the composition of the coating, and (iii) optimization of AlN concentration as an additive in the precursor.

5.5.3.1 Effect of the particle size distribution of Al powder precursor

Two Al powder samples with different particle-size distributions were used in the plasma suspension feedstock, that is, small-sized particles (1–5 μm) and big-sized particles (17–35 μm).

Figure 5-14 provides the XRD patterns obtained by changing the Al powder particle size, which indicates the concentration of AlN formed in the coatings. The results demonstrate that when the Al powders were comparatively finer 100% of (1–5 µm), less AlN was formed in the coatings (10%) as shown in Figure 5-14 (a), possibly because small Al powder particles vaporize or lead to fast nitridation reaction and then the AlN hardens before reaching the substrate and cannot stick (Shahien *et al.*, 2011d). A 10% addition of (17–35 µm) Al particle size led to an increased formation of AlN (13%), as shown in Figure 5-14(b), while Figure 5-14(c) represents a further improvement to 36% AlN with the addition of 20% (17–35 µm) Al particle size.

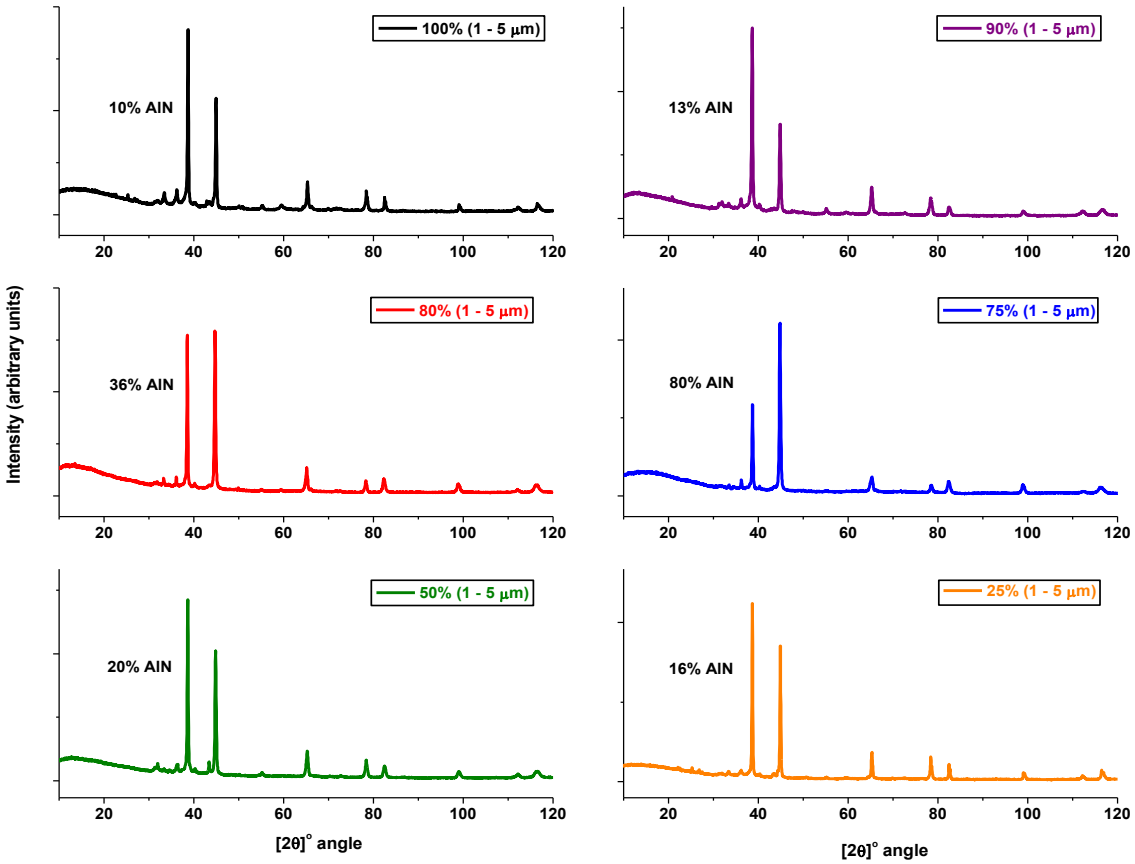

Figure 5-14. XRD patterns showing composition of AlN in the coatings produced by addition of mass X of (17 – 35 µm) particle size of Al powder into (1 – 5 µm) Al particle size, where X is: (a) 0%; (b) 10%; (c) 20%; (d) 25%; (e) 50%; and (f) 75%.

Although decreasing the particle size of the feedstock powder has been found to enhance the specific surface area of the particles, which increases the probability of surface nitridation (Shahien, Yamada and Fukumoto, 2016), in this work, it was observed that the addition of bigger Al particles promotes the formation of AlN in the coating. The maximum amount of AlN formed

(80%) in the coating was achieved in the mixture of 75% (1–5 µm) particle size with 25% (17–35 µm) particle size as revealed in Figure 5-14(d). The bigger particles of Al played a role, possibly as a matrix, which helps the deposited particles to stick to the substrate during the coating formation. However, the addition of more than 25% of bigger-sized particles (17–35 µm) lowered the AlN formation because a lot of energy is required to completely vaporize the particles and react while still in the plasma plume. This is exemplified in Figure 5-14(e) where only 20% AlN was produced with the addition of 50% of (17–35 µm) Al particle size, while Figure 5-14(f) shows 16% AlN was formed by the addition of 75% of (17–35 µm) Al particle size. It has been observed that the reaction of the precursor powder with the plasma gases depends on the powder's particle size, which influences the powder's flowability, melting, and particle behavior while in the plasma (Shahien *et al.*, 2011d).

The plot in Figure 5-15 is a summary of the optimized mixture of the Al particle sizes in order to maximize the production of AlN. The best composition consisted of 75% of (1–5 µm) Al particle size mixed with 25% of (17–35 µm) Al particle size. Due to the tendency of the smaller particles to agglomerate, it was still difficult to steadily inject the finer particles into the plasma jet alone. The slow injection rate makes their introduction into the plasma more challenging despite using SPS technology. Flowability of the feedstock and steady injection is an important parameter that should be considered during SPS to have reproducible coatings with a homogenous structure (Vardelle *et al.*, 2001).

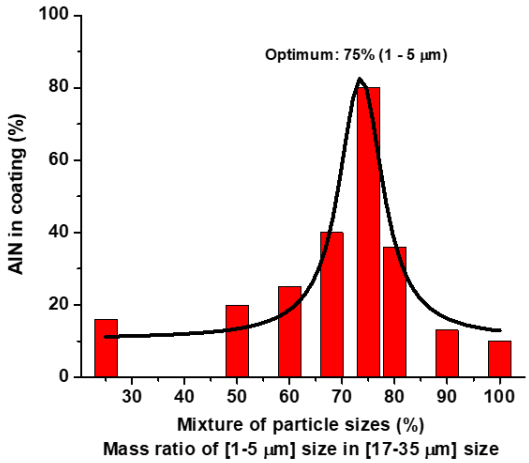

Figure 5-15. The quantity of AlN in the coating plotted against the mass ratio of Al powder particle sizes (1–5 µm) to (17–35 µm), indicating an optimum at 75% of (1–5 µm).

It has been observed that the addition of larger particles to the feedstock improves the powder flowability with more constant and steadier injection that minimizes clogging of the pipes and the atomization probe (Shahien *et al.*, 2011d). However, the vaporization of larger particles takes longer. Normally, the Biot number compares the heat transfer inside a particle to the heat transfer from the surface, and a high Biot number (greater than 1) means that there is more heat transfer taking place through convection on the surface. On the other hand, the Nusselt number alludes to the relationship between conduction and convection on the surface liquid, giving the ratio of external conduction resistance of a fluid to the external convection resistance to the fluid. The Biot number has been evaluated to be higher than unity for a Nusselt number of 2 (Young and Pfender, 1987). Upon impact, the big droplets break down and produced higher fresh surface exposed to the nitrogen rich atmosphere (Yang *et al.*, 2013).

5.5.3.2 Effect of promotional additives

In order to enhance the nitridation process, BN, B, AlN, Mo, Y_2O_3, and Al_4C_3 were included in the precursors as additives, and this seemed to improve the injection flow rate as well. The motivation for the inclusions stemmed from the fact that the additives are resistant to corrosion when in contact with molten Al alloy. The addition of BN to the precursor was for two reasons: (i) its decomposition releases nitrogen into plasma, which would be useful for nitridation of Al, and (ii) if it does not decompose, its inclusion in the coating will add to the non-wetting properties of the final coating (Reusch, Gmbh and Rudolph, 2015). Boron as an additive would react with nitrogen in plasma to produce BN, which is good for enhancing non-wetting properties of the coating towards molten Al (Fujii, Nakae and Okada, 1993) however with the risk of scavenging nitrogen from the Al.

Molybdenum was also considered for its anti-wetting properties in contact with molten Al with a melting point close to the temperature of formation of AlN. Al_4C_3 is resistant to corrosion when in contact with molten Al alloy below 1273 K (Sarina Bao *et al.*, 2016) and if it decomposes during SPS it can introduce more reactive Al species, which are beneficial for the nitridation process. On the other hand, fine Y_2O_3 has been found to act as a promoting additive by creating a wetting agent in the form of yttrium aluminate Y–Al–O around solid AlN particles (Shahien, Yamada and Fukumoto, 2018). Should some of these promotionals remain stable in

the plasma without decomposing, they would be deposited in the final coating and contribute to its corrosion resistance.

Since Al powders have an affinity to agglomerate during the peristaltic pumping, these additives also help in dispersing the particles that stick together and can clog the injection pipes and the atomization probe. By using SPS technology we overcame the problem of irregular injection of powders (Gitzhofer, Bouyer and Maher Boulos, 1997). Moreover, these additives were observed to promote the reaction between Al powder and decomposed melamine (the nitriding agent) based on the XRD results. Figure 5-16 provides the XRD patterns of the samples containing the additives, where Figure 5-16(a) was promoted by Y_2O_3 with 40% AlN in the coating (30% cubic and 10% hcp); Figure 5-16(b) is for boron giving 25% AlN (20% cubic and 5% hcp); Figure 5-16(c) is for BN giving 50% AlN (50% cubic and 0% hcp); Figure 5-16(d) is for Al_4C_3 giving 68% of cubic AlN only in the coating; Figure 5-16(e) is for Mo giving 66% cubic AlN without hcp, and Figure 5-16(f) is for AlN giving 40% AlN (33% cubic and 7% hcp).

It was observed that the worst performance was exhibited from pure B , followed by Y_2O_3 and AlN under similar reaction conditions, since they did not produce substantial quantities of AlN, giving 25, 40 and 40%, respectively. The best performance was for Mo and Al_4C_3 (66 and 68% AlN respectively), while BN generated 50% AlN. This is summarized pictorially in Figure 5-17. Although the addition of AlN in this experiment produced poor results, changing the reaction conditions by varying the AlN concentration improved its performance, and this is discussed in the next section.

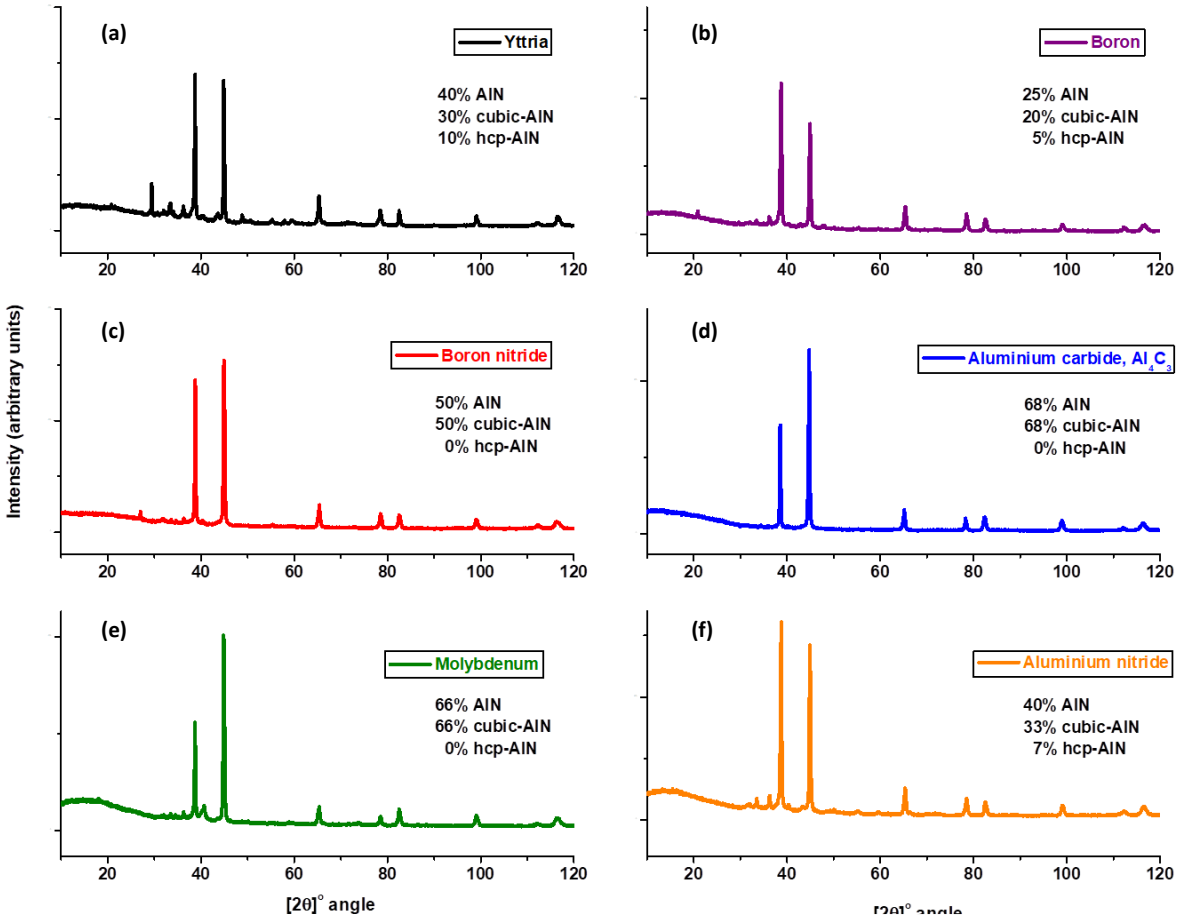

Figure 5-16. XRD patterns showing the composition of AlN in the coatings produced by the addition of (a) Y_2O_3; (b) Boron; (c) BN; (d) Al_4C_3; (e) Mo; and (f) AlN.

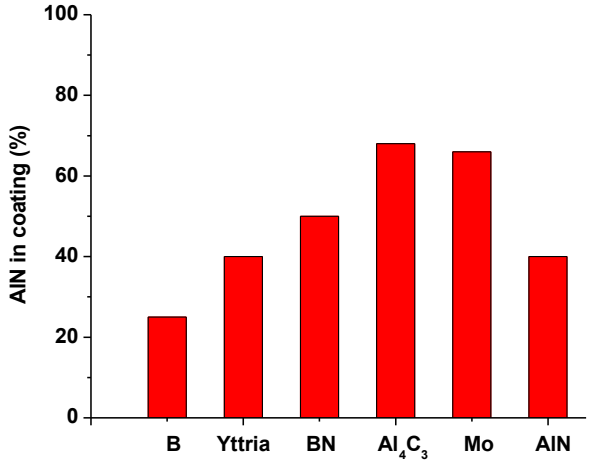

Figure 5-17. Plot showing how the concentration of AlN in a plasma synthesized coating is influenced by the addition of 10% of Y_2O_3, B, BN, Al_4C_3, Mo, AlN.

5.5.3.3 AlN as a promotional additive in the precursor

Preliminary findings showed that injecting AlN powder into the plasma always produces metallic Al peaks in the coatings as detected by XRD analysis, implying that AlN has a high propensity to decompose in plasma. It has been claimed that there is a narrow formation and decomposition temperature range for AlN in plasma and the fabrication of AlN coatings by conventional thermal spraying is problematic owing to its decomposition at 2000-2300 ºC (Yamada *et al.*, 2005). In this project, preliminary results confirmed that it was experimentally impossible to produce an AlN coating on a carbon steel substrate by direct spraying of AlN powder using plasma. The same observation has been reported by other authors (Shahien, Yamada and Fukumoto, 2016). For this reason, we resorted to the in-situ plasma synthesis and deposition of AlN as a coating. However, when the precursors were doped with different quantities of AlN promoter, the amount of AlN in the coatings improved significantly. XRD analysis of the plasma synthesized coatings indicated enhanced concentration of AlN as exemplified in Figure 5-18.

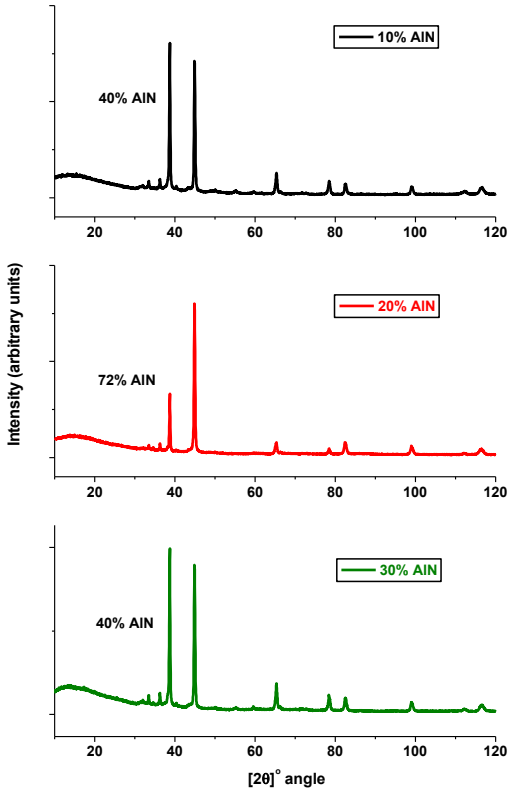

Figure 5-18. XRD patterns of samples containing AlN were promoted by the addition of 10%, 20%, and 30% of AlN in Al powder.

A mixture of 10wt% AlN in pure Al powder (0.11% of the total mass of the suspension) produced 40% of AlN in the final coating as summarized in Figure 5-19. The addition of 20% AlN in pure Al powder (0.22% of the total mass of the suspension) produced 72% of AlN in the coating while 30% of AlN in Al powder (0.33% of the total mass of the suspension) was produced 40% of AlN in the coating. Using AlN and other additives as a dispersion agent prevents agglomeration of Al metal in the feedstock and therefore, nitriding agents can diffuse to a larger surface area of Al and synthesize AlN. Moreover, the additives improve the flowability of injection of precursor feedstocks as noticed experimentally.

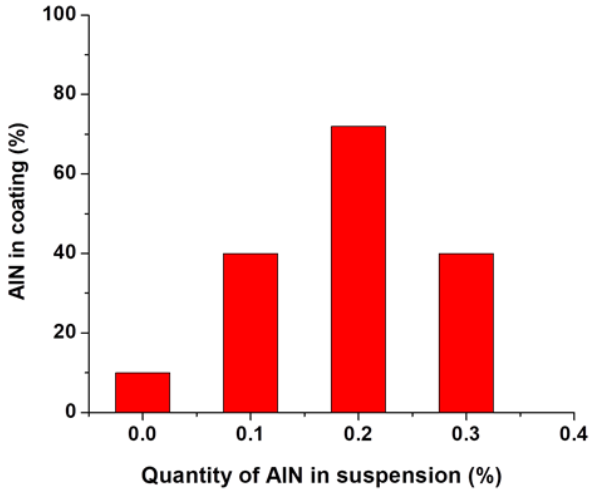

Figure 5-19. A plot summarizing the quantity of AlN formed in the coating versus the amount of AlN additive.

Among all the additives tested, using AlN led to lower byproducts such as Al_4C_3, C etc. in comparison to other additives, besides increasing the nitride component in the coating. The presence of AlN promoter in the feedstock improves the dispersion of Al powder particles, and mixing of the feedstock, thereby causing rapid and near-complete nitridation of Al in plasma (Shahien *et al.*, 2011b). Moreover, the presence of AlN and other additives prevented agglomeration of molten and unreacted Al on the deposited coating and by continuous interaction between the nitriding species in the plasma and the molten Al, post-deposition nitridation of Al was improved (Shahien *et al.*, 2010a).

5.5.4 Materials testing

5.5.4.1 Microscopic (SEM) analysis of plasma synthesized coatings

Figure 5-20 is a typical SEM image characterizing the surface of a fresh plasma synthesized AlN coating sample, and it shows a homogenous distribution of the particles in the coating with a mix of splats and partially molten morphologies. After exposure to molten Al-5wt%Mg alloy at 1123 K, the coating remained unreacted and stable. This is evident from the equal distribution of Al and N in the matrix as seen in Figure 5-21, which means that the two elements did not decompose and could still be associated. Figure 5-21(a) is the secondary electron image (SEI) of AlN coating after exposure to molten Al-Mg alloy, while Figure 5-21(b) portrays the mixed EDX elemental mapping for both Al and N. Figure 5-21(c), (d) and (e) represent the individual elemental mapping of Al, N, and O, respectively.

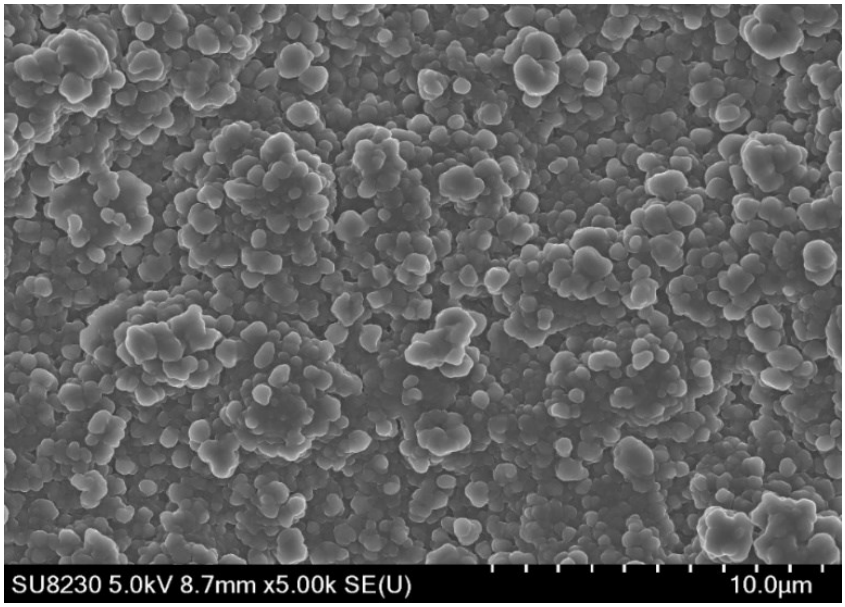

Figure 5-20. Typical SEM image characterizing the surface of a fresh plasma synthesized AlN coating sample

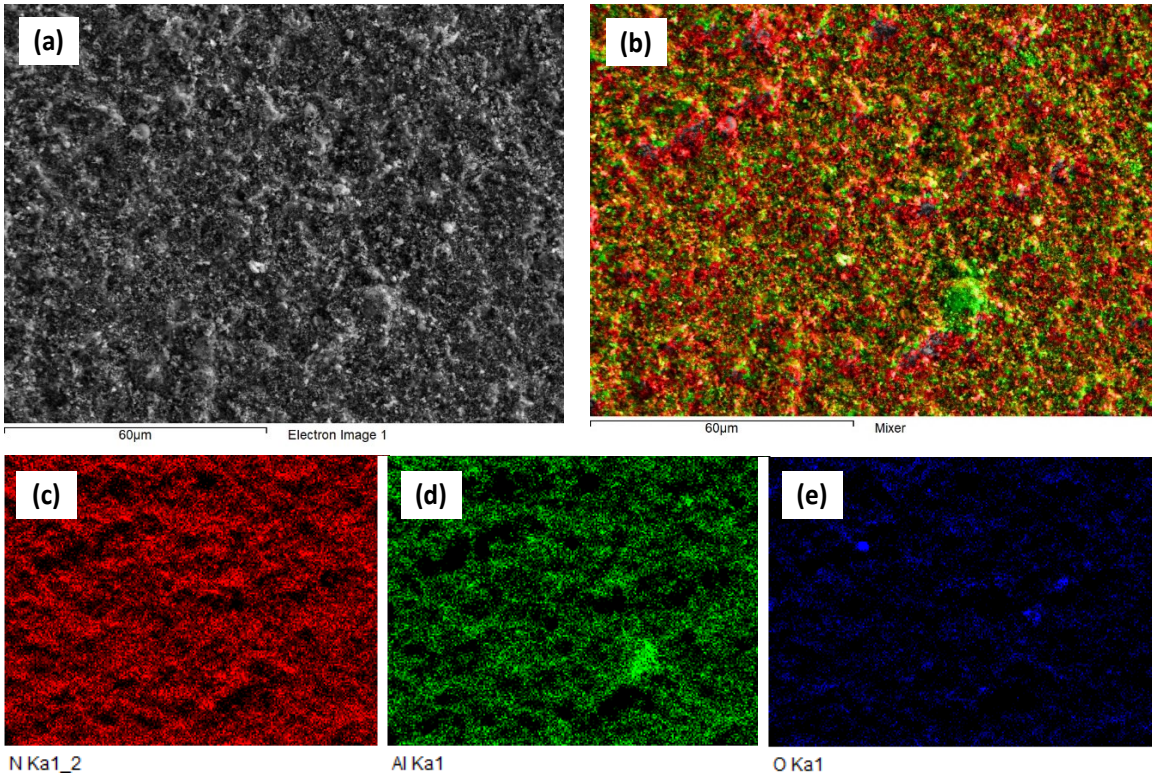

Figure 5-21. (a) SEM image of AlN coating after exposure to a molten Al-Mg alloy; (b) the mixed EDX elemental mapping of Al and N; and (c, d, e) individual elemental mapping of Al, N, and O, respectively.

Figure 5-22 (a) shows the SEM images of samples that were synthesized using the optimized the Al particle size mixture (75% (1-5µm) plus 25% (17-35µm)), where the image in (a) represents the sample with 82% AlN in the coating. The coating was observed to be more homogenous in morphology. In contrast, Figure 5-22(b) was synthesized using Al powder of particle size (1-5µm) only, with 0.22wt% AlN as an additive to produce a coating containing 72% AlN, and the coating was seen to be less homogenous. Similarly, Figure 5-22 (c) was synthesized using Al powder of particle size (1-5µm) only, but with 0.11wt% Al_4C_3 as an additive to produce 68% AlN in the coating, which was less homogenous also.

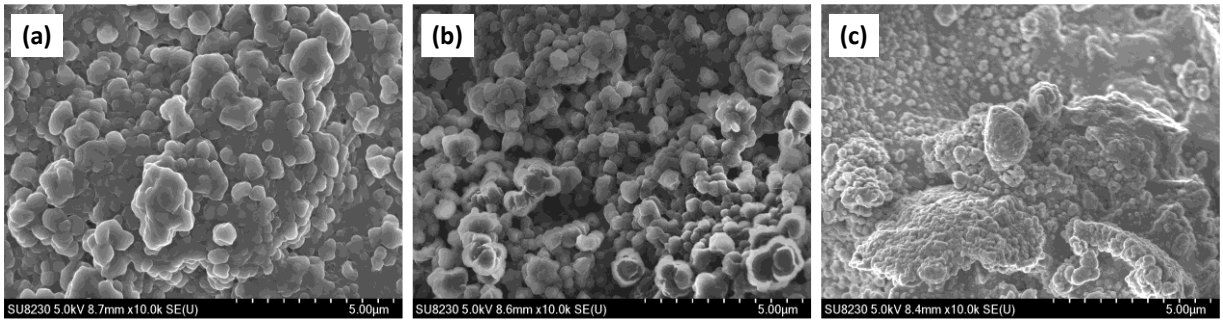

Figure 5-22. SEM images of samples consisting of (a) 82% AlN (b) 72%, and (c) 68% AlN in the coating

5.5.4.2 Hardness test on plasma synthesized coatings

The carbon steel substrate gave a Vickers hardness (Hv) value of 354 Hv, while the coated sample showed a hardness of 1644 Hv, which is related to the constant force of 300 g. This kind of hardness is achieved by 200 loops of deposition by SPS and can be improved by more deposition cycles. Figure 5-23 represents images of the hardness test results for the coated sample containing 80% AlN. The test was repeated three times for each sample and the results are summarized in Table 5-3, indicating that increasing the amount of AlN in the coating enhances the coating hardness.

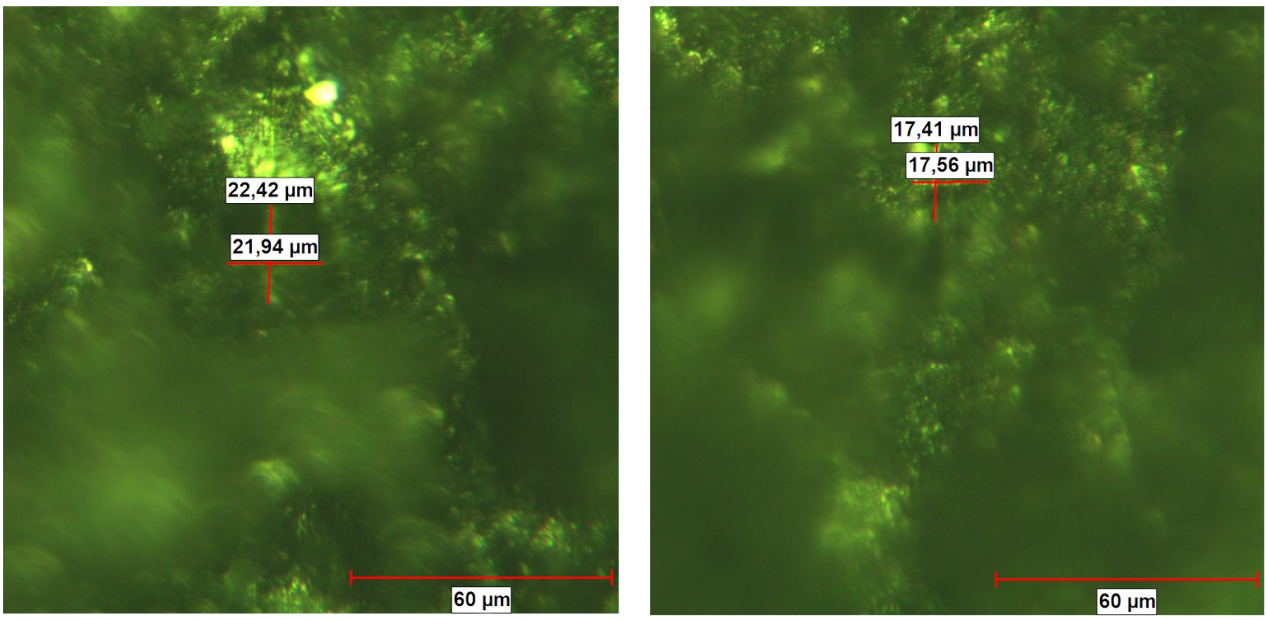

Figure 5-23. Representative image of the hardness test indicating how the “d” value used in Equation 1 was determined

Table 5-3. Summary of the hardness test results on samples containing different percentages of AlN

Sample	Vickers hardness (Hv)			
	Test 1	Test 2	Test 3	Average
Substrate carbon steel (0% AlN)	349	337	376.3	354
Coated carbon steel (10% AlN)	783	731	710	741
Coated carbon steel (40% AlN)	1061	991.3	1146	1066
Coated carbon steel (80% AlN)	1819	1628	1486	1644

5.5.4.3 Optical profilometry of plasma synthesized coatings

The average roughness (Sa) of a surface measures the deviation of a surface from a mean height, with a horizontal line, which runs through the profile representing the arithmetic mean height. The Root Mean Square (RMS) of a surface measures microscopic peaks and valleys. For the plasma-coated sample containing 80% AlN, its Sa value was found to be 1.98 µm with a measurement uncertainty of 0.03, defining the error margin (Kubátová and Melichar, 2018). The RMS surface roughness (Sq) of the same sample was found to be 2.75 µm with a measurement uncertainty of 0.05. These low roughness results were obtained by imaging from the optical profilometer analysis as shown in Figure 5-24. the result of the roughness test with 40% AlN and 80% AlN are summarized in Table 5-4.

Table 5-4. Roughness results of plasma coated substrates

Sample	**Average Roughness Sa (µm)**	**RMS Roughness Sq (µm)**
Coated carbon steel (80% AlN)	1.98 ± 0.03	2.75 ± 0.05
Coated carbon steel (40% AlN)	1.40 ± 0.04	2.10 ± 0.20
Carbon steel substrate	0.50 ± 0.03	0.70 ± 0.05

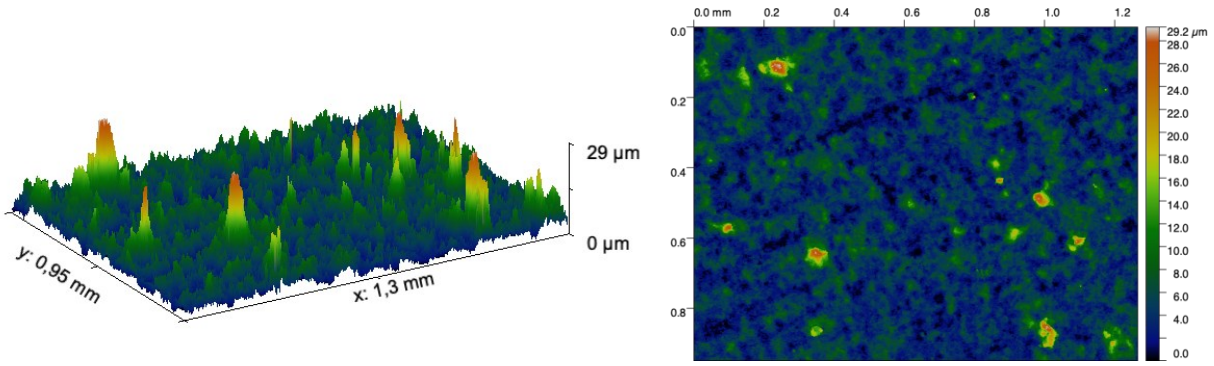

Figure 5-24. Topography of the plasma sprayed coating with 80% AlN

5.6 Conclusions

Modeling by FactSage™ indicated that AlN should remain stable without reacting when in direct contact with molten Al-Mg alloy at the test temperature (1123 K). In addition, modeling the interaction between amorphous Al melt and AlN (100) surface was successfully simulated using ab initio Born-Oppenheimer molecular dynamics (BOMD) at 1200 K. The hypothesis behind BOMD modelling is to use electronic structure calculations to try and understand the chemical structure and reactivity of AlN coating in contact with molten Al alloy. The results showed that at the interface between AlN and molten Al, (i) no reaction occurs, and (ii) there is an epitaxial arrangement of the molten Al atoms taking after the AlN crystal lattice structure. The interfacial energy between the molten Al and AlN coating at 1200 K was calculated to be approximately 18.2 $kJ.mol^{-1}$ for hcp-AlN and 56.4 $kJ.mol^{-1}$ for cubic-AlN, normalized per unit cell area, which implies weak van der Waals interactions, with an average Al-N bond length of 1.9 Å. This means that molten Al does not interact strongly with the coating to cause a reaction, while a typical reaction requires energy in the chemisorption regime (200 – 400 $kJ.mol^{-1}$). It has been observed that the surface energetics alone cannot be used to explain thermodynamic processes fully. One of the limitations of BOMD simulation is that very few atoms are used to represent a large heterogeneous system.

In this study, Radio-frequency (RF) Induction Suspension Plasma Spray (SPS) technology has been used to synthesize AlN coatings from a mixture of pure Al powder and melamine ($C_3H_6N_6$) suspended in hexadecane ($C_{16}H_{34}$). The coatings were both produced and deposited in-situ on a Fe-based substrate. Experimental results indicated that there was need to mix finer Al powder

particles with larger ones to prevent particle agglomeration and clogging of the pipes and the probe of the SPS system. In addition, the mixing leads to the smooth delivery of the suspension and improves post-deposition nitridation of Al in plasma. It was observed that the optimum powder combination involved adding 25% of Al powder in the larger size (17–35 μm) to 75% of (1–5 μm) particle size, which improves the coating composition to 80% cubic AlN. However, more of the larger particles result in extensive partial reactions. A large particle prevents nitrogen from diffusing into the core of the Al precursor, due to the short residence time the particle has in plasma. This leads to the nitridation reaction being limited to the surface of the Al particles.

Moreover, it was observed that promoting the reaction between Al powder and melamine in the liquid suspension by use of ceramic and metallic additives in various quantities initiates the in-situ formation and deposition of AlN through SPS. Among them, Mo, BN, Al_4C_3, and AlN present the best results by improving the dispersion of Al while preventing the agglomeration of Al particles both in the precursor suspension and in the deposited coating. Furthermore, using AlN instead of other additives was found to diminish the formation of impurities and by-products in the final coating. The optimum amount of AlN in the precursor was found to be 20% of AlN in Al powder by mass (0.22wt% AlN of the total mass of the suspension), producing up to 72% cubic-AlN in the coating. The plasma sprayed coating with 80% AlN indicated a surface roughness value of 2.75 μm which implies the sample is not very rough. The substrate hardness of 354 Hv, but gradual addition of AlN in the coating enhanced the coating hardness to 1644 Hv. SEM imaging confirmed that the SPS-synthesized AlN coatings were both chemically and thermally stable and did not decompose after exposure to molten Al alloy. Therefore, the experimental results validated the findings of modelling about corrosion resistant of AlN in contact with molten Al.

CHAPTER 6 CONCLUSION

6.1 Conclusion in English

The aluminum industry is a $147.2 billion market in 2018 in the world owing to the numerous applications of Al and Al alloys. However, corrosion of refractories that are in direct contact with molten Al or its alloys has remained as one of the main concerns of this industry with significant economic and environmental implications. The corrosion of refractories causes contaminations of the final Al products and shortens the lifespan of the refractories. The reviewed literature suggests two approaches to overcome this issue: a) the addition of non-wetting additives (NWAs) to refractories' composition and b) deposition of the coating on the refractories' surface. Although NWAs have their advantages in the protection of refractories, this approach is not cost-effective because the industry has to replace big bulk of refractories when corrosion occurs. This leads to a loss of time when the production line is stopped to replace the refractories and disposal problems with damaged refractories. Whereas coatings are effectively used as either thin or thick films of expensive coatings on cheaper bulk material. Furthermore, degraded portions of coatings are easy to repair, save energy, time, and increase the lifespan of refractories which helps to preserve the environment.

In the first part of the thesis (first paper in the thesis), an experimental investigation of the impact of several i.e., $BaSO_4$, CaF_2, Secar®71 cement, and wollastonite non-wetting agents (NWA) on the corrosion resistance of the white fused mullite (WFM) refractory was studied. The results showed that cracks formed in samples promoted with only $BaSO_4$, CaF_2, Secar®71 cement, or wollastonite. However, in samples promoted with both CaF_2 (1-wt%) and $BaSO_4$ (1-wt%), cracks did not appear because of improved anti-wetting properties. A combination of CaF_2 and $BaSO_4$ seems to partially inhibit spinel formation, which is the major cause of cracking.

Following physio-chemical characteristics and corrosion resistance analyses using FactSage, the synthesis and deposition of cubic AlN on Ti, Mo, and carbon steel substrates using SPS technology was pursued in the second part of the thesis. The second article details the analysis of the effect of the nitriding agent, the suspension liquid carrier, the substrate materials, and the standoff distance on the AlN formation. The results show higher AlN content in the coatings deposited on a carbon steel substrate (~82%) using melamine as a nitriding agent suspended in

hexadecane. After exposing the coatings to a molten Al-Mg alloy at 850 °C, an improvement was observed in their corrosion resistance when compared to the uncoated substrates. In the third article of the thesis, the effects of Al particle size, as well as promotional additives on formation of AlN, were investigated. The results show that the best AlN coating formulation was produced using Al powder with 3:1 particle size ratio between (-5+1µm) (-35+17µm) mixed with melamine suspended in hexadecane. Phase quantification (RQA) by XRD analysis indicated that the coating consisted of 82% AlN (80% cubic phase and 2% hexagonal AlN). Promotional additives such as B, BN, Mo, Y_2O_3, AlN, or Al_4C_3 enhanced the formation of AlN with a cubic crystal lattice. The optimum amount of AlN additive was found to be 0.22-wt% of the total suspension mass, producing up to 72% AlN in the coating.

The article also discussed the experimental analysis of corrosion resistance of the plasma synthesized AlN coating by direct contact with molten Al-5wt%Mg alloy at 1123 K. The results indicated that AlN remained stable before and after the test as observed through microscopic (optical and SEM) imaging. The findings of the experimental work were further validated by modeling of the Al-Mg alloy and AlN reaction using FactSage™ thermochemical software where the results show that at thermodynamic equilibrium no reaction occurs between pure AlN and a molten Al-Mg alloy at the test temperature of 1123 K (850 ºC). Furthermore, the simulation of the interaction between pure AlN coating and molten Al using *ab initio* Born-Oppenheimer molecular dynamics (BOMD) at 1200 K showed weak van der Waals interaction, with an $AlN_{(s)}$–$Al_{(l)}$ interfacial energy of 18.2 kJ.mol^{-1} for the hexagonal (hcp) AlN phase and 56.4 kJ.mol^{-1} for the cubic (c-AlN phase). Low interaction energy means that it lies within the physisorption regime, and therefore, no reaction occurs between molten Al and solid AlN (chemisorption requires an energy of 200–400 kJ.mol^{-1}).

Although the optimum parameters setup yielded the formation of 82% AlN, the following future research directions may potentially improve the coating purity:

- Installing a graphite tube in the exit of the plasma torch to increase residence time and keep the reaction temperature high to enhance interaction between species,
- Improving the quantity of reactive species in the plasma jet using different Al and N sources

- Controlling coating microstructure by adding hierarchical roughness to the structure to enhance non-wettability and subsequent corrosion resistance of the produced coatings
- Develop experimental system to deposit AlN coatings on large-size substrates and adapt the process to DC torches
- Doing modeling for interaction between cubic rock-salt AlN and Al-Mg alloy
- Using OES to monitor the temperature gradient in plasma, and formed active gases and species during the experiment
- Applying the AlN coating on ceramic refractories used in the Al industry such as mullite, high alumina refractories, and fused silica substrates is of paramount importance!!.

Among the abovementioned, the latter is the most challenging part due to the low thermal conductivity and poor thermal shock resistance of the ceramics. When the ceramic substrates such as aluminosilicate refractories are exposed to the hot temperature of the plasma, the severe thermal shocks induce cracks. Therefore, AlN coatings sprayed on a ceramic substrate is a potential subject worth of consideration.

6.2 Conclusion en français

L'industrie de l'aluminium représente un marché de 147,2 milliards de dollars en 2018 dans le monde en raison des nombreuses applications de l'aluminium et de ses alliages. Cependant, la corrosion des réfractaires qui sont en contact direct avec l'Al fondu ou ses alliages est restée l'une des principales préoccupations de cette industrie avec des implications économiques et environnementales importantes. La corrosion des réfractaires provoque des contaminations du produit final d'Al et une durée de vie raccourcie des réfractaires en raison de la dégradation. La littérature examinée suggère deux approches pour surmonter ce problème : a) l'ajout d'additifs non mouillants (NWA) à la composition des réfractaires et b) le dépôt du revêtement sur la surface des réfractaires. Bien que les NWA aient leurs avantages dans la protection des réfractaires, cette approche n'est pas rentable car l'industrie doit remplacer une grande partie des réfractaires lorsque la corrosion se produit. Ceci entraîne une perte de temps lorsque la ligne de production est arrêtée pour remplacer les réfractaires et des problèmes d'élimination des réfractaires endommagés. Alors que les revêtements sont effectivement utilisés sous forme de films minces ou épais de revêtements coûteux sur des matériaux de base moins chers. De plus, les parties dégradées des revêtements sont faciles à réparer, économisent de l'énergie, du temps et augmentent la durée de vie des réfractaires, ce qui contribue à préserver l'environnement.

Dans la première partie de la thèse (premier article de la thèse), une étude expérimentale de l'impact de plusieurs agents non mouillants (NWA) tels que le $BaSO_4$, le CaF_2, le ciment Secar®71 et la wollastonite (NWA) sur la résistance à la corrosion du réfractaire incluant de la mullite fondue (WFM) a été étudié. Les résultats ont montré que les fissures formées dans les échantillons étaient favorisées en utilisant uniquement du ciment avec $BaSO_4$, CaF_2, Secar®71 ou de la wollastonite. Cependant, dans les échantillons promus à l avec CaF_2 (1 % en poids) et BaSO4 (1 % en poids), aucune fissure n'est apparue en raison des propriétés anti-mouillantes améliorées. Une combinaison de CaF_2 et de $BaSO_4$ semble inhiber partiellement la formation de spinelle, qui est la principale cause de fissuration.

Après des analyses de caractéristiques physico-chimiques et de résistance à la corrosion à l'aide de FactSage, la synthèse et le dépôt d'AlN cubique sur des substrats de Ti, Mo et d'acier au carbone en utilisant la technologie SPS ont été poursuivis dans la deuxième partie de la thèse. Le deuxième article détaille l'analyse de l'effet de l'agent de nitruration, du support liquide en

suspension, des matériaux du substrat et de la distance de sécurité sur la formation d'AIN. Les résultats montrent une teneur en AlN plus élevée dans les revêtements déposés sur un substrat en acier au carbone (~82 %) en utilisant de la mélamine comme agent de nitruration en suspension dans l'hexadécane. Après avoir exposé les revêtements à un alliage Al-Mg fondu à 850 °C, une amélioration de leur résistance à la corrosion a été observée par rapport aux substrats non revêtus. Dans le troisième article de la thèse, l'effet de la taille des particules d'Al, ainsi que des additifs promotionnels sur la formation d'AlN ont été étudiés. Les résultats montrent que la meilleure formulation de revêtement d'AlN a été produite en utilisant de la poudre d'Al avec un rapport granulométrique de 3:1 entre (-5+1μm) (-35+17μm) mélangé avec de la mélamine en suspension dans de l'hexadécane. La quantification de phase (RQA) par analyse XRD a indiqué que le revêtement était constitué de 82 % d'AIN (80 % de phase cubique et 2 % d'AIN hexagonal). Les additifs promotionnels tels que B, BN, Mo, Y_2O_3, AlN ou Al_4C_3 ont amélioré la formation d'AlN avec un réseau cristallin cubique. La quantité optimale d'additif AIN s'est avérée être de 0,22 % en poids de la masse totale de la suspension, produisant jusqu'à 72 % d'AIN dans le revêtement.

L'article a également discuté de l'analyse expérimentale de la résistance à la corrosion du revêtement d'AlN synthétisé par plasma par contact direct avec un alliage Al-5wt%Mg fondu à 1123 K. Les résultats ont indiqué que l'AlN est resté stable avant et après le test, comme observé au microscope (optique et imagerie SEM). Les résultats des travaux expérimentaux ont ensuite été validés par la modélisation de l'alliage Al-Mg et de la réaction AlN à l'aide du logiciel thermochimique FactSage™ où les résultats montrent qu'à l'équilibre thermodynamique, aucune réaction ne se produit entre l'AlN pur et un alliage Al-Mg fondu à la température d'essai. de 1123 K (850 °C). De plus, la simulation de l'interaction entre le revêtement d'AlN pur et l'Al fondu à l'aide de la dynamique moléculaire de Born-Oppenheimer ab initio (BOMD) à 1200 K a montré une faible interaction de van der Waals, avec une énergie interfaciale AlN(s)–Al(l) de 18,2 kJ.mol-1 pour la phase hexagonale (hcp-AlN) et 56,4 $kJ.mol^{-1}$ pour la phase cubique (c-AlN). Une faible énergie d'interaction signifie qu'elle se situe dans le régime de physisorption et par conséquent, aucune réaction ne se produit entre l'Al fondu et l'AlN solide (la chimisorption nécessite une énergie de 200 à 400 $kJ.mol^{-1}$).

Bien que la configuration optimale des paramètres ait permis la formation de 82 % d'AlN, les futures directions de recherche suivantes pourraient potentiellement améliorer la pureté du revêtement :

• Installation d'un tube en graphite à la sortie de la torche à plasma pour augmenter le temps de séjour et maintenir la température de réaction élevée pour améliorer l'interaction entre les espèces,

• Augmentation de la concentration des espèces réactives dans le plasma

• Contrôle de la microstructure du revêtement en ajoutant une rugosité hiérarchique à la structure pour améliorer la non-mouillabilité et la résistance à la corrosion ultérieure des revêtements produits

• Développer des technologies pour déposer des revêtements d'AlN sur des substrats de grande taille

• Faire de la modélisation pour l'interaction entre l'AlN de structure cubique sel gemme et l'alliage Al-Mg

• Utilisation de l'OES pour surveiller le gradient de température dans le plasma, et les gaz et espèces actifs formés au cours de l'expérience

• L'application du revêtement AlN sur les réfractaires céramiques utilisés dans l'industrie de l'aluminium tels que la mullite, les réfractaires à haute teneur en alumine et les substrats de silice fondue est nécessaire à étudier.

Parmi les éléments mentionnés ci-dessus, ce dernier est la partie la plus difficile en raison de la faible conductivité thermique et de la faible résistance aux chocs thermiques de la céramique. Lorsque les substrats céramiques sont exposés à la température élevée du plasma, ils subissent un choc thermique sévère et des fissures. Par conséquent, le revêtement sur le substrat en céramique est un sujet potentiel qui mérite d'être pris en considération.

REFERENCES

Abdulagatov, A. I. *et al.* (2018) 'Atomic Layer Deposition of Aluminum Nitride Using Tris (diethylamido) aluminum and Hydrazine or Ammonia', *Russian Microelectronics*, 47(2), pp. 118–130. doi: 10.1134/S1063739718020026.

Abkenar, A. P. (2007) *Wire-arc Spraying System: Particle Production, Transport, and Deposition*, *Library and Archives Canada*.

Adabifiroozjaei, E. *et al.* (2015) 'Interfacial reactions between $BaAl_2Si_2O_8$ and molten Al alloy at 850°C', *journal of American ceramic society*, 98(10), pp. 3299–3307. doi: 10.1111/jace.13650.

Adabifiroozjaei, E., Koshy, P. and Sorrell, Charles Chris (2012) 'Effects of different boron compounds on the corrosion resistance of andalusite-based low-cement castables in contact with molten Al alloy', *Metallurgical and materials transactions*, 43(1), pp. 5–13. doi: 10.1007/s11663-011-9619-x.

Adabifiroozjaei, E., Koshy, P. and Sorrell, Charles Christopher (2012) 'Effects of V_2O_5 addition on the corrosion resistance of andalusite-based low-cement castables with molten Al-alloy', *Journal of the European Ceramic Society*, 33(6), pp. 1463–1471. doi: 10.1016/j.jeurceramsoc.2012.11.005.

Adabifiroozjaei, E., Koshy, P. and Sorrell, C. C. (2013) 'Effects of $AlPO_4$ addition on the corrosion resistance of andalusite-based low-cement castables with molten Al-alloy', *Journal of the European Ceramic Society*, 33(6), pp. 1067–1075. doi: 10.1016/j.jeurceramsoc.2012.11.005.

Adabifiroozjaei, E., Koshy, P. and Sorrell, C. C. (2015) 'Assessment of non-wetting materials for use in refractories for aluminium melting furnaces', *Journal of the Australian Ceramic Society*, 51(1), pp. 139–145.

Afshar, S. and Allaire, C. (1996) 'The corrosion of refractories by molten aluminum', *JOM Journal of the Minerals Metals and Materials Society*, pp. 23–27. Available at: https://link.springer.com/article/10.1007%2FBF03222938.

Afshar, S. and Allaire, C. (2000) 'The corrosion of refractory aggregates by molten aluminum', *JOM Journal of the Minerals Metals and Materials Society*, 52(5), pp. 43–46. doi: 10.1007/s11837-000-0034-z.

Afshar, S. and Allaire, C. (2001) 'Furnaces : Improving Low Cement Castables by Non-Wetting Additives', *JOM Journal of the Minerals Metals and Materials Society*, 53(8), pp. 24–27. doi: 10.1007/s11837-001-0130-8.

Afshar, S. and Allaire, C. (2004) 'Protection of aluminosilicate aggregates against corrosion by molten aluminum', *Report*, pp. 1–13. Available at: https://0901.nccdn.net/4_2/000/000/056/7dc/cim-2004-2.pdf.

Afshar, S., Allaire, C. and Dajoux, E. (2004) 'Effects of salts on metal oxidation and refractory corrosion induced by molten aluminum alloys', *43rd Annual Conference of Metallurgists of CIM*, p. 15. Available at: www.d4m.com › soluss › cir › documentaire_ouvrir.

Ageorges, H. *et al.* (1993) 'Synthesis of aluminum nitride in transferred arc plasma furnaces', *Plasma Chemistry and Plasma Processing*, 13(4), pp. 613–632. doi: 10.1007/BF01570134.

Aguilar-Santillan, J. (2008) 'Wetting of Al2O3 by molten aluminum: The influence of $BaSO_4$ additions', *Journal of Nanomaterials*, 2008(l), pp. 1–12. doi: 10.1155/2008/629185.

Ahn, J. *et al.* (2016) 'Synthesis of AlN particles by microwave-assisted urea route', *Applied Mechanics and Materials*, 851, pp. 191–195. doi: 10.4028/www.scientific.net/AMM.851.191.

Ahn, J. *et al.* (2017) 'Synthesis of AlN particles by chemical route for theral interface material', *Advanced materials letters*, 8(9), pp. 939–943. Available at: doi:10.5185/amlett.2017.1666.

Alamdari, H. (2017) 'Aluminium production process: challenges and opportunities', *Metals*, 7(4), pp. 5–7. doi: 10.3390/met7040133.

Allahverdi, M., Afshar, S. and Allaire, C. (1996) 'Corrosion resistance of aluminosilicate ceramics to molten Al-5%Mg alloy', in *Advances in Refractories for the Metallurgical Industries II*, pp. 295–303.

Allahverdi, M., Afshar, S. and C.Allaire (1998) 'Additives and the corrosion resistance of aluminosilicate refractories in molten Al-5Mg', *JOM Journal of the Minerals Metals and Materials Society*, pp. 30–34. Available at: https://doi.org/10.1007/s11837-998-0245-2.

Allaire, C. (2000a) 'Mechanisms of corundum growth in refractories ecposed to Al-Mg alloys', *Aluminum Transactions*, 3(1), pp. 105–120. Available at: http://www.cirlaboratory.com/publications/aluminum trans-2000.pdf.

Allaire, C. (2000b) 'Refractories for metal aluminum confinement', *J. Can. Ceram. Soc.*, 69(1), pp. 14–20.

Allaire, C. (2001) 'Interfacial phenomena', in *Fundamentals of Refractory Technology,*. Am. Ceram. Soc., pp. 289–307.

Allaire, C. (no date) 'Refractories for the Lining of Holding and Melting Furnaces.pdf'.

Allaire, C. and Guermazi, M. (1999) *Protecting refractories against corundum growth in aluminum treatment furnaces*. Available at: https://0901.nccdn.net/4_2/000/000/038/2d3/tms-2000_d884_v1.pdf.

Alsaad, A. M. *et al.* (2020) 'Measurement and ab initio Investigation of Structural, Electronic, Optical, and Mechanical Properties of Sputtered Aluminum Nitride Thin Films', *Frontiers in Physics*, 8(May), pp. 1–14. doi: 10.3389/fphy.2020.00115.

Aluminum Association et al. (1984) *Aluminum: properties and physical metallurgy*. Edited by

J. E. Hatch. ASM International.

Amama, P. B. *et al.* (2013) 'Wetting behavior and activity of catalyst supports in carbon nanotube carpet growth', *Nanoscale*, 5(7), pp. 2642–2646. doi: 10.1039/c3nr33634d.

Amin, S. and Panchal, H. (2016) 'A Review on Thermal Spray Coating Processes', *International Journal of Current Trends in Engineering & Research*, 2(4), pp. 556–563. Available at: http://www.ijcter.com.

Amirhossein Pakseresht (2018) *Production, Properties, and Applications of High Temperature Coatings*. IGI Global.

Andersson, J. O. *et al.* (2002) 'Thermo-Calc and DICTRA, Computational tools for materials science', *calphad*, 26, pp. 273–312.

Asadollahi, S. (2017) *Development of an organosilicon-based superhydropobic/ icephobic surface using and atmosperic pressure plasma jet*. Ph.D Thesis, Université du Québec à Chicoutimi.

Ayyagari, A. *et al.* (2018) 'Corrosion, erosion and wear behavior of complex concentrated alloys: A review', *Metals*, 8(8), pp. 1–40. doi: 10.3390/met8080603.

Baba, K., Shohata, N. and Yonezawa, M. (1989) 'Synthesis and properties of ultrafine AlN powder by rf plasma', *Applied Physics Letters*, 54(23), pp. 2309–2311. doi: 10.1063/1.101111.

Bale, C W *et al.* (2016) 'CALPHAD : Computer Coupling of Phase Diagrams and Thermochemistry FactSage thermochemical software and databases , 2010 – 2016', *Calphad*, 54, pp. 35–53. doi: 10.1016/j.calphad.2016.05.002.

Bale, C. W. *et al.* (2016) 'FactSage Thermochemical Software and Databases,2010-2016', *calphad*, 54, pp. 35–53. Available at: www.factsage.com.

Balomens, E. and Panias, D. (2013) 'Iron Recovery and Production of High Added Value Products From the Metallurgical By-Products of Primary Aluminium and', *... -The transition to ...*, (March), pp. 161–172. Available at: http://www.slag-valorisation-symposium.eu/images/papers/s2_4_Panias.pdf.

Barandehfard, F. *et al.* (2020a) 'Improving corrosion resistance of aluminosilicate refractories towards molten Al-Mg alloy using non-wetting additives: A short review', *Materials*, pp. 1–28. doi: 10.3390/ma13184078.

Barandehfard, F. *et al.* (2020b) 'Improving corrosion resistance of aluminosilicate refractories towards molten Al-Mg alloy using non-wetting additives: A short review', *Materials*, 13(18), pp. 1–28. doi: 10.3390/ma13184078.

Barandehfard, F., Aluha, J. and Gitzhofer, F. (2021) 'Synthesis of Cubic Aluminum Nitride (AlN) Coatings Through Suspension Plasma Spray (SPS) Technology', *Coatings*, 11, p. 500. Available at: https://doi.org/10.3390/coatings11050500.

Barbieri, L. (2007) *Wetting properties of flat-top periodically structured superhydrophobic surfaces*, *Techniques*. PhD Thesis, École polytechnique fédérale de Lausanne (EPFL).

Baseden, K. A. and Tye, J. W. (2014) 'Introduction to density functional theory: Calculations by hand on the helium atom', *Journal of Chemical Education*, 91(12), pp. 2116–2123. doi: 10.1021/ed5004788.

Belkerk, B. E. *et al.* (2012) 'Structural-dependent thermal conductivity of aluminium nitride produced by reactive direct current magnetron sputtering', *Applied Physics Letters*, 101(15), pp. 1–5. doi: 10.1063/1.4757298.

Belkerk, B. E. *et al.* (2014) 'Substrate-dependent thermal conductivity of aluminum nitride thin-films processed at low temperature', *Applied Physics Letters*, 105(22). doi: 10.1063/1.4903220.

Bocardo, J. C. E. and Torres, J. T. (2010) 'The effect of $SrSO_4$ and $BaSO_4$ on the corrosion and wetting by molten aluminum alloys of mullite ceramics', *Ceramics International*, 36, pp. 1205–1210. doi: 10.1016/j.ceramint.2010.01.015.

Bolelli, G. *et al.* (2006) 'Plasma-sprayed graded ceramic coatings on refractory materials for improved chemical resistance', *Journal of the European Ceramic Society*, 26(13), pp. 2561–2579. doi: 10.1016/j.jeurceramsoc.2005.07.066.

Bonadia, P. *et al.* (2006) 'Refractory selection for long-distance molten-aluminum delivery', *American Ceramic Society Bulletin*, 85(8), pp. 9301–9309. Available at: http://ceramics.org/wp-content/bulletin/2006_pdf_files/Bonadia_Pando.pdf.

Bonner, S. J. (2015) *A microstructural and kinetic study of molten aluminium oxidation in relation to dross formation*. Ph.D Thesis, The university of Queensland.

Bormashenko, E. (2015) 'Progress in understanding wetting transitions on rough surfaces', *Advances in Colloid and Interface Science*, 222, pp. 92–103. doi: 10.1016/j.cis.2014.02.009.

Bormashenko, E. and Grynyov, R. (2012) 'Plasma treatment induced wetting transitions on biological tissue (pigeon feathers)', *Colloids and Surfaces B: Biointerfaces*, 92, pp. 367–371. doi: 10.1016/j.colsurfb.2011.11.053.

Boulos, M. I. (1992) 'RF induction plasma spraying: State-of-the-art review', *Journal of Thermal Spray Technology*, 1(1), pp. 33–40. doi: 10.1007/BF02657015.

Brauer, G. (1938) 'Naturewissenschaften', 26, p. 710.

Bretterbauer, K. and Schwarzinger, C. (2012) 'Melamine derivatives - A review on synthesis and application', *Current Organic Synthesis*, 9(3), pp. 342–356. doi: 10.2174/157017912801270612.

Brondyke, K. J. (1953) 'Effect of molten aluminum on alumina-silica refractories', *The American Ceramic Society*, 56(5), pp. 171–174. Available at: https://doi.org/10.1111/j.1151-2916.1953.tb12860.x.

Büchel, G. *et al.* (1980) 'Bonite – A new raw material alternative for refractory innovations', 6, pp. 2–7.

Cai, W. X. *et al.* (2002) 'Fabrication of AlN thin films on different substrates at ambient temperature', *Superconductor Science and Technology*, 15(12), pp. 1781–1783. doi: 10.1088/0953-2048/15/12/333.

Cai, Y. *et al.* (2016) 'Superhydrophobic ceramic coatings by solution precursor plasma spray', *Scientific Reports*, 6, pp. 1–7. doi: 10.1038/srep24670.

Cao, J., Liu, Y. and Ning, X. S. (2018) 'Influence of AlN(0001) surface reconstructions on the wettability of an Al/AlN system: A first-principle study', *Materials*, 11(5), pp. 1–10. doi: 10.3390/ma11050775.

Capuzzi, S. and Timelli, G. (2018) 'Preparation and melting of scrap in aluminum recycling: A review', *Metals*, 8(4). doi: 10.3390/met8040249.

Cassie, A. B. D. and Baxter, S. (1944) 'Wettability of porous surfaces', *Trans. Faraday Soc.*, 40(5), pp. 546–551. Available at: https://doi.org/10.1039/TF9444000546.

Chaundhuri, M. G. (2016) 'Feasibility study of synthesis of nanostructured aluminum nitride through sol-gel route', *Int. J. Eng. Res. Appl.*, 6(4), pp. 20–22.

Chen, D. *et al.* (2019) 'High temperature properties of AlN coatings deposited by chemical vapor deposition for solar central receivers', *Surface and Coatings Technology*, 377(July), p. 124872. doi: 10.1016/j.surfcoat.2019.07.083.

Chen, W. *et al.* (1999) 'Ultrahydrophobic and ultralyophobic surfaces: some comments and examples', *Langmuir*, 15(10), pp. 3395–3399. doi: 10.1021/la990074s.

Cheng, H. *et al.* (2003) 'AlN films deposited under various nitrogen concentrations by RF reactive sputtering', *Journal of Crystal Growth*, 254(1–2), pp. 46–54. doi: 10.1016/S0022-0248(03)01176-X.

Cheng, W. J. and Wang, C. J. (2009) 'Growth of intermetallic layer in the aluminide mild steel during hot-dipping', *Surface and Coatings Technology*, 204(6–7), pp. 824–828. doi: 10.1016/j.surfcoat.2009.09.061.

Choudhary, R. K. *et al.* (2015) 'Mechanical and tribological properties of crystalline aluminum nitride coatings deposited on stainless steel by magnetron sputtering', *Journal of Nuclear Materials*, 466, pp. 69–79. doi: 10.1016/j.jnucmat.2015.07.036.

Choudhary, R. K., Mishra, P. and Hubli, R. C. (2016) 'Optical properties of cubic AlN films grown by sputtering', *Surface Engineering*, 32(4), pp. 304–306. doi: 10.1179/1743294414Y.0000000399.

Cobden, R. and Banbury, A. (1994) 'Aluminium: Physical properties, characteristics and alloys', in *TALAT lecture 1501*. European Aluminium Association, p. 60. doi: 1994.

Da Cruz, A. C. and Munz, R. J. (1999) 'Review on the vapour-phase synthesis of aluminum nitride powder using thermal plasmas', *KONA Powder and Particle Journal*, 17, pp. 85–94. doi: 10.14356/kona.1999015.

Dallaev, R. *et al.* (2020) 'Aluminum nitride nanofilms by atomic layer deposition using alternative precursors hydrazinium chloride and triisobutylaluminum', *Coatings*, 10, p. 195. Available at: doi:10.3390/coatings10100954.

'Dassault Systèmes BIOVIA. Materials Studio.' (2019).

Davies, R., Dinsdale, A. and Gisby, J. (2002) 'MTDATA - Thermodynamic and Phase Equilibrium Software from the National Physical Laboratory', *calphad*, 26, pp. 229–271.

Davis, J. R. (2001) 'Aluminum and aluminum alloys', in *Alloying: Understanding the Basics*, pp. 351–416. doi: 10.1361/autb2001p351.

Decker, J. (2011) 'Phosphate bonded monolithic refractory materials with improved hot strengths as a potential replacement for phosphate bonded bricks', *Materials Science Forum*, 693, pp. 90–103. doi: 10.4028/www.scientific.net/MSF.693.90.

Dutta, G., Apujani, P. and Gupta, N. (2016) 'An introduction to the aluminum industry and survey of or applications in an integrated aluminum', *Indian institute of management Ahmedabad*, p. 31. Available at: http://www.esocialsciences.org/Download/repecDownload.aspx?fname=A2016719142839_53.pdf&fcategory=Articles&AId=11097&fref=repec.

Elagin, A. A. *et al.* (2013a) 'Aluminum nitride. Preparation methods', *Refractories and Industrial Ceramics*, 54(1), pp. 44–50. doi: 10.1007/s11148-013-9546-2.

Elagin, A. A. *et al.* (2013b) 'Aluminum nitride. Preparation methods (Review)', *Refractories and Industrial Ceramics*, 53(6), pp. 395–403. doi: 10.1007/s11148-013-9534-6.

Elliott, R. (1988) 'Liquid metal preparation', in *Cast Iron Technology*. Butterworth-Heinemann, pp. 46–90. doi: https://doi.org/10.1016/B978-0-408-01512-7.50005-7.

Engel, R. (2015) 'Refractory considerations for aluminum melting and holding furnaces', *The refractories engineer*, pp. 22–25. Available at: http://www.refractoryexpert.com/Publications_files/RefracConsid.pdf.

Engineering ToolBox (2003) *Coefficients of Linear Thermal Expansion*.

Engineering ToolBox (2005) *Thermal conductivity of common metals, metallic elements and Alloys*. Available at: https://www.engineeringtoolbox.com/thermal-conductivity-metals-d_858.html (Accessed: 31 March 2021).

Eustathopoulos, N. (2015) 'Wetting by Liquid Metals—Application in Materials Processing: The Contribution of the Grenoble Group', *Metals*, 5(1), pp. 350–370. doi: 10.3390/met5010350.

Farokhzadeh, K. and Edrisy, A. (2017) 'Surface hardening by gas nitriding', *Comprehensive Materials Finishing*, 2–3, pp. 107–136. doi: 10.1016/B978-0-12-803581-8.09163-3.

Fauchais, P., Rat, V., *et al.* (2008) 'Operating parameters for suspension and solution plasma-spray coatings', *Surface and Coatings Technology*, 202(18), pp. 4309–4317. doi: 10.1016/j.surfcoat.2008.04.003.

Fauchais, P., Etchart-Salas, R., *et al.* (2008) 'Parameters controlling liquid plasma spraying: Solutions, sols, or suspensions', *Journal of Thermal Spray Technology*, 17(1), pp. 31–59. doi: 10.1007/s11666-007-9152-2.

Fauchais, P. *et al.* (2015) 'Key Challenges and Opportunities in Suspension and Solution Plasma Spraying', *Plasma Chemistry and Plasma Processing*, 35(3), pp. 511–525. doi: 10.1007/s11090-014-9594-5.

Fauchais, P. L., Heberlein, J. V. R. and Boulos, M. I. (2014) *Thermal Spray Fundamentals*. Boston (MA), USA: Springer. doi: https://doi.org/10.1007/978-0-387-68991-3.

Fauchais, P. and Montavon, G. (2010) 'Latest developments in suspension and liquid precursor thermal spraying', *Journal of Thermal Spray Technology*, 19(1–2), pp. 226–239. doi: 10.1007/s11666-009-9446-7.

Fauchais, P. and Vardelle, A. (2012) 'Solution and Suspension Plasma Spraying of Nanostructure Coatings', *Advanced Plasma Spray Applications*, pp. 149–188. doi: 10.5772/1921.

Fauchais, P., Vardelle, A. and Denoirjean, A. (1997) 'Reactive thermal plasmas: Ultrafine particle synthesis and coating deposition', *Surface and Coatings Technology*, 97(1–3), pp. 66–78. doi: 10.1016/S0257-8972(97)00294-6.

Fauchais, P., Vardelle, A. and Dussoubs, B. (2001) 'Quo Vadis thermal spraying?', *Journal of Thermal Spray Technology*, 10(1), pp. 44–66. doi: 10.1361/105996301770349510.

Fowkes, F. M. (1964) 'Attractive Forces at Interfaces', *Industrial & Engineering Chemistry Research*, 56(12), pp. 40–52. doi: https://doi.org/10.1021/ie50660a008.

Freiberg, B. (2018) 'Nitriding of Aluminum and Its Alloys', *Heat Treating of Nonferrous Alloys*, 4, pp. 302–307. doi: 10.31399/asm.hb.v04e.a0006273.

Fujii, H. and Nakae, H. (1996) 'Equilibrium contact in the magnesium system oxide/aluminium', *Acta Materialia*, 44(9), pp. 3567–3573.

Fujii, H., Nakae, H. and Okada, K. (1993) 'Interfacial reaction wetting in the boron nitride/molten aluminum system', *Acta Metallurgica Et Materialia*, 41(10), pp. 2963–2971. doi: 10.1016/0956-7151(93)90111-5.

Fujji, H., Nakae, H. and Okada, K. (1993) 'Four wetting phases in AlN/Al and AlN composites/Al systems, models of nonreactive, reactive, and composite systems', 24(June), pp.

1391–1397.

Gálvez, M. E. *et al.* (2009) ‘Production of AlN by carbothermal and methanothermal reduction of Al2O3 in a N2 flow using concentrated thermal radiation’, *Industrial and Engineering Chemistry Research*, 48(1), pp. 528–533. doi: 10.1021/ie8011193.

Gao, J., Afshar, S. and Allaire, C. (2004) ‘Corrosion Kinetics of Refractory by Molten Aluminium’, *Light Metals*, pp. 619–622. Available at: http://www.cirlaboratory.com/publications/jom-2000.pdf.

Giannozzi, P. (2009) ‘QUANTUM ESPRESSO: A modular and open-source software project for quantum simulations of materials’, *Journal of Physics Condensed Matter*, 21(39). doi: 10.1088/0953-8984/21/39/395502.

Gitzhofer, F., Bouyer, E. and Boulos, Maher (1997) ‘Suspension Plasma Spray. U.S. Patent 5,609,921, 26’.

Gitzhofer, F., Bouyer, E. and Boulos, MI (1997) ‘Suspension Plasma Spray (SPS)’.

Good, R. J., Chaudhury, M. K. and Oss, C. J. van (1991) ‘Theory of Adhesive Forces Across Interfaces’, in *Fundamentals of Adhesion*. Springer, Boston, MA., pp. 153–154. Available at: https://doi.org/10.1007/978-1-4899-2073-7_4.

Grigoriu, C. *et al.* (2000) ‘Synthesis of nanosized aluminum nitride powders by pulsed laser ablation’, *Journal of the American Ceramic Society*, 83(10), pp. 2631–2633. Available at: https://doi.org/10.1111/j.1151-2916.2000.tb01604.x.

Grimme, S. *et al.* (2010) ‘A consistent and accurate ab initio parametrization of density functional dispersion correction (DFT-D) for the 94 elements H-Pu’, *Journal of Chemical Physics*, 132(15). doi: 10.1063/1.3382344.

Guan, P. *et al.* (2019) ‘Corrosion behavior of Fe-Ni-Al alloy inert anode in cryolite melts’, *Metals*, 9(4), pp. 1–13. doi: 10.3390/met9040399.

Guo, Z., Liu, W. and Su, B. L. (2008) ‘Why so strong for the lotus leaf?’, *Applied Physics Letters*, 93(20), pp. 1–3. doi: 10.1063/1.3036535.

H. M. Rietveld (1969) ‘A profile refinement method for nuclear and magnetic structures’, *journal of Applied crystallography*, 2(2), pp. 65–71.

Haglund, J. *et al.* (1993) ‘No Title’, *Physical Review B - Condensed Matter and Materials Physics*, 48, p. 11685.

Han, S. *et al.* (2004) ‘Aluminum nitride films synthesized by dual ion beam sputtering’, *Journal of Materials Research*, 19(12), pp. 3521–3525. doi: 10.1557/JMR.2004.0451.

Haraldsson, J. and Johansson, M. T. (2018) ‘Review of measures for improved energy e ffi ciency in production-related processes in the aluminium industry – From electrolysis to

recycling', *Renewable and Sustainable Energy Reviews*, 93(May), pp. 525–548. doi: 10.1016/j.rser.2018.05.043.

Harvey, J. *et al.* (2020) 'On the Application of the FactSage Thermochemical', *Processes*, 8(1156), pp. 1–31. doi: 10.3390/pr8091156.

Hemrick, J. G., Headrick, W. L. and Peters, K. M. (2008) 'Development and application of refractory materials for molten aluminum applications', *International Journal of Applied Ceramic Technology*, 5(3), pp. 265–277. doi: 10.1111/j.1744-7402.2008.02213.x.

Hild, F. (2009) *Surface Energy of Plastics*. Available at: https://www.tstar.com/blog/bid/33845/surface-energy-of-plastics.

Hlavac, J. (1982) 'Melting temperatures of refractory oxides: Part I', *Pure and Applied Chemistry*, 54(3), pp. 681–688. doi: 10.1351/pac198961081461.

Hohenberg, P. and W.Kohn (1964) 'Inhomogeneous electron gas', *Physical Review*, 136(1962). Available at: http://users.wfu.edu/natalie/s15phy752/lecturenote/HohenbergPhysRev.136.B864.pdf.

Hou, L. F. *et al.* (2013) 'Erosion process analysis of die-casting inserts for magnesium alloy components', *Engineering Failure Analysis*, 33, pp. 457–464. doi: 10.1016/j.engfailanal.2013.06.018.

Hu, K. *et al.* (2019) 'Boosting electrochemical water splitting: via ternary NiMoCo hybrid nanowire arrays', *Journal of Materials Chemistry A*, 7(5), pp. 2156–2164. doi: 10.1039/c8ta11250a.

Huang, T. C. *et al.* (1990) 'Advances in X-Ray Analysis', 33, p. 295.

Ibarra C, M. N. *et al.* (2015) 'Chemical interaction between Ba-celsian ($BaAl_2Si_2O_8$) and molten aluminum', *Ceramics International*, 42(2), pp. 3491–3496. doi: 10.1016/j.ceramint.2015.10.152.

Ibarra Castro, M. N. *et al.* (2010) 'The effect of $SrSO_4$ and $BaSO_4$ on the corrosion and wetting by molten aluminum alloys of mullite ceramics', *Ceramics International*, 36(4), pp. 1205–1210. doi: 10.1016/j.ceramint.2010.01.015.

Iizuka, T. and Ouyang, Q. (2014) 'Microstructures and mechanical properties of $MgAl_2O_4$ particle-reinforced AC4C aluminum composites', *Transactions of Nonferrous Metals Society of China*, 24(7), pp. 2337–2345. doi: 10.1016/S1003-6326(14)63354-9.

Iqbal, A. and Mohd-Yasin, F. (2018) 'Reactive sputtering of aluminum nitride (002) thin films for piezoelectric applications: A review', *Sensors (Switzerland)*, 18(6), pp. 1–21. doi: 10.3390/s18061797.

Ishino, C. and Okumura, K. (2008) 'Wetting transitions on textured hydrophilic surfaces', *The European physical journal*, 25, pp. 415–424. doi: 10.1140/epje/i2007-10308-y.

Ishino, C., Okumura, K. and Quéré, D. (2004) 'Wetting transitions on rough surfaces', *EUROPHYSICS LETTERS*, 68(3), pp. 419–425. doi: 10.1209/epl/i2004-10206-6.

Iwata, M. *et al.* (2004) 'Synthesis of purified AlN nano powder by transferred type arc plasma', *Journal of Physics D: Applied Physics*, 37(7), pp. 1041–1047. doi: 10.1088/0022-3727/37/7/014.

Jackson, T. B. *et al.* (1997) 'High-thermal-conductivity aluminum nitride ceramics: The effect of thermodynamic, kinetic, and microstructural factors', *journal of American ceramic society*, 80(6), pp. 1421–1435. doi: 10.2165/00023210-199504010-00001.

Jafari, R., Asadollahi, S. and Farzaneh, M. (2013) 'Applications of plasma technology in development of superhydrophobic surfaces : A review', *Plasma Chemistry and Plasma Processing*, 33(1), pp. 177–200. Available at: https://doi.org/10.1007/s11090-012-9413-9.

Jakovics, A. *et al.* (2002) 'Influence of melt flow and temperature on erosion of refractory and deposit formation in aluminium melting furnaces', *Energy Conversion and Management*, 43(3), pp. 345–352. doi: 10.1016/S0196-8904(01)00113-3.

Jin, W. *et al.* (2018) 'First principles calculations of interfacial properties and electronic structure of the AlN(0 0 0 1)/Ti(0 0 0 1) interface', *Chemical Physics Letters*, 713(October), pp. 153–159. doi: 10.1016/j.cplett.2018.10.034.

Johnson, R. E. (1964) 'Contact angle hysteresis II. contact angle measurements on rough surfaces', in *Contact Angle, Wettability, and Adhesion*, pp. 136–144. Available at: https://doi.org/10.1021/ba-1964-0043.ch008.

Joshi and Nylen (2019) 'Advanced Coatings by Thermal Spray Processes', *Technologies*, 7(4), p. 79. doi: 10.3390/technologies7040079.

Jung, I. H. and Van Ende, M. A. (2020) 'Computational Thermodynamic Calculations: FactSage from CALPHAD Thermodynamic Database to Virtual Process Simulation', *Metallurgical and Materials Transactions B: Process Metallurgy and Materials Processing Science*, 51(5), pp. 1851–1874. doi: 10.1007/s11663-020-01908-7.

Jung, W. S. and Ahn, S. K. (2000) 'Synthesis of aluminium nitride by the reaction of aluminium sulfide with ammonia', *Materials Letters*, 43(1), pp. 53–56. doi: 10.1016/S0167-577X(99)00229-3.

Karthikeyan, J. (2018) 'Cold Spray Process', *Thermal Spray Technology*, 5, pp. 54–59. doi: 10.31399/asm.hb.v05a.a0005714.

Kassner, H. *et al.* (2008) 'Application of suspension plasma spraying (SPS) for manufacture of ceramic coatings', *Journal of Thermal Spray Technology*, 17(1), pp. 115–123. doi: 10.1007/s11666-007-9144-2.

Kato, T. and Sugawara, K. (2019) 'Low-Temperature Synthesis of Aluminum Nitride by Addition of Ammonium Chloride', *ACS Omega*, 4(12), pp. 14714–14720. doi:

10.1021/acsomega.9b01140.

Kaupuzs, J. *et al.* (2003) 'Influence of melt flow and temperature on erosion of refractory and deposit formation in induction furnaces', in *International Scientific Colloquium*, pp. 279–284. doi: 10.1016/S0196-8904(01)00113-3.

Kazemi, N. (2019) 'Reasons for crack propagation and strength loss in refractory castables based on changes in their chemical compositions and micromorphologies with heating: special focus on the large blocks', *Journal of Asian Ceramic Societies*, 7(2), pp. 109–126. doi: 10.1080/21870764.2019.1597957.

Ke, P. L. *et al.* (2005) 'Study on thermal barrier coatings deposited by detonation gun spraying', *Surface and Coatings Technology*, 200(7), pp. 2271–2276. doi: 10.1016/j.surfcoat.2004.07.107.

Kessman, A. J. *et al.* (2009) 'Zirconia sol-gel coatings on alumina-silica refractory material for improved corrosion resistance', *Surface and Coatings Technology*, 204(4), pp. 477–483. doi: 10.1016/j.surfcoat.2009.08.024.

Kim, H.-H. *et al.* (2017) 'Studies on preparation and characterization of aluminum nitride-coated carbon fibers and thermal conductivity of epoxy matrix composites', *Coatings*, 7(8). doi: 10.3390/coatings7080121.

Kim, J. *et al.* (2015) 'Growth and characterization of high quality AlN using combined structure of low temperature buffer and superlattices for applications in the deep ultraviolet', *Japanese Journal of Applied Physics*, 54(8). doi: 10.7567/JJAP.54.081001.

Kim, K.-I., Choi, S.-C., Kim, J.-H., *et al.* (2014) 'Synthesis and characterization of high-purity aluminum nitride nanopowder by RF induction thermal plasma', *Ceramics International*, 40(6), pp. 8117–8123. doi: 10.1016/j.ceramint.2014.01.006.

Kim, K.-I., Choi, S.-C., Han, K.-S., *et al.* (2014) 'Synthesis of high purity aluminum nitride nanopowder in ammonia and nitrogen atmosphere by RF induction thermal plasma', *Journal of the Korean Ceramic Society*, 51(3), pp. 201–207. doi: 10.4191/kcers.2014.51.3.201.

Kim, K. (2005) 'Plasma synthesis and characterization of nanocrystalline aluminum nitride particles by aluminum plasma jet discharge', *Journal of Crystal Growth*, 283(3–4), pp. 540–546. doi: 10.1016/j.jcrysgro.2005.06.018.

Kim, T.-H., Choi, S. and Park, D.-W. (2013) 'Effects of NH3 flow rate on the thermal plasma synthesis of AlN nanoparticles', *Journal of the Korean Physical Society*, 63(10), pp. 1864–1870. doi: 10.3938/jkps.63.1864.

Kim, T., Choi, S. and Park, D. (2011) 'Chemical Reaction Considered Numerical Simulation on Preparation of AlN Nano Powder by Non-transferred Thermal Plasma', *Ispc_20*, (November 2014), pp. 3–6.

Kitamura, J. *et al.* (2011) 'Structural, mechanical and erosion properties of yttrium oxide coatings by axial suspension plasma spraying for electronics applications', *Journal of Thermal*

Spray Technology, 20(1–2), pp. 170–185. doi: 10.1007/s11666-010-9585-x.

Kolaklieva, L. *et al.* (2019) 'Pulsed laser deposition of aluminum nitride films: Correlation between mechanical, optical, and structural properties', *Coatings*, 9(3). doi: 10.3390/COATINGS9030195.

Koshy, P. (2009) *Effect of chemical additives on the interfacial phenomena of high alumina refractories with Al-alloys*, *Faculty of Science. School of Materials Science and Engineering*. PhD Thesis, University of New South Wales.

Koshy, P. *et al.* (2011) 'Effect of $BaSO_4$ on the interfacial phenomena of high-alumina refractories with Al-alloy', *Journal of Materials Science*, 46(2), pp. 468–478. doi: 10.1007/s10853-010-4931-4.

Kozeschnik, E. *et al.* (2004) 'Modelling of kinetics in multi-component multi-phase systems with spherical precipitates II: Numerical solution and application', *Materials Science and Engineering A*, 385(1–2), pp. 157–165. doi: 10.1016/j.msea.2004.06.016.

Kubátová, D. and Melichar, M. (2018) 'Uncertainty of surface measurement', *Annals of DAAAM and Proceedings of the International DAAAM Symposium*, 29(1), pp. 1239–1248. doi: 10.2507/29th.daaam.proceedings.179.

Kubiak, K. J. and Mathia, T. G. (2014) 'Anisotropic wetting of hydrophobic and hydrophilic surfaces-modelling by Lattice Boltzmann method', *Procedia Engineering*, 79, pp. 45–48. doi: 10.1016/j.proeng.2014.06.307.

Kudyakova, V. S. *et al.* (2017) 'Aluminium nitride cubic modifications synthesis methods and its features. Review', *Journal of the European Ceramic Society*, 37, pp. 1143–1156. doi: 10.1016/j.jeurceramsoc.2016.11.051.

Kühne, T. D. *et al.* (2007) 'Efficient and accurate car-parrinello-like approach to born-oppenheimer molecular dynamics', *Physical Review Letters*, 98(6), pp. 1–4. doi: 10.1103/PhysRevLett.98.066401.

Kumar, S., Handa, A. and Kumar, R. (2019) 'Overview of Wire Arc Spray Process : A Review', *journal of composition theory*, XII(Vii), pp. 900–907. Available at: http://jctjournal.com/gallery/106-july2019.pdf.

Latthe, S. S. *et al.* (2014) 'Superhydrophobic surfaces developed by mimicking hierarchical surface morphology of lotus leaf', pp. 4256–4283. doi: 10.3390/molecules19044256.

Lee, W. E. and Zhang, S. (1999) 'Melt corrosion of oxide and oxide–carbon refractories', *International Materials Reviews*, 44(3), pp. 77–104. doi: 10.1179/095066099101528234.

Lejaeghere, K. (2016) 'Reproducibility in density functional theory calculations of solids', *Science*, 351(6280). doi: 10.1126/science.aad3000.

Li, B. *et al.* (2021) 'Corrosion behaviour and related mechanism of lithium vapour on aluminium

nitride ceramic', *Corrosion Science*, 178, p. 109058. doi: 10.1016/j.corsci.2020.109058.

Li, C. H. *et al.* (2012) 'Rapid preparation of aluminum nitride powders by using microwave plasma', *Journal of Alloys and Compounds*, 542, pp. 78–84. doi: 10.1016/j.jallcom.2012.07.086.

Li, L. *et al.* (2003) 'Low-temperature solvent thermal synthesis of cubic AlN', *Journal of Crystal Growth*, 258(3–4), pp. 268–271. doi: 10.1016/S0022-0248(03)01553-7.

Li, P., Xi, S. and Zhou, J. (2009) 'Phase transformation and gas-solid reaction of Al_2O_3 during high-energy ball milling in N2 atmosphere', *Ceramics International*, 35(1), pp. 247–251. doi: 10.1016/j.ceramint.2007.10.030.

Lidsay, J. G., Bakker, W. T. and Dewing, E. W. (1964) 'Chemical resistance of refractories to Al and Al-Mg alloys', *Journal of The American Ceramic Society*, 47(2), pp. 90–94. Available at: https://doi.org/10.1111/j.1151-2916.1964.tb15662.x.

Lima, R. S. and Marple, B. R. (2007) 'Thermal spray coatings engineered from nanostructured ceramic agglomerated powders for structural, thermal barrier and biomedical applications: A review', *Journal of Thermal Spray Technology*, 16(1), pp. 40–63. doi: 10.1007/s11666-006-9010-7.

Liu, L. M. *et al.* (2003) 'Adhesion of metal – carbide / nitride interfaces : Al / TiC and Al / TiN Adhesion of metal – carbide / nitride interfaces : Al / TiC and Al / TiN'.

Liu, W., Zhou, D. and Zhao, Z. (2019) 'Progress in Application of Energy-Saving Measures in Aluminum Reduction Cells', *Jom*, 71(7), pp. 2420–2429. doi: 10.1007/s11837-019-03487-8.

Long, G. and Foster, L. M. (1959) 'Aluminum nitride, a refractory for aluminum to 2000 °C', *Journal of the American Chemical Society*, 42(2), pp. 53–59.

Louer, D. (2004) 'No Title', *Chantepie France, private communication*.

Luz, A. P. *et al.* (2011a) 'Thermodynamic evaluation of spinel containing refractory castables corrosion by secondary metallurgy slag', *Ceramics International*, 37(4), pp. 1191–1201. doi: 10.1016/j.ceramint.2010.11.043.

Luz, A. P. *et al.* (2011b) 'Thermodynamic evaluation of spinel containing refractory castables corrosion by secondary metallurgy slag', *Ceramics International*, 37(4), pp. 1191–1201. doi: 10.1016/j.ceramint.2010.11.043.

Luz, A. P., Gomes, D. T. and Pandolfelli, V. C. (2015) 'High-alumina phosphate-bonded refractory castables: Al(OH)3 sources and their effects', *Ceramics International*, 41(7), pp. 9041–9050. doi: 10.1016/j.ceramint.2015.03.276.

Majeed, M. H. (2014) 'Static contact angle and large water droplet thickness measurements with the change of water temperature', *College of Engineering Journal (NUCEJ)*, 1717(11), pp. 114–128.

Mao, X.-X. *et al.* (2017) 'Synthesis of AlN Powder by Carbothermal Reduction-nitridation of Alumina/Carbon Black Foam', *Journal of cermic society of Japan*, 32(10). doi: 10.15541/jim20170067.

Marzari, N., Vanderbilt, D. and Payne, M. C. (1997) 'Ensemble density-functional theory for ab initio molecular dynamics of metals and finite-temperature insulators', *Physical Review Letters*, 79(7), pp. 1337–1340. doi: 10.1103/PhysRevLett.79.1337.

Mashimo, T. *et al.* (1999) 'Yield properties, phase transition, and equation of state of aluminum nitride (AIN) under shock compression up to 150 GPa', *Journal of Applied Physics*, 86(12), pp. 6710–6716. doi: 10.1063/1.371749.

Mayer, I. and Schneider, S. (1988) 'ICDD Grant-in-Aid'.

Mazur, M. M. *et al.* (2015) 'Deposition and characterization of AlN thin films on ceramic electric insulators using pulsed DC magnetron sputtering', *Surface and Coatings Technology*, 284, pp. 247–251. doi: 10.1016/j.surfcoat.2015.06.082.

Metel, A. *et al.* (2020) 'Synthesis of aluminum nitride coatings assisted by fast argon atoms in a magnetron sputtering system with a separate input of argon and nitrogen', *Surface and Coatings Technology*, 398(April), p. 126078. doi: 10.1016/j.surfcoat.2020.126078.

Modi, T. and Properties, S. (2016) 'Influence of Thermal Modification on Surface Properties and Chemical Composition of Beech Wood (Fagus sylvatica L .) Utjecaj toplinske modifikacije na površinska svojstva i kemijski sastav bukovine (Fagus', 67(1), pp. 65–71. doi: 10.5552/drind.2016.1520.

Mouradoff, L. *et al.* (1994) 'Study of the interaction between liquid aluminum and silicon nitride', *Journal of the European Ceramic Society*, 13, pp. 323–328. doi: 10.1016/0955-2219(94)90006-X.

Munoz, V., Camelli, S. and Martinez, T. (2017) 'Slag corrosion of alumina-magnesia-carbon refractory bricks: Experimental data and thermodynamic simulation', *Ceramics International*, 43(5), pp. 4562–4569. doi: 10.1016/j.ceramint.2016.12.114.

Musa, I. *et al.* (2020) 'Fabrication and characterization of aluminum nitride nanoparticles by RF magnetron sputtering and inert gas condensation technique', *Coatings*, 10(4), p. 411'. doi: 10.3390/coatings10040411.

Mutale, C. T., Weirauch, D. A. and Cramb, A. W. (2008) 'Determination of interfacial properties between AlN and aluminum beneath salt at high temperature', *Materials Science and Engineering A*, 495(1–2), pp. 60–64. doi: 10.1016/j.msea.2007.10.106.

Muz, İ., Kurban, H. and Kurban, M. (2021) 'A DFT study on stability and electronic structure of AlN nanotubes', *Materials Today Communications*, 26(February). doi: 10.1016/j.mtcomm.2021.102118.

Nagasaka, M. *et al.* (2015) 'Corrosion resistance of Y2Ti2O7 coating on molten aluminum

filter', *Zairyo to Kankyo/ Corrosion Engineering*, 64(6), pp. 240–243. doi: 10.3323/jcorr.64.240.

Nandy, R. N. and Jogai, R. K. (2013) 'Selection of proper refractory materials for energy saving in aluminium melting and holding furnaces', *International Journal of Metallurgical Engineering*, 1(6), pp. 117–121. doi: 10.5923/j.ijmee.20120106.04.

Nguyen, S. T. *et al.* (2015) 'Synthesis of molten-metal corrosion resistant yttria-based refractory by hot-pressing and densification', *Journal of the European Ceramic Society*, 35(9), pp. 2651–2662. doi: 10.1016/j.jeurceramsoc.2015.02.023.

Nogi, K. *et al.* (2004) 'Wettability of solid by liquid at high temperature, Report No. 2001MB037'.

Ntakaburimvo, N. and Allaire, C. (2004) 'Abrasion wear of aluminosilicate refractories', *Report*, pp. 1–16. Available at: http://www.d4m.com/soluss/cir/web/document/cim-2004-1.pdf.

Nwaogu, U. C. and Tiedje, N. S. (2011) 'Foundry coating technology: A review', *Materials Sciences and Applications*, 02(08), pp. 1143–1160. doi: 10.4236/msa.2011.28155.

Obaidat, M. *et al.* (2018) 'Energy and exergy analyses of different aluminum reduction technologies', *Sustainability (Switzerland)*, 10(4), pp. 1–21. doi: 10.3390/su10041216.

Oh, S. M. and Park, D. W. (1998) 'Preparation of AlN fine powder by thermal plasma processing', *Thin Solid Films*, 316(1–2), pp. 189–194. doi: 10.1016/S0040-6090(98)00413-1.

Oksa, M. *et al.* (2011) 'Optimization and characterization of high velocity oxy-fuel sprayed coatings: Techniques, materials, and applications', *Coatings*, 1(1), pp. 17–52. doi: 10.3390/coatings1010017.

Ortiz-Covarrubias, K. E. *et al.* (2015) 'Synthesis of $Al_6Si_2O_{13}$-$BaAl_2Si_2O_8$-ZrO_2-based composites and their wettability by molten Al and an Al-Si alloy', *Ceramics International*, 41(3), pp. 4360–4373. doi: 10.1016/j.ceramint.2014.11.126.

Owens, D. K. (1969) 'Estimation of the Surface Free Energy of Polymers', *Journal of applied polymer science*, 13, pp. 1741–1747. doi: https://doi.org/10.1002/app.1969.070130815.

P.Giannozzi (2017) 'Advanced capabilities for materials modelling with Quantum ESPRESSO', *Journal of Physics: Condensed Matter*, 29, pp. 1–30. Available at: https://doi.org/10.1088/1361-648X/aa8f79.

Pawlowski, L. (2009) 'Suspension and solution thermal spray coatings', *Surface and Coatings Technology*, 203(19), pp. 2807–2829. doi: 10.1016/j.surfcoat.2009.03.005.

Perdew JP, Burke K, E. M. (1996) 'Generalized gradient approximation made simple', *Phys Rev Lett.*, 77(18), pp. 3865–3868. Available at: doi: 10.1103/PhysRevLett.77.3865.

Pfender, E. (1999) 'Thermal plasma technology: Where do we stand and where are we going?',

Plasma Chemistry and Plasma Processing, 19(1), pp. 1–31. doi: 10.1023/A:1021899731587.

Pfrommer, B. G. *et al.* (1997) 'Relaxation of Crystals with the Quasi-Newton Method', *Journal of Computational Physics*, 131(1), pp. 233–240. doi: 10.1006/jcph.1996.5612.

Pradhan, S. *et al.* (2015) 'Wear characteristics of Al-AlN composites produced in-situ by nitrogenation', *IOP Conference Series: Materials Science and Engineering*, 75(1). doi: 10.1088/1757-899X/75/1/012034.

Pratap, B., Bhatt, V. and Chaudhary, V. (2015) 'A Review on Thermal Spray Coating', *International Journal of Scientific & Engineering Research*, 6(5), pp. 53–61.

Pulay, P. and Fogarasi, G. (2004) 'Fock matrix dynamics', *Chemical Physics Letters*, 386(4–6), pp. 272–278. doi: 10.1016/j.cplett.2004.01.069.

Qiu, Y. and Gao, L. (2003) 'Nitridation reaction of aluminum powder in flowing ammonia', *Journal of the European Ceramic Society*, 23(12), pp. 2015–2022. doi: 10.1016/S0955-2219(03)00014-1.

Quesnel, S., Afshar, S. and Allaire, C. (1996) 'Corrosion of refractories at the bellyband of aluminum melting and holding furnaces', in *Light Metals 1996 Annual meeting and exhibition of the Minerals, Metals and Materials Society (TMS), Anaheim (CA), USA, 4-8 Feb. 1996; Ed. W. Hale*, pp. 661–667.

Quesnel, S., Allaire, C. and Afshar, S. (1998) 'Criteria for choosing refractories in aluminum holding and melting furnaces', in *Light Metals 1998 Annual meeting and exhibition of the Minerals, Metals and Materials Society (TMS), San Antonio (TX), USA, 15-19 Feb. 1998; Ed. B. Welch*, pp. 1391–1402.

Raczkowski, D., Canning, A. and Wang, L. W. (2001) 'Thomas-Fermi charge mixing for obtaining self-consistency in density functional calculations', *Physical Review B - Condensed Matter and Materials Physics*, 64(12), pp. 1–4. doi: 10.1103/PhysRevB.64.121101.

Reusch, F., Gmbh, D. U. and Rudolph, S. (2015) 'Use of Boron Nitride Coatings with Aluminum Casting Technology', *Scanning*, pp. 77–80. Available at: https://www.alu-stop.de/download/pdf/gi0893.pdf.

Ribeiro, G. C. *et al.* (2016) 'Thermal shock resistance of a refractory castable containing andalusite aggregate', *Ceramics International*, 42(16), pp. 19167–19171. doi: 10.1016/j.ceramint.2016.09.079.

Rivoaland, L. (2016) 'Development of a new type of cathode for aluminium electrolysis', in *Proceedings of ICSOBA 2016 Conference*, p. 9.

Rizolli, C. *et al.* (2002) 'No Title', *Journal of Alloys and Compounds*, 343, pp. 135–141.

Roberts, W. H. (1987) 'Surface engineering.', 5, pp. 10–30.

Rounaghi, S. A. *et al.* (2012) 'Formation of nanocrystalline h-AlN during mechanochemical decomposition of melamine in the presence of metallic aluminum', *Journal of Solid State Chemistry*, 190, pp. 8–11. doi: 10.1016/j.jssc.2012.01.005.

Rounaghi, S. A. *et al.* (2016) 'Mechanochemical route to the synthesis of nanostructured Aluminium nitride', *Scientific Reports*, 6, pp. 1–11. doi: 10.1038/srep33375.

Rounaghi, S. A. *et al.* (2017) 'A combined experimental and theoretical investigation of the Al-Melamine reactive milling system: A mechanistic study towards AlN-based ceramics', *Journal of Alloys and Compounds*, 729, pp. 240–248. doi: 10.1016/j.jallcom.2017.09.168.

Rounaghi, S. A. *et al.* (2019) 'Mechanochemical reaction of Al and melamine: A potential approach towards the: In situ synthesis of aluminum nitride-carbon nanotube nanocomposites', *Physical Chemistry Chemical Physics*, 21(39), pp. 22121–22131. doi: 10.1039/c9cp04577e.

Rulison, C. (1999) 'Measure surface energy: A tutorial designed to provide basic understanding of the concept of solid surface energy', *Kruss USA*, p. 40.

Rulison, C. (2005) 'Effect of Temperature on the Surface Energy of Solids Effect of Temperature on the Surface Energy of Solids - Sometimes It Does Matter', *Energy*, pp. 1–2.

Rulison, C. (no date) 'Kruss Thechnical Note. So You Want to Measure Surface Energy ?', 49(40).

S.-L.Chen *et al.* (2002) 'The PANDAT Software Package and and its Applications', *Calphad*, 26(2), pp. 175–188.

Sadik, C., Amrani, I. E. El and Albizane, A. (2014) 'Recent advances in silica-alumina refractory : A review', *Journal of Asian Ceramic Societies*, 2(2), pp. 83–96. doi: 10.1016/j.jascer.2014.03.001.

Sakamoto, A. H. (2013) 'Fused siliceous refractory and production method thereof'. Available at: https://patentimages.storage.googleapis.com/ce/e2/35/405619c09feaef/EP1840101A2.pdf.

Salomon, A. *et al.* (2017) 'Formation of different alumina phases and magnesium aluminate spinel during contact of molten AlSi7Mg0.6 alloy with mullite and amorphous silica', *Corrosion Science*, 114, pp. 79–87. doi: 10.1016/j.corsci.2016.10.023.

Sardar, K. and Rao, C. N. R. (2005) 'AlN nanocrystals by new chemical routes', *Solid State Sciences*, 7(2), pp. 217–220. doi: 10.1016/j.solidstatesciences.2004.10.008.

Sarina Bao *et al.* (2016) 'Light metals 2012', in Suarez C.E (ed.) *Light Metals 2012*, pp. 1057–1062. doi: 10.1007/978-3-319-48179-1.

Scheid, A., Schreiner, W. H. and D'Oliveira, A. S. C. M. (2012) 'Effect of temperature on the reactivity between a CoCrMoSi alloy and 55 wt% AlZn baths', *Corrosion Science*, 55, pp. 363–367. doi: 10.1016/j.corsci.2011.10.040.

Shahien, M. *et al.* (2010a) 'Cubic aluminum nitride coating through atmospheric reactive plasma nitriding', *Journal of Thermal Spray Technology*, 19(3), pp. 635–641. doi: 10.1007/s11666-010-9469-0.

Shahien, M. *et al.* (2010b) 'Fabrication of AlN coatings by reactive atmospheric plasma spray nitriding of Al powders', *Materials Transactions*, 51(5), pp. 957–961. doi: 10.2320/matertrans.T-M2010804.

Shahien, M. *et al.* (2011a) 'Controlling of nitriding process on reactive plasma spraying of Al particles', *IOP Conference Series: Materials Science and Engineering*, 18(SYMPOSIUM 14). doi: 10.1088/1757-899X/18/20/202006.

Shahien, M. *et al.* (2011b) 'In situ fabrication of AlN coating by reactive plasma spraying of Al/AlN powder', *Coatings*, 1(2), pp. 88–107. doi: 10.3390/coatings1020088.

Shahien, M. *et al.* (2011c) 'In Situ Fabrication of AlN Coating by Reactive Plasma Spraying of Al/AlN Powder', *Coatings*, 1(2), pp. 88–107. doi: 10.3390/coatings1020088.

Shahien, M. *et al.* (2011d) 'Reactive atmospheric plasma spraying of AlN coatings: Influence of aluminum feedstock particle size', *Journal of Thermal Spray Technology*, 20(3), pp. 580–589. doi: 10.1007/s11666-010-9582-0.

Shahien, M. *et al.* (2012) *Controlling of Feedstock Powder Material upon Fabrication of AlN Coating in Reactive Atmospheric Plasma Spray Process*. Toyohashi University of Technology, Japan.

Shahien, M. *et al.* (2013a) 'N_2 and H_2 plasma gasses' effects in reactive plasma spraying of Al2O3 powder', *Surface and Coatings Technology*, 216, pp. 308–317. doi: 10.1016/j.surfcoat.2012.11.062.

Shahien, M. *et al.* (2013b) 'Synthesis of cubic aluminum nitride coating from Al_2O_3 powder in reactive plasma spray process', *Materials Transactions*, 54(2), pp. 207–214. doi: 10.2320/matertrans.T-M2012831.

Shahien, M., Yamada, M. and Fukumoto, M. (2016) 'Challenges Upon Reactive Plasma Spray Nitriding: Al Powders and Fabrication of AlN Coatings as a Case Study', *Journal of Thermal Spray Technology*, 25(5), pp. 851–873. doi: 10.1007/s11666-016-0412-x.

Shahien, M., Yamada, M. and Fukumoto, M. (2018) 'Influence of Transient Liquid Phase Promoting Additives upon Reactive Plasma Spraying of AlN Coatings and Its Properties', *Advanced Engineering Materials*, 20(6), pp. 1–14. doi: 10.1002/adem.201700917.

Shatnawi, M., Al-Mansi, W. and Arafa, I. (2008) 'Formation of Si-C-N ceramics from melamine-carbosilazane single source precursors', *Journal of Solid State Chemistry*, 181(1), pp. 150–157. doi: 10.1016/j.jssc.2007.11.009.

Shen, P. *et al.* (2003a) 'Reactive wetting of molten Al on different oriented α-Al_2O_3 single crystals at high temperatures', *Scripta Materialia*, 49(6), pp. 563–569. doi: 10.1016/S1359-

6462(03)00336-1.

Shen, P. *et al.* (2003b) 'The influence of surface structure on wetting of α-Al_2O_3 by aluminum in a reduced atmosphere', *Acta Materialia*, 51(16), pp. 4897–4906. doi: 10.1016/S1359-6454(03)00332-X.

Shi, L. *et al.* (2016a) 'Reactive wetting of amorphous silica by molten Al-Mg alloys and their interfacial structures', *Applied Surface Science*, 377, pp. 340–348. doi: 10.1016/j.apsusc.2016.03.162.

Shi, L. *et al.* (2016b) 'Reactive wetting of amorphous silica by molten Al-Mg alloys and their interfacial structures', *Applied Surface Science*, 377, pp. 340–348. doi: 10.1016/j.apsusc.2016.03.162.

Shukla, D. P. (2009) *Anti wetting additives for aluminosilicate refractories in molten aluminum contact applications*. Ph.D Thesis, Missouri university of science and thechnology.

Sidhu, T. S., Prakash, S. and Agrawal, R. D. (2005) 'State of the art of HVOF coating investigations - A review', *Marine Technology Society Journal*, 39(2), pp. 53–64. doi: 10.4031/002533205787443908.

Siegel, A., Parlinski, K. and Wdowik, U. D. (2006) 'Ab initio calculation of structural phase transitions in AlN crystal', *Physical Review B - Condensed Matter and Materials Physics*, 74(10), pp. 1–6. doi: 10.1103/PhysRevB.74.104116.

Siegel, D. J., Hector, L. G. and Adams, J. B. (2003) 'Ab initio study of Al-ceramic interfacial adhesion', *Physical Review B - Condensed Matter and Materials Physics*, 67(9), pp. 1–4. doi: 10.1103/PhysRevB.67.092105.

Siljan, O. *et al.* (2002) 'Refractories for Molten Aluminum Contact Part I : Thermodynamics and', *Refractories Applications and News*, 7(6), pp. 17–25. Available at: file:///C:/Users/fbara/Downloads/Refractories for Molten Aluminum Contact Part I-TH (1).pdf.

Smolen, D. and Dominik, P. (2013) 'Synthesis of aluminium nitride nanopowder', *Ceramic materials*, 65(1), pp. 4–7.

Sobczak, N. (2005) 'Wettability and reactivity between molten aluminum and selected oxides', *Solid State Phenomena*, 101–102, pp. 221–226. doi: 10.4028/www.scientific.net/SSP.101-102.221.

Sobczak, N. *et al.* (2010) 'The mystery of molten metal', *China Foundry*, 7(4), pp. 425–437.

Solheim, A. (2018) 'Inert Anodes---the Blind Alley to Environmental Friendliness?', in Martin, O. (ed.) *Light Metals 2018*. Cham: Springer International Publishing, pp. 1253–1260.

Solheim, A. (2019) *Is aluminium electrolysis using inert anodes a blind alley?*, *SINTEF*. Available at: https://blog.sintef.com/sintefenergy/energy-effici (Accessed: 15 May 2020).

Song, K. *et al.* (2019) 'Interaction of surface energy components between solid and liquid on wettabilit', *Polymers*, 11(3), p. 498. doi: 10.3390/polym11030498.

Soofi, M., Binz, L. and Anderson, M. W. (2018) 'Protective coating composition for molten aluminium and alkali metal environments'. Available at: https://data.epo.org/publication-server/rest/v1.0/publication-dates/20180214/patents/EP3281929NWA1/document.pdf.

Von Stackelberg, M. and Spiess, K. F. (1935) 'Z. Phys. Chem., Abt. A: Chem. Therm., Kin., Elek., Eigen.', 175, p. 140.

Sudha, P. N. *et al.* (2018) 'Corrosion of ceramic materials', in Thomas, S., Balakrishnan, P., and Sreekala, M. S. (eds) *Fundamental Biomaterials: Ceramics*. 1st edn. Duxford, United Kingdom: Woodhead Publishing, pp. 223–250. doi: 10.1016/B978-0-08-102203-0.00009-3.

Sun, J. F. *et al.* (2009) 'Synthesis of titanium nitride powders by reactive ball milling of titanium and urea', *Journal of Alloys and Compounds*, 482(1–2), pp. 29–31. doi: 10.1016/j.jallcom.2009.04.043.

Sung, M.-C. *et al.* (2017) 'Two-stage plasma nitridation approach for rapidly synthesizing aluminum nitride powders', *Journal of Materials Research*, 32(07), pp. 1279–1286. doi: 10.1557/jmr.2016.505.

Sutcliffe, B. T. and Woolley, R. G. (2012) 'On the quantum theory of molecules', *Journal of Chemical Physics*, 137(22). doi: 10.1063/1.4755287.

Tao, Y. *et al.* (2015) 'Adhesion strength and nucleation thermodynamics of four metals (Al, Cu, Ti, Zr) on AlN substrates', *Applied Surface Science*, 357, pp. 8–13. doi: 10.1016/j.apsusc.2015.08.243.

Taranets, N. Y. and Naidich, Y. V. (1996) 'Wettability of aluminum nitride by molten metals', *Powder Metallurgy and Metal Ceramics*, 35, pp. 282–285. Available at: https://doi.org/10.1007/BF01328834.

Tejero-Martin, D. *et al.* (2019) *Beyond Traditional Coatings: A Review on Thermal-Sprayed Functional and Smart Coatings*, *Journal of Thermal Spray Technology*. Springer US. doi: 10.1007/s11666-019-00857-1.

The-Aluminum-Association (2011) 'Aluminum: The element of sustainability', *A-North-American-Aluminum-Industry-Sustainability-Report*, (September), pp. 1–70. Available at: https://www.aluminum.org/sites/default/files/Aluminum_The_Element_of_Sustainability.pdf.

Thompson, M. P. *et al.* (2001) 'Deposition factors and band gap of zinc-blende AIN', *Journal of Applied Physics*, 89(6), pp. 3331–3336. doi: 10.1063/1.1346999.

Tost, M. *et al.* (2018) 'Metal mining's environmental pressures: A review and updated estimates on CO2 emissions, water use, and land requirements', *Sustainability*, 10(8), pp. 1–14. doi: 10.3390/su10082881.

Toy, C. and Scott, W. D. (1997) 'Wetting and spreading of molten aluminium against AIN surfaces', *Journal of Materials Science*, 32(12), pp. 3243–3248. doi: 10.1023/A:1018671222266.

Tsunekawa, Y. *et al.* (1996) 'Chromium-nitride in situ composites with a compositional gradient formed by reactive DC plasma spraying', *Journal of Thermal Spray Technology*, 5(2), pp. 139–144.

Tsunekawa, Y., Hiromura, M. and Okumiya, M. (2000) 'Nitride Formation in Synthesis of Titanium Aluminide Matrix Composite Coatings by Reactive RF Plasma Spraying', *Journal of Thermal Spray Technology*, 9(1), pp. 83–89. doi: 10.1361/105996300770350096.

V.M. Bulanova *et al.* (2005) 'No Title', *Dopov. Nats. Akada. Ukr*, 4, pp. 87–94.

Vardelle, M. *et al.* (2001) 'Controlling particle injection in plasma spraying', *Journal of Thermal Spray Technology*, 10(2), pp. 267–284. doi: 10.1361/105996301770349367.

Venkatramani, N. (2002) 'Industrial plasma torches and applications', *Current Science*, 83(3), pp. 254–262. doi: 10.2307/24106883.

Vicario, I. *et al.* (2015) 'A novel procedure for the evaluation of new refractories for aluminium furnaces', *10th European conference on industrial furnaces and boilers (INFUB-10)*, (April). Available at: http://hdl.handle.net/11556/135%0AISBN: 978-972-99309-7-3.

Visuttipitukul, P., Aizawa, T. and Kuwahara, H. (2003) 'Advanced plasma nitriding for aluminum and aluminum alloys', *Materials Transactions*, 44(12), pp. 2695–2700. doi: 10.2320/matertrans.44.2695.

Vollstadt, H. *et al.* (1990) 'Ser. B', *Proceedings of japan academy*, 62, p. 7.

W.McCauley, J. (1994) 'Structure and properties of Aluminum Nitride and ALON ceramics', *Army research laboratory*, 11(September 1973), pp. 1–7.

Weirauch, D. A. (2005) 'Technologically significant capillary phenomena in high-temperature materials processing. Examples drawn from the aluminum industry', *Current Opinion in Solid State and Materials Science*, 9(4–5), pp. 230–240. doi: 10.1016/j.cossms.2006.02.004.

Wenzel, R. N. (1936) 'Resistance of solid surfaces to wetting by water', *Industrial and Engineering Chemistry Research*, 28(8), pp. 988–994. doi: 10.1021/ie50320a024.

Wu, N. C. *et al.* (2000) 'Morphology and formation mechanism of aluminum nitride nanocrystals synthesized by chemical vapor deposition', *Journal of Crystal Growth*, 208(1), pp. 189–196. doi: 10.1016/S0022-0248(99)00390-5.

Wynn, B. A., Coppack, J. and Steele, T. (2014) *Methods of assessing monolithic refractories for material selection in aluminium melt-hold furnaces*, *Aluminium International Today*.

Yadav, S. K., Wang, J. and Liu, X.-Y. (2016) 'First-principles modeling of zincblende AlN

layer in Al-AlN-TiN multilayers', (19 (2)), pp. 1–17.

Yaddanapudi, K. (2018) 'First-principles study of structural phase transformation and dynamical stability of cubic AlN semiconductors', *AIP Advances*, 8(12). doi: 10.1063/1.5054697.

Yamada, M. *et al.* (2004a) 'Fabrication of silicon nitride thick coatings by reactive RF plasma spraying', *Materials Transactions*, 45(12), pp. 3304–3308. doi: 10.2320/matertrans.45.3304.

Yamada, M. *et al.* (2004b) 'Fabrication of Silicon Nitride Thick Coatings by Reactive RF Plasma Spraying', 45(12), pp. 3304–3308. Available at: doi:10.2320/matertrans.45.3304.

Yamada, M. *et al.* (2005) 'Fabrication of aluminum nitride coating by reactive RF plasma spraying', *Yosetsu Gakkai Ronbunshu/Quarterly Journal of the Japan Welding Society*, 23(1), pp. 143–149. doi: 10.2207/qjjws.23.143.

Yamada, M., Nakamura, H., *et al.* (2006) 'Influence of substrate materials upon fabrication of aluminum nitride coatings by reactive RF plasma spraying', *Materials Transactions*, 47(7), pp. 1671–1676. doi: 10.2320/matertrans.47.1671.

Yamada, M., Akamura, H., *et al.* (2006) 'Influence of substrate materials upon fabrication of aluminum nitride coatings by reactive RF plasma spraying', *Materials Transactions*, 47(7), pp. 1671–1676. doi: 10.2320/matertrans.47.1671.

Yamada, M. *et al.* (2007) 'Nitridation of aluminum particles and formation process of aluminum nitride coatings by reactive RF plasma spraying', *Thin Solid Films*, 515(9), pp. 4166–4171. doi: 10.1016/j.tsf.2006.02.054.

Yan, M. and Fan, Z. (2001) 'Durability of materials in molten aluminum alloys', *Journal of Materials Science*, 36(2), pp. 285–295. doi: 10.1023/A:1004843621542.

Yang, K. *et al.* (2013) 'Role of substrate temperature on microstructure formation in plasma-sprayed splats', *Surface and Coatings Technology*, 214, pp. 138–143. doi: 10.1016/j.surfcoat.2012.11.016.

Yang, W. *et al.* (2017) 'Thermodynamics analysis of carbothermal-chlorination reduction in aluminum production', *Applied Thermal Engineering*, 111, pp. 876–883. doi: 10.1016/j.applthermaleng.2016.09.156.

Yang, Y. Sen and Cho, T. P. (2013) 'Effect of annealing temperature on the water contact angle of PVD hard coatings', *Materials*, 6(8), pp. 3373–3386. doi: 10.3390/ma6083373.

Yildirim, I. (2001) 'Surface Free Energy Characterization of Powders', (April), pp. 1–50. Available at: https://vtechworks.lib.vt.edu/handle/10919/27525.

Yin, S. *et al.* (2018) 'Cold spray additive manufacturing and repair: Fundamentals and applications', *Additive Manufacturing*, 21(April), pp. 628–650. doi: 10.1016/j.addma.2018.04.017.

Young, E. J. *et al.* (2000) 'Low pressure plasma spray coatings', *Thin Solid Films*, 377–378, pp. 788–792. doi: 10.1016/S0040-6090(00)01452-8.

Young, R. . and Pfender, E. (1987) 'Nusselt number correlations for heat transfer to small spheres in thermal plasma flows', *Plasma Chem Plasma Process*, 49(7), pp. 211–229. Available at: https://doi.org/10.1007/BF01019179.

Yurkov, A. (2015) *Refractories for aluminium: Electrolysis and the cast house*, *springer*. Moscow, Russia. doi: 10.1007/978-3-319-11442-2.

Yurkov, A. (2017) *Refractories for aluminum: Electrolysis and the cast house*. Moscow, Russia: Springer International Publishing. doi: 10.1007/978-3-319-53589-0.

Yurkov, A. L. and Pikhutin, I. A. (2009) 'Corrosion of aluminosilicate refractories by molten aluminum and melts based upon it in melting and casting units', *Refractories and industrial*, 50(3), pp. 212–219. Available at: https://doi.org/10.1007/s11148-009-9184-x%0A%0A.

Zatorski, R. A. and Davis, G. D. (2005) 'Thermal spray processes', *Handbook of Adhesion: Second Edition*, 5, pp. 542–545. doi: 10.1002/0470014229.ch18.

Zhang, J., Hosemann, P. and Maloy, S. (2010) 'Models of liquid metal corrosion', *Journal of Nuclear Materials*, 404(1), pp. 82–96. doi: 10.1016/j.jnucmat.2010.05.024.

Zhang, X. and Chen, W. (2015) 'Review on corrosion-wear resistance performance of materials in molten aluminum and its alloys', *Transactions of Nonferrous Metals Society of China*, 25(6), pp. 1715–1731. doi: 10.1016/S1003-6326(15)63777-3.

Zhang, X. M. and Chen, W. P. (2015) 'Review on corrosion-wear resistance performance of materials in molten aluminum and its alloys', *Transactions of Nonferrous Metals Society of China (English Edition)*, 25(6), pp. 1715–1731. doi: 10.1016/S1003-6326(15)63777-3.

Zhao, H. *et al.* (2006) 'Facile route to metal nitrides through melamine and metal oxides', *Journal of Materials Chemistry*, 16(45), pp. 4407–4412. doi: 10.1039/b611381h.

Zheng, J. *et al.* (2008) '[0001] Oriented aluminum nitride one-dimensional nanostructures: Synthesis, structure evolution, and electrical properties', *ACS Nano*, 2(1), pp. 134–142. doi: 10.1021/nn700363t.

Zhou, X. B. and De Hosson, J. T. M. (1995) 'Influence of surface roughness on the wetting angle', *Journal of Materials Research*, 10(08), pp. 1984–1992. doi: 10.1557/JMR.1995.1984.

Zisman, W. A. (1964) 'Relation of the Equilibrium Contact Angle to Liquid and Solid Constitution', in Fowkes, F. M. (ed.) *Contact Angle, Wettability, and Adhesion*. AMERICAN CHEMICAL SOCIETY, pp. 1–51. doi: 10.1021/ba-1964-0043.ch001.

Zoriasatin, S. *et al.* (2006) 'No Title', *Journal of Magnetism and Magnetic Materials*, 300, pp. 525–531.

APPENDIX A IMAGES OF RF INDUCTION PLASMA INSTRUMENT AND ITS ACCESSORIES

Figure A-1. RF plasma generator.

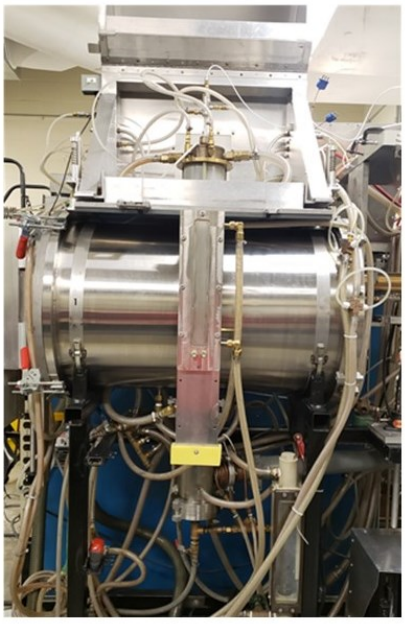

Figure A-2. Deposition chamber and Faraday cage.

Figure A-3. Plasma torch PL-50.

Figure A-4. Atomization probe.

Figure A-5. Supersonic Nozzle.

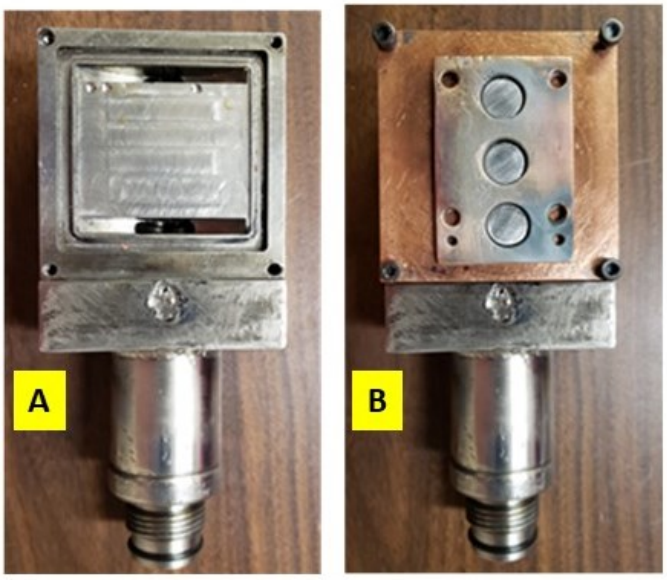

Figure A-6. Sample holder with high-pressure water film circulation channel a) before installing copper plate and substrates and b) after their installation.

Figure A-7. Liquid suspension feedstock preparation system.

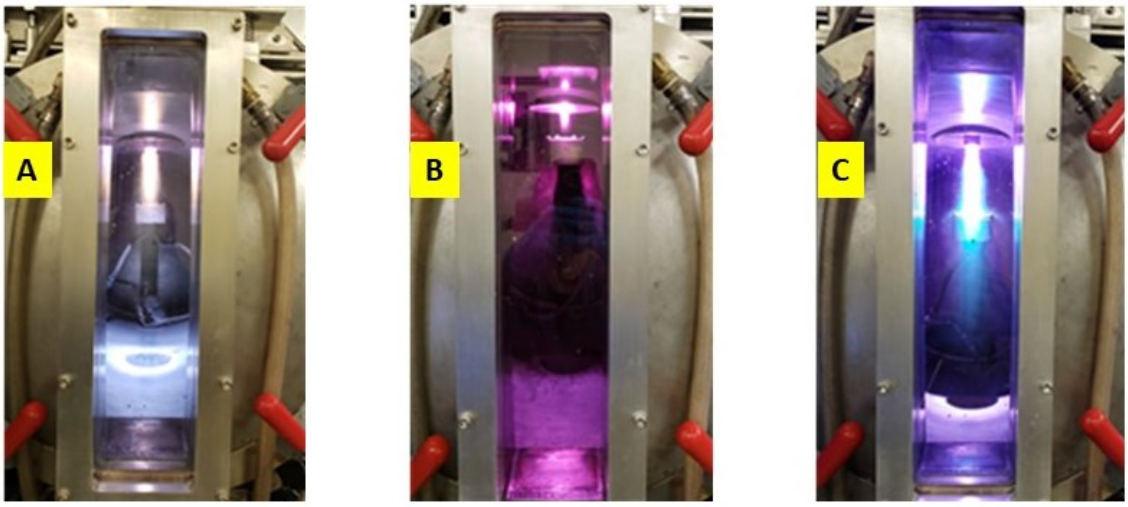

Figure A-8. Plasma plume after (A) ignition with Ar, (B) addition of H_2, (C) suspension injection.

APPENDIX B SURFACE ENERGY CACULATION USING VAN OSS THEORY

In laboratories, the wettability of a solid sample can be studied using the sessile-drop test with the contact angle being measured on a Krüss Advance goniometer. The water contact angle was measured by using a drop shape analyzer (DSA25, KRÜSS, Matthews, NC, USA), equipped with a high-speed camera and a humidity chamber where the temperature can be controlled (See Figure). The analyzer was equipped with a 500-µL syringe with a 24−gauge needle which was used to deposit precisely 2-µL droplets of water at a rate of 2.67 µL/s at the surface of the sample. The height between the sample and the needle tip was set at 5-mm to avoid splashing. The droplet was illuminated from behind through a frosted glass by a blue uniform LED lighting and high-quality optical components to ensure that the dispensed drop is portrayed with the correct shape. The dynamic impact and the image of the droplet at the sample surface was captured via the high-speed camera at a high frame rate of 350 frames per second and analyzed with the ADVANCE software attached to the KRÜSS® apparatus to obtain the contact angle value. This provides the interaction energy between two surfaces by application of the Van Oss-Chaudhury-Good (VCG) theory of wettability (Good, Chaudhury and Oss, 1991), and it works best for inorganic surfaces (Rulison, 1999). In the approach, diiodomethane (CH_2I_2) can be used as a non-polar liquid, while water (H_2O) and formamide (CH_3NO) are used as polar liquids (Amama *et al.*, 2013). In the VCG theory represented by Equation B-1, the surface energy calculation is dependent on the contact angle between the liquid and the solid materials, which are related by Equation B-2 (Barandehfard *et al.*, 2020b).

$$(1+\cos\theta)\gamma_L = 2\left(\sqrt{\gamma_S^{LW}\gamma_L^{LW}} + \sqrt{\gamma_S^{+}\gamma_L^{-}} + \sqrt{\gamma_S^{-}\gamma_L^{+}}\right) \quad \text{Equation B-1}$$

$$\gamma_S = \gamma_S^{LW} + \gamma_S^{AB} = \gamma_S^{LW} + 2\sqrt{\gamma_S^{+}\gamma_S^{-}} \quad \text{Equation B-2}$$

where θ is the contact angle;

γ_L and γ_S are the surface tensions of the liquid and the solid, respectively.

γ_L^{LW} and γ_S^{LW} are the apolar or Lifshitz–van der Waals (LW) interactions;

γ_S^{AB}, $\gamma_L^+\gamma_S^-$ and $\gamma_S^+\gamma_L^-$ are polar or Lewis acid-base (AB) interactions for the liquid (L) and the solid (S).

Surface energy estimation mathematical demonstration:

Table B-1 shows the values of the used liquids total surface tension (γ_L) and their basic (γ_L^-), acid (γ_L^+), and dispersive (γ_L^{LW}) components values.

Table B-1. The values of surface tension and surface tension components of water, formamide, and diiodomethane presented in mJ/m^2 (Modi and Properties, 2016)

Liquid	γ_L (mN/m)	$(\gamma_L^{LW}(mN/m)$	$\gamma_L^+(mN/m)$	$\gamma_L^-(mN/m)$
diiodomethane	50.8	50.8	0.0	0.0
Water	72.8	21.8	25.5	25.5
formamide	58.0	39.0	2.3	39.6

When Diiodomethane (diiodo) was used as contact liquid:

$\gamma_{diiodo}^+, \gamma_{diiodo}^-$ = 0, hence Equation B-1 changed:

$$(1+\cos\theta)\gamma_L = 2\left(\sqrt{\gamma_S^{LW}\gamma_{Diiodo}^{LW}}\right)` \quad \text{Equation B-3}$$

When water was used as contact liquid:

γ_{water}^{LW}= 0, hence Equation B-1 changed:

$$(1+\cos\theta)\gamma_{water} = 2\left(\sqrt{\gamma_S^+\gamma_{water}^-} + \sqrt{\gamma_S^-\gamma_{water}^+}\right) \quad \text{Equation B-4}$$

When formamide (form) was used as contact liquid:

$\gamma_{from}^{LW}, \gamma_{from}^+, \gamma_{from}^- \neq 0$, hence

$$(1+\cos\theta)\gamma_{form} = 2\left(\sqrt{\gamma_S^{LW}\gamma_{form}^{LW}} + \sqrt{\gamma_S^{+}\gamma_{form}^{-}} + \sqrt{\gamma_S^{-}\gamma_{form}^{+}}\right) \quad \text{Equation B-5}$$

The obtained system of Equations (B-3, B-4, B-5) where the contact liquid $\gamma_L, \gamma_L^{LW}, \gamma_L^{-}, \gamma_L^{+}$ are well-known Table B-1 was used to estimate the solid : (1) dispersive surface energy component γ_S^{LW}, (2) acid surface energy component (γ_S^{+}), and (3) basic surface energy component (γ_S^{-}). Finally, Equation B-2 was used to estimate the total surface energy of the surface (γ_S).

Normally, polycarbonate is used as reference material in the analysis and the surface energy is benchmarked against literature data (Hild, 2009), and since surface energies of solids are usually measured at room temperature, for most adhesion energy works, it can be assumed to be similar at elevated temperatures (Rulison, 2005). This assumption is valid for several solids such as chrome-plated steel and not for aluminum foils for instance. It is worth mentioning that the contact angle measurement for the system of Al-ceramic is not simple for two main reasons:

a) The oxidation of Al: the presence of the oxide layer on the surface of the Al will prevent the interface to move, so a non-reliable contact angle will be obtained.
b) Al is a highly reactive metal and due to interfacial reaction between Al and the ceramic, the contact angle will change over time (Fujii and Nakae, 1996).

APPENDIX C INTERFACE OF PLASMA SPRAYED COATINGS AND SUBSTRATE

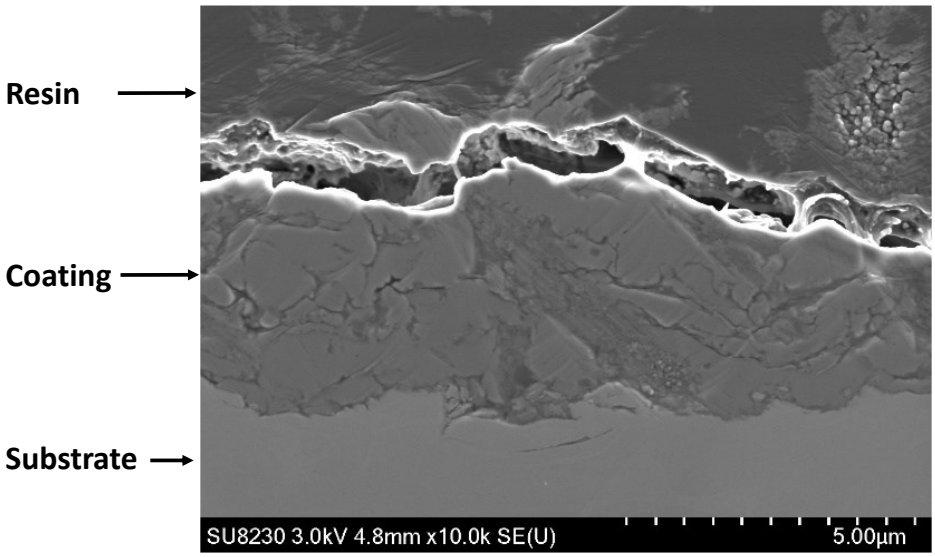

Figure C-1. Cross-sectional view of the AlN-rich coating on carbon steel by SEM imaging.

APPENDIX D FACTSAGE CALCULATION IMAGE

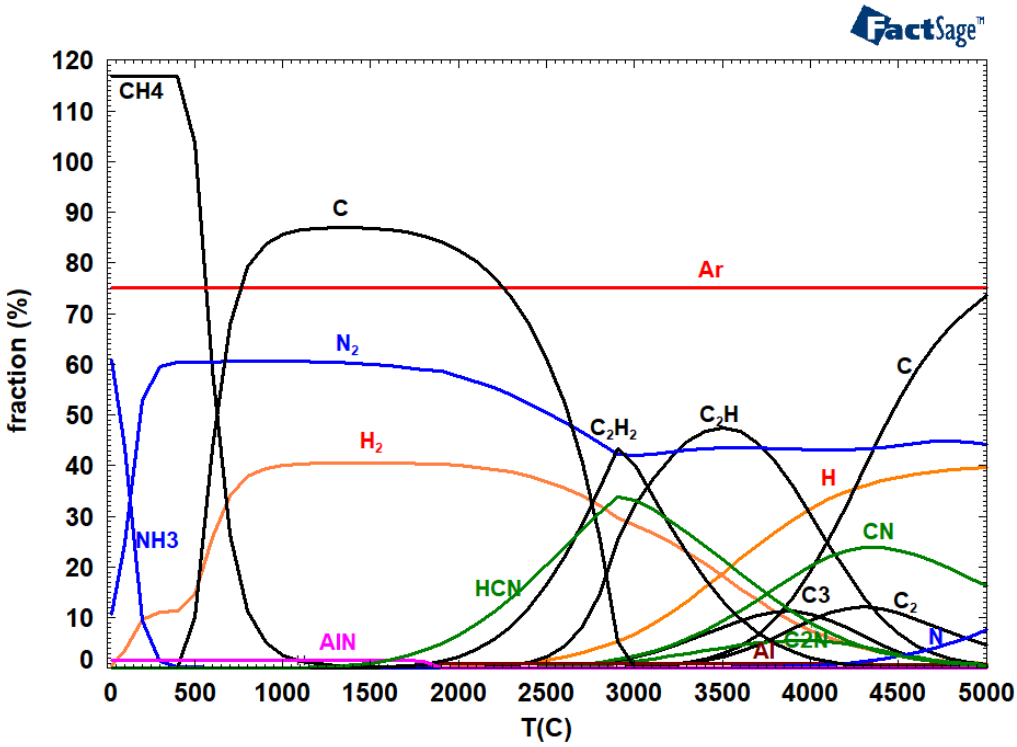

Figure D-1. Thermodynamics plots show the potential of producing AlN from melamine through plasma synthesis. Input in gr: 10 Al, 9 $C_3H_6N_6$, 100 $C_{16}H_{34}$, 75 Ar, 25 H_2, 55 N_2.

"This is not the end

It is not even the beginning of the end

But it is, perhaps, end of the beginning."

Winston Churchill